

Controlled Source Radiomagnetotelluric Method Applications in Near Surface Geophysics

Inaugural-Dissertation
zur Erlangung des Doktorgrades
der Mathematisch-Naturwissenschaftlichen Fakultät
der Universität zu Köln

vorgelegt von
Imamal Muttaqien
Aus Magelang, Indonesien

Köln, 2018

Gutachter: Prof. Dr. B. Tezkan
Prof. Dr. A. Junge

Tag der mündlichen Prüfung: 17.07.2018

Abstract

This thesis deals with the application of the newly developed controlled source radio-magnetotelluric (CSRMT) method in near-surface geophysics. There are three field experiments discussed in this thesis with different objectives and challenges.

The CSRMT method with a horizontal electric dipole as a source is a new and innovative method of near-surface geophysics which development started at around 2010. The transmitter in the CSRMT system generates rectangular signals operating in frequency band 1 - 150 kHz and is then connected to a grounded horizontal electric dipole with a length between 100 - 1000 m. The advantages of the rectangular signals produced by the transmitter that their odd harmonics can be received along the main frequencies. Therefore, by only using 3 - 4 main frequencies, all the CSRMT frequency ranges can be fulfilled on one sounding. Furthermore, the new developed 5 channel CSRMT receivers enable us to estimate the impedance data (apparent resistivity and impedance phase) in tensor form and also to extract the tipper data. During this project, a new processing algorithm was also developed to process the data in both scalar and tensor (apparent resistivity and impedance phase) and also to estimate the tipper data.

The first measurement was carried out in Vuoksa Region around 100 km north of St. Petersburg, Russia in May 2015. The main aim of the survey was the detection of buried faults with the CSRMT method in the far-field zone. The 2D conductivity structures in the far field profile of the survey area are known from geology and mainly consist of crystalline bedrock covered by thin (5 - 10 m) sediments. The profile was also extended to the source, where the plane wave approximation fails. The data from all the field zones were successfully modelled and interpreted using 2D conductivity model including the source.

The second measurement was carried out in Krauthausen (near Aachen), Germany in June 2016. The objective of the survey is to study the conductivity distribution in the hydro-geological test area with CSRMT method. The survey area (on the receiver site) has been studied intensively by many geophysical methods. From the previous DC and RMT measurements, it is assumed that the survey area has 1D conductivity structure down to 20 m. However, both on transmitter and receivers site are contaminated heavily by cultural noises such as pipelines, powerlines, and railways. It is important to understand the effect of cultural noise on CSRMT data to know the limitations of the CSRMT method since it is now hard to find a place without any cultural noises except for very remote areas. One of the effects of cultural noise (pipeline) is current channelling, where the current density flows in one particular direction since the pipeline is much more conductive than the surrounding regardless the polarizations of the injected currents. This current

channelling results in shifted zones (or transmitter), from far-field zone to near-field and transition zone. In this case, the measured data can only be interpreted by considering the buried pipeline as the source.

The third measurement was carried out in Radevormwald (near Wuppertal), Germany in May 2017. The objective of the survey is to investigate probable hydrocarbon contamination in Luftsportverein (LSV) Radevormwald Germany around the simple filling station. The system of the filling station in the LSV Radevormwald is a simple one. The fuel dispensers are placed above the ground. In the past, there was no concrete on the top of the filling stations to cover the ground from possible spill to the ground when the plane was refuelled. After analysing the data, the hydrocarbon contamination was not found.

Zusammenfassung

Die vorliegende Arbeit befasst sich mit der Anwendung der neu entwickelten Controlled Source Radio Magnetotelluric Methode in der oberflächennahen Geophysik. Hier soll auf drei Feldmessungen mit ihren jeweiligen Fragestellungen und Herausforderungen eingegangen werden.

Die CSRMT Methode nutzt einen horizontalen elektrischen Dipol als Quelle und ist eine neue und innovative Methode der oberflächennahen Geophysik, die seit 2010 entwickelt wird. Der Sender des CSRMT Systems generiert Rechtecksignale mit einer Bandbreite zwischen 1-150 kHz und nutzt einen geerdeten horizontalen Dipol mit Längen zwischen 100 m und 1000 m zur Stromeinspeisung. Der Vorteil eines Rechtecksignals als Anregesignal ist die Möglichkeit, neben der Haupt-Frequenz auch die ungeraden Harmonischen des Anregesignals nutzen zu können. Daher kann mit lediglich 3-4 verschiedenen Hauptfrequenzen die komplette CSRMT Bandbreite abgedeckt werden. Zusätzlich kann mit Hilfe des neu entwickelten 5-Kanal CSRMT Empfängers sowohl der Impedanz Datensatz (scheinbarer Widerstand und Impedanz Phase) in Tensorform als auch die Tipperdaten ausgelesen werden.

Die erste Messung wurde im Mai 2015 in der Vuoksa Region ca. 100 km nördlich von St. Petersburg, Russland, durchgeführt. Das Ziel der Messung war die Detektion einer überdeckten Verwerfung mit Hilfe der CSRMT Methode im Fernfeld. Die vorherrschenden 2D Leitfähigkeitsverteilung im Fernfeld-Profil des Messgebietes sind durch geologische Informationen bekannt und bestehen hauptsächlich aus mit gering mächtigen Sedimenten (5-10 m) überdeckten kristallinem Grundgestein. Das Messprofil wurde bis zur Quelle ausgedehnt, nahe der das Sendesignal nicht mehr mit einer ebenen Welle approximiert werden kann. Der Datensatz aus allen Feldzonen konnte erfolgreich modelliert und mit Hilfe eines 2D Leitfähigkeitsmodelles und Hinzunahme der Quelle interpretiert werden.

Die zweite Messung wurde im Juni 2016 in Krauthausen (nahe Aachen), Deutschland, durchgeführt. Mit Hilfe der CSRMT Methode soll die Leitfähigkeitsverteilung in einem hydrogeologischen Testgebiet untersucht werden. Das Messgebiet (empfängerseitig) wurde bereits intensiv mittels verschiedener geophysikalischer Methoden untersucht. Aus den vorangegangenen DC und RMT Messungen ist bekannt, dass in den obersten 20 m des Messgebietes eine 1D Leitfähigkeitsverteilung vorherrscht. Sowohl das Gebiet, in dem die Empfänger stationiert sind, als auch die Region um den Sender ist stark durch kulturelles Rauschen (wie Rohrleitungen, Stromleitungen und der Eisenbahn) kontaminiert. Da inzwischen fast überall kulturelles Rauschen anwesend ist, ist es, um die Grenzen der CSRMT Methode festzustellen, wichtig, den Effekt von kulturellen

Störsignalen auf CSRMT Daten zu verstehen. Ein Effekt von kulturellem Rauschen durch eine Rohrleitung ist die Stromkanalisierung, bei der die Stromdichte unabhängig von der Polarisierung der eingespeisten Ströme in eine bestimmte Richtung fließt, da die Rohrleitung eine höhere elektrische Leitfähigkeit besitzt als ihre Umgebung. Diese Stromkanalisierung resultiert in eine Verschiebung der Feldzonen (oder des Senders), i.e. vom Fernfeld in das Nahfeld/Übergangszonen. In einem solchen Fall können die Messdaten nur interpretiert werden, wenn die Gasleitung als Sender angesehen wird.

Die dritte Messung wurde im Mai 2017 in Radevormwald (nahe Wuppertal) durchgeführt. Ziel der Messung war die Untersuchung einer möglichen Kohlenwasserstoffkontamination im Gebiet des Luftsportvereins (LSV) Radevormwald Deutschland durch eine einfach konstruierte Befüllungsanlage: Die Zapfsule ist oberirdisch angebracht, allerdings war in der Vergangenheit keine Abdeckung auf der Befüllungsanlage angebracht, die den Untergrund vor einer möglichen Kontamination beim Befüllen der Flugzeuge schützt. Die Auswertung der Daten ergab keinen Hinweis auf eine Kohlenwasserstoffkontamination.

Contents

Abstract	i
Zusammenfassung	iii
Contents	v
List of Figures	ix
List of Tables	xvii
1 Introduction	1
1.1 Motivation	1
1.2 Organization of This Thesis	7
1.3 Preliminary Note	8
2 The Controlled Source RMT Method	9
2.1 Electrical Properties of Rocks	9
2.2 Maxwell's Equations	11
2.2.1 Constitutive relation and Boundary Conditions	12
2.2.2 TE and TM modes	13
2.2.3 Electromagnetic wave equations	15
2.3 EM Fields by Horizontal Electric Dipole	17
2.3.1 The CSRMT Field Zones	19
2.4 The SLDMEM3f Forward Modelling Code	28
2.4.1 Finite Difference Approximation in Staggered Grid	28
2.4.2 Material Averaging Scheme	29
2.4.3 The Lanczos Method	30
2.4.4 Griding Scheme	32
2.4.5 Convergence of The Solution	34
2.5 Displacement currents	37
2.6 Cultural Noise	40

3	Inversion of the CSRMT Data	45
3.1	Formulation of the Problem	47
3.2	Non-uniqueness problem	48
3.3	Nonlinearity and Ill-Posedness	50
3.4	Regularization Problem	50
3.5	Rund2Inv code	53
3.5.1	Algorithm	53
3.5.2	Depth of Investigation	55
3.6	Rebocc code	58
3.6.1	Algorithm	58
3.6.2	Representer	60
3.6.3	Calculation of λ	60
3.7	Trial and Error	61
3.8	MARE2DEM	62
3.8.1	Algorithm	62
3.8.2	Point Dipole vs Finite Dipole	66
3.9	MARE2DEM Synthetic Tests	70
3.9.1	Inline Configuration	71
3.9.2	Broadside Configuration	72
3.9.3	Comments and Parameter Selection	76
4	Instrumentation and Data Processing	79
4.1	CSRMT Instrument	79
4.1.1	Transmitter	79
4.1.2	Receiver	81
4.2	Time Series Processing	83
4.3	Fourier Transform on SM25M	85
4.4	Impedance Data Processing	86
4.4.1	Scalar Estimation	86
4.4.2	Tensor Estimation	87
4.4.3	Siegel's Repeated Median Estimator	88
4.4.4	Comparison of Processing Algorithm	89
4.5	Tipper Data Processing	90
4.5.1	Rotation of tipper data	92
4.5.2	Validation of tipper processing	94

5	Field Measurements: Vuoksa Region, St Petersburg, Russia	95
5.1	Introduction	95
5.2	Survey Design and Geology of Test Site	96
5.3	Raw Data and Processing	98
5.4	Modelling	104
5.4.1	The Far Field Zone	104
5.4.2	The Near Field Zone	109
5.4.3	All zones impedance	113
5.5	Discussion	114
6	Field Measurements: Krauthausen Area, Germany	115
6.1	Introduction	115
6.2	Survey Design and Geological Setting	116
6.3	Raw Data and Processing	119
6.4	Additional Measurement	122
6.5	Modelling	123
6.5.1	Inversion of Both Data Sets	123
6.5.2	3D Forward Modelling Study	125
6.5.3	Inversion with MARE2DEM	129
6.6	Discussion	131
7	Field Measurements: Radevormwald Airport, Germany	133
7.1	Introduction	133
7.2	Hydrocarbon Contamination in Soil	134
7.3	Problem with the Connection	135
7.4	Survey Design	138
7.5	Raw Data and Processing	139
7.6	Modelling	141
7.7	Discussion	145
8	Summary & Conclusion	147
	Bibliography	151

Appendix A Example of SLDMEM3f Grid	159
A.1 Grid Example	160
A.2 Output	162
Appendix B Vuoksa Experiment Extended	163
B.1 The far field zone	163
B.2 The near field zone	164
Appendix C Krauthausen Experiment Extended	165
C.1 DOI	165
Appendix D Radervormwald Experiment Extended	167
D.1 DOI	167
D.2 Additional Data Fit	168

List of Figures

1.1	Depth of penetration of various EM methods for 100 Ωm halfspace. Modified after http://emgeo.sdsu.edu/foreward.html	2
1.2	Distributions of radio transmitters compiled by Dr. A. Shlykov. Figure taken from https://www.csrmt.info/rmt-map-eng retrived 19.07.2018. The colours on the transmitter have no meaning. The figure is to be updated on the website.	2
1.3	Illustration of CSRMT method on filed with two perpendicular horizontal electric dipole share common center point as a source. The sounding locations can be anywhere depending on the target(s). Modified after Grayver (2013).	3
2.1	The conductivity of some Earth materials, note that some rocks have overlapping conductivity values. Figure taken from Miensopust (2010), the original is from Palacky (1988).	10
2.2	A very simple 2D conductivity earth model with the strike direction along x axis. The TE mode E_x, H_y, H_z and TM mode H_x, E_y, H_z . Modified after Simpson and Bahr (2005).	14
2.3	Response of simple 2D model of apparent resistivity, phase and tipper for frequency 1 kHz. The solutions are calculated with <code>SLDMEM3f</code> in MT mode. The vertical contact as in Figure 2.2 is located on 400 m, the reisiitivity $\rho_1 = 1/\sigma_1$ on the left is 10 Ωm and on the right, $\rho_2 = 1/\sigma_2$, is 100 Ωm	15
2.4	Theoretical field zones for 100 $\Omega\text{ m}$ halfspace. To be safe in far-field zone, the measurement should start at least 800 m from the source. The skin depth δ is calculated with Equation (2.45).	23
2.5	(a) Apparent resistivity and (b) phase plotted against the distance for inline and broadside configuration for frequency 1 kHz. The dashed black line is 100 Ωm in apparent resistivity and 45° in phase respectively.	24
2.6	Individual components of electric and magnetic fields for inline and broadside configuration for 100 $\Omega\text{ m}$ halfspace.	26
2.7	Individual components of electric and magnetic fields for inline and broadside configuration for 1D situation.	26
2.8	Apparent resistivity and phase curves for inline (left) and broadside (right) configuration for 100 $\Omega\text{ m}$ halfspace for different distance between transmitter and receiver. It is clear that in inline configuration, far-field zone is achieved in shorter distance than broadside configuration.	27

2.9	Apparent resistivity and phase curves for inline (up) and broadside (down) configuration for layered Earth for different distance between transmitter and receiver.	27
2.10	(a) Yee-Lebedev grid cell (b) Material averaging scheme on <code>SLDMEM3f</code> . Figures from Yogeshwar (2014), with the original figure on the right hand side from Weidelt (2000)	29
2.11	Grid design for <code>SLDMEM3f</code> . In vertical direction the grid is discretized with modified logspace according to Martin (2009). While on horizontal direction, the grid is discretized with a non symmetric Cartesian grid. The black line is the dipole.	34
2.12	Evolution of RES, PROGN and EPS during the iteration, printed every 100 Krylov subspace.	35
2.13	Grid check for inductive sources (RMT case).	36
2.14	Grid check for galvanic sources (CSRMT case). Computational time = 78 seconds.	36
2.15	Grid check for galvanic sources (CSRMT case) with modified logspaced grid in all directions. Computational time = 316 seconds.	36
2.16	Individual electromagnetic fields: (a) electric field (E_x) and magnetic fields H_y on (b) and H_z on (c) for x directed 200 m dipole, $x = 0$, $y = 40$ m. The influence on displacement current are seen only on high frequency > 500 kHz on E_x and H_y , while on H_z on all frequency range.	38
2.17	The transfer function for Figure 2.16: (a) apparent resistivity, (b) phase, (c) real tipper and (d) imaginary tipper plotted against frequency. Even the individual components are different, their ratio in forms of transfer functions almost undistorted.	38
2.18	Individual electromagnetic fields: (a) electric field (E_x) and magnetic fields H_y on (b) and H_z on (c) for x directed 200 m dipole, $x = 0$, $y = 1500$ m. The influence on displacement current are seen on frequency from 10 kHz on E_x and H_y , while on H_z on all frequency range.	39
2.19	The transfer function for Figure 2.18: (a) apparent resistivity, (b) phase, (c) real tipper and (d) imaginary tipper plotted against frequency. Even the individual components are different, their ratio in forms of transfer functions almost undistorted.	39
2.20	Typical cultural noise that can be easily found in central Europe: (a) pipeline signs for different purposes, (b) powerline and (c) railway. Not all buried cultural noise have a sign on the ground. All photos by Imamal Muttaqien around Cologne.	41
2.21	Galvanic effects for a conductive (left) and a resistive inclusion (right). Figure from Mien-sopust (2010) original with from Jiracek (1990).	41
2.22	Site 24 MT time series ((a) and (b)) and responses of 1-h time series segment recorded at 128 Hz: apparent resistivity between the measured and predicted electric field components when the controlled source was inactive ((c) and (e)) and during the NS source configuration ((d) and (f)). The XY polarisation refers to the NS direction, and the YX refers to the EW direction. Figure and caption modified from (Escalas et al., 2013)	43
3.1	The simplistic inverse problem.	46
3.2	The inverse problem viewed as a combination of an estimation problem plus an appraisal problem.	47

3.3	An example of a convex function.	48
3.4	A function with local and global minima. Both minimum have zero gradient (first derivative) and also positive curvature.	49
3.5	L curve criterion for real data from Krauthausen Germany with starting model of 50 Ωm , the value of the regularizing parameter λ are in red (a) profile 1 where it is hard to find optimum λ , (b) for profile 2 with oscillatory features.	52
3.6	Figure 3.5(a) is plotted on different scale, the corner is moving depending on the scale of the axis and on the chosen regularization parameter.	52
3.7	Inversion result for resistive basement. Solid white line is sensitivity -3.5, solid black line is $2z^*$ and dashed black line is DOI. The $2z^*$ depth and DOI give overshooting and lies on very small sensitivity	57
3.8	Inversion result for conductive basement. Solid white line is sensitivity -3.5, solid black line is $2z^*$ and dashed black line is DOI. The $2z^*$ depth agrees with the sensitivity while DOI underestimate.	57
3.9	Examples of subsets of data used to calculate the representers. Representers are calculated for data corresponding to the filled squares; the open squares represent the remaining data. (a) First example: p^{th} -stripe pattern where every p^{th} period is selected for all sites (here $p = 6$). (b) Second example: $p^{\text{th}}, s^{\text{th}}$ -checker (with $p = 4$ and $s = 2$) pattern where the selected data form a checker pattern. Figure and text are from Siripunvaraporn and Egbert (2000).	60
3.10	Geometry used in MARE2DEM, x is the strike direction. Only the green region is safe for the inversion of CSEM data in low frequency as marine settings. The red region is where the solutions have some singularities. Figure taken from http://mare2dem.ucsd.edu/?page_id=251	66
3.11	Grid check for MARE2DEM for inline configuration. The dashed black line is the true solution (100 Ωm of apparent resistivity and 45° of phase).	67
3.12	(a) Apparent resistivity and (b) phase plotted against the distance for frequency 1 kHz for inline configuration.	67
3.13	Relative and absolute difference between finite dipole and point dipole length for inline configuration. (a) Apparent resistivity of 100 m (b) phase of 100 m, (c) Apparent resistivity of 1000 m, and (d) phase of 1000 m. The relative difference for apparent resistivity is given in percent, while the absolute difference in phase is given in degree.	68
3.14	Grid check for MARE2DEM for broadside configuration. The dashed black line is the true solution (100 Ωm of apparent resistivity and 45° of phase).	69
3.15	(a) Apparent resistivity and (b) phase plotted against the distance for frequency 1 kHz for broadside configuration.	69
3.16	Relative and absolute difference between finite dipole and point dipole length for broadside configuration. (a) Apparent resistivity of 100 m (b) phase of 100 m, (c) Apparent resistivity of 1000 m, and (d) phase of 1000 m. The relative difference for apparent resistivity is given in percent, while the absolute difference in phase is given in degree.	70

3.17	Synthetic model with few blocky vertical contacts. The source is located at 0,0 m.	71
3.18	The model from the inversion results of synthetic RMT data with MARE2DEM with different w_{hv} (a) 0.3, (b) 0.5, (c) 1, (d) 2, (e) 3.	73
3.19	Inversion results of the synthetic impedance data considering the source with modification of MARE2DEM: (a) impedance data only. (b) joint inversion with the synthetic RMT data. The joint inversion result in (b) is better than the result of single inversion in (a).	74
3.20	1D synthetic model for broadside configuration, the source is located at 0,0 m. In the first option (Figure 3.21)(a), the receivers were located at $-100 - 100$ m with the source on y direction, while in the second option from $20 - 220$ m as in the figure (see also Figure 3.21(b)), with the source in x direction.	74
3.21	The modelling study of broadside configuration can be viewed in two ways (a). The transmitter is in y direction. (b) The transmitter is in x direction. This figure is modified version of Figure 3.10, the red region is where the solutions have many singularities.	75
3.22	Inversion results for broadside configuration of the conductivity model in Figure 3.20 (a) point dipole source, (b) 1000 m finite dipole source. For both inversion, the starting model is homogeneous halfspace of $50 \Omega\text{m}$ with $w_{hv} = 1$	76
3.23	An example of grid design in MARE2DEM. (a) The whole grid, extended to 100 km to all directions in order to satisfy Dirichlet boundary condition, the area of interest where the receivers are located is marked with green rectangle. (b) Zoom in the area of interest of (a) on the yellow box including 500 m air layer. The air resistivity is $10^{13} \Omega\text{m}$	77
4.1	(a) Transmitter, (b) rectangular transmitted signal by the transmitter, note that the frequency is not used in the field. It is for simple illustration only, (c) coherency and (d) an autospectra of 0.5 kHz received on the receiver at 900 m distance from the experiment in Vuoksa, Region Russia in Chapter 5. It is clearly seen the harmonics of the transmitted signal up to 19 th . Note that the main frequency is not shown here.	80
4.2	An example one of the dipole grounding. This picture is from the experiment in Rader-vormwald in Chapter 7.	81
4.3	New data logger, electric antennae and magnetic coils	82
4.4	Comparison of data processed with SM25M and SFA. The data observed from Krauthausen test site on profile 2.	89
4.5	Tipper magnitude on Aachener Weiher Köln along the profile for all frequencies, (a) scalar, azimuth 30° (b) scalar, azimuth 90° (c) tensor, azimuth 30° , (d) tensor, azimuth 90° . Note on different colour scale.	91
4.6	Tipper test on Aachener Weiher Koeln 23.4 kHz (left), 183 kHz right. The blue dots represent non rotated tipper, the red dot represents the rotated tipper. The rotation angles for 23.4 kHz is 30° while for 183 kHz is 40°	93
4.7	Comparison of tipper from new 5 channel receiver derived from SFA with CHYN on Aachener Weiher Köln.	94
5.1	The location of the survey area north of St. Petersburg and the simplified unpublished local geological map of the survey area by the Institute of Earth Sciences of the St. Petersburg University. The CSRMT profile crossing two faults is also indicated.	96

5.2	Locations of the 700 m long transmitter dipole and the CSRMT profile crossing two fault structures. Near-field - transition and far-field zones are marked. TM-mode CSRMT transfer functions in the far-field zone are interpreted by a 2D conductivity model.	97
5.3	Photos from survey (a) the transmitter was located on the car, (b) the profile is located on the road	98
5.4	The coherency (a) and the autospectra (b) of 11.3 kHz received at 900 m distance in the Vuoksa experiment. It is clearly seen the harmonics of the transmitted signal up to 7 th which is the last harmonics on the D2 band (10 – 100 kHz). The sharp lines beside the main frequencies and its harmonics were coming from distant radio transmitters.	99
5.5	Apparent resistivity and phase for frequency 1.5 kHz plotted as a function of distance, the transmitter is located at the right side at 1950 m (not shown). There is a jump on the phase at around 1130 m marked by black dashed line which is considered as the boundary between near-field zone and far field zones.	99
5.6	Data examples from the far field zone: (a) Apparent resistivity, (b) impedance phase from CSRMT and RMT data from station 14. (c) Apparent resistivity, (d) impedance phase from CSRMT and RMT data from station 18.	100
5.7	Data examples from the near field zone: (a) Apparent resistivity, (b) impedance phase from CSRMT and RMT data from station 63. (c) Apparent resistivity, (d) impedance phase from CSRMT and RMT data from station 93.	101
5.8	Tipper data along the profile in the far field zone for frequency 66.6 kHz, rotation -30°. . .	102
5.9	Tipper data along the profile in the near field zone for frequency 66.6 kHz from RMT data, rotation -35°.	103
5.10	L curve of the inversion of CSRMT far field data for different starting models (a) $\rho_0 = 50 \Omega\text{m}$, (b) $\rho_0 = 100 \Omega\text{m}$, (c) $\rho_0 = 250 \Omega\text{m}$, and (d) $\rho_0 = 1000 \Omega\text{m}$. The optimal regularization parameter λ is marked for each curve.	105
5.11	L curve of the inversion of RMT far field data for different starting models (a) $\rho_0 = 50 \Omega\text{m}$, (b) $\rho_0 = 100 \Omega\text{m}$, (c) $\rho_0 = 250 \Omega\text{m}$, and (d) $\rho_0 = 1000 \Omega\text{m}$. The optimal regularization parameter λ is marked for each curve.	105
5.12	(a) Conductivity model from the CSRMT data, $\rho_0 = 100 \Omega\text{m}$, $\lambda = 20$ RMS=1.99%. (b) Conductivity model from the RMT data, $\rho_0 = 100 \Omega\text{m}$, $\lambda = 20$ RMS=1.5%.	106
5.13	Data fit for two stations of the CSRMT data in Figure 5.6. The error bar in the figures are the error floor used in the inversion.	106
5.14	Data fit for frequency 1.5 kHz against the distance. The error bar in the figures are the error floor used in the inversion.	107
5.15	Inversion results of RMT data with <code>Rebbocc</code> including tipper data in the far field zone profile.	107
5.16	Data fit for tipper for selected frequency 66.6 kHz in the far field zone of the RMT data. . .	108
5.17	Inversion results of impedance CSRMT data with <code>MARE2DEM</code> including source in the far field zone profile.	108

5.18	L curve of the inversion of RMT near field data for different starting models (a) $\rho_0 = 50 \Omega\text{m}$, (b) $\rho_0 = 100 \Omega\text{m}$, (c) $\rho_0 = 250 \Omega\text{m}$, and (d) $\rho_0 = 1000 \Omega\text{m}$. The optimal regularization parameter λ is marked for each curve.	109
5.19	Inversion of the RMT data in the near field zone with the starting model of $\rho_0 = 100 \Omega\text{m}$ $\lambda = 20$	110
5.20	Inversion of CSRMT data in the near field zone with <code>MARE2DEM</code> the starting model $100 \Omega\text{m}$ halfspace with $w_{hv} = 1$	110
5.21	Data fitting for station 63 (offset 700 m) and 93 (offset 100 m) plotted against frequency.	111
5.22	Data fit for frequency 1.5 kHz plotted against the distance.	111
5.23	Inversion results of RMT data with <code>Rebbocc</code> including tipper data on the near field zone.	112
5.24	Data fit of tipper, frequency 66.6 kHz in the near field zone.	112
5.25	Impedance inversion of CSRMT data in the all field zone with <code>MARE2DEM</code> with starting model $1000 \Omega\text{m}$ halfspace $w_{hv} = 0.8$	113
5.26	Data fit for frequency 1.5 kHz plotted against the distance in all zones considering the source.	113
6.1	Krauthausen location and field setup. The perpendicular dipole is located at around 1.5 km from the test site (yellow box). (Google, 2018)	116
6.2	The Krauthausen test site area during the survey. Photos by Imamal Muttaqien.	117
6.3	Simplified sketch of the receiver site, modified from Englert (2003). Note that the pipeline was found after analyzing the data. The distance between the profiles to the pipeline are 15, 25 and 35 m. The location of VES sounding is on the profile 2 at 40 m.	118
6.4	Lithology of Krauthausen test site, taken from Englert (2003)	119
6.5	Autospectra for (a) inline and (b) broadside configuration for station 1 in the second profile.	120
6.6	(a) Azimuth distribution of data from inline transmitter, (b) azimuth distribution of data from broadside transmitter. Most of the data from both transmitter were observed from $157.5 - 202.5^\circ$ which is defined for polarization 1. (c) Apparent resistivity, (d) impedance phase of CSRMT data from inline and broadside transmitter derived from the spectra in Figure 6.5.	121
6.7	(a) Apparent resistivity, (b) impedance phase for CSRMT data from all profiles plotted with RMT data.	121
6.8	The measured VES data (left) and 1D inversion of the data (right)	122
6.9	L curve for CSRMT data with different starting model (a) $10 \Omega\text{m}$, (b) $20 \Omega\text{m}$, (c) $50 \Omega\text{m}$, (d) $100 \Omega\text{m}$. The optimal regularization parameter for each starting model is hard to find due to a high oscillation.	123
6.10	L curve for RMT data with different starting model (a) $10 \Omega\text{m}$, (b) $20 \Omega\text{m}$, (c) $50 \Omega\text{m}$, (d) $100 \Omega\text{m}$. The optimal regularization parameter for each starting model is quite hard to find due to a small oscillation.	124

6.11	Inversion result of (a) CSRMT and (b) RMT data for profile 2. Note on different color scale used in both models. The inversion from the CSRMT data show a more resistive structure while the inversion from the RMT data show a more conductive structure.	124
6.12	Simplified pipeline modelling of the observed data. Note that for extended dipole, the pipeline acts as transmitter	126
6.13	RMT data fit by considering the presence of the pipeline. Note that the data are almost not affected on both polarizations.	126
6.14	CSRMT data modelling by considering the presence of the pipeline. The data can not be fitted and the problem of mixing polarizations can not be explained.	127
6.15	Data fitting by considering the pipeline as the shifted/extended dipole for first profile (top), second profile (middle), and third profile (bottom). The error bar on the data is the standard error bar used in the inversion, 5% in the apparent resistivity and 2° in the phase. The solutions for the inline and broadside configuration in this case coincide. . . .	128
6.16	Inversion results of MARE2DEM. The pipeline is approximated as a finite dipole length (1000 m) in broadside configuration. There are in total 21 pairs consist of 2 (a) and 3 stations (b).	129
6.17	Data fit as Figure 6.15 after the inversion with MARE2DEM by considering the pipeline as the transmitter. Instead of apparent resistivity, the data were transformed into \log_{10} impedance.	130
6.18	A quasi 2D conductivity model of profile 2. The 1D conductivity models were extracted from Figure 6.16.	130
7.1	(a) Problematic time series from a loose connection on the electric field antennae, (b) Good (normal) time series.	136
7.2	Autospectra from the problematic (Figure 7.1(a)) and good (Figure 7.1(b)) times series of the electric fields.	136
7.3	The calculated tipper magnitude from the problematic and good time series. When there is no nearby sources of the electromagnetic fields, only the impedance are affected by the problematic while the tipper data are not affected.	137
7.4	Apparent resistivity and phase derived from problematic time series (left) and normal time series (right)	137
7.5	Survey design of CSRMT experiment in Radevormwald airport. Tx is the transmitter location, Rx is the receiver location on the airport, Rx2 is the reference profile.	138
7.6	Geology situation in Radervormwald. The location of the main profile is dominated by clay, siltstone and subordinate sandstone. Figure from https://www.geoportal.nrw/themenkarten	138
7.7	The simple filling station on Radervormwald airport. There was no concrete in the past covering the ground. There might be some hydrocarbon spills into the soil.	139
7.8	A typical electric field time series, blue is N-S, green E-W.	140
7.9	A typical transfer functions from CSRMT measurements on the Radevormwald airport.	140

7.10	Tipper magnitude derived from RMT data on profile 1 and profile 2. Notice on different colour scale. Both maximum magnitude were > 1 .	141
7.11	L curve for different starting model in profile 1.	142
7.12	L curve for different starting model in profile 2.	142
7.13	Conductivity models from profile 1 and profile 2. There is only a small variation from the model	143
7.14	An example of data fitting of apparent resistivity and phase against the frequency in station 10 of profile 1.	143
7.15	An example of data fitting of frequency 65.5 kHz against the distance of profile 1.	144
7.16	Conductivity model of the reference profile. The second layer in the reference profile is more resistive than the second layer from the main profiles	144
7.17	(a) VES data and (b) the resistivity model from the VES data.	145
7.18	1D inversion results of station 10 of profile 1 (near to the filling station), station 2 of reference profile and VES sounding on E-W direction.	146
B.1	Sensitivity of 10^{-3} in white solid line, DOI according to Seher and Tezkan (2007) in dashed back line and $2z^*$ in solid black line of (a) CSRMT data and (b) RMT data in the far field zone profile of Vuoksa experiment in Chapter 5. With this reason, the models are plotted up to 100 m.	163
B.2	Sensitivity of 10^{-3} in white solid line, DOI according to Seher and Tezkan (2007) in dashed back line and $2z^*$ in solid black line of CSRMT data (up) and RMT data (down) in the near field zone profile of Vuoksa experiment in Chapter 5. With this reason, the models are plotted up to 100 m.	164
C.1	Sensitivity of 10^{-3} in white solid line, DOI according to Seher and Tezkan (2007) in dashed back line and $2z^*$ in solid black line of (a) Profile 1 and (b) Profile 2 (c) Profile 3 for the RMT data measured in Krauthausen test area discussed in Chapter 6. With this reason, the models are plotted up to 30 m.	165
D.1	Sensitivity of 10^{-3} in white solid line, DOI according to Seher and Tezkan (2007) in dashed back line and $2z^*$ in solid black line of (a) Profile 1 and (b) Profile 2 for the measured data discussed in Chapter 7. Note that for the Profile 2, the CSRMT and RMT data were inverted together, thus the $2z^*$ shows an oscillation due to different lowest frequency in both methods. With this reason, the models are plotted up to 30 m.	167
D.2	Data fit for station 1 (up) and 17 (down) of Profile 1	168
D.3	Data fit for station 1 (up) and 17 (down) of Profile 2.	168
D.4	Data fit for station 1 (up), 10 (middle) and 17 (down) for the reference profile.	169

List of Tables

2.1	Basic Variables and their symbols and units used in EM geophysics	12
2.2	Electromagnetic fields behaviour generated by horizontal electric dipole in different zones	28
3.1	The inversion codes available in IGM Cologne used in this thesis. The descriptions are given in the text.	45
4.1	The frequency band of the new receiver and the suggested sample length of each band during the experiments.	81
5.1	Current injected during CSRMT measurements in Vuoksa region, Russia	97
6.1	Compilation of the average resistivity from previous DC and EM measurements. The $\bar{\rho}$ is calculated after Spies (1989), with the maximum depth of penetration derived from various method is assumed 20 m, after Langenbach (2017).	115
6.2	Current injected during CSRMT measurements in Krauthausen, Germany	117
6.3	Compilation of the average resistivity from the inversion of RMT data and CSRMT data inverted with MT algorithm. The CSRMT models are not consistent with previous studies and geology.	125
6.4	A revisited compilation of the average resistivity of Table 6.3 from the inversion of RMT data inverted with MT algorithm and CSRMT data inverted with <code>MARE2DEM</code> . The CSRMT models are now consistent with previous studies and geology.	131
7.1	Current injected during CSRMT measurements in Radevormerwald, Germany	139

Chapter 1

Introduction

1.1 Motivation

Electromagnetic methods have been used for about a century to characterize Earth conductivity distribution since the Schlumberger brothers started applying direct current (DC) method. In 1950's magnetotellurics method was introduced by Tikhonov in Russia (Tikhonov, 1950), Rikitake in Japan (Rikitake, 1951) and Cagniard in France (Cagniard, 1953) independently. The magnetotelluric (MT) method uses natural sources which comes from the interaction between solar wind plasma and the geomagnetic field and ionizing effects of solar radiation on the upper atmosphere. The frequency range of the MT method is between 10^{-4} – 10 Hz (even longer periods/lower frequency for crustal studies). Nowadays the MT method has many varieties depending on the frequencies used including audiomagnetotellurics (AMT, 1 Hz – 10 kHz) by also using the signal from worldwide lightning and thunderstorms, and radiomagnetotellurics (RMT, 10 – 1000 kHz) with the distant radio transmitters as the sources. The locations of the sources for all the variants of the MT methods are very far away from the soundings' locations (MT stations) hence the plane wave assumption is valid. In an urbanized area the electromagnetic methods suffer from cultural noises such as pipelines, railways, powerlines. These cultural noises have been known to deteriorate the quality of the useful electromagnetic signals. As a consequence, in order to get better signal to noise ratio and better data quality, controlled source electromagnetic methods (CSEM) were introduced both in time domain (for example: transient electromagnetics (TEM), long offset transient electromagnetics (LOTEM)) and also in frequency domain (for example: controlled source AMT (CSAMT)). The depth of investigations for 100 Ω m halfspace of various EM geophysical methods is depicted in Figure 1.1.

In near-surface geophysics, the radiomagnetotelluric (RMT) method now has gained in popularity especially in Europe where many VLF (very low frequency) transmitters are located (Pedersen et al., 2006) as shown in Figure 1.2. In the first development, it was used for hydrogeological purposes and was in scalar form (Turberg et al., 1994). This RMT method is an extension of the VLF method which operates on frequency range 10 - 30 kHz to higher frequencies up to 1000 kHz. It uses all available radio transmitters located far away from the soundings location (far-field zone) in the frequency range 10 - 1000 kHz. Some successful applications of the RMT method in IGM Cologne are:

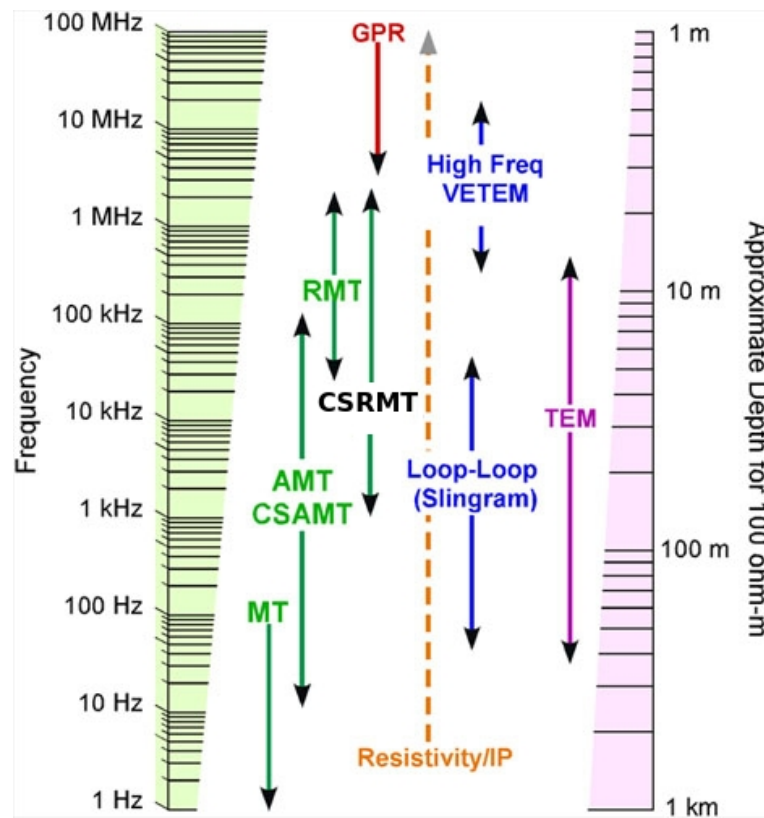


Figure 1.1: Depth of penetration of various EM methods for 100 Ω m halfspace. Modified after <http://emgeo.sdsu.edu/foreward.html>



Figure 1.2: Distributions of radio transmitters compiled by Dr. A. Shlykov. Figure taken from <https://www.csrmt.info/rmt-map-eng> retrieved 19.07.2018. The colours on the transmitter have no meaning. The figure is to be updated on the website.

waste site investigations (Newman et al., 2003), oil-contaminated area study (Tezkan et al., 2005), a characterization of conduction soils (Seher and Tezkan, 2007), locating pipelines (Tezkan, 2008), mapping groundwater contaminations (Yogeshwar et al., 2012), and mapping faults (Widodo et al., 2016).

The RMT method encounters limitations in remote areas where radio transmitters are not available and/or the signals are not strong enough which make RMT soundings not possible (see Figure 1.2). Moreover, sometimes the VLF transmitters are turned off which make the situation for RMT method is even worse. To overcome the problem of lack of stable “natural” sources, a modification of the RMT method with a controlled source in the form of a horizontal electric dipole (HED), as in the CSAMT (Goldstein and Strangway, 1975), with length vary from 100 - 1000 m (depending on many factors: grounding, location, etc.) is introduced. This modification is called controlled source radiomagnetotellurics (CSRMT) and is intended to be applied in remote areas (Saraev et al., 2017).

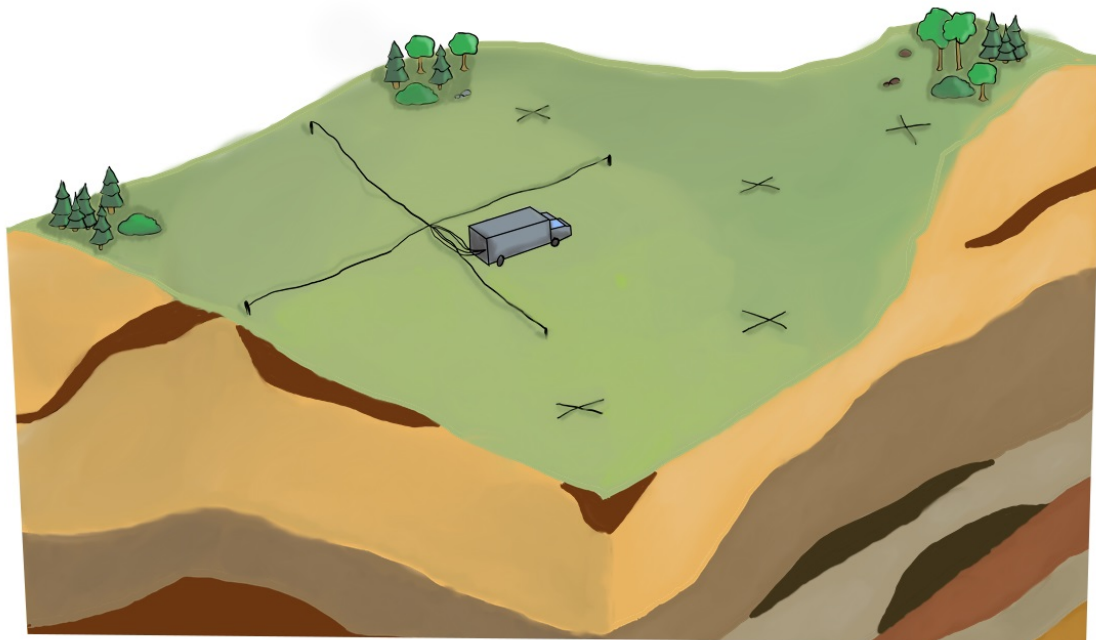


Figure 1.3: Illustration of CSRMT method on filed with two perpendicular horizontal electric dipole share common center point as a source. The sounding locations can be anywhere depending on the target(s). Modified after Grayver (2013).

The field set-up of the CSRMT method is illustrated in Figure 1.3 for a tensor measurement. There are two perpendicular dipoles sharing a common centre point act as the sources for the electromagnetic fields in all directions. This deployment is the ideal scheme, but unfortunately, it is hard to deploy in a field experiment due to many limitations. Consequently, most of the times only one polarizations (a scalar measurement) can be deployed on the field experiments either an inline¹ or a broadside transmitter. The tensor measurements as shown in Figure 1.3 are best used in areas where the structure is very complex and when soundings are far apart relative to the size of geologic features under investigation and in areas with strong regional anisotropy (Zonge and

¹this term is being used in this thesis as in other CSEM method rather than collinear as in CSAMT

Huges, 1991). Moreover, the frequency of the CSRMT is extended to the AMT band to 1 kHz. By lowering to this frequency, the skin depth of the CSRMT triples than the standard RMT. One of the advantages of using the CSRMT is the high signal to noise ratio and better data quality. However, compared to the standard RMT, the CSRMT needs more logistics in the field (also more field crews), is more time consuming for one sounding (3 - 4 times) and for setting up the transmitter, and also needs low grounding resistance for a transmitter which should be less than 100Ω . Salt and/or bentonite could be added to the transmitters' grounding to achieve a low grounding resistance in a high resistive zone. The working area for this CSRMT system starting from 20 m (by taking into account the near-field data) and up to 3 - 4 km where the signal is still strong enough (the signal to noise ratio is still high). In addition, cultural noises such as pipelines, railways, power-lines etc. must also be minimized since they will influence the data that leads to wrong model and interpretations (Zonge and Huges, 1991). For the CSRMT (Controlled Source Radiomagnetotellurics) which is operating from 1 - 1000 kHz, in $100 \Omega \text{ m}$ halfspace, the depth of penetration is approximately between 5 - 100 m (see Figure 1.1).

The Uppsala University in Sweden developed the Enviro-MT system (Bastani, 2001) with double vertical magnetic dipoles as the source for frequency 1 - 12 kHz and combined with available radio transmitter signal. Compared to the horizontal electric dipole, the magnetic dipole is advantageous as they are easier to install. The magnetic dipoles have little coupling to nearby conductive structures compared to the electric dipoles, and they are therefore generally expected to provide better plane-wave conditions and have smaller galvanic distortion effects than electric dipoles (Bastani, 2001). However, their working area is limited to 400 - 800 m. To fulfil far-field conditions which sometimes is hard to achieve when working on a very resistive area and still to have enough signal to noise ratio. The signal from a loop source is weaker than from a dipole source (Zonge and Huges, 1991). Other than that the Enviro-MT system is integrated with a phase-lock technique that helps in estimating reasonably stable transfer functions for CSAMT measurements. The Enviro-MT offers full tensor transfer function. The introduction of this transmitter system was mainly aimed to get deeper depth of investigation of RMT method. Only recently the near-field data from the Enviro-MT system were interpreted (Wang, 2017). Several successful application of Enviro-MT system to investigate groundwater resources (Pedersen et al., 2005; Ismail et al., 2011), investigate quick clay landslides and mapping the fault (Bastani et al., 2011).

The transmitter developed by the University of St. Petersburg generates rectangular signals operating in frequency band 1 - 150 kHz and then connected to a grounded electric dipole. The advantages of the rectangular signals are their odd harmonics besides the main injected frequencies. Therefore, by only using 3 - 4 main frequencies, the whole CSRMT frequency ranges can be fulfilled on one sounding. Furthermore, the new developed 5 channel CSRMT receivers enable us to process/estimate the impedance data (apparent resistivity and phase) in tensor form and also to extract tipper data. However, up to now, the data were only processed in scalar form within the *SM25M* and the *SM+* software and wholly ignored the vertical magnetic field (tipper data). During this project, a new processing algorithm was also developed by Dr Marcus Gurk to process the data in both scalar and tensor (apparent resistivity and phase) and also to estimate the tipper data. The data then were saved in *EDI* file that can be further processed in industrial software such as *WinGlink* and *MTS2DPlot* (Smirnov, 2003) and can be easily exchanged

to the MT community.

The CSRMT method, as the CSAMT method, was originally introduced as a method that worked as the conventional RMT. The measurements were only carried out in the far-field zone where the plane wave approximation is valid (Saraev et al., 2017). However, the electromagnetic fields generated by a finite source behave differently in three different zones: near-field, transition and far-field zones. They are controlled by the induction number $|kr| = r\sqrt{2}/\delta$ where r is the distance between transmitter and receiver and δ is the magnetotelluric skin depth $500\sqrt{\rho/f}$ m. The zone is called near-field zone when $kr \ll 1$. This zone is characterized by steep apparent resistivity slope, more than 45° in a double logarithmic plot, and also zero phase. In the transition zone, the behaviour of apparent resistivity and phase curves are more complex, for example, there is an inflexion point on apparent resistivity and also some negative value of the impedance phase data (I use the convention of $0 < \theta < 90$ on the impedance phase data for “normal” RMT). On these two zones, the waves generated by the HED cannot be approximated as plane waves. In the far-field zones, when plane wave approximation is fulfilled, the electromagnetic fields behave as in the magnetotellurics method even though the source effects might be still present (Zonge and Huges, 1991). Only in the far-field zone, the MT inversion algorithm can be applied to interpret the data. Note that in the MT code the horizontal attenuation of EM fields is not considered. The signal to noise ratio is much higher in the near-field and the transition zones than in the far-field zone (Zonge and Huges, 1991). To maximize the potential of the CSRMT method, the data collected in the near-field and transition zones which are often neglected should also be interpreted and modelled. Furthermore, by incorporating the source in the inversion, the field zones, which are hard to define in the field experiments, could be neglected as in other CSEM method (see for example a review by Streich (2016)).

There are two different methods to interpret CSAMT data (more generally CSEM)². First, by inverting individual components of the electric and magnetic fields, and second, by inverting the impedance data. Sasaki et al. (2015) showed with synthetic data that for near-field and transition zones data the inversion of electric and magnetic fields yields a stable and better solution than the inversion of apparent resistivity and impedance phase in broadside configuration with two conductors as the targets. This result occurs mainly in the transition zone, where both the electric and magnetic fields change with the frequency in a complex manner (for example the magnetic fields dependence on the distance between the transmitter and receiver r is changing from $1/r^2$ to $1/r^3$). In this case, some information might be lost on the conversion from individual electromagnetic fields to apparent resistivity and phase, as described in Zonge and Huges (1991). On the far-field zone, when the target (conductor) located farther away from the source is better defined by apparent resistivity and phase (Sasaki et al., 2015). However, Sasaki et al. (2015) only shows one example with a broadside configuration, hence their result could not be generalized. Note that in a real field situation, sometimes it is hard to define the boundary of the field zones correctly. The condition that the far-field zone satisfies $r/\delta > 5$ can only be applied on homogeneous halfspace and at best in a 1D conductivity

²this term could be interchangeable see <http://zonge.com/geophysical-methods/electrical-em/csamt/>, but in this thesis my definition of the CSEM method is when the data are in the form of the electric and magnetic fields, while the CSMT method is when the data are in the form of impedance (apparent resistivity and phase impedance as well as amplitude), like the MT method.

structure which is rare to be found in the field experiments. The situation is more complicated when the injected currents are channelled in such a way that the field zones are shifted. In other words, it is not an easy task to categorize in which field zones the data belong. In our system, there is no synchronization between the transmitter and receiver and also the injected current was not recorded. As a result, the data are only processed in the impedance (apparent resistivity, phase and impedance amplitude). There is also an alternative approach to interpret the near-field/transition zones data by correcting the apparent resistivity data, so the corrected data can be considered as the far-field zone data. In this approach, the phase data are ignored because they cannot be corrected. The problems with this approach are the followings: (i) The correction cannot be evaluated quantitatively; (ii) it is physically impossible to correct CSAMT data to be MT data when the subsurface conductivity model is unknown. Therefore, some artefacts can be introduced into the resulting conductivity model which might lead to the wrong interpretation (Lu et al., 1999). This alternative approach will not be discussed any further in this thesis.

As stated before, the EM fields generated by HED (and the signal to noise (S/N) ratio) depend on the distance between the transmitter and receiver (offset). In this thesis, the data in the near-field and transition zone were also collected to maximize the potential of the CSRMT method. To interpret these data, a modified `MARE2DEM` (Key, 2016; Wang, 2017) was applied in all the field zones by removing the zones' boundaries. This new approach would lead us to more flexibility in the future. On `MARE2DEM` that I use in this thesis, the dipole is approximated as a point source for inline configuration while on broadside configuration a finite dipole length could also be applied in two dimensions. In addition, `SLDMEM3f` is also applied to interpret the near-field data with trial and error process qualitatively as the first approximation. Both `SLDMEM3f` and `MARE2DEM` could be used as a complementary approach to interpreting the CSRMT data in all zones.

All the developed codes used in this thesis neglecting the role of displacement currents. Thus, the MT approximation should be discussed in this case since the frequency of the CSRMT method is quite high (at least in the transition between low (MT) and high (GPR)). The displacement currents on high frequencies (VLF/RMT) were considered by Persson and Pedersen (2002) and Kalscheuer et al. (2008). However Shlykov and Saraev (2015) showed that displacement current could be neglected if only apparent resistivity and impedance phase data are processed. Shlykov and Saraev (2015) stated that displacement current influenced individual components of electric and magnetic fields and also tipper data.

During my PhD studies, three different CSRMT measurements were carried out for different purposes. The first CSRMT measurement was carried out in Vuoksa Region around 100 km north of St. Petersburg, Russia in May 2015. The main aim of the survey was the detection of buried faults with the CSRMT method in the far-field zone. Two-dimensional conductivity structures on the far-field profile of the survey area are known from previous RMT surveys and mainly consist of crystalline bedrock covered by thin (5 - 10 m) sediments. Some publications have reported the correlation between conductivity structures and earthquakes, i.e. Wannamaker et al. (2004); Nurhasan et al. (2006); Widodo et al. (2016). Suzuki et al. (2000) stated that CSAMT is an effective method for defining an outline of geological structures around a fault several hundred meters deep and also

to identify a resistivity boundary between different kinds of bedrock with a fault contact. The profile was also extended to the near-field and transition zones.

The second measurement of CSRMT method was carried out in Krauthausen (near Aachen), Germany in June 2016. The objective of the survey is to study the conductivity distribution in a hydro-geological test area with CSRMT method. The survey area (on the receivers) has been studied intensively by many geophysical methods, for example, RMT (Nix, 2005), DC (Gössling, 2004), a velocity of groundwater measurement (Englert, 2003) and hydraulic conductivity from IP measurement (Hördt et al., 2007). From the previous DC and RMT measurements, the survey area has a one-dimensional conductivity structure down to 20 m depth. However, both on transmitter and receivers site are contaminated heavily by cultural noises such as pipelines, powerlines, and railways. It is essential to understand the effect of cultural noise on CSRMT data to know the limitations of this method since it is now hard to find a place without any cultural noises except for very remote areas. Cultural noises have been long known to influence electromagnetic geophysical data (Szarka, 1988; Zonge and Huges, 1991; Junge, 1996). One of the effects of cultural noise (pipeline) is current channelling, where the current density flows in one particular direction since the pipeline is much more conductive than the surrounding regardless the polarizations of the injected currents (Babaour and Mosnier, 1980; Jones, 1983; Lezaeta and Haak, 2003; Jones, 2012).

The third measurement with the CSRMT method was carried out in Radevormwald (near Wuppertal) Germany in May 2017. The objective of the survey was to investigate probable hydrocarbon contamination in Luftsportverein (LSV) Radevormwald Germany around a simple filling station. The system of the filling station in the LSV Radevormwald is a simple one. The fuel dispensers are placed above the ground. In the past, there was no concrete top of the filling stations to cover the ground from a possible spill to the ground when the plane was refuelled. There are several successful studies on hydrocarbon contaminated areas using RMT method for example Tezkan et al. (1996), Newman et al. (2003), Beylich et al. (2004), Tezkan et al. (2005). Indeed in an urbanized area, the cultural noise was also present in the survey area. Unfortunately, it is not known which cultural noise play the dominant role in the observed data. The effect of the cultural noise is more or less were also observed in MT data by Escalas et al. (2013). The other challenge during the survey was to lower contact resistance between the electrodes and the ground. However geophysical studies must consider the spatial variations in the physical properties during survey design, data analysis, and interpretation. Geophysical data interpretation from surveys conducted at hydrocarbon contaminated sites without a microbial and geochemical context may lead to ambiguous conclusions (Atekwana and Atekwana, 2010).

1.2 Organization of This Thesis

This thesis consists of 8 Chapters. Chapter 1 is the introduction and motivation of this thesis. In Chapter 2, I reviewed the theory of electromagnetic fields generated by a horizontal electric dipole, then the algorithm of `SLDMEM3.f` a 3D forward modelling CSEM code in the frequency domain. Afterwards the validity of quasistatic approximation on

the CSRMT method which should be addressed and also discusses the effect of cultural noise effects on the measured CSRMT data. The last part is really necessary when applying the CSRMT method on “noisy” area. In the Chapter 3 the inversion of CSRMT data are discussed. There are 3 codes, namely: `Rund2Inv`, `Rebbocc`, and `MARE2DEM` applied for the inversion of CSRMT data. The impedance of the far-field zone is inverted with `Rund2Inv` and the tipper with `Rebbocc`. The near-field data were interpreted with `SLDMEM3f` and `MARE2DEM`. Synthetic tests were also performed to validate the `MARE2DEM` on the impedance data from HED source as in our CSRMT. The instrument and data processing are discussed in Chapter 4 in a practical way. The new processing algorithm is validated for apparent resistivity, impedance phase, and also tipper data. Chapter 5 discusses the experiment in Russia, Chapter 6 discusses the experiment in Krauthausen, and Chapter 7 discusses the experiment in Radervormwald with its problem and challenges. Finally to sum up all the works during the PhD studies is given in Chapter 8 as well as the direction of the future CSRMT research.

1.3 Preliminary Note

In this thesis, the transfer function data are plotted with increasing frequency as in (Zonge and Huges, 1991; Saraev et al., 2017). This display is the opposite with data presented in the MT method in which the data are plotted with increasing periods/decreasing frequencies.

To simplify the CSRMT filed zones, for the non-plane wave zone, I would only call these zones data as the near-field zone unless stated. Several algorithms (forward modelling, inversion and processing) are applied in this thesis, the references are given below and will not be repeated later unless stated:

- `SLDMEM3f`: Druskin and Knizhnerman (1994).
- `CS1D`: Shlykov and Saraev (2015).
- `Rund2Inv`: Rodi and Mackie (2001).
- `Rebbocc`: Siripunvaraporn and Egbert (2000).
- `MARE2DEM`: Key (2016); Wang (2017).
- `SM25M`: Mickrokor (2005, 2015).
- `MTS2DP1ot`: Smirnov (2003).

Chapter 2

The Controlled Source RMT Method

In this chapter, the basic electromagnetic geophysics theory is reviewed. The theory of the RMT method is borrowed here since the CSRMT method is an extension of the RMT method. I start with the electrical properties of rocks, then the discussion of Maxwell's equations including the boundary conditions which leads to the TE and TM modes in the MT method. Afterwards, the electromagnetic fields generated by HED as in the CSRMT method is discussed in a classical way with the field zones (even only characterized with "simple" homogeneous halfspace solution). A more general solution of the EM fields by HED can only be described by a 3D conductivity models. Consequently, a 3D CSEM frequency domain code is needed to obtain the solutions. Since the software has never been applied to any CSEM frequency domain method despite its age, a validation of the gridding scheme is needed. The discussion of displacement current could not be neglected in the CSRMT frequency ranges between 1 – 1000 kHz. Finally, during the experiments, cultural noise should be considered which is discussed at the end of this chapter.

2.1 Electrical Properties of Rocks

Understanding the response of earth materials to given electromagnetic fields is a key aspect of interpreting the measured CSRMT data. The most basic assumption in the electromagnetic (and electrical) geophysics method is that the earth is electrically neutral. It means that the numbers of positive and negative charge carriers are equal. Some of the charges (electrons) are free or quasi-free to move from place to place within the geological medium. The other charges are bounded by lattice atoms or other microscopic, localized charge centers, or they are held at material interfaces (Jonscher, 1977). The electrical conductivity, (σ), measures the capability of material to sustain long-term current flow via the charge migration mechanism.

Earth conductivity varies as great as 20 orders of magnitude, from highly conductive ore minerals to highly insulating minerals such as micas (Palacky, 1988) (see Figure 2.1), making electromagnetic geophysics as a favourable method to characterize one of its physical properties. However, this is not a straightforward problem to relate the measured conductivity to the lithology. That is, if the conductivity of a region of the

subsurface is known, the lithology of that region is not necessarily known. Porosity and permeability (therefore the water content), for instance, often dominate to the average conductivity compared to the actual contribution of mineral chemistry composition. This situation will result in what may normally be a poorly conductive (when dry) mineral appear to be more conductive several orders of magnitude than it is (Grant and West, 1965). Moreover, some rocks also have overlapping conductivity values as shown in Figure 2.1. It is worth to note that the interpretation of the data regarding rock properties is only as good as the extent laboratory data on conductivity. Up to now, even though there are some good and significant results in this area but the unknowns remain (Evans, 2012).

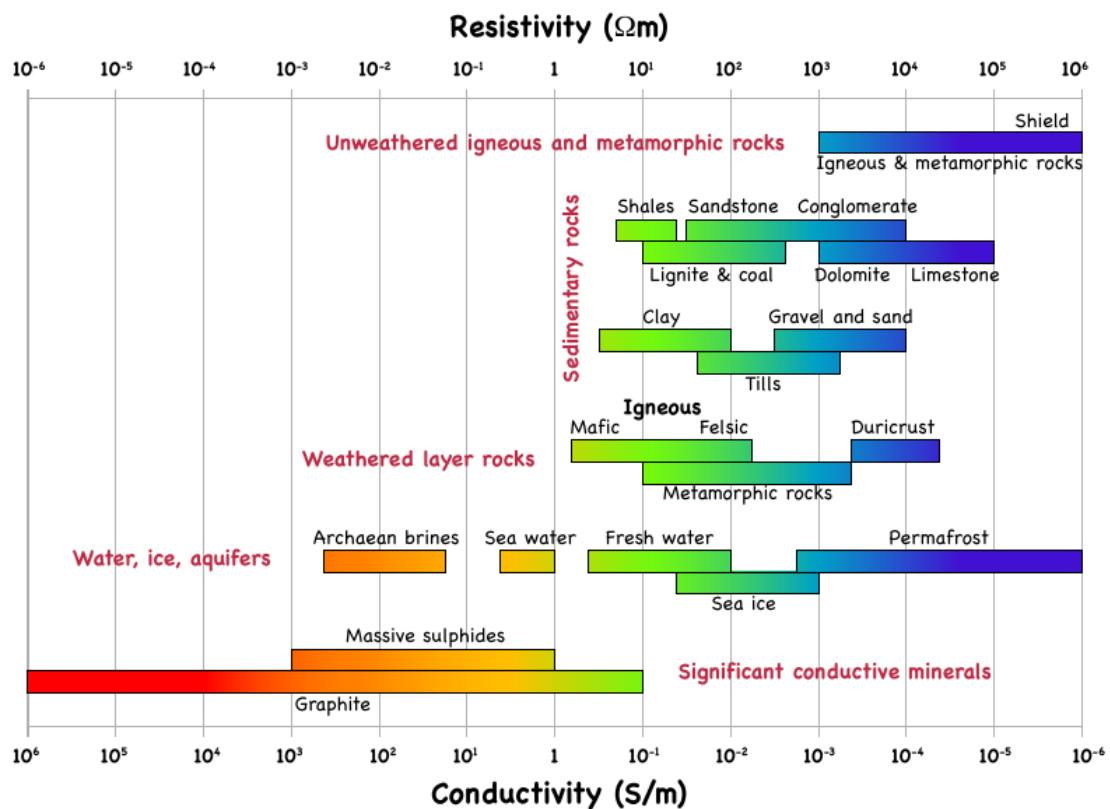


Figure 2.1: The conductivity of some Earth materials, note that some rocks have overlapping conductivity values. Figure taken from Miensopust (2010), the original is from Palacky (1988).

In rocks and minerals inside the earth, the electric currents may propagate in three different ways: electronic (Ohmic), electrolytic and also dielectric conduction (Telford et al., 1990). The **Ohmic conduction** is the most common type of current flow in materials containing free electron at a rapid rate such as in metals. While in the **electrolytic conduction**, the current is carried by ions at a slow rate. The electrolytic conduction is the most common conduction mechanism in the rocks. Since most of the rocks are poor conductors, their resistivity would be much higher if they are not porous and filled with fluids (water). Electrolytic conductivity depends proportionally on the salinity, porosity and also temperature. In very resistive rocks and high frequency, the **dielectric conduction** is the most common propagation of the electric currents. When an external alternating current (high frequency) is injected, the atomic electrons on the host rocks are shifted slightly with respect to the nuclei which is known as displacement current.

Archie (1942) gave a relation between electrical conductivity, water saturation and porosity as

$$\sigma = a\sigma_W S_W^n \phi^m, \quad (2.1)$$

where a is a constant that can widely vary, σ_W is electrical conductivity of the fluid, S_W^n is water saturation, n is a saturation exponent. Both a and n values depend on the porosity type of the rocks. The exponent m is commonly called cementation factor which depends on the degree of formation compaction and lithology. The cementation factor has the range between 1.2 - 2.3 depends on the size of the grain (Archie, 1942). The equation represents the resistivity of sandstones under ideal conditions, such as uniform sand.

2.2 Maxwell's Equations

To interpret CSRMT data one must understand the physical laws of electromagnetics (electric and magnetic fields), especially how the fields behave/interact with Earth materials. The dynamics of electric and magnetic fields are described by Maxwell's equations which consist of Gauss' law, Faraday's law and also Ampere's law.

In the frequency domain, Maxwell's equations (using $e^{i\omega t}$ in the Fourier transformation) can be written as:

$$\nabla \cdot \mathbf{D} = Q, \quad (2.2)$$

$$\nabla \cdot \mathbf{B} = 0, \quad (2.3)$$

$$\nabla \times \mathbf{E} = -i\omega\mathbf{B}, \quad (2.4)$$

$$\nabla \times \mathbf{H} = \mathbf{J} + i\omega\mathbf{D}, \quad (2.5)$$

the quantities of Maxwell's equations are given in Table 2.1. The first and second equations are Gauss' law for electric and magnetic fields respectively. Equation (2.2) states that the electric flux leaving a volume is proportional to the charge inside the volume while the second equation, Equation (2.3) states that no magnetic monopole exists. Equation (2.4) is Ampere-Faraday law, which is the voltage induced in a closed circuit is proportional to the rate of change of the magnetic flux it encloses. The last equation is Ampere's circuit law (with Maxwell's addition) the magnetic field induced around a closed loop is proportional to the electric current plus the displacement current (rate of change of electric field) it encloses. In short, the last two equations state that a change in electric (magnetic) field in space generates magnetic (electric) field. These last two equations are the basis for EM induction in geophysical prospecting.

From Maxwell's equations, the continuity equation (in time domain) can be derived as

$$\nabla \cdot \mathbf{J} + \frac{\partial Q}{\partial t} = 0. \quad (2.6)$$

This equation is also known as charge conservation. If a charge is moving out of a differential volume (in the form of current), then the amount of charge within that volume is going to decrease, so the rate of change of charge density is negative.

Table 2.1: Basic Variables and their symbols and units used in EM geophysics

Variables	Symbol	SI Units
Electric field intensity	\mathbf{E}	V/m
Electric displacement field	\mathbf{D}	As/m ²
Magnetic field	\mathbf{B}	T = Vs/m ²
Magnetic field intensity	\mathbf{H}	A/m
Current density	\mathbf{J}	A/m ²
Electric charge density	Q	As/m ³
Electrical permittivity in vacuum	$\epsilon_0 = 8.85 \times 10^{-12}$	As/Vm
Electrical permittivity	$\epsilon = \epsilon_0 \epsilon_r$	As/Vm
Relative dielectric permittivity	ϵ_r	-
Magnetic permeability in vacuum	$\mu_0 = 4\pi \times 10^{-7}$	Vs/Am
Magnetic permeability	$\mu = \mu_0 \mu_r$	Vs/Am
Relative magnetic permeability	μ_r	-
Electrical conductivity	σ	S/m = A/Vm
Electrical resistivity	ρ	$\Omega\text{m} = \text{Vm}/\text{A}$
frequency	f	Hz = 1/s
Angular frequency	$\omega = 2\pi f$	Hz = 1/s
Wavenumber	$k = 2\pi/\lambda$	1/m

2.2.1 Constitutive relation and Boundary Conditions

To apply Maxwell's equations on Earth models to see the earth responses to any given electric and magnetic fields, all the relations between displacement field \mathbf{D} and the electric field \mathbf{E} , as well as the magnetizing field \mathbf{H} and the magnetic field \mathbf{B} have to be specified. The equations specifying this relation are called constitutive equations. There are two basic assumptions are made to simplify the constitutive relation: (i) all media are linear, isotropic, homogeneous and their electrical properties are independent of time, temperature as well as pressure which has to be considered for example in geothermal exploration or deep crustal studies. (ii) The magnetic permeability has the same value as in the free space $\mu = \mu_0$.

Mathematically the "simplified" constitutive relations can be written as:

$$\mathbf{D} = \epsilon \mathbf{E}, \quad (2.7)$$

$$\mathbf{J} = \sigma \mathbf{E}, \quad [\text{Ohm's law}], \quad (2.8)$$

$$\mathbf{B} = \mu_0 \mathbf{H}. \quad (2.9)$$

where $\mu_0 = 4\pi \times 10^{-7}$ H/m and $\epsilon_0 = 8.85 \times 10^{-12}$ F/m. By applying constitutive equation above, Maxwell's equations can be written as:

$$\nabla \times \mathbf{E} + i\mu\omega \mathbf{H} = 0, \quad (2.10)$$

$$\nabla \times \mathbf{H} - (\sigma + i\epsilon\omega) \mathbf{E} = 0, \quad (2.11)$$

where the permeability and permittivity are assumed to be constant. By introducing impedance $\hat{z} = i\mu\omega$ and admittivity $\hat{y} = \sigma + i\epsilon\omega$, Equation (2.10) and Equation (2.11) might

be written as

$$\nabla \times \mathbf{E} + \hat{z}\mathbf{H} = 0, \quad (2.12)$$

$$\nabla \times \mathbf{H} - \hat{y}\mathbf{E} = 0. \quad (2.13)$$

The differential equations are solved with one or more conditions (boundary value problem and initial value problem). In general, the vector fields \mathbf{E} , \mathbf{B} , \mathbf{D} and \mathbf{H} as the solution of Equation (2.2)-(2.5) will be discontinuous at a boundary between two different media, or at a surface that carries a charge density σ or a current density \mathbf{K} .

In the case of linear media (as assumed in the earth materials) and free current in the interface, then we have

$$\epsilon_1 \mathbf{E}_1^\perp - \epsilon_2 \mathbf{E}_2^\perp = 0, \quad (2.14)$$

$$\mathbf{E}_1^\parallel - \mathbf{E}_2^\parallel = 0, \quad (2.15)$$

$$\mathbf{B}_1^\perp - \mathbf{B}_2^\perp = 0, \quad (2.16)$$

$$\mathbf{B}_1^\parallel - \mathbf{B}_2^\parallel = 0, \quad (2.17)$$

where the symbol \parallel and \perp denote parallel and perpendicular respectively. The only component discontinues across the boundary is the normal electric field to the boundary, while the electric field perpendicular to the boundary and both magnetic fields continue across the boundary.

2.2.2 TE and TM modes

In a perfect 2D conductivity distribution (by assuming that the strike direction goes to infinity/far away), the electromagnetic fields are separated into two modes, transverse electric (TE) mode where electric fields parallel to the strike direction and transverse magnetic (TM) where magnetic fields parallel to the strike directions. These two modes come as the consequences of boundary conditions on electromagnetic fields. By assuming x is the strike direction as in Figure 2.2, the transverse electric (TE) modes couples E_x to B_y and B_z by following equations

$$\frac{\partial E_x}{\partial E_y} = i\omega B_z, \quad (2.18)$$

$$\frac{\partial E_x}{\partial E_z} = i\omega B_y, \quad (2.19)$$

$$\frac{\partial B_z}{\partial y} - \frac{\partial B_y}{\partial z} = \mu_0 \sigma E_x, \quad (2.20)$$

while transverse magnetic (TM) modes couples B_x to E_y and E_z

$$\frac{\partial B_x}{\partial y} = \mu_0 \sigma E_z, \quad (2.21)$$

$$-\frac{\partial B_x}{\partial z} = \mu_0 \sigma E_y, \quad (2.22)$$

$$\frac{\partial E_z}{\partial y} - \frac{\partial E_y}{\partial z} = i\omega B_x. \quad (2.23)$$

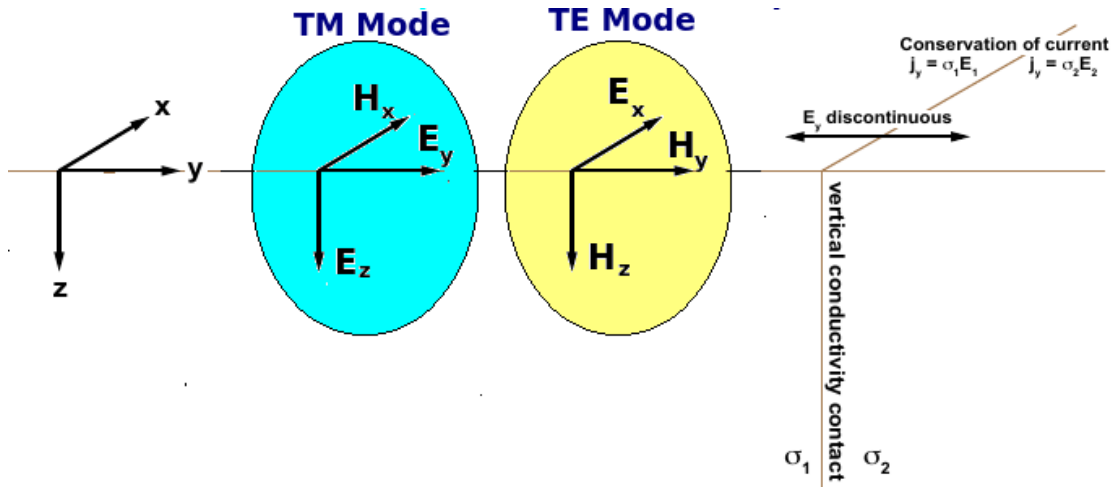


Figure 2.2: A very simple 2D conductivity earth model with the strike direction along x axis. The TE mode E_x, H_y, H_z and TM mode H_x, E_y, H_z . Modified after Simpson and Bahr (2005).

In a 2D/3D conductivity structure, the most comprehensive and reliable information on the conductivity of the Earth's interior can be obtained using both modes (Berdichevsky et al., 1998; Ledo, 2005):

- On the far-field zone to distinguish lateral changes along the profile, TM mode might be favourable, but TE mode has tipper data that can be used to diagnose lateral conductivity contrast.
- TM mode is more sensitive to near surface structure, while TE mode is more sensitive to deeper structure.
- On the 3D effects, TM mode is more robust to the effects of a conductive structure while TE mode is more robust to the effects of resistive structure.
- TM mode is affected by a static shift, TE mode is almost non distorted.
- When the 3-D body is normal to the regional strike, the TE-mode is affected mainly by inductive effects, while the TM-mode is affected by galvanic and inductive effects. In this case, a 2-D interpretation of the TM-mode is prone to error.
- When the 3-D body is parallel to the regional 2-D strike, the TE-mode is affected by galvanic and inductive effects and the TM-mode is affected mainly by galvanic effects, 2D interpretation of TM mode is more suitable.

For CSRMT with HED as a source, the polarization of electromagnetic fields (as well as the TE and TM mode) depend also on the transmitter direction.

An example of a response of simple 2D model is given in Figure 2.3. The vertical contact as in Figure 2.2 is located on 400 m, the resistivity $\rho_1 = 1/\sigma_1$ on the left is 10 Ωm and on the right, $\rho_2 = 1/\sigma_2$, is 100 Ωm . In the TM mode, it is clear that the apparent resistivity is not smooth along the profile, while in TE mode the apparent resistivity is

smooth along the profile. In 2D conductivity structure tipper data are only defined for the TE mode, in the TM mode, the tipper is zero (not shown). A typical behaviour of the TM mode is “overshoot” and “undershoot” along the profile when the structure is 2D which is the function of frequency, conductivity contrast etc. Furthermore, most information of the tipper data is on the real part (real part > imaginary part).

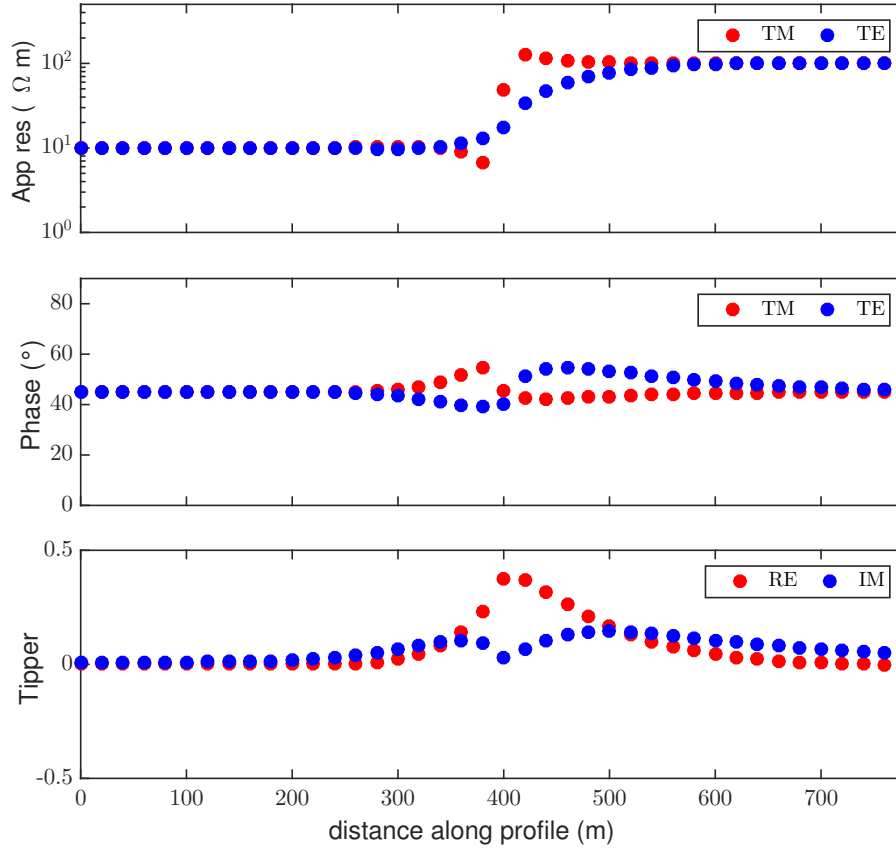


Figure 2.3: Response of simple 2D model of apparent resistivity, phase and tipper for frequency 1 kHz. The solutions are calculated with `SLDMEM3f` in MT mode. The vertical contact as in Figure 2.2 is located on 400 m, the resistivity $\rho_1 = 1/\sigma_1$ on the left is 10 Ωm and on the right, $\rho_2 = 1/\sigma_2$, is 100 Ωm .

2.2.3 Electromagnetic wave equations

One of the consequences/predictions of Maxwell's equations is electromagnetic waves travelling at the speed of light (3×10^8 m/s in the vacuum). This wave equations cannot be derived by only taking Gauss, Faraday or Ampere laws separately. To derive the electromagnetic waves equation, we start with vector identity¹:

$$\nabla \times \nabla \times A = \nabla(\nabla \cdot A) - \nabla^2 A,$$

¹the derivation of this identity can be found in a mathematical physics book, for example Tang (2007)

where A is a vector field. The first term $\nabla(\nabla \cdot A) = 0$ and applying the curl ($\nabla \times$) to Equation (2.12) and (2.13):

$$\nabla^2 \mathbf{E} + (\mu\epsilon\omega^2 - i\mu\sigma\omega)\mathbf{E} = 0 \Rightarrow \nabla^2 \mathbf{E} + k^2 \mathbf{E} = 0, \quad (2.24)$$

$$\nabla^2 \mathbf{H} + (\mu\epsilon\omega^2 - i\mu\sigma\omega)\mathbf{H} = 0 \Rightarrow \nabla^2 \mathbf{H} + k^2 \mathbf{H} = 0, \quad (2.25)$$

with $k^2 = \mu\epsilon\omega^2 - i\mu\sigma\omega = -\hat{z}\hat{y}$.

For the frequencies 1 – 1000 kHz and resistivity $< 1000 \Omega\text{m}$, in this case displacement current is much less than conduction current $\mu\epsilon\omega^2 \ll \mu\sigma\omega$:

$$\frac{\epsilon\omega}{\sigma} = 10^{-5} - 0.01, \quad (2.26)$$

the wave equation reduces to:

$$\nabla^2 \mathbf{E} - i\mu\sigma\omega \mathbf{E} = 0, \quad (2.27)$$

$$\nabla^2 \mathbf{H} - i\mu\sigma\omega \mathbf{H} = 0, \quad (2.28)$$

with $k^2 = (-i\mu\sigma\omega)$. This is known as a quasistatic approximation (MT approximation) which is valid for most of Earth materials. The validity of this approximation on CSRMT data will be discussed later in Section 2.5. The quasistatic approximation reduces the wave equation to the diffusion equation.

In the time domain, Equation (2.27) and (2.28) may be written as

$$\nabla^2 \mathbf{e} - \mu\sigma \frac{\partial \mathbf{e}}{\partial t} = 0, \quad (2.29)$$

$$\nabla^2 \mathbf{h} - \mu\sigma \frac{\partial \mathbf{h}}{\partial t} = 0. \quad (2.30)$$

The solution of (2.29) and (2.30) on a wave travelling on $-z$ direction are:

$$\mathbf{e} = \mathbf{e}_0^+ e^{-i\alpha z} e^{-\beta z} e^{i\omega t},$$

$$\mathbf{h} = \mathbf{h}_0^+ e^{-i\alpha z} e^{-\beta z} e^{i\omega t},$$

the wave number k in the solutions is written as $k = \alpha - i\beta$ with

$$\alpha = \omega \left\{ \frac{\mu\epsilon}{2} \left[\left(1 + \frac{\sigma^2}{\epsilon^2 \omega^2} \right)^{1/2} + 1 \right] \right\}^{1/2},$$

$$\beta = \omega \left\{ \frac{\mu\epsilon}{2} \left[\left(1 + \frac{\sigma^2}{\epsilon^2 \omega^2} \right)^{1/2} - 1 \right] \right\}^{1/2},$$

where α is known as propagation constant and β is attenuation constant.

2.3 EM Fields by Horizontal Electric Dipole

The CSRMT method uses horizontal electric dipole (afterwards HED) with length vary from 100 – 1000 m as a source which is grounded at both ends of the dipole. The solutions of Maxwell's equations in general 3D conductivity distribution can only be computed numerically. The analytic solutions are only available for homogeneous halfspace and 1D conductivity structure.

The full field solutions of Maxwell's equations for the electric and magnetic fields in 1D conductivity structure generated by HED with length dl directed along $-x$ axis in Cartesian coordinates and measured on the surface ($z = 0$) is given by (Ward and Hohmann, 1988):

$$E_x = -\frac{I dl}{4\pi} \frac{\partial}{\partial x} \frac{x}{r} \int_0^\infty \left((1 - r_{TM}) \frac{u_0}{\hat{y}_0} + (1 + r_{TE}) \frac{\hat{z}_0}{u_0} \right) \frac{1}{m} J_0(mr) dm - \frac{\hat{z}_0 I dl}{4\pi} (1 + r_{TE}) \frac{m}{u_0} J_0(mr) dm, \quad (2.31)$$

$$E_y = -\frac{I dl}{4\pi} \frac{\partial}{\partial x} \frac{y}{r} \int_0^\infty \left((1 - r_{TM}) \frac{u_0}{\hat{y}_0} + (1 + r_{TE}) \frac{\hat{z}_0}{u_0} \right) \frac{1}{m} J_0(mr) dm, \quad (2.32)$$

$$H_x = \frac{I dl}{4\pi} \frac{\partial}{\partial x} \frac{y}{r} \int_0^\infty (r_{TM} + r_{TE}) e^{u_0 z} J_1(mr) dm, \quad (2.33)$$

$$H_y = -\frac{I dl}{4\pi} \frac{\partial}{\partial x} \frac{y}{r} \int_0^\infty (r_{TM} + r_{TE}) e^{u_0 z} J_1(mr) dm - \frac{I dl}{4\pi} \int_0^\infty (1 - r_{TE}) e^{u_0 z} J_0(mr) dm, \quad (2.34)$$

$$H_z = \frac{I dl}{4\pi} \frac{y}{r} \int_0^\infty (1 + r_{TE}) e^{u_0 z} \frac{m^2}{u_0} J_1(mr) dm, \quad (2.35)$$

where $r = \sqrt{x^2 + y^2 + z^2}$, $J_0(x)$ and $J_1(x)$ are the first kind of Bessel functions of the order 0 and 1 respectively, $\hat{y}_0 = i\omega\epsilon_0$, $\hat{z}_0 = i\omega\mu_0$, and

$$\begin{aligned} Y_n &= Y_n^* = u_n, \\ u_n &= \sqrt{k_x^2 + k_y^2 - k_n^2} = \sqrt{m^2 - k_n^2}, \\ m &= \sqrt{u_n^2 + k_n^2}, \\ k_n^2 &= \omega^2 \mu_n \epsilon_n - i\omega \mu_n \sigma_n. \end{aligned}$$

Also

$$\begin{aligned} Y_0 &= \frac{u_0}{\hat{z}_0} && \text{intrinsic admittance of free space,} \\ Z_0 &= \frac{u_0}{\hat{y}_0} && \text{intrinsic impedance of free space,} \end{aligned}$$

and

$$\begin{aligned} r_{TE} &= \frac{Y_0 - \hat{Y}_1}{Y_0 + \hat{Y}_1}, \\ r_{TM} &= \frac{Z_0 - \hat{Z}_1}{Z_0 + \hat{Z}_1}. \end{aligned}$$

Here, \hat{Y}_1 and \hat{Y}_2 are admittances of lower halfspace which can be expressed recursively by:

$$\begin{aligned}\hat{Y}_1 &= Y_1 \frac{\hat{Y}_2 + Y_1 \tanh(u_1 h_1)}{Y_2 + \hat{Y}_1 \tanh(u_1 h_1)}, \\ \hat{Y}_1^* &= Y_1 \frac{\hat{Y}_2^* + Y_1^* \frac{\sigma_2}{\sigma_1} \tanh(u_1 h_1)}{Y_2^* \frac{\sigma_2}{\sigma_1} + \hat{Y}_1^* \tanh(u_1 h_1)}, \\ \hat{Y}_n &= Y_n \frac{Y_{n+1} + Y_n \tanh(u_n h_n)}{Y_{n+1} + \hat{Y}_n \tanh(u_n h_n)}, \\ \hat{Y}_n^* &= Y_n \frac{Y_{n+1}^* + Y_n^* \frac{\sigma_{n+1}}{\sigma_n} \tanh(u_n h_n)}{Y_{n+1}^* \frac{\sigma_{n+1}}{\sigma_n} + \hat{Y}_n^* \tanh(u_n h_n)}.\end{aligned}$$

The homogeneous halfspace solutions (Equation (2.31) to (2.35)) for the electric and magnetic fields are:

$$E_x = \frac{I dl (3 \cos^2 \theta - 1)}{2\pi\sigma r^3} \left[1 + e^{-ikr} (1 + ikr) \right], \quad (2.36)$$

$$E_y = \frac{I dl \sin 2\theta}{2\pi\sigma r^3} \left[2 - e^{-ikr} (1 + ikr) \right], \quad (2.37)$$

$$\begin{aligned}H_x &= \frac{I dl \sin 2\theta}{2\pi r^2} \left[3I_1 \left(\frac{ikr}{2} \right) K_1 \left(\frac{ikr}{2} \right) + \right. \\ &\quad \left. \frac{ikr}{2} \left(I_1 \left(\frac{ikr}{2} \right) K_0 \left(\frac{ikr}{2} \right) - I_0 \left(\frac{ikr}{2} \right) K_1 \left(\frac{ikr}{2} \right) \right) \right], \quad (2.38)\end{aligned}$$

$$H_y = -\frac{I dl (3 \cos^2 \theta - 1)}{2\pi r^3} \left[I_1 \left(\frac{ikr}{2} \right) K_1 \left(\frac{ikr}{2} \right) \right], \quad (2.39)$$

$$H_z = -\frac{3I dl \sin \theta}{2\pi k^2 r^4} \left[1 - e^{-ikr} \left(1 + ikr - \frac{1}{3} k^2 r^2 \right) \right], \quad (2.40)$$

where $k_1 = \sqrt{i\omega\mu_0\sigma_1}$ is the wavenumber, I_n and K_n are the modified Bessel function of first and second kind, I is the injected current, dl is the length of the transmitter, θ is the angle between the receiver and the transmitter, and r is distance between the receiver and the transmitter.

It is worth to note that the electromagnetic fields generated by HED depend on the length of the dipole and the injected current known as a dipole moment ($I dl$ term). To get a high signal to noise ratio we need to have high dipole moment which can be achieved either by having longer dipole or higher current. Unfortunately, this might be limited either the land restriction and also a very resistive underground. One of the suggestion in this situation is to measure in the near-field zone only.

As in the magnetotellurics method, the electric and magnetic fields are related through:

$$\mathbf{E} = \mathbf{ZH}, \quad (2.41)$$

which can be written in components as

$$\begin{bmatrix} E_x \\ E_y \end{bmatrix} = \begin{bmatrix} Z_{xx} & Z_{xy} \\ Z_{yx} & Z_{yy} \end{bmatrix} \begin{bmatrix} H_x \\ H_y \end{bmatrix}, \quad (2.42)$$

where \mathbf{Z} is known as impedance tensor, which can be transformed into apparent resistivity and impedance phase. The impedance tensor can tell us the underlying conductivity distribution. In 1D conductivity distribution $Z_{xy} = Z_{yx}$ and $Z_{xx} = Z_{yy} = 0$. In 2D conductivity distribution $Z_{xy} \neq Z_{yx}$ and $Z_{xx} = Z_{yy} = 0$. While in 3D conductivity distribution $Z_{xy} \neq Z_{yx}$ and $Z_{xx} \neq Z_{yy} \neq 0$.

The vertical and horizontal magnetic fields are related through complex valued vertical magnetic transfer function known as tipper vector

$$\begin{bmatrix} H_z \end{bmatrix} = \begin{bmatrix} A_x & B_y \end{bmatrix} \begin{bmatrix} H_x \\ H_y \end{bmatrix}, \quad (2.43)$$

where A_x and B_y are the components tipper vector. In the MT method (as well as in the CSRMT far-field zone), the tipper vector can only be observed in 2D (TE modes) and 3D conductivity distribution. However, this is not true in the near-field and transition zones which will be discussed in the following section. Furthermore, in field experiments, it is more likely to observe mode mixing which results in the tipper on TM mode are not zero. In this case, the tipper (and impedance tensor) should be rotated.

2.3.1 The CSRMT Field Zones

Impedance Data

In the CSRMT method, the electromagnetic fields generated by HED behave differently in three different zones depending on the distance between transmitter and receiver(s) (horizontal attenuation), frequency and conductivity distributions, namely: near-field, transition, and far-field zones. The zones are characterized by the induction number given by

$$|kr| = \frac{r\sqrt{2}}{\delta}, \quad (2.44)$$

where r is the offset between transmitter and receivers and δ is the skin depth, as in MT, given by

$$\delta = 503 \sqrt{\frac{\rho}{f}} \quad [\text{m}]. \quad (2.45)$$

However, in the field experiment when analyzing the measured data, it is not always easy to define “clearly” the boundary between all the zones. The classical approach is just to interpret the far-field zone data and ignoring the near-field zone data, although in some cases the data were still in the transition zones (Zonge and Huges, 1991). In other CSEM methods, both in the time domain and frequency domain, where the data are in the form of electric and magnetic fields, these zones are neglected (see for example (Streich, 2016)).

The near-field Zone

The near-field zones is where the distance between transmitter and receiver is close and satisfy $|kr| \ll 1$. The electromagnetic fields are given by (Zonge and Huges, 1991)

$$E_x \approx \frac{I dl(3 \cos^2 \theta - 1)}{2\pi\sigma r^3}, \quad (2.46)$$

$$E_y \approx \frac{I dl \sin 2\theta}{4\pi\sigma r^3}, \quad (2.47)$$

$$H_x \approx \frac{I dl \sin 2\theta}{4\pi r^2}, \quad (2.48)$$

$$H_y \approx \frac{I dl(3 \cos^2 \theta - 1)}{2\pi r^2}, \quad (2.49)$$

$$H_z \approx \frac{I dl \sin \theta}{4\pi r^2}. \quad (2.50)$$

In this case, the electrical components depend only on the conductivity distribution and are insensitive to the frequency of the injected currents, while the magnetic fields do not depend on both conductivity and frequency. In this situation, the magnetic field is saturated. If we apply the magnetotelluric formula to calculate apparent resistivity and impedance phase:

$$Z = \left| \frac{E_y}{H_x} \right| = \frac{2}{\sigma r}, \quad (2.51)$$

and

$$\rho_a = \frac{r}{2} \left| \frac{E_y}{H_x} \right|. \quad (2.52)$$

The apparent resistivity in the near-field zone on a double logarithmic plot has a slope of 45° or more, while the impedance phase is zero (no imaginary part of the electromagnetic field solutions).

In this thesis the data from all zones are interpreted with a new modified code of MARE2DEM (Key, 2016; Wang, 2017) in impedance form Z_{xy} , Z_{yx} and their phase. It would be shown in Chapter 3 for synthetic data and Chapter 5 and Chapter 6 for the field data.

The far-field Zone

In the far-field zone, where $kr \gg 1$, or the distance between transmitter and receiver is greater than 5δ , the components of the electromagnetic fields generated by HED are given by:

$$E_x \approx \frac{I dl}{2\pi\sigma r^3} (3 \cos^2 \theta - 2), \quad (2.53)$$

$$E_y \approx -\frac{I dl \sin 2\theta}{4\pi\sigma r^3}, \quad (2.54)$$

$$H_x \approx \frac{I dl}{2\pi r^3 \sqrt{\mu\sigma\omega}} (\cos^2 \theta + 2) e^{-i\pi/4}, \quad (2.55)$$

$$H_y \approx \frac{3I dl}{4\pi r^3 \sqrt{\mu\sigma\omega}} (\sin 2\theta) e^{i\pi/4}, \quad (2.56)$$

$$H_z \approx -\frac{3I dl \sin \theta}{2\pi \mu\sigma\omega r^4} e^{-i\pi/2}. \quad (2.57)$$

Note that in the far-field zone, the horizontal magnetic field components are also the function of square root of conductivity and frequency, unlike the near-field solution. In this zone, the wave impedance can be calculated from the perpendicular electric and magnetic fields:

$$Z_{xy} = \frac{E_x}{H_y}, \quad Z_{yx} = \frac{E_y}{H_x}. \quad (2.58)$$

The wave impedance in above equations can be transformed to apparent resistivity:

$$\rho_{a,xy} = \frac{1}{\omega\mu_0} |Z_{xy}|^2, \quad \rho_{a,yx} = \frac{1}{\omega\mu_0} |Z_{yx}|^2, \quad (2.59)$$

and phase impedance

$$\phi_{xy} = \tan^{-1} \frac{\text{Im}[Z_{xy}]}{\text{Re}[Z_{xy}]}, \quad \phi_{yx} = \tan^{-1} \frac{\text{Im}[Z_{yx}]}{\text{Re}[Z_{yx}]}. \quad (2.60)$$

In the far-field zone, where the plane wave approximation is valid, then the standard MT processing can be applied to invert and interpret the data. Even though the effect of the finite source is still weakly present (Zonge and Huges, 1991). However, the EM fields generated by HED are dependent on the distance (horizontal attenuation) which is not the case for the MT/RMT method. The best method to ensure the far-field zone data is to compare the CSRMT data and RMT data in the processing. When the measurement is carried out from the near-field zone in a continuous way to the far-field zone, then plotting the processed data would also help (Chapter 5). Otherwise, the theoretical calculation could also go wrong (Chapter 6).

In 1-D layered earth, the apparent resistivity and impedance phase on the top ($z = 0$) can be computed with the Wait recursion formula (Wait, 1954). An hypothetical MT sounding penetrating the n -th layer could measure E_{xn} and B_{yn} . This condition would allow the following transfer functions to be computed:

$$C_n(z) = \frac{E_{xn}(z)}{i\omega B_{yn}(z)}, \quad (2.61)$$

$$q(n) = \sqrt{i\mu_0\sigma_n\omega}. \quad (2.62)$$

and the transfer functions on layer $n - 1$:

$$C_n(z_{n-1}) = \frac{1}{q_n} \frac{q_n C_{n+1}(z_n) + \tanh(q_n l_n)}{1 + q_n C_{n+1}(z_n) \tanh(q_n l_n)}, \quad (2.63)$$

where z_n is the depth on n -th layer. And then the impedance can be calculated as:

$$Z = i\omega C_1, \quad (2.64)$$

where C_1 is the transfer function on the top. Afterwards the apparent resistivity and phase can be calculated through the Equation (2.60). On 1D conductivity distribution $Z_{xy} = Z_{yx}$ and $Z_{xx} = Z_{yy} = 0$. The Wait recursion formula Equation (2.63) is an analytic expression of the impedance in 1D layered Earth.

Weidelt (1972) showed that the impedance Z is an analytic function in the upper complex half-plane. As a result, the real part (apparent resistivity) and imaginary part (phase)

are related each other known as Kramers-Kronig relation which can be written as:

$$\phi(\omega) = \frac{\pi}{4} - \frac{\omega}{\pi} \int_0^{\infty} \log \frac{\rho_a(\omega')}{\rho_0} \frac{d\omega'}{\omega'^2 - \omega^2}. \quad (2.65)$$

Equation (2.65), also known as Weidelt's dispersion formula, shows that apparent resistivity can be predicted from the phase impedance or vice versa. The scaling factor ρ_0 plays an important role for multidimensional conductivity distributions which can result in shifted apparent resistivity. This relation is strictly valid in the 1D and 2D TM mode of plane wave transfer functions which are smooth functions of frequency (Weidelt, 1972; Weidelt and Kaikkonen, 1994). For TE mode, the smoothness is questionable (Parker, 2010), but the example which consists of a variable conductivity, thin sheet at the surface, over an insulating layer, terminated by a perfect conductor is not geologically plausible. So it can be said that Equation (2.65) applies to the transfer function of the CSRMT method.

There are two methods to estimate the underlying conductivity distribution on the MT method which is satisfied on the far-field zone data, namely Schmucker's $\rho^*(z^*)$ (Schmucker, 1970) and Niblett - Bostick transformation (Niblett and Sayn-Wittgenstein, 1960; Bostick, 1977). Both transformations are often used to calculate a first approximation of conductivity distributions under the sounding's location.

The $\rho^*(z^*)$ method estimates the effective depth of penetration as:

$$z^* = \sqrt{\frac{\rho_a}{\omega\mu_0}} \sin \phi, \quad (2.66)$$

and the conductor in that depth as:

$$\rho^* = \begin{cases} \rho_a / (2 \sin^2 \phi), & \text{for } 0 \leq \phi \leq \frac{\pi}{4}, \\ 2\rho_a \cos^2 \phi, & \text{for } \frac{\pi}{4} \leq \phi \leq \frac{\pi}{2}. \end{cases} \quad (2.67)$$

The $\rho^*(z^*)$ performs well when $\phi > \pi/4$ with more underlying conductive structures. On the other hand, in the case of a resistor below good conductor, the resistivity starts to increase significantly within the conductor before reaching the resistor. In particular, in the extreme case of a uniform layer of thickness d over an insulator, $\rho^* = \infty$, $z_{\max}^* = d/3$.

The second mapping is the Niblett-Bostick transformation. The slope $m(T)$ on double logarithmic plot of ρ_a against T is given by:

$$m(T) = \partial_{\log T} \log \rho_a(T), \quad (2.68)$$

then the Niblett-Bostick transform of $\rho_b(D)$ given by:

$$D = \sqrt{\frac{T\rho_a}{2\pi\mu_0}}, \quad (2.69)$$

$$\rho_b = \rho_a \frac{1+m}{1-m}. \quad (2.70)$$

For an earth model with increasing conductivity, the $\rho_b(D)$ performs quite well. How-

ever, the opposite is for a less conductive structure, this method, as $\rho^*(z^*)$, does not perform well and gives a stronger overshooting. In general, the approximate depth given by Equation (2.66) and Equation (2.69) are equal.

The Transition Zone

The zone between the near-field and far-field zones is called a transition zone. The behaviour of electric and magnetic field is very complicated. The magnetic fields dependence on the distance change between $1/r^2$ to $1/r^3$. In a non-homogeneous Earth, the impedance depends on resistivity contrast. In the transition zone, the phase impedance might be low and negative. The inflexion of the phase curve is also indicative of the transition zone response. Another characteristic is a notch on apparent resistivity curves on some frequencies. The magnitude of the inflexion point and the notch depend on the resistivity contrast between the earth layers. In this transition zones, applying the MT formula to calculate the impedance might lead us to lose valuable information (Zonge and Huges, 1991). The standard way to process the CSEM data is on the electric and magnetic field only (see for example Streich et al. (2011)).

Field Zones Illustration

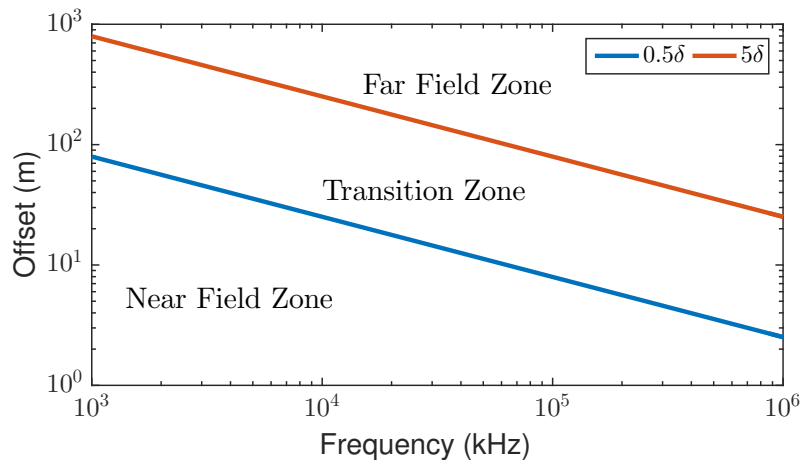


Figure 2.4: Theoretical field zones for 100 Ω m halfspace. To be safe in far-field zone, the measurement should start at least 800 m from the source. The skin depth δ is calculated with Equation (2.45).

To illustrate, an example of the field zones of CSRMT for 100 Ω m halfspace with the criteria discussed above: $< 0.5\delta$ is near-field zone, and $> 5\delta$ is far-field zone is given in Figure 2.4. Figure 2.5 shows apparent resistivity and phase plotted against the distance for inline and broadside configuration for 100 Ω m halfspace for frequency 1 kHz (lowest frequency of the CSRMT method). Note that the transitions from the near-field zone to the far-field zone is smooth in both figures. The measurement should start at least 800 m from the source, so all the data are in the far-field zone. One also might notice that the highest frequency (1 MHz) is already in the far-field zone at 100 m. Between 100 – 800 m, the data are mixed between transition and far-field zones.

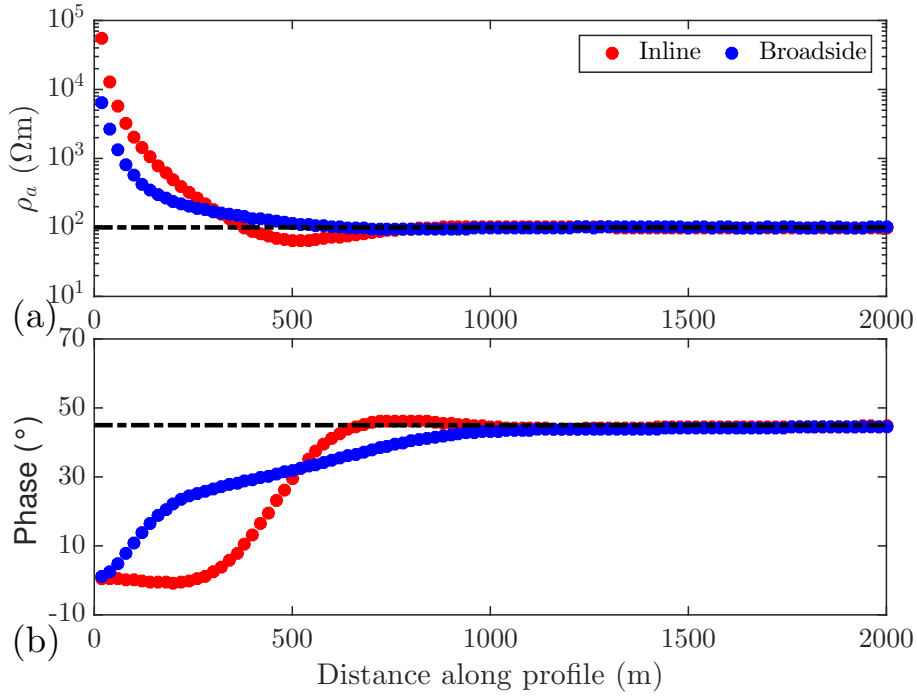


Figure 2.5: (a) Apparent resistivity and (b) phase plotted against the distance for inline and broadside configuration for frequency 1 kHz. The dashed black line is 100 Ωm in apparent resistivity and 45° in phase respectively.

Tipper Data

In the RMT/MT, when the conductivity structure of the earth is 2D/3D, a vertical magnetic component H_z can be observed. The primary horizontal magnetic field (from the distant transmitters) induces eddy currents in conductive bodies in the subsurface. These eddy currents create the secondary vertical magnetic field H_z . The relation between vertical H_z and horizontal H_x , H_y magnetic fields on Equation (2.43) can be written as:

$$H_z(\omega) = A_x(\omega)H_x(\omega) + B_y(\omega)H_y(\omega). \quad (2.71)$$

The transfer functions $A(\omega)$ and $B(\omega)$ are known as the tipper. Both functions are complex numbers and frequency dependent. To solve Equation (2.71) for the two unknowns A_x and B_y at least data from two transmitters at roughly equal frequencies and sufficiently different azimuthal angles from the receiver site are available for all components. For a certain period (or frequency), the tipper can be displayed as induction arrows:

$$\vec{P} = \text{Re}[A_x]\hat{x} + \text{Re}[B_y]\hat{y}, \quad (2.72)$$

$$\vec{Q} = \text{Im}[A_x]\hat{x} + \text{Im}[B_y]\hat{y}, \quad (2.73)$$

where \hat{x} and \hat{y} are the unit vector in x and y direction respectively.

When the EM fields are generated by HED, in the near-field and transition zones, even the conductivity distribution is homogeneous halfspace or 1D, the H_z component, as a result the tipper data, is present as we see from the solution in Equation (2.48) to (2.50) all the magnetic fields decay as $\sim 1/r^2$. In this case, the ratio between vertical and horizontal magnetic fields will not be zero. In the far-field zone, the vertical magnetic

fields decay much faster than the horizontal magnetic fields $H_z \ll H_x, H_y$, their ratio (tipper) is small (≈ 0). Moreover in inline configuration, $\theta = 0$, in all fields zone $H_z = 0$ and tipper is zero. The synthetic example of tipper data in transition zones of CSRMT method in 1D conductivity structure is given by Shlykov and Saraev (2015). The tipper information is really useful to define the boundary between near-field/transition zones to the far-field zones in addition to the ratio between offset(s) and average of the skin depth. On the natural sources (RMT) case, as well as the lateral change of conductivity structure, the tipper information might also show the nearby cultural noise which might affect the observed data when the magnitude of tipper are > 1 .

The graphical representation of the real induction arrows can be reversed (Parkinson convention (Parkinson, 1959)) or non-reversed (Schmucker or Weise convention (Wiese, 1962)). The Parkinson convention the real induction arrow points to more conductive zones while the Wiese convention is the opposite. In the case of near-field and transition zones, the induction arrows point to the source (Qian and Pedersen, 1991). However, in this thesis, I only plot the tipper data as the amplitude of real and imaginary part against distance without the induction arrows. Furthermore, Marcuello et al. (2005) argued that the real and imaginary part of tipper data are also related by dispersion relation as the impedance data.

Illustration

To illustrate the electromagnetic fields generated by horizontal electric dipole, consider a halfspace and a simple 1 D model (2 layer case, with $\rho_1 = 100 \Omega\text{m}$, $h_1 = 20\text{m}$ and $\rho_2 = 50 \Omega\text{m}$) for 200 m $-x$ directed dipole. The inline configuration is when the receivers are located on $y = 0$, while the broadside configuration is when the receivers are located on $x = 0$. The individual components of electric and magnetic fields are given on Figure 2.6 and 2.7 for homogeneous halfspace and 1D layered earth respectively. It is clear that the electromagnetic fields depend on the distance between transmitter and receiver which is not considered on the magnetotelluric and the radiomagnetotelluric methods.

Figure 2.8 shows apparent resistivity and phase for 100 Ωm halfspace for different configurations of the transmitter (inline and broadside) for the same offset of receivers 30, 100 and 1000 m. The effects of near-field and transition zones are stronger on inline configuration than in broadside configuration. The electric fields are much stronger while the magnetic fields are weaker, so the ratio is higher. In broadside configuration, interpreting the data sometimes quite challenging (in case of shifted transmitter due to cultural noise). The data already behaves like far-field zone with more resistive basement. This will lead to wrong interpretation of the data. Furthermore, this might also be hard to define the boundary between far-field zone and near-field/transition zones data.

Figure 2.9 shows apparent resistivity and phase for simple 1D model (layered halfspace, $\rho_1 = 100 \Omega\text{m}$, $h_1 = 20\text{m}$, $\rho_2 = 50 \Omega\text{m}$) with the same configurations as 2.8. When the offset is 30 m, the responses are almost the same between 100 Ωm homogeneous halfspace and 1D layered Earth (some information might be lost here for layered Earth). In 100 m offset, there are only little bit differences between homogeneous halfspace to the

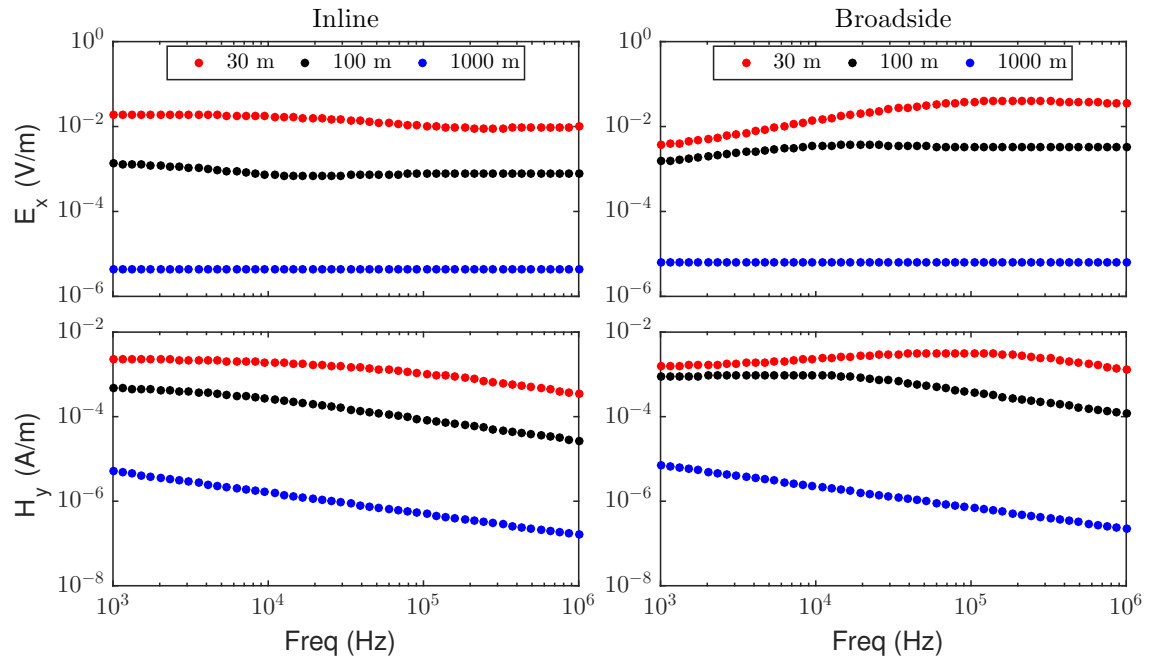


Figure 2.6: Individual components of electric and magnetic fields for inline and broadside configuration for $100 \Omega \text{ m}$ halfspace.

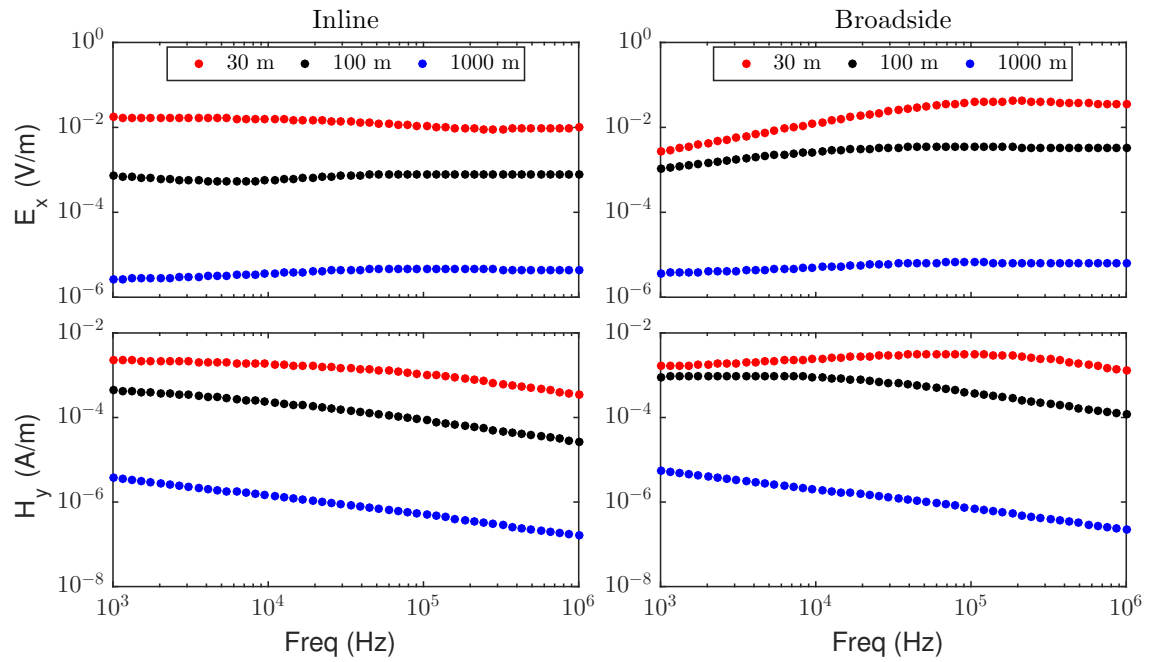


Figure 2.7: Individual components of electric and magnetic fields for inline and broadside configuration for 1D situation.

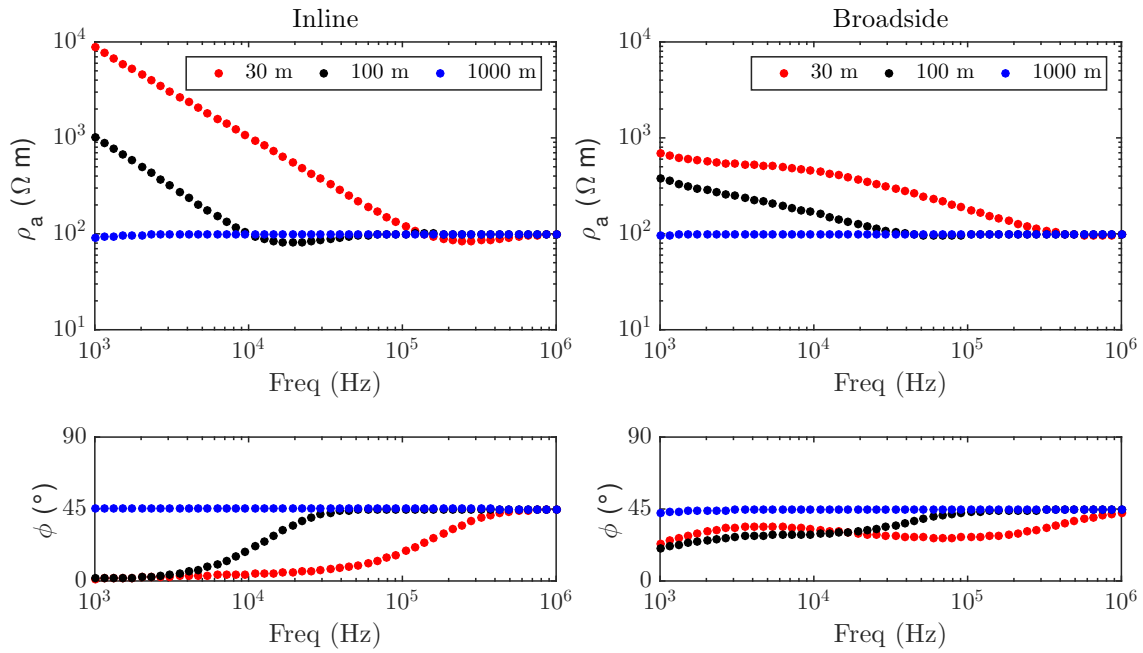


Figure 2.8: Apparent resistivity and phase curves for inline (left) and broadside (right) configuration for 100 Ω m halfspace for different distance between transmitter and receiver. It is clear that in inline configuration, far-field zone is achieved in shorter distance than broadside configuration.

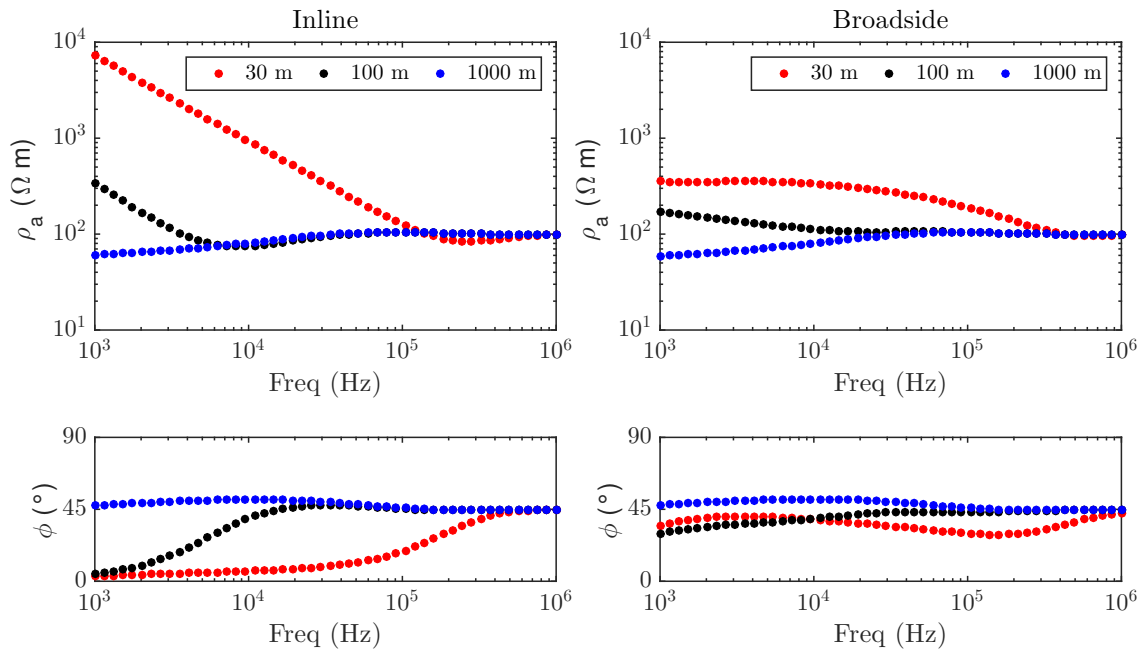


Figure 2.9: Apparent resistivity and phase curves for inline (up) and broadside (down) configuration for layered Earth for different distance between transmitter and receiver.

1D earth (again lost of information). In 1000 m when the electromagnetic fields are in the far-field zone, the response of homogeneous halfspace and 1D earth can be distinguished as expected.

Summarize

To summarize, the field behaviour of electric and magnetic fields due to the horizontal electric dipole is given in Table 2.2, where r is the distance from the source to the receiver and $d \cong 503\sqrt{\rho/f}$ [m] is the MT skin depth.

Table 2.2: Electromagnetic fields behaviour generated by horizontal electric dipole in different zones

-	near-field	Transition Zone	far-field
r/d	< 0.5	$0.5 - 3(5)$	$> 3(5)$
E	r^{-3}	r^{-3}	r^{-3}
H_x, H_y	r^{-2}	$r^{-2}-r^{-3}$	r^{-3}
H_z	r^{-2}	$r^{-2}-r^{-3}$	r^{-4}
Imp phase	0	low/negative	around 45
DOI	geometry	geometry and frequency	frequency
Tipper	all ρ dist.	all ρ dist.	2D/3D

2.4 The SLDMEM3f Forward Modelling Code

The analytic (and “simple”) solutions of Maxwell’s equations generated by HED on the previous section were only available for homogeneous halfspace and 1D layered earth which is most of the times not valid on the field experiments. A 3D CSEM code is needed to compute the response of the 3D conductivity of the earth generated by HED. There exists (at least in our institute), a 3D code of Druskin and Knizhnerman (1994) that has never been applied to any CSEM frequency domain method before. The time domain variant is now a routine to interpret the time domain CSEM method in IGM Cologne. One of the objectives of this thesis is to apply the frequency domain variant to frequency domain CSEM method. The SLDMEM3f would be very useful to define the boundary between the field zones on the survey design before the field experiments and also when analyzing the measured data.

2.4.1 Finite Difference Approximation in Staggered Grid

Maxwell’s equations in frequency domain and quasistatic approximation can be written as:

$$\nabla \times \mathbf{H} = \sigma \mathbf{E} + \mathbf{J}, \quad \nabla \times \mathbf{E} + i\omega\mu\mathbf{H} = 0, \quad (2.74)$$

where \mathbf{J} is the density of source current, by applying curl ($\nabla \times$) to above equation and rearranging

$$\sigma^{-1}\nabla \times \nabla \times \mathbf{E} + i\omega\mathbf{E} = i\omega\sigma^{-1}\mathbf{J}, \quad (2.75)$$

In SLDMEM3f, to solve Equation (2.75) in three dimensions, finite difference method is used and applying staggered grid approach (Yee, 1966). With the Yee grid, the physical boundary conditions of Maxwell's equations are satisfied and divergence free also an elegant approximation to the curl equation. Within SLDMEM3f the electric field components are obtained along the edges of each cell and are edge-averaged. While the magnetic field components are obtained on faces by taking the curl of the electric field and are face averaged, see Figure 2.10 (a). Note that the electric and magnetic fields are sampled on a different location. With this in mind, care must be taken when designing the grid on dipole sources when modelling the electromagnetic fields on nearly inline ($\theta \approx 0$) or broadside configuration ($\theta \approx 90$). This might also be done by interpolation to a certain position from several other receivers. However, since the EM-fields are non-linear in space, it is better to avoid any interpolations and include grid-lines at positions, where the solution is required (Martin, 2009).

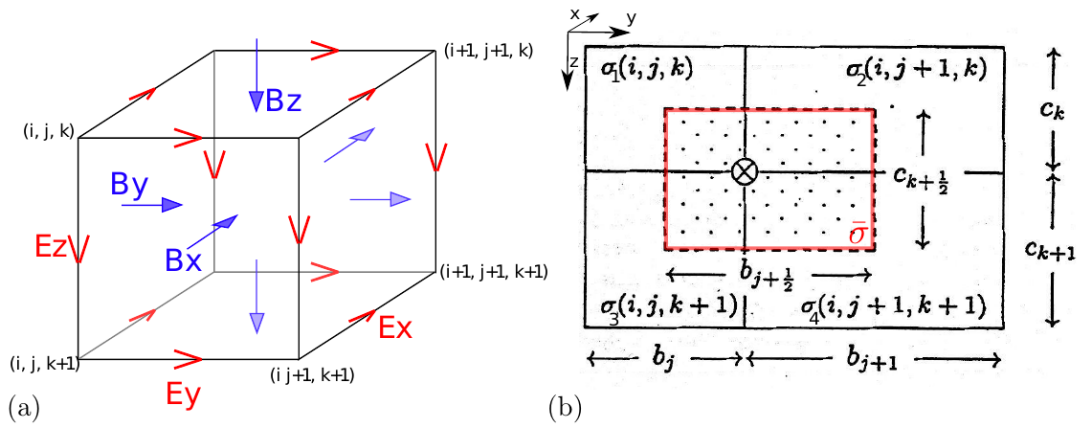


Figure 2.10: (a) Yee-Lebedev grid cell (b) Material averaging scheme on SLDMEM3f. Figures from Yogeshwar (2014), with the original figure on the right hand side from Weidelt (2000)

2.4.2 Material Averaging Scheme

Any material averaging scheme aims to estimate an effective material property of a composite medium. In numerical methods, there is a problem when the media exhibit discontinuities, e.g., thin layers with high contrasts, earth formations with cross-bedding structures or fluid-filled fractures. To achieve high accuracy in this situation, the finite difference and finite element method would require a very high number of grids. In SLDMEM3f the material averaging scheme allows an arbitrary model parameterization independent of the grid discretization.

In SLDMEM3f, the material averaging scheme is implemented as follows (Figure 2.10 (b)). The red boxed prism exhibits the arithmetic average $\bar{\sigma}(i, j+1/2, k+1/2)$ of the adjacent cell $\sigma_1, \dots, \sigma_4$. The prism has the size of $a_i \times b_{j+1/2} \times c_{k+1/2}$ and is centered on \otimes where the electric field $E_x(i, j+1/2, k+1/2)$ is calculated. The weights are the square root of the conductivity integrated over the prism centred around the field component. By applying the material averaging scheme, in theory, SLDMEM3f can calculate the electric and magnetic fields of arbitrary conductivity models. However, since the models do not

coincide with the grid, the question arises whether the calculated fields represent true conductivity structure or not.

The 3D rectangular blocks are used to parameterize the conductivity model with arbitrary location and size. In a 1D situation, the blocks are extended to infinity (in computational terms) in the horizontal direction, while in a 2D situation the blocks are extended to infinity in the strike direction. A large number of blocks (could be thousands of blocks) is needed to approximate more complex structures. In this case, the grid design is very crucial otherwise the conductivity models are averaged out by the material averaging scheme. Even though the model can be arbitrary and does not coincide with the grid, it will be much better to choose the model parameterization according to the grid of the forward calculation and vice versa.

2.4.3 The Lanczos Method

To begin with the Lanczos process, first define the curl-curl operator on Maxwell's equations and also a quantity including source current:

$$\mathbf{A} \equiv \sigma^{-1} \nabla \times \nabla \times \quad \text{and} \quad \varphi \equiv \sigma^{-1} \mathbf{J}, \quad (2.76)$$

then Equation (2.75) becomes

$$(\mathbf{A} + i\omega \mathbf{I}) \mathbf{E} = i\omega \varphi. \quad (2.77)$$

where \mathbf{I} is the identity matrix. Equation (2.77) has a solution in the form

$$\mathbf{E} = -i\omega^{-1} (\mathbf{A}^{-1} - i\omega^{-1} \mathbf{I})^{-1} \mathbf{A}^{-1} \varphi, \quad (2.78)$$

The first boundary conditions to the Equation (2.74) is

$$n \times \mathbf{E} = 0, \quad (2.79)$$

this boundary condition requires the boundary located several skin depth away from the source and the second boundary conditions located at the earth-air interface (at $z = 0$)

$$n \cdot \mathbf{E} = 0, \quad (2.80)$$

enforcing that the current cannot leak into the air. The initial conditions for `SLDMEM3f`:

$$\mathbf{J}(X, t) = \begin{cases} 0, & t < 0, \\ -\sigma \varphi(X) \exp(i\omega t), & \text{otherwise,} \end{cases} \quad (2.81)$$

where $X = x^\lambda$, $\lambda = 1, 2, 3$ is the spatial Cartesian coordinates in three dimension, $\omega = 2\pi f > 0$ is the radial frequency of the excited field.

The matrix \mathbf{A} in Equation (2.76) is a high dimensional $n \times n$, sparse (at most 13 entries per row or column) and symmetric $\mathbf{A} = \mathbf{A}^T$ and its eigenvalues $\lambda_1 \leq \lambda_2 \leq \dots \leq \lambda_n$. Let the eigenvalue and eigenvector pairs of this matrix \mathbf{A} be (λ_i, z_i) for $i = 1, \dots, n$. The more general problem of Equation (2.78) is

$$u = f(\mathbf{A})\varphi, \quad (2.82)$$

The whole Lancsoz process can be written as:

$$\mathbf{A}\mathbf{Q} = \mathbf{Q}\mathbf{H} + \underbrace{\beta_{m+1}q_{m+1}\mathbf{I}_m^T}_{\mathbf{R}\approx 0}, \quad (2.89)$$

where \mathbf{I}_m^T is the m^{th} column of the $m \times m$ identity matrix. The second term on the right hand side of Equation (2.89) can be neglected, after rearranging

$$\mathbf{A} = \mathbf{Q}\mathbf{H}\mathbf{Q}^T. \quad (2.90)$$

Let (θ_i, s_i) be pairs of eigenvalues and normalized eigenvectors of \mathbf{H} respectively. Denote $e_1 = (1, 0, \dots, 0)^T$ and $y_i = \mathbf{Q}s_i$, we have

$$\varphi = \|\varphi\| \sum_{i=1}^m s_{1,i} y_i,$$

where $s_{1,i}$ is the first component of the vector s_i . The spectral Lanczos decomposition method (SLDM) is to write the solution of the function u in the form:

$$u = \|\varphi\| \sum_{j=1}^m s_{j,1} (\theta_j - i\omega)^{-1} y_j = \|\varphi\| \mathbf{Q}f(\mathbf{H})e_1. \quad (2.91)$$

Collecting all together and calculating for $\mathcal{K}^m(\mathbf{A}^{-1}, \varphi)$ (by putting Equation (2.91) to Equation (2.77) or Equation (2.78)), we finally have the expression for electromagnetic fields

$$\mathbf{E}_m(\omega) = \mathbf{Q}(\mathbf{H} + i\omega\mathbf{I})^{-1}\|\varphi\| e_1. \quad (2.92)$$

In this process, $\mathbf{E}_m(\omega)$ is a good approximation of \mathbf{E} in Equation (2.78).

2.4.4 Griding Scheme

The most important issue when applying `SLDMEM3f` is designing a grid which gives an accurate solution of Maxwell's equations. Martin (2009) and then expanded by Yogeshwar (2014) gave detailed explanation how the grid should be designed for `SLDMEM3t`. The rule of thumb of the grid design is, for coarse grid the solutions are not accurate while solutions from the very fine grid are accurate, but the computational costs are also higher. The computational cost depends on the number of grids $n_x \times n_y \times n_z$. So we need to find a balance between the two. And the question: Is the gridding scheme designed for `SLDMEM3t` applicable for `SLDMEM3f`?

There are already two things that must be taken with great care in designing the grid on `SLDMEM3f`: (i) electromagnetic fields are sampled at different locations. (ii) The conductivity models where the fields calculated are averaged. The grid lines do not coincide with the model boundaries: lateral nor vertical. When checking the grid accuracy against 1D analytical solutions, the latter can cause a systematical error. For large deviations, additional grid lines have to be incorporated.

When designing the grid, three parameters are crucial and must be specified: number of the grid in vertical (n_z) and horizontal directions (n_x, n_y). The minimum and maximum of the conductivity value and also the highest and lowest frequency. Furthermore,

additional grid lines may be necessary to either better reflect the model structure or to allow the calculation of certain receiver positions. The latter can also be done by interpolation to a certain position from several other receivers (Martin, 2009). Since the EM-fields are non-linear in space, it is more accurate to avoid interpolation and include grid-lines at locations, where the solution is required.

Martin (2009) suggested the following grid discretization of SLDMEM3t on all directions, with t replaced by $1/f$:

$$g_i = d_{\min}((i - 1) + q^{(i-1)}), \quad (2.93)$$

where d_{\min} is the minimum grid spacing, with

$$q = \left(\frac{d_{\max}}{d_{\min}} - (N_g - 1) \right)^{\frac{1}{N_g - 1}},$$

where

$$d_{\min} = \sqrt{\frac{\rho_{\min}}{\pi\mu_0 f_{\max}}} \quad \text{and} \quad d_{\max} = b_n \sqrt{\frac{\rho_{\max}}{\pi\mu_0 f_{\min}}}.$$

where $b_n = 3 - 9$ and N_g is number of grid. The grid is designed according to/starting from the transmitter. Yogeshwar (2014) found that the optimum grid is between 40 - 70 in all directions. Martin (2009) and Yogeshwar (2014) used symmetric grid on horizontal direction. Since the receivers' locations depend on the grid (the electromagnetic fields are sampled on the cell), it is cumbersome to modify the location of the receivers with the modified log-spaced grid on the horizontal direction. In this thesis, a Cartesian grid was applied in the horizontal direction, while in the vertical direction, the grids were discretized by modified logspace according to Equation (2.93). An example of the grid design for SLDMEM3f is given in Figure 2.11. Note that the grid is not symmetric in x and y direction. Another advantage of this grid design is when dealing with natural sources (RMT/MT case). We do not need to redesign the grid, what we need to do is to set the input file that it is a natural source. This grid design would be very efficient in defining the CSRMT field zones that is by comparing the solution of CSRMT and RMT on some sounding points or along the profile. In this thesis, it is found that smaller d_{\min} in the vertical direction is needed in designing the grid to get an accurate solution. It is also faster (less computational time) to calculate with Cartesian discretization than modified logspace discretization on the horizontal direction.

The transmitter (dipole/bipole) in CSRMT case on SLDMEM3f are discretized by one or more current lines between two adjacent cells as in traditional Yee-Lebedev FD scheme, and it is denoted by a point in the centre of the adjacent cells. The orientation of the current is specified by the user (x , y or z direction) and the current amplitude might be positive or negative. The whole transmitter is a direct summation of the individual single dipole sources on the same orientation with each dipole lengths according to the spacing between neighbouring grid cells (Martin, 2009). As an example of the dipole is shown as a black line in Figure 2.11.

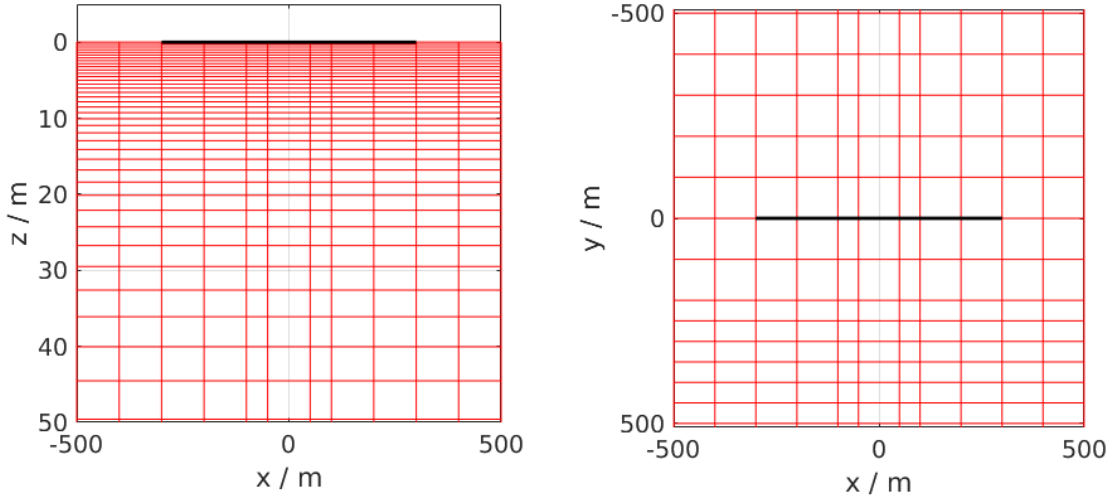


Figure 2.11: Grid design for `SLDMEM3f`. In vertical direction the grid is discretized with modified logspace according to Martin (2009). While on horizontal direction, the grid is discretized with a non symmetric Cartesian grid. The black line is the dipole.

2.4.5 Convergence of The Solution

The convergence of `SLDMEM3f` depends on the minimum eigenvalue λ_0 and maximum eigenvalue λ_n (Druskin and Knizhnerman, 1994) which can be calculated as:

$$\lambda_0 = \frac{\pi}{d_{\max}^2 \sigma_{\max} \mu_0}, \quad (2.94)$$

and

$$\lambda_n = \frac{13}{d_{\min}^2 \sigma_{\min} \mu_0}, \quad (2.95)$$

where d_{\min} and d_{\max} are the smallest and largest grid discretization respectively and the number 13 is the maximum number of non-zero elements of matrix **A**.

The arithmetical work M (minimum number of `SLDMEM3f` steps) to get required convergence of solution is given by (Martin, 2009):

$$M = \frac{12}{d_{\min}} \sqrt{\frac{1}{\mu_0 \sigma_{\min} f_{\min}}}. \quad (2.96)$$

In the modelling studies in the thesis, the value of M is taken larger than it is suggested by the Equation (2.96) that is 50000. However, if the solution is converged before, say for example 6000, then the code will stop and print the output.

To check the convergence of the solution of `SLDMEM3f` during the modelling study, three output parameters are important namely: RES, PROGN and EPS. The output parameters are printed at every 100 subspaces.

- RES: this parameter is the last time point of one specified control receiver. For a dipole source, the receiver with the shortest offset to the transmitter is used since it has the largest dynamic range in the electric field. A stable solution in the nearest receiver indicates that receivers with larger offsets have also converged. (Yogeshwar,

2014; Haroon, 2016). Since the frequency domain solutions have real and imaginary parts, both parts should be converged to the certain value.

- PROGN: this parameter is the absolute difference between current iteration to the previous iteration. When the solution converges, this value should be zero or close to zero. The real part could be 5 orders of magnitude compared to RES parameters.
- EPS: this parameter is the relative difference of current iteration to the previous iterations:

$$\text{EPS}_i = \frac{\text{PROGN}_i}{\text{RES}_i} = \frac{\text{RES}_i - \text{RES}_{i-1}}{\text{RES}_i} \times 100\%, \quad (2.97)$$

where i denotes the actual iteration. The EPS parameter is set by the user to truncate the calculation when the value has been reached. However, as the value of RES often oscillates at small iterations, the threshold may also be surpassed before the solution has actually converged. Therefore it is better to set the value as low as 10^{-10} to ensure that the calculation is not truncated.

An example of these three values is given in Figure 2.12. The real part is given with red dots, while the imaginary part is given in black dots. The units for RES and PROGN are (V/m), while the EPS is given in percent.

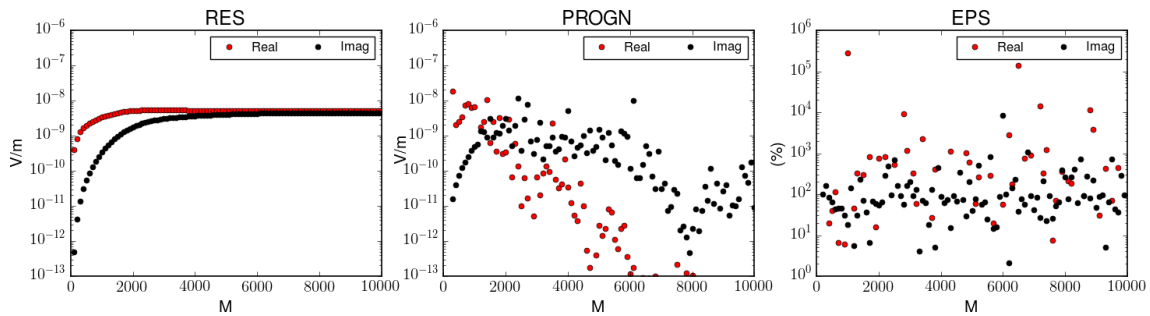


Figure 2.12: Evolution of RES, PROGN and EPS during the iteration, printed every 100 Krylov subspace.

To check the designed grid in Figure 2.11, 1D conductivity with $\rho_1 = 80\Omega\text{m}$, $h_1 = 10\text{m}$, $\rho_2 = 400\Omega\text{m}$, $h_2 = 40\text{m}$, and $\rho_3 = 40\Omega\text{m}$ is considered for both inductive (Figure 2.13) and galvanic sources (Figure 2.14) and compared with Wait recursion formula (Equation (2.63)). The designed grid on Figure 2.11 is also compared with the grid design by Martin (2009) (Figure 2.15). The results between the Cartesian grid and log-spaced grid on horizontal direction are similar regarding accuracy. Moreover, the Cartesian grid needs less computational time. It is found that the accuracy of SLDMEM3f only sensitive to the grid discretization in the vertical direction. The grid design for the horizontal discretization can be chosen quite arbitrary, but the resulting grid should be checked afterwards.

It is clear that the designed grid performs well for both inductive and galvanic sources with maximum error (relative difference) around 2%. This maximum error value is then taken as the error on the modelling for all CSRMT field zones and moreover also for 2D conductivity structure.

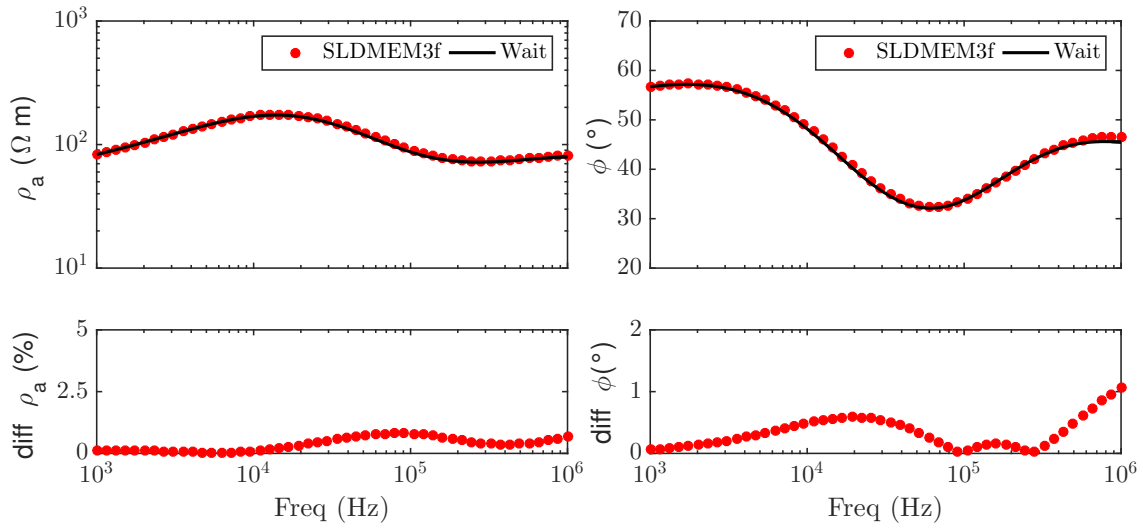


Figure 2.13: Grid check for inductive sources (RMT case).

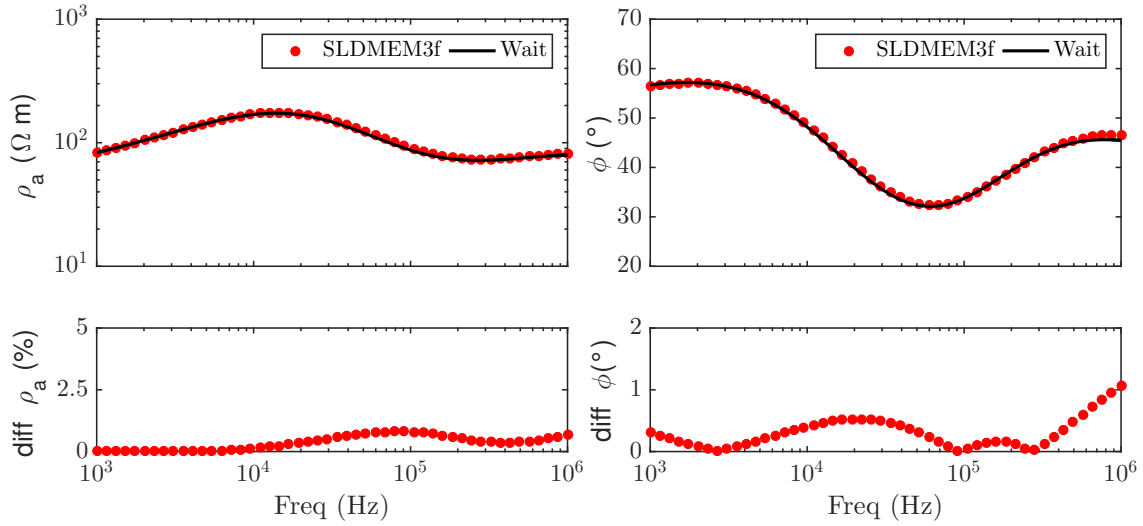


Figure 2.14: Grid check for galvanic sources (CSRMT case). Computational time = 78 seconds.

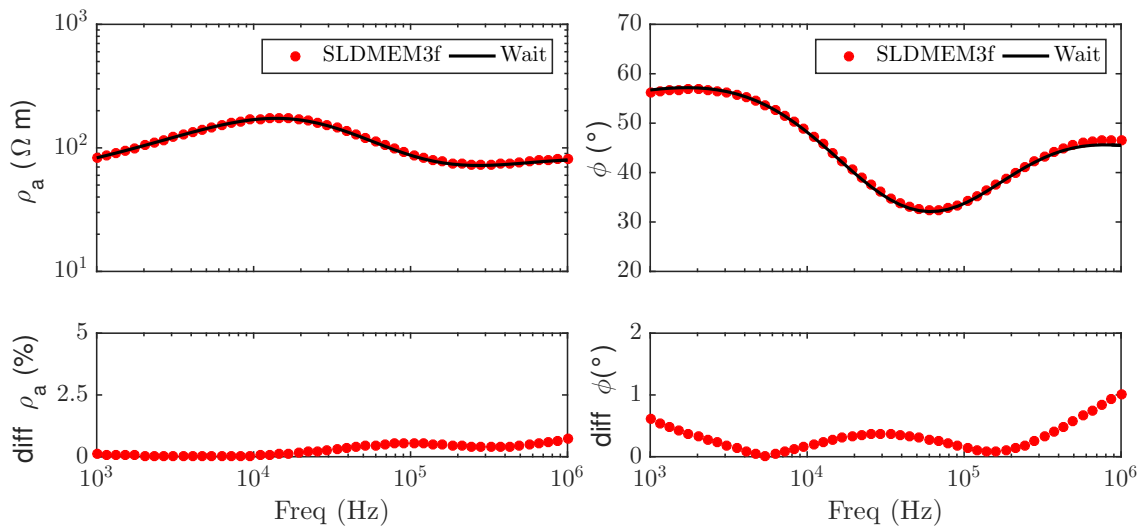


Figure 2.15: Grid check for galvanic sources (CSRMT case) with modified logspaced grid in all directions. Computational time = 316 seconds.

2.5 Displacement currents

In the EM frequency domain method, there are two extremes: a diffusion type method on low frequency < 10 kHz (MT, AMT) and a wave type method on high frequency > 10 MHz (GPR). The question arises about the validity of quasistatic approximation on the “transition” frequency range 10 kHz - 10 MHz. Do we need to take into account the displacement current? Take an example of very high frequency $> 10^5$ Hz and a very resistive region $> 20000 \Omega \text{ m}$ such as crystalline bedrock which is a typical rock in Northern Sweden and Russia. In this case, the displacement currents might play some role in the observed data. First, let's calculate again the contribution of displacement current on resistive region $10000 \Omega \text{ m}$ and high frequency $10^5 - 10^6$ Hz

$$\frac{\epsilon_0 \omega}{\sigma} = 0.001 - 0.5,$$

which simply can't be neglected on the highest frequency and in this very resistive region it must be included in the calculation of electric and magnetic fields. However, the CSRMT data are the impedances (apparent resistivity and impedance phase) which are the ratio between the electric and magnetic fields.

The effects of displacement currents on RMT data have been studied by Pedersen and his group (Persson and Pedersen, 2002; Kalscheuer et al., 2008) and recently for the CSRMT method in 1D anisotropic conductivity structure by (Shlykov and Saraev, 2015; Saraev et al., 2017). Persson and Pedersen (2002) and Kalscheuer et al. (2008) concluded that displacement currents affect RMT data which lead to misinterpretation when neglecting their effects, while Shlykov and Saraev (2015) concluded that displacement current only affects on individual components of electric and magnetic fields as well as tipper data but not on the impedance data.

To give an illustration, we compare the solution of `SLDMEM3f` (a quasistatic approximation code) - see Section 2.4- with a 1D CSEM code `CS1D` (a code considering displacement current) for a simple 1D model in the near-field zone and in the far-field zone. The dipole is $-x$ directed with length of 200 m (from $x = -100$ m to $x = 100$ m). The receivers are located at $x = 0$, $y = 40$ m for the near-field zone and at $x = 0$, $y = 1500$ m for the far-field zone. The earth conductivity is $\rho_1 = 80 \Omega \text{ m}$, $h_1 = 10$ m and $\rho_2 = 40 \Omega \text{ m}$. Note that this is a broadside configuration and the resistivity considered here is not that high as in Sweden or Russia.

The individual components of electric (E_x) and magnetic field (H_y , H_z) for transition zones are given in Figure 2.16. The influence of the displacement current on the E_x and H_y are seen on high frequency > 700 kHz, while on H_z the displacement current affect the vertical magnetic field on the whole CSRMT frequency range. The transfer functions: apparent resistivity, phase, real tipper and imaginary tipper for the electromagnetic fields on Figure 2.16 are given in Figure 2.17. The apparent resistivity, phase and imaginary tipper are almost the same between `SLDMEM3f` and `CS1D`, while there is slight difference of the real part of the tipper. Keep in mind that tipper is not zero for near-field and transition zone even for 1D situation and their magnitude might be bigger than unity.

Figure 2.18 shows the individual components of electric (E_x) and magnetic field (H_y , H_z) for far-field zone. The influence of the displacement current on the E_x and H_y are seen on

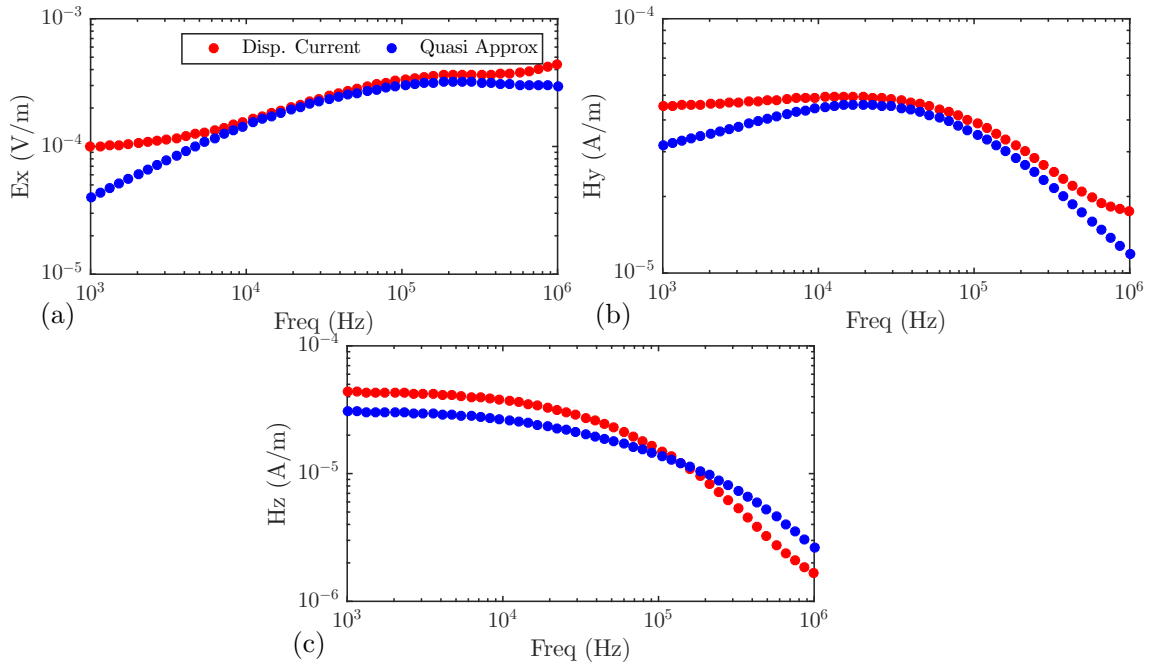


Figure 2.16: Individual electromagnetic fields: (a) electric field (E_x) and magnetic fields H_y on (b) and H_z on (c) for x directed 200 m dipole, $x = 0$, $y = 40$ m. The influence on displacement current are seen only on high frequency > 500 kHz on E_x and H_y , while on H_z on all frequency range.

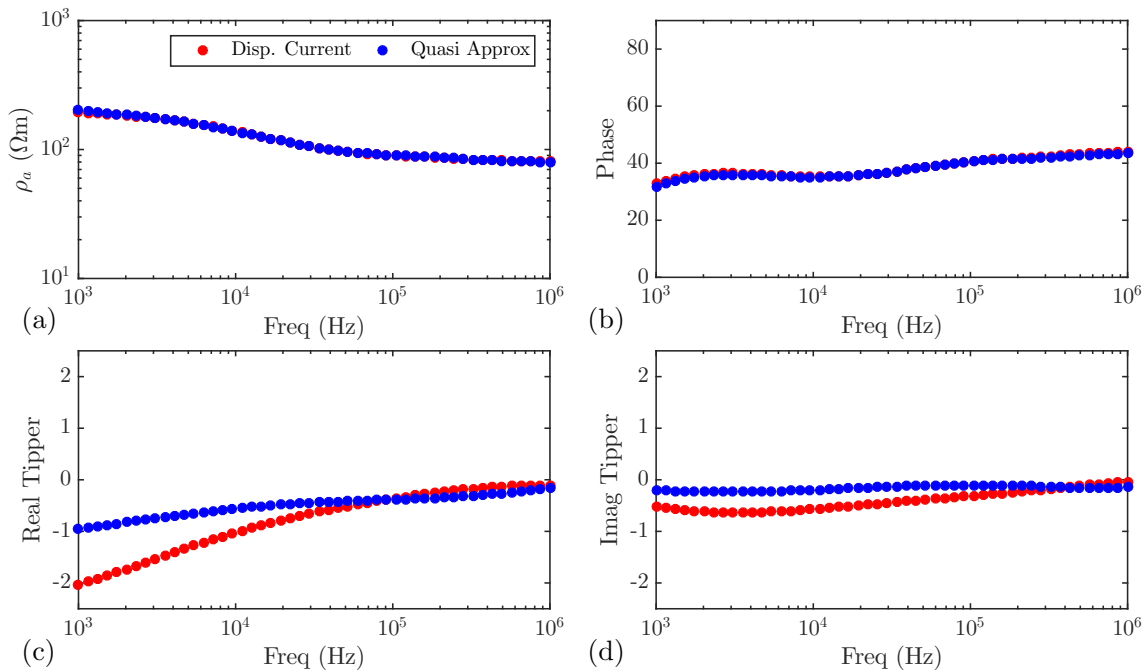


Figure 2.17: The transfer function for Figure 2.16: (a) apparent resistivity, (b) phase, (c) real tipper and (d) imaginary tipper plotted against frequency. Even the individual components are different, their ratio in forms of transfer functions almost undistorted.

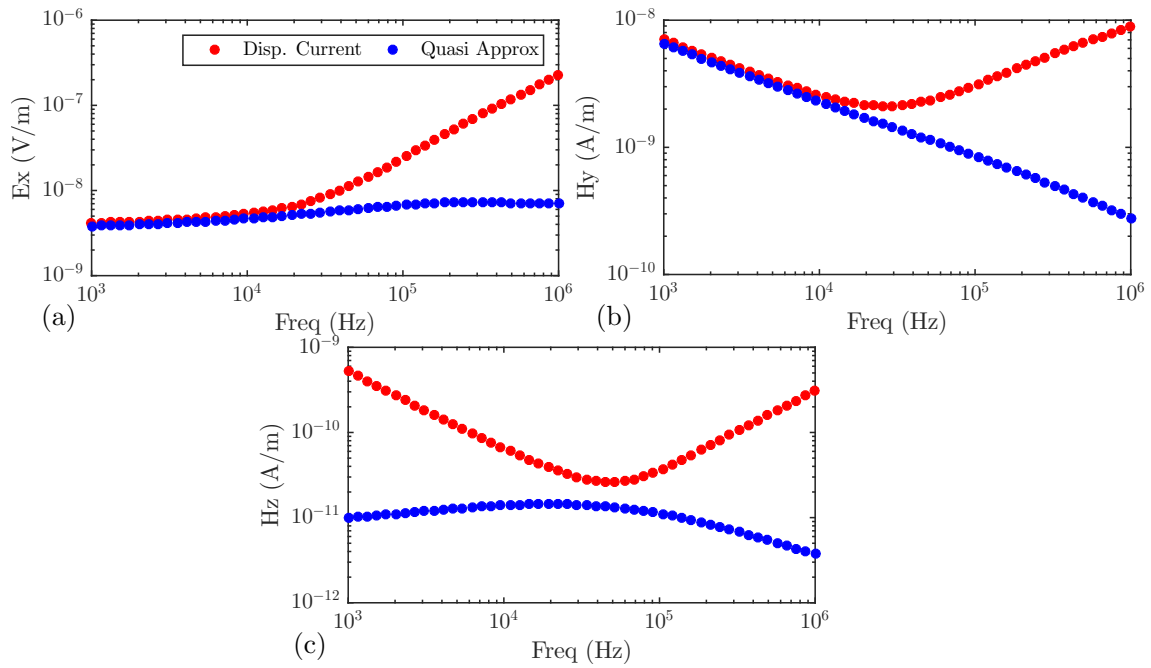


Figure 2.18: Individual electromagnetic fields: (a) electric field (E_x) and magnetic fields H_y on (b) and H_z on (c) for x directed 200 m dipole, $x = 0, y = 1500$ m. The influence on displacement current are seen on frequency from 10 kHz on E_x and H_y , while on H_z on all frequency range.

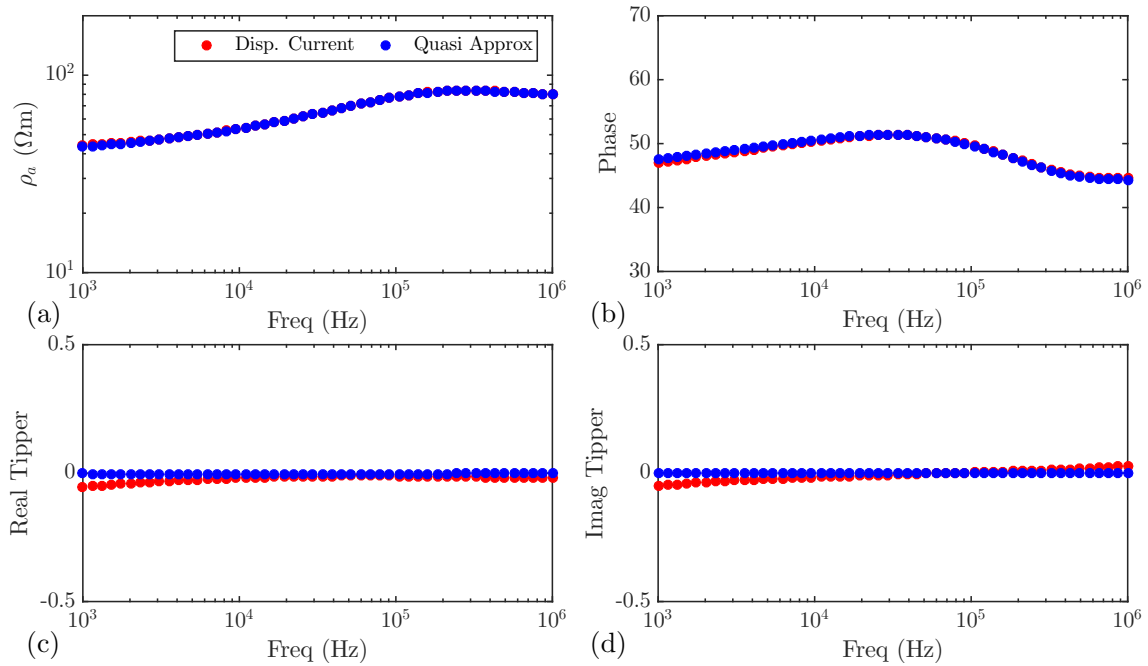


Figure 2.19: The transfer function for Figure 2.18: (a) apparent resistivity, (b) phase, (c) real tipper and (d) imaginary tipper plotted against frequency. Even the individual components are different, their ratio in forms of transfer functions almost undistorted.

frequency > 10 kHz, while on H_z the displacement current affect the vertical magnetic field on the whole CSRMT frequency range as H_z in the transition zones. The influence of displacement current on the individual components of electromagnetic fields depend on frequency, distance and the conductivity structure. The transfer functions: apparent resistivity, phase, real tipper and imaginary tipper for the electromagnetic fields in Figure 2.18 are given in Figure 2.19. The apparent resistivity, phase and real tipper and imaginary tipper are almost the same between `SLDMEM3f` and `CS1D`. In a 1D situation, tipper data is zero as in magnetotelluric since there is no lateral change in conductivity structure.

From the discussion and simple example above, the displacement current only influences the individual component of the electromagnetic fields. However, once we look the transfer function, the displacement currents influence only on the tipper data but not on the apparent resistivity and impedance phase. This result is an agreement with the result of Shlykov and Saraev (2015) but different with the conclusion of Persson and Pedersen (2002) and Kalscheuer et al. (2008). With this in mind, the modelling code is safe to apply on the CSRMT data, but one must pay attention to the tipper data. Indeed, having a code accounting displacement current would be more beneficial.

2.6 Cultural Noise

Dealing with cultural noise in an urbanized area, such as pipelines, power lines, power plants, railways, (see Figure 2.20) has always been very challenging tasks for electromagnetic geophysics both in active and passive methods. Cultural noise -which is not related to the conductivity structure of the area- causes much more complex geological interpretation of this type of data. Berdichevsky et al. (1973) classified the distortion caused by cultural noise into two significant effects: the galvanic and inductive effects. The galvanic effect is also known as current gathering, current deflection, current leakage, current concentration or current channelling (Jones, 1983) depending on the conductivity of the noise source. This galvanic distortion affects both electric and magnetic fields. The other effect that also plays a role is 2D topographic effect (Jiracek, 1990) which will not be discussed in this thesis.

The effects of conductive and resistive bodies are the opposite. For conductive case, a secondary field caused by the boundary charges. This secondary field is antiparallel to the primary field along the sides of the body and over it. This situation makes the total field reduced around the body and enhanced off the body. For resistive case, the total field is enhanced by the body and reduced of the body (the fields are deflected). Figure 2.21 shows a sketch of this behaviour (Jiracek, 1990). In MT, the soundings directly above this body will make the apparent resistivity shifted downwards (conductive case) and shifted upwards (resistive case), but the phase remains undistorted. This upward and downward shift is known as static shift. However, for a conductive body, the current channelling on CSRMT has a different effect. The injected current is carried away in such a way that the body is acting as the transmitter. This makes the field zones shifted as will be discussed in Chapter 6.

The effects of cultural noise on CSRMT data cannot be generalized. They depend on many criteria such as geological structure, position, array orientation, dipole, azimuth



Figure 2.20: Typical cultural noise that can be easily found in central Europe: (a) pipeline signs for different purposes, (b) powerline and (c) railway. Not all buried cultural noise have a sign on the ground. All photos by Imamal Muttaiqien around Cologne.

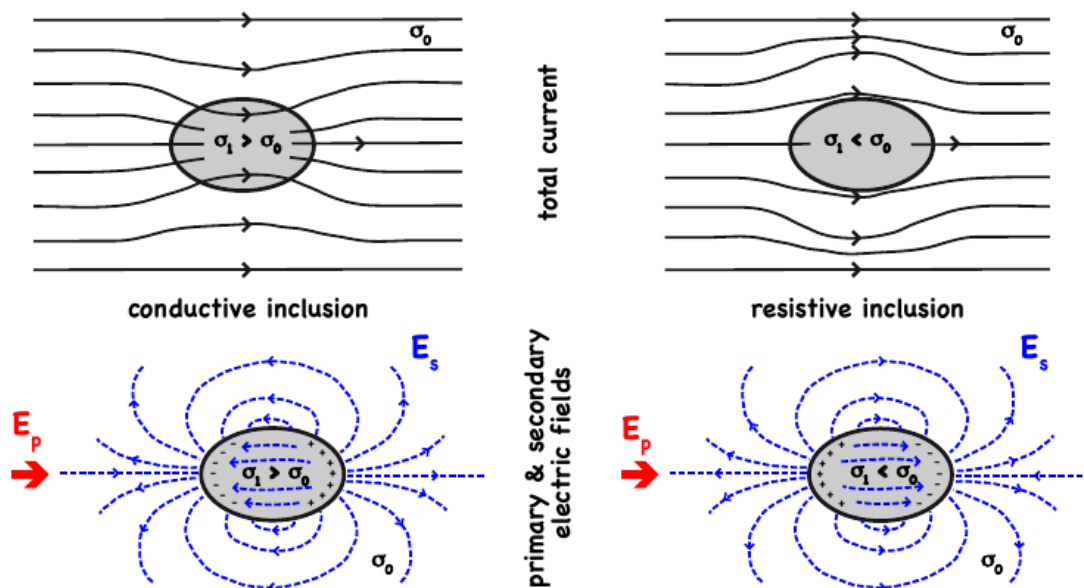


Figure 2.21: Galvanic effects for a conductive (left) and a resistive inclusion (right). Figure from Mienso-pust (2010) original with from Jiracek (1990).

and many more (Simakov, 2016). It means that the effects are different in the different area. The situation is much worse when their location sometimes unknown and the detail information of their presence is hard to obtain from the authorities. Moreover, from our experiences, the effects are seen in the time series and transfer functions. In the time series case, there are “good” and “bad” segments can be seen directly because of nearby cultural noise (see Figure 2.22 (b)). The data estimated from these time series are unreliable and should be excluded from further processing and interpretation. On a “good” time series, the estimated apparent resistivity and phase behave differently from the theoretical calculations. Thus to have interpretable data in electromagnetic geophysics, the effects of the cultural noises should be minimized and understood. Zonge and Huges (1991) suggested the following to be minimized when carrying out the CSAMT measurement which also applicable to the CSRMT method: (i) making a direct connection between the source and the sounding site, (ii) placing the E-field dipole parallel to a nearby grounded metal structure, (iii) placing an electrode close to a cultural feature (at least 100 m, it might be less for CSRMT case). Unfortunately, we made the point (i) on the experiment in Krauthausen and probably the point (ii) and (iii) on the experiment in Radervormwald.

Several distortion correction techniques have been proposed to deal with or to remove the unwanted galvanic distortion due to near-surface inhomogeneities and topography: mathematically, statistically or physically based approaches have been used (Groom and Bahr, 1992). In this thesis, to deal with this contaminated data (only on good time series), a physical approach (for example (Qian and Pedersen, 1991)) by trial and error forward modelling with the `SLDMEM3f` code is applied, and inversions with `MARE2DEM` are also carried out.

A successful land-based CSEM experiment in high noise region is described in (Streich et al., 2011), but they processed only single (individual) component of the electric fields (amplitude and phase) not regarding impedances (apparent resistivity and phase as in the MT method). Furthermore, a wavelet-based approach is applied to magnetotelluric time series to detect and characterize cultural noise (Escalas et al., 2013). Escalas et al. (2013) designed and performed a field experiment to obtain the MT time series contaminated by a controlled EM source (see Figure 2.22 (a) and (b)) and the corresponding apparent resistivity and phase in Figure 2.22. It is also seen from the derived apparent resistivity and phase on Figure 2.22 that the controlled source noise affect the N-S polarization on all period and the E-W polarization on longer period only. Inverting this type of data (even only on E-W polarization including the longer period) directly by MT inversion algorithm will yield wrong conductivity model. There are two effects considered here, first is the current channelling (see Chapter 6) and second is the effect of a grounded dipole in MT data (see Chapter 7). Both effects are identical: polarization problem and causing near-field transition zones data.

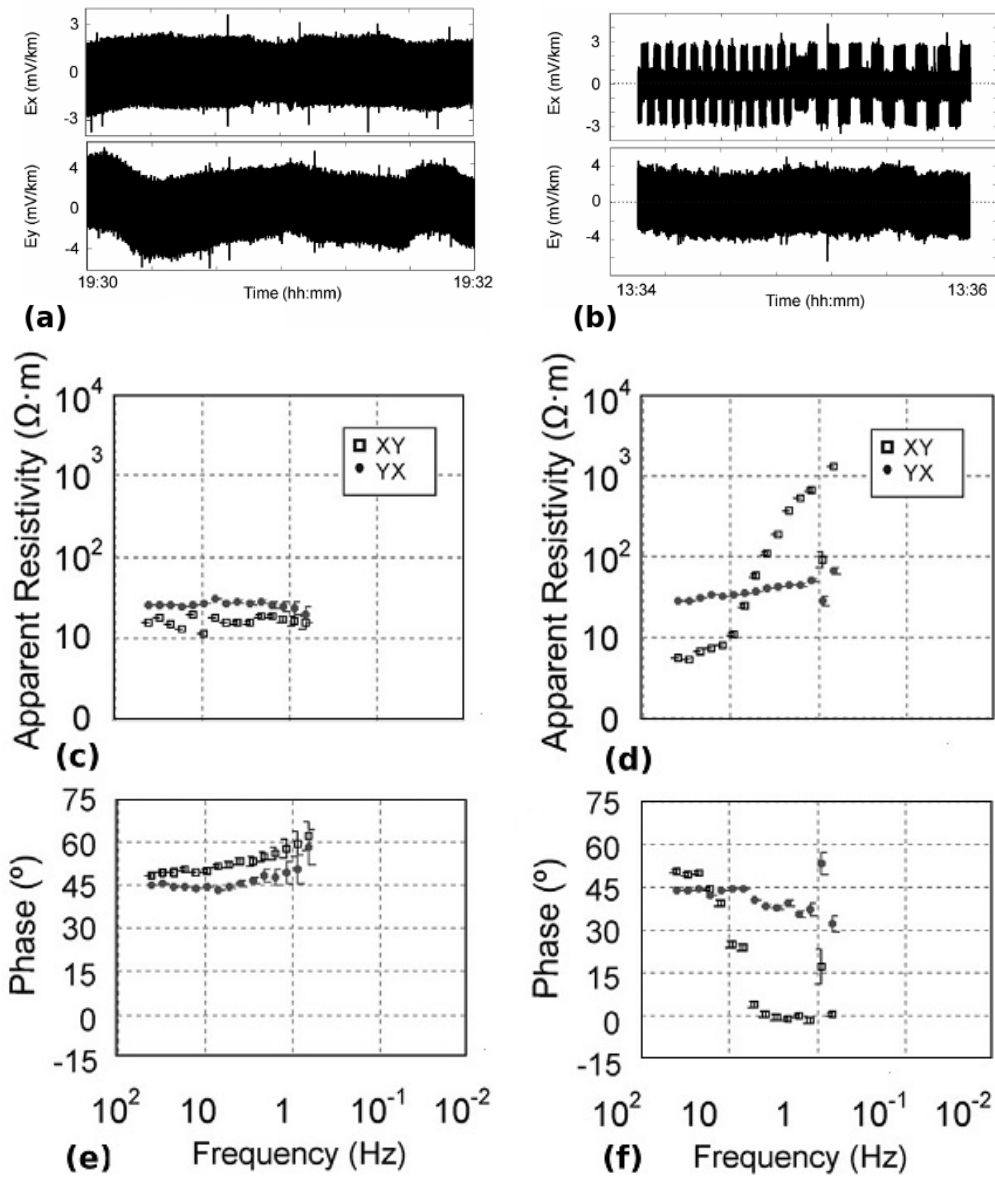


Figure 2.22: Site 24 MT time series ((a) and (b)) and responses of 1-h time series segment recorded at 128 Hz: apparent resistivity between the measured and predicted electric field components when the controlled source was inactive ((c) and (e)) and during the NS source configuration ((d) and (f)). The XY polarisation refers to the NS direction, and the YX refers to the EW direction. Figure and caption modified from (Escalas et al., 2013)

Chapter 3

Inversion of the CSRMT Data

This chapter is a review of the geophysical inversion process and algorithms used in this thesis as well as two synthetic tests of a new modified algorithm (`MARE2DEM`) considering the near field zone data. Furthermore, an analysis of the depth of investigation (DOI) is also discussed together with a sensitivity analysis of `Rund2Inv`.

The CSRMT forward problem described in Chapter 2 predicts the data (electric and magnetic fields, impedance and tipper) for a given earth conductivity model. What we want to do is to find a conductivity model that explain the measured field data. The process of finding conductivity model from the measured data is known as inversion (geophysical electromagnetic inversion). As in the CSAMT where the far field zone data are interpreted with MT algorithm, the inversion algorithms developed for the magnetotelluric method can be directly applied to the far field CSRMT data, for example, `Rund2Inv` and `Rebbocc`. Both inversion algorithms will be described briefly in this chapter without any forward problem applied to those codes. `Rund2Inv` is the main code in IGM Cologne, while `Rebbocc` (and its variant with displacement current (Kalscheuer et al., 2008)) is the main code in Uppsala University, for the RMT data interpretation. For the near field and transition zones data, the approaches are a trial and error forward modelling with `SLDMEM3f` and inversion with a modified `MARE2DEM`¹ code. A synthetic modelling study for the near-field data inversions with impedance data is given at the end of this chapter.

Table 3.1: The inversion codes available in IGM Cologne used in this thesis. The descriptions are given in the text.

Codes	Reg. freq	Reg. Stat	Tipper	Sens	Anisotropy	Topo
<code>Rund2Inv</code>	No	No	No	Yes	No	Yes
<code>Rebbocc</code>	No	Yes	Yes	No	No	Yes
<code>MARE2DEM</code>	No	No	Yes	Yes	Yes	Yes

The reason to use many different algorithms for inversions is due to the scalar nature of the RMT data (one specific frequency can only be seen in one polarization and sometimes absent in other stations) and the regularity of the data that can be read as the

¹Freely available on <http://mare2dem.ucsd.edu/>, however, the modified version of the code is provided directly by Dr Wang.

input of those codes. In *Rebbocc*, the evaluation frequencies can be different for different modes, but the data must be seen in all stations (regularity on stations). In *Rund2Inv* and *MARE2DEM*, it is much more flexible, one does not need the same evaluation frequencies and does not need to be in all stations (no regularity on frequencies and stations). However, *Rund2Inv* in IGM Cologne does not have an option invert the tipper data. Therefore, all the mentioned codes should be complementary. Furthermore, *Rund2Inv* and *Rebbocc* are finite difference codes while *MARE2DEM* is a finite element code with an adaptive finite element mesh refinement. Therefore, *MARE2DEM* is more suitable to handle topography.

A very simple illustration of the inversion process is given in Figure 3.1. In this figure, the model can be directly obtained from the measured data in 1-on-1 mapping without taking into account the errors both on the numerical errors on the forward problem and in the measured data.

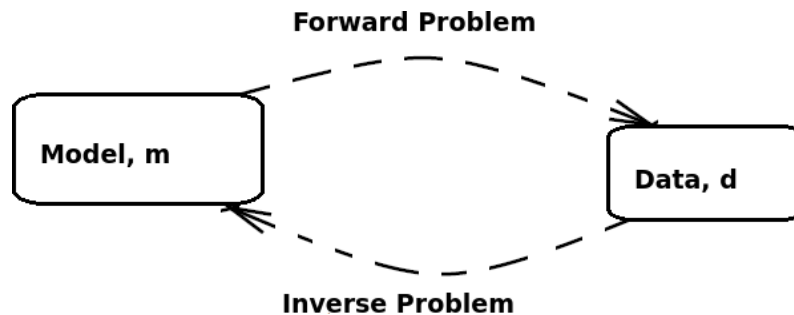


Figure 3.1: The simplistic inverse problem.

The physical parameters that we would like to know are continuous. However one normally conduct the experiments in a non-continuous way. For instance in the (CS)RMT method, the conductivity distributions are only sampled every 10 – 20 meters along the profile. Moreover, every measurement also contains some uncertainties² due to noise, precision etc. Therefore, the model derived from the inversion of the measured data do not necessarily/always equals to the true model. The non-continuity on the measurements will lead to many models that explain and fit the data equally well (a non-uniqueness problem). As a result, the inversion problem is becoming an appraisal problem. That is to find a model with unique properties, which is in the form of averages, of all solutions that fit the data at an acceptable level (by considering the errors on the measurement and modelling). In general, there are two steps in the inversion process. Let the true model be denoted by m and the data by d . The first step is an estimation problem. One reconstructs an estimated model \tilde{m} from the measured data d , see Figure 3.2. The second step is an appraisal problem, where one determines what properties of the true model are recovered by the estimated model and what errors are attached to it.

²this term may be more precise than errors

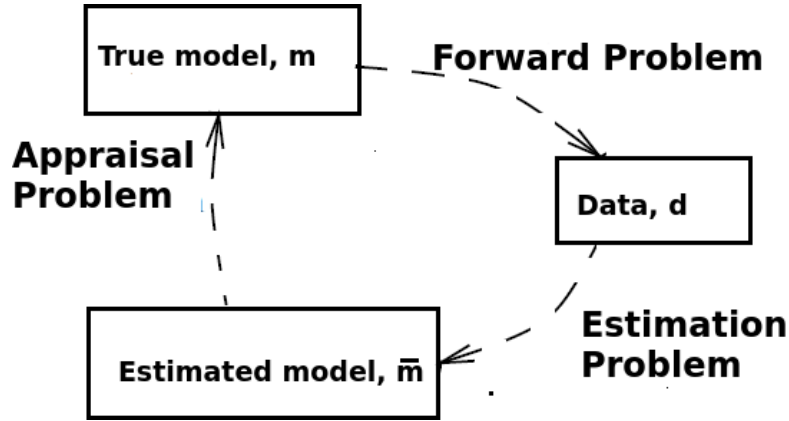


Figure 3.2: The inverse problem viewed as a combination of an estimation problem plus an appraisal problem.

3.1 Formulation of the Problem

A relation between the measured data and model parameters can be written as

$$d_i = F_i(m_1, m_2, \dots, m_M) + e_i, \quad i = 1, 2, \dots, M \quad (3.1)$$

where F_i is the forward operator which is in general a non linear problem. Here, m_j is the model parameters which in electromagnetics geophysics are conductivity distributions (including the information of the thickness as well as horizontal distribution in a 2D/3D case). F_i theoretically predicts d_i for a given value of m_j , and e_i is the error from the measured data and forward modelling error. The data d_i in this thesis are $\log_{10}(\rho_a)$ and phase impedance, log impedance, and tipper for a particular observation, polarization (TE or TM mode) and frequency. Within the inverse problem, the unknown parameters m_j (conductivity distribution) from Equation (3.1) are estimated.

It is better and simpler to write Equation (3.1) in a matrix notation, let m_j be the components of an M - dimensional column vector \mathbf{m} :

$$\mathbf{m} = (m_1 \quad m_2 \quad \dots \quad m_M)^T, \quad (3.2)$$

and the observed data and errors to be components of N - dimensional column vectors

$$\mathbf{d} = (d_1 \quad d_2 \quad \dots \quad d_N)^T, \quad (3.3)$$

$$\mathbf{e} = (e_1 \quad e_2 \quad \dots \quad e_N)^T. \quad (3.4)$$

Now Equation (3.1) can be written as

$$\mathbf{d} = F(\mathbf{m}) + \mathbf{e}. \quad (3.5)$$

One of the methods to minimize the misfit between the data \mathbf{d} and the forward modelling $F(\mathbf{m})$ is known as the least square method, which also known as L_2 norm (by taking into account the errors). This optimization problem can be written as an objective function:

$$\Phi(\mathbf{m}) = (\mathbf{d} - F(\mathbf{m}))^T \mathbf{W}(\mathbf{d} - F(\mathbf{m})), \quad (3.6)$$

where \mathbf{W} is a positive definite matrix containing pre-assigned weights.

3.2 Non-uniqueness problem

The minimization of Equation (3.6) is sought with the least square method by minimizing the objective function Φ , which satisfies:

$$\Phi(\mathbf{m}) \geq \Phi(\tilde{\mathbf{m}}), \quad (3.7)$$

for every model \mathbf{m} in the domain of Φ . The model $\tilde{\mathbf{m}}$ is a unique local least square solution. The solution exists under weak assumption that the norm of residual vector $\mathbf{d} - F(\mathbf{m})$ tends to infinity as $\|\mathbf{m}\|$ tends to infinity. The solution is unique if and only if Φ is a convex function:

$$\Phi(\lambda\mathbf{m}_1 + (1 - \lambda)\mathbf{m}_2) < \lambda\Phi(\mathbf{m}_1) + (1 - \lambda)\Phi(\mathbf{m}_2), \quad (3.8)$$

for all models \mathbf{m}_1 and \mathbf{m}_2 and $0 \leq \lambda \leq 1$. This equation means that between any two points, the value of the function is less than a linear interpolation of the function between those two points as in Figure 3.3. If $\tilde{\mathbf{m}}$ is unique, then

$$\Phi(\mathbf{m}) > \Phi(\tilde{\mathbf{m}}). \quad (3.9)$$

In this case $\tilde{\mathbf{m}}$ can be said to be a unique global least square solution. However, it is not

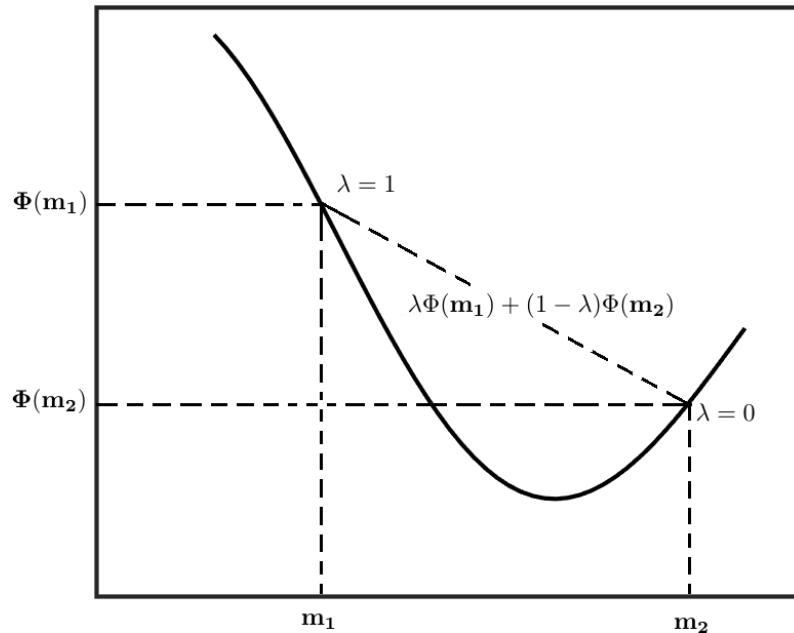


Figure 3.3: An example of a convex function.

easy to identify the properties of F which make Φ convex. A function with the global minimum is having a zero gradient (first derivative) and also positive curvature (second derivative). Assume F is at least twice continuously differentiable (to get the first and second derivative of the function otherwise it is not possible to make any assessment),

then its gradient vector is given by

$$[\mathbf{g}_m]_j = \frac{\partial \Phi(\mathbf{m})}{\partial m_j}, \quad (3.10)$$

$$= 2\mathbf{A}_m^T \mathbf{W}(F(\mathbf{m}) - \mathbf{d}), \quad (3.11)$$

where \mathbf{A}_m is the Jacobian of F exists at each \mathbf{m} . The second derivatives, the Hessian matrix of the function:

$$[\mathbf{H}_m]_{jk} = \frac{\partial^2 \Phi(\mathbf{m})}{\partial m_j \partial m_k}, \quad (3.12)$$

$$= 2\mathbf{A}_m^T \mathbf{W} \mathbf{A}_m + \mathbf{H}_m^{\text{nl}}, \quad (3.13)$$

where

$$[\mathbf{H}_m^{\text{nl}}]_{jk} = 2 \sum_{i,l=1}^N \frac{\partial^2 F_i}{\partial m_j \partial m_k} W_{il} (F_l(\mathbf{m}) - d_l). \quad (3.14)$$

Under this assumption, a necessary condition for $\tilde{\mathbf{m}}$ to be unique local minimizer of Φ is that it be a stationary point at which $\mathbf{g}_{\tilde{\mathbf{m}}} = 0$. To satisfy this stationary point, $\tilde{\mathbf{m}}$ must be a solution of:

$$\mathbf{A}_m^T \mathbf{W}(\mathbf{d} - F(\mathbf{m})) = 0. \quad (3.15)$$

When $\tilde{\mathbf{m}}$ has a zero gradient and positive definite Hessian, $\tilde{\mathbf{m}}$ is a unique, local least-square solution. The Hessian requirement is sufficient but not necessarily in general. These results do not address the question of whether stationary points with a positive definite Hessian exist or, when they do, how many there are and which achieve a global minimum of Φ . An example to illustrate a function which has local and global minima is

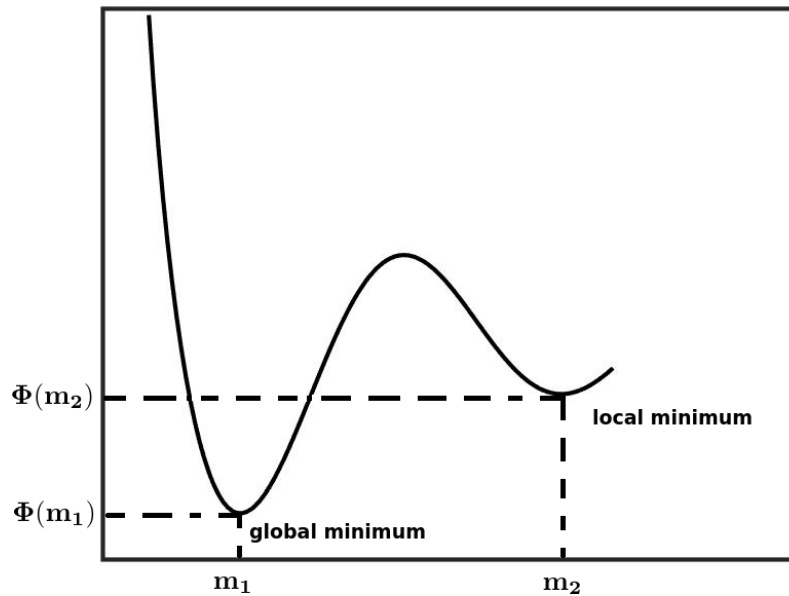


Figure 3.4: A function with local and global minima. Both minimum have zero gradient (first derivative) and also positive curvature.

given in Figure 3.4. Both minima have zero gradient and also positive curvatures.

3.3 Nonlinearity and Ill-Posedness

There are two issues in the geophysical inversion that have to be taken into account and treated carefully: nonlinearity and ill-posedness. In most practical problems, a nonlinear inversion is treated as a linear optimization problem where a suitably chosen measure of the data misfit is reduced as a function of the model parameters. A system (function) is called linear system if the following identity holds:

$$F(c_1 \mathbf{m}_1 + c_2 \mathbf{m}_2) = c_1 F(\mathbf{m}_1) + c_2 F(\mathbf{m}_2), \quad (3.16)$$

for all real numbers c_1 and c_2 and all model vectors \mathbf{m}_1 and \mathbf{m}_2 .

The Maxwell's equations behave in a non-linear way due to the product of electrical conductivity and the electric field. The most common approach to solve a non-linear inverse problem is to linearize the original problem by expanding the forward solution in a Taylor series around a reference model \mathbf{m}_0 :

$$F(\mathbf{m}) = F(\mathbf{m}_0) + \mathbf{A}_{\mathbf{m}_0}(\mathbf{m} - \mathbf{m}_0) + \mathcal{O}(\|\mathbf{m} - \mathbf{m}_0\|), \quad (3.17)$$

where $\mathbf{A}_{\mathbf{m}_0}$ is a linear transformation known as Fréchet derivative of F and $\mathcal{O}\|\dots\|$ is the Landau operator from asymptotic theory describing the error. In general, the Fréchet derivative depends on the reference model \mathbf{m}_0 . In a finite dimensional data and model spaces, this Fréchet derivative is a matrix of partial derivatives of the forward operator, known as the Jacobian matrix, and in geophysics also known as the sensitivity matrix:

$$[\mathbf{A}_{\mathbf{m}_0}]_{ij} = \left. \frac{\partial F_i(\mathbf{m})}{\partial m_j} \right|_{\mathbf{m}=\mathbf{m}_0}. \quad (3.18)$$

The first order approximation, only keeping two first terms on the Equation (3.17) and dropping second and higher order terms, known as the linearized form of the forward problem:

$$F(\mathbf{m}) = F(\mathbf{m}_0) + \mathbf{A}_{\mathbf{m}_0}(\mathbf{m} - \mathbf{m}_0). \quad (3.19)$$

A well-posed problem must satisfy the following conditions (Hadamard, 1902): (i) the problem must have a solution, (ii) the solution must be unique, (iii) the solution must be stable against a perturbation to the problem inputs. If any of these are violated, the problem is ill-posed. In general, the inverse problems are ill-posed.

3.4 Regularization Problem

The fact that most geophysical inverse problems are ill-posed (partly underdetermined and partly overdetermined) and ill-conditioned (small errors in the data causes large variations in the model), which result in non-unique solutions. The objective function (Equation (3.6)) should be extended or regularized in the sense that the solution is not too sensitive to small changes of the data. The idea behind regularization is to replace an unstable problem with a closely related stable problem, or really a family of stable

problems. This is known as the damped least square or the “regularized” problems introduced by Levenberg (1944). A damped least squares estimate of \mathbf{m} can be defined as a constrained least square estimate with a constraint is given by

$$\Omega(\mathbf{m}) \leq \mu, \quad (3.20)$$

where $\mu > 0$ and Ω is a positive value function known as stabilizing functional. In application to a geophysical inverse problem, the stabilizing functional $\Omega(\mathbf{m})$ is typically chosen to be the measure of the spatial roughness of the unknown model and given in the form (Rodi and Mackie, 2012)

$$\Omega(\mathbf{m}) = \int_V dV |Lm|^2, \quad (3.21)$$

where V is the domain of the model function, L is the differential operator and $|\dots|$ is the absolute value of a vector. When \mathbf{m} is a finite differential model, Equation (3.21) becomes:

$$\Omega(\mathbf{m}) = \mathbf{m}^T \mathbf{L}^T \mathbf{V} \mathbf{L} \mathbf{m}, \quad (3.22)$$

The method minimizing the least square objective function of Equation (3.6) subject to (3.20) is known as Lagrange multiplier. This is also called as a regularized solution of the inverse problem. The objective function then is given by:

$$\Psi(\mathbf{m}) = \Phi(\mathbf{m}) + \lambda \Omega(\mathbf{m}), \quad (3.23)$$

where λ is known as regularization parameter. Choosing the best value of λ which yields the best solution is an important task. As $\lambda \rightarrow 0^+$ the regularized problem converges to the unstable original problem, and as λ increases the regularized problem becomes much more stable, but the differences are large with the original problem we would like to solve in the first place.

There are two methods to solve Equation (3.23): the Marquardt method and the Occam method. On a Marquardt type inversion, the regularization parameter λ is kept constant during the inversion. While on an Occam type inversion, the regularization parameter λ can be varied on specific value ranges until the desired misfit is reached. `Rund2Inv` is a Marquardt type inversion algorithm. While `Rebbocc` and `MARE2DEM` are Occam type algorithms. The optimum value of each algorithm is sought in different ways.

One of the methods approximating optimal trade-off between data misfit and model roughness, λ , is called L curve criterion (Hansen and OLeary, 1993). The goal is to find the corner (the maximum curvature point) of the trade-off curve $\Phi(\tilde{\mathbf{m}})$ (model norm, I will use symbol Φ_m) versus $\Omega(\tilde{\mathbf{m}})$ (data norm, I will use Φ_d) with varied λ . Others are plotting between RMS vs sum squared misfit, RMS vs roughness measure. The final goal is to find a model which is geologically reasonable with data residuals are consistent with the errors in the data. However, this method has two drawbacks. First, with the reconstruction of very smooth exact solutions, that is the solution dominated by the first few SVD (singular value decomposition) solution. This will make L curve criterion fail. Second, the asymptotic behaviour of the regularized problem. As the problem size (n) increase that is the regularization parameter λ_L computed by the L-curve criterion may not

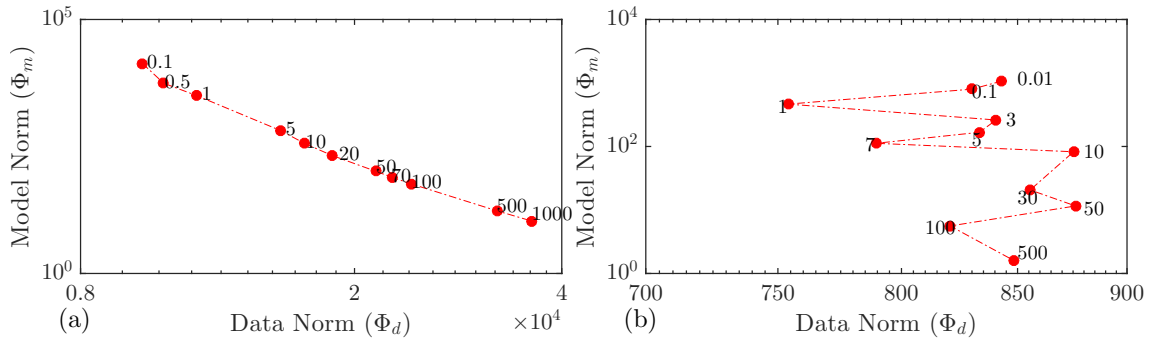


Figure 3.5: L curve criterion for real data from Krauthausen Germany with starting model of $50 \Omega\text{m}$, the value of the regularizing parameter λ are in red (a) profile 1 where it is hard to find optimum λ , (b) for profile 2 with oscillatory features.

behave consistently with the optimal parameter λ_{opt} as n increases (Hansen and OLeary, 1993). Furthermore, as it has been shown by Constable et al. (2015) that the “corner” depends on the scaling of the axes which could move around.

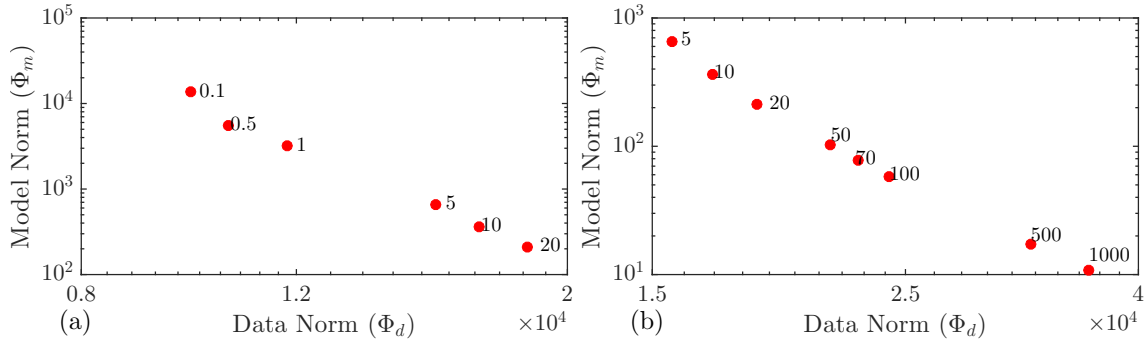


Figure 3.6: Figure 3.5(a) is plotted on different scale, the corner is moving depending on the scale of the axis and on the chosen regularization parameter.

In `Rund2Inv`, to find the optimal λ with L curve criterion is a tedious process since it is not automatic. One needs to run many inversions with different λ (for example the value between 0.1 - 1000) and then plot the model norm versus the model roughness with different λ . It is often that the real corner with maximum curvature not achieved within this process as shown in Figure 3.5 (a). In addition, the L curve might also have some oscillatory curves as in Figure 3.5 (b). Figure 3.6 is actually Figure 3.5 (a) plotted with different axis that is cutting the x and y axis. In Figure 3.6 (a) the L-curve is plotted from 8000 - 15000 with y axis from 10^2 to 10^5 and in Figure 3.6 (b) the L-curve is plotted from 15000 - 40000, while the y axis is from $10 - 1000$. It is clearly seen that the “corner” is moving around, this has been shown by Constable et al. (2015). However, for `Rund2Inv`, there is no better way to find the optimum regularization parameter.

In `Rebbocc` and `MARE2DEM`, the parameter λ is used in each iteration not only as a smoothing parameter but also as a step length control. The objective function is solved for a series of trial values of λ and the misfit (the difference between observed and predicted data) for each λ is evaluated by solving the 2-D forward problem until the desired misfit is reached. The inversion processes in `Rebbocc` and `MARE2DEM` are divided into two phases. The phase I is to find a model which satisfies the desired misfit. After that, then Phase II is to vary λ to search the model with the smallest norm by keeping the misfit

on the desired level. Note that the desired misfit might not be reached. The detail of the calculation of the regularization parameter λ in `Rebbocc` and `MARE2DEM` will be given later.

3.5 Rund2Inv code

The first inversion algorithm used to invert the RMT data is `Rund2Inv`. This code has been applied for many years in the IGM Cologne to interpret the RMT data. One of the nice features of this code is the sensitivity output of the inversion, that is the Jacobian is calculated in a classical way. As stated before, this code does not have an option for inversion of the tipper data.

3.5.1 Algorithm

In order to get the conductivity model in automatic way the observed CSRMT far-field zone data and RMT data were inverted with non-linear conjugate gradient (NLCG) algorithm of Rodi and Mackie (2001) known as `Rund2Inv`³. In this section, the algorithm is described briefly. Let's start with the damped least square objective functional by putting (3.22) to (3.23) and setting $\mathbf{V} = 1$, with the functional given by (3.6):

$$\Psi(\mathbf{m}) = (\mathbf{d} - F(\mathbf{m}))^T \mathbf{W}(\mathbf{d} - F(\mathbf{m})) + \lambda \mathbf{m}^T \mathbf{L}^T \mathbf{L} \mathbf{m}, \quad (3.24)$$

for given λ , \mathbf{L} and \mathbf{W} . The forward operator $F(\mathbf{m})$ is discretized Maxwell's equations in finite difference for 2D magnetotellurics problem (Mackie et al., 1988; Madden and Mackie, 1989). The positive-definite matrix \mathbf{W} plays the role of the variance of the error vector \mathbf{e} . The second term of $\Psi(\mathbf{m})$ defines a stabilizing functional on the model space. The regularization parameter, λ , is a positive number in which optimum value for a specific problem is selected with L curve criterion. The matrix \mathbf{L} is a simple, second-difference operator such that $\mathbf{L}\mathbf{m}$ approximates the Laplacian of $\log \rho$.

Before starting the algorithm, let's define the gradient and Hessian of the objective function by:

$$\begin{aligned} g^j(\mathbf{m}) &= \partial_j \Psi(\mathbf{m}), \\ H^{jk}(\mathbf{m}) &= \partial_j \partial_k \Psi(\mathbf{m}) \quad j, k = 1, \dots, M, \end{aligned}$$

where \mathbf{g} is a M -dimensional vector and \mathbf{H} is a $M \times M$ symmetric matrix. While the Jacobian of the forward operator defined by:

$$A^{ij}(\mathbf{m}) = \partial_j F^i(\mathbf{m}), \quad i = 1, \dots, N. \quad j = 1, \dots, M.$$

³The older version of the code (a standalone one) is used in this thesis, the new version is implemented in `WinGlink`

With the above definition, the gradient and Hessian of (3.24):

$$\mathbf{g}(\mathbf{m}) = -2\mathbf{A}(\mathbf{m})^T \mathbf{W}(\mathbf{d} - F(\mathbf{m})) + 2\lambda \mathbf{L}^T \mathbf{L} \mathbf{m}, \quad (3.25)$$

$$\mathbf{H}(\mathbf{m}) = 2\mathbf{A}(\mathbf{m})^T \mathbf{W} \mathbf{A}(\mathbf{m}) + 2\lambda \mathbf{L}^T \mathbf{L} - 2 \sum_{i=1}^N q^i \mathbf{B}^i(\mathbf{m}), \quad (3.26)$$

where \mathbf{B}^i is the Hessian of F^i and $q = \mathbf{W}(\mathbf{d} - \mathbf{F}(\mathbf{m}))$.

If F is linearized about a model \mathbf{m}_{ref} , the approximate objective function, its gradient and Hessian matrix:

$$\begin{aligned} \tilde{F}(\mathbf{m}; \mathbf{m}_{\text{ref}}) &= F(\mathbf{m}_{\text{ref}}) + \mathbf{A}(\mathbf{m}_{\text{ref}})(\mathbf{m} - \mathbf{m}_{\text{ref}}), \\ \tilde{\Psi}(\mathbf{m}; \mathbf{m}_{\text{ref}}) &= (\mathbf{d} - \tilde{F}(\mathbf{m}; \mathbf{m}_{\text{ref}}))^T \mathbf{W}(\mathbf{d} - \tilde{F}(\mathbf{m}; \mathbf{m}_{\text{ref}})) + \lambda \mathbf{m}^T \mathbf{L}^T \mathbf{L} \mathbf{m}. \end{aligned}$$

In the linearized problem, Ψ is the quadratic function that results from replacing F to \tilde{F} . In this linear problem, the gradient and Hessian become:

$$\tilde{\mathbf{g}}(\mathbf{m}; \mathbf{m}_{\text{ref}}) = -2\mathbf{A}(\mathbf{m})_{\text{ref}}^T \mathbf{W}(\mathbf{d} - F(\mathbf{m}; \mathbf{m}_{\text{ref}})) + 2\lambda \mathbf{L}^T \mathbf{L} \mathbf{m}, \quad (3.27)$$

$$\tilde{\mathbf{H}}(\mathbf{m})_{\text{ref}} = 2\mathbf{A}(\mathbf{m})_{\text{ref}} \mathbf{W} \mathbf{A}(\mathbf{m})_{\text{ref}} + 2\lambda \mathbf{L}^T \mathbf{L}, \quad (3.28)$$

$\tilde{\Psi}$ is quadratic in \mathbf{m} , $\tilde{\mathbf{g}}$ is linear in \mathbf{m} , while $\tilde{\mathbf{H}}$ is independent of \mathbf{m} . So

$$\begin{aligned} \tilde{\Psi}(\mathbf{m}; \mathbf{m}_{\text{ref}}) &= \Psi(\mathbf{m}_{\text{ref}}) + \mathbf{g}(\mathbf{m}_{\text{ref}})^T (\mathbf{m} - \mathbf{m}_{\text{ref}}) \\ &\quad + \frac{1}{2} (\mathbf{m} - \mathbf{m}_{\text{ref}})^T \tilde{\mathbf{H}}(\mathbf{m}_{\text{ref}}) (\mathbf{m} - \mathbf{m}_{\text{ref}}), \end{aligned} \quad (3.29)$$

$$\tilde{\mathbf{g}}(\mathbf{m}; \mathbf{m}_{\text{ref}}) = \mathbf{g}(\mathbf{m}_{\text{ref}}) + \tilde{\mathbf{H}}(\mathbf{m}_{\text{ref}}) (\mathbf{m} - \mathbf{m}_{\text{ref}}), \quad (3.30)$$

now we have $\tilde{F}(\mathbf{m}; \mathbf{m}_{\text{ref}}) = F(\mathbf{m}_{\text{ref}})$, $\tilde{\Psi}(\mathbf{m}; \mathbf{m}_{\text{ref}}) = \Psi(\mathbf{m}_{\text{ref}})$ and $\tilde{\mathbf{g}}(\mathbf{m}; \mathbf{m}_{\text{ref}}) = \mathbf{g}(\mathbf{m}_{\text{ref}})$, but $\tilde{\mathbf{H}}(\mathbf{m}_{\text{ref}})$ is only approximation of $\mathbf{H}(\mathbf{m}_{\text{ref}})$.

A sequence of line searches is used to determine the model sequence for NLCG along computed search directions, \mathbf{p} :

$$\begin{aligned} \mathbf{m}_0 &= \text{given}, \\ \Psi(\mathbf{m}_l + \alpha_l \mathbf{p}_l) &= \min_{\alpha} \Psi(\mathbf{m}_l + \alpha \mathbf{p}_l), \\ \mathbf{m}_{l+1} &= \mathbf{m}_l + \alpha_l \mathbf{p}_l. \quad l = 1, 2, \dots \end{aligned} \quad (3.31)$$

The \mathbf{m}_0 is selected by the user. The most common selection is homogeneous halfspace of the measured average apparent resistivity. Different starting models should be tested to see the effect of the starting model to the inversion results which can also be used to determine the depth of investigation with the method introduced by Oldenburg and Li (1999). Some type of iterative schemes is required to solve the line search problem (3.31) which is not quadratic. The univariate function to be minimized can be defined as:

$$\psi(\alpha) \equiv \Psi(\mathbf{m}_l + \alpha \mathbf{p}_l). \quad (3.32)$$

The line search generates a minimizing sequence $\alpha_{l,k}$, $k = 0, 1, \dots, K$ with $\alpha_{l,0} = 0$ and

with $\alpha_{l,k}$ taken as the solution of (3.31). For each step, the quantities

$$\mathbf{m}_{l,k} = \mathbf{m}_l + \alpha_{l,k} \mathbf{p}_l, \quad (3.33)$$

$$\mathbf{A}_{l,k} = \mathbf{A}_{\mathbf{m}_{l,k}}. \quad (3.34)$$

A Gauss-Newton approximation of ψ at k th step is given by

$$\psi_k(\alpha) = \Psi_{l,k}(\mathbf{m}_{l,k} + \alpha \mathbf{p}_l), \quad (3.35)$$

and the Gauss-Newton update finally given by

$$\alpha_{l,k+1} = \alpha_{l,k} - \frac{\mathbf{g}_{l,k}^T \mathbf{p}_l}{\mathbf{p}_l^T \mathbf{H}_{l,k} \mathbf{p}_l}. \quad (3.36)$$

As in the linear conjugate gradient method, the search directions are also iterated:

$$\begin{aligned} \mathbf{p}_0 &= -\mathbf{C}_0 \mathbf{g}_0, \\ \mathbf{p}_l &= -\mathbf{C}_l \mathbf{g}_l + \beta_l \mathbf{p}_{l-1}, \quad l = 1, 2, \dots \end{aligned} \quad (3.37)$$

where β_l is calculated by using the Polak-Ribiere version of NLCG (Polak, 1971) as:

$$\beta_l = \frac{\mathbf{g}_l^T \mathbf{C}_l (\mathbf{g}_l - \mathbf{g}_{l-1})}{\mathbf{g}_{l-1}^T \mathbf{C}_l \mathbf{g}_{l-1}}.$$

During the iteration C_l is allowed to vary. Unlike in linear CG, the search direction are not necessarily conjugate with respect to some fixed matrix, but they do satisfy a weaker condition

$$\mathbf{p}_l^T (\mathbf{g}_l - \mathbf{g}_{l-1}) > 0, \quad l > 0. \quad (3.38)$$

Finally, to check the quality of the inversion results, the root mean square (RMS) of Rund2Inv is calculated by the following formula:

$$\text{RMS} = \sqrt{\frac{(\mathbf{d} - F(\mathbf{m}))^T \mathbf{W} (\mathbf{d} - F(\mathbf{m}))}{N}} \times 100\%, \quad (3.39)$$

where \mathbf{W} is the error covariance matrix. By choosing optimal regularization parameter, the RMS error should be in the range 1 – 1.5% to have a good quality conductivity model. The RMS value represents the reduced chi-square value or the average standard deviation between the model data and the observed data.

3.5.2 Depth of Investigation

The Niblett-Bostick and $\rho - z^*$ transformation on Chapter 2 gives the first idea to estimate the depth of investigation of the MT method. Furthermore Spies (1989) also introduced that the depth of investigation is 1.5 of the skin depth:

$$z_{sp} \equiv 1.5\delta, \quad (3.40)$$

where δ is the skin depth. Seher and Tezkan (2007) applied the method of Oldenburg and Li (1999) which originally applied to the DC and IP methods. This Oldenburg's method based on the choice of the initial models. The main idea is to determine which parts of the inversion results do not depend on the initial models which fit the data. To realize this, at least 3 inversions with different starting model should be performed with their optimal regularization parameter. The DOI is then defined as (Seher and Tezkan, 2007):

$$\text{DOI} = \frac{1 - C}{2}, \quad (3.41)$$

where C is the cross correlation between two resistivity models.

Adrian (2017) suggested the following choice of the initial models. The measured data are inverted with homogenous halfspace of $\rho_0 = \bar{\rho}_a$ that is the average value of apparent resistivity. However, from my experience, a factor 2 is usually enough to calculate the DOI (the results do not differ using factor 2 or 10). The two additional inversions have starting model of $\rho_1 = 10\rho_0$ and $\rho_2 = \rho_0/10$. The cross-correlation function of a cell is calculated as the followings. 3 rows including 5 cells each are selected, and the resulting value was assigned to the central cell. When the model is constrained by the data, the C is high, and the DOI is close to zero. The other case is when C is low, that is the inversion result depends on the initial model. Oldenburg and Li (1999) suggested the value of 0.1 – 0.2 that limits reliable inversion results from non-reliable one. Seher and Tezkan (2007) concluded that $2z^*$, DOI, and z_{sp} yield the same order of magnitude, but could also vary about a factor 2 order of magnitude for different resistivity distributions.

In addition to the above DOI estimates, one should also perform a sensitivity analysis. The sensitivity analysis can be realized by looking into the Jacobian matrix. Unfortunately, the computation of the Jacobian matrix in the inversion process is computationally expensive. `Rund2Inv` on the IGM Cologne has two variants with and without computing the sensitivity. Within `Rund2Inv` without sensitivity, the explicit computation of Jacobian is not needed but only the product of the Jacobian on specific vectors (details can be found on the appendix of Rodi and Mackie (2001)) which is then applied to the code incorporated to the `WinGlink` software. In `Rund2Inv`, the sensitivity analysis first applied to RMT data by (Recher, 2002) and for MT data by (Schwalenberg et al., 2002). The sensitivity matrix in `Rund2Inv` is given by

$$s_j = \frac{1}{\Delta_j} \sum_1^N \left\| \frac{1}{\sigma_i} \frac{\partial f_i(\mathbf{m})}{\partial m_j} \right\|, \quad (3.42)$$

where σ_i is the standard deviation, Δ_j is the respective grid element (Schwalenberg et al., 2002). The results of the sensitivity matrix are given in logarithmic value.

Recher (2002) and Schwalenberg et al. (2002) found that when the value of the sensitivity is less than 10^{-4} for RMT and MT data respectively, the results are not reliable and can be left out from further interpretation. In the TEM method, Martin (2009) suggested that the value $1 - 10^{-2}$ is well resolved $10^{-3} - 10^{-4}$ are poorly resolved and smaller than 10^{-4} are not reliable anymore. The term reliable here means that the structures below the threshold are not important to fit the data. Therefore, it can be used to distinguish between the real conductivity structures and inversion artefacts or the starting model.

Moreover, the sensitivity analysis can also be used to constrain the depth of investigation of the (CS)RMT method.

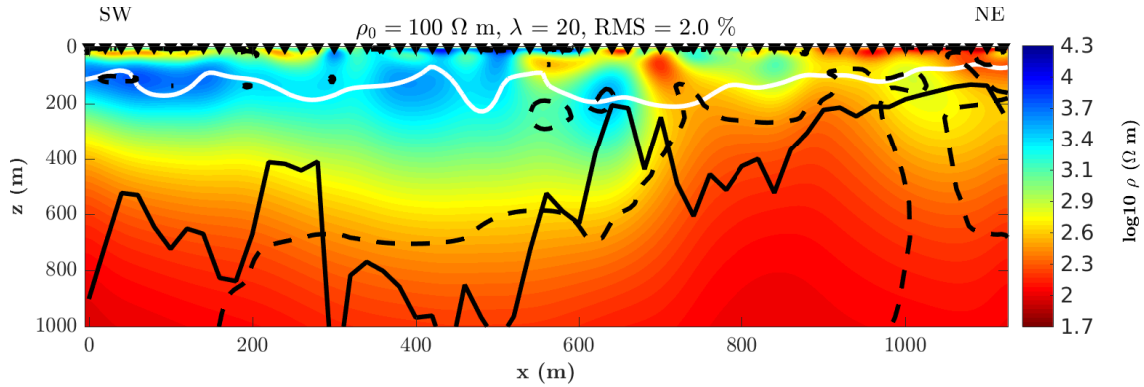


Figure 3.7: Inversion result for resistive basement. Solid white line is sensitivity -3.5, solid black line is $2z^*$ and dashed black line is DOI. The $2z^*$ depth and DOI give overshooting and lies on very small sensitivity

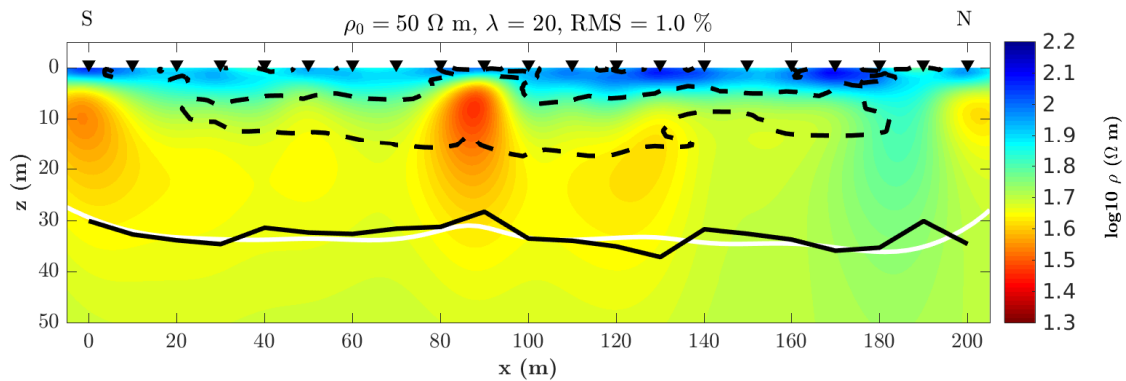


Figure 3.8: Inversion result for conductive basement. Solid white line is sensitivity -3.5, solid black line is $2z^*$ and dashed black line is DOI. The $2z^*$ depth agrees with the sensitivity while DOI underestimate.

In the more resistive basement (conductive layer over resistive layer), the Schmuker $2z^*$ (and Nibblet-Bostick), as well as DOI, will give an overshoot of depth of investigation as discussed before. An example of this overshoot is given in Figure 3.7. For more conductive basement (resistive layer over conductive layer) where (CS)RMT works at its best as the other EM geophysics methods, the situation is different. The $2z^*$ gives good approximate depth of investigation as shown in Figure 3.8 while DOI seems to underestimate. In this thesis, I use the sensitivity value as the first approximation of the depth of investigation (DOI). The value $< 10^{-4}$ I take as the threshold for a poorly resolved model. Since it would not make any sense to use any DOI methods (for example $2z^*$) on a more resistive second layer. Indeed, the DOI and sensitivity analysis is only an indication of the well-resolved model to the less resolved model. There is no strict limit between those two (Adrian, 2017).

3.6 Rebocc code

The standalone `Rund2Inv` available in the IGM Cologne could not invert the tipper data. In this thesis, `Rebocc` is applied to invert the measured tipper data. However, `Rebocc` in our Institute does not have sensitivity analysis like `Rund2Inv`.

The algorithm of `Rebocc` is started with transforming the objective function from the model space into the data space. Grayver (2013) showed that both formulations are equivalent. The transformation from the model space into the data space is to express the solution as a linear combination of rows of the sensitivity matrix smoothed by the model covariance. This would also reduce the system of equations to be solved from $M \times M$ in the model space method to the $N \times N$ in the data space method which also reduces the CPU time and memory requirement (generally $M > N$) (Siripunvaraporn and Egbert, 2000). Furthermore, the Weidelt dispersion formula generally can be applied to the MT data. Therefore the MT data are smooth and “redundant”. A subset of the basis function with dimension L ($L < N < M$) is sufficient to construct the model without significant loss of detail. With this approximation, it is unnecessary to compute all sensitivities, and the size of the system of equations that must be solved can be significantly reduced. This approach is called REduced Basis OCCam’s (REBOCC) inversion. Since the system of equations to be solved is significantly reduced, as a consequence `Rebocc` would only need small CPU time and memory requirement compared to `Rund2Inv`.

3.6.1 Algorithm

Let’s start with the objective function, which also might be written as:

$$\tilde{\mathbf{W}}(\mathbf{m}) = (\mathbf{m} - \mathbf{m}_0)^T \mathbf{C}_m^{-1} (\mathbf{m} - \mathbf{m}_0) + \lambda^{-1} (\mathbf{d} - F(\mathbf{m}))^T \mathbf{C}_d^{-1} (\mathbf{d} - F(\mathbf{m})), \quad (3.43)$$

where \mathbf{C}_m^{-1} is the covariance matrix. By linearizing the forward problem as Equation (3.19), we have

$$\begin{aligned} \tilde{\mathbf{W}} &= (\mathbf{m}_{k+1} - \mathbf{m}_0)^T \mathbf{C}_m^{-1} (\mathbf{m}_{k+1} - \mathbf{m}_0) \\ &+ \lambda^{-1} \left(\left(\hat{\mathbf{d}}_k - \mathbf{J}_k (\mathbf{m}_{k+1} - \mathbf{m}_0) \right)^T \mathbf{C}_d^{-1} \left(\hat{\mathbf{d}}_k - \mathbf{J}_k (\mathbf{m}_{k+1} - \mathbf{m}_0) \right) \right), \end{aligned} \quad (3.44)$$

where \mathbf{J}_k is the Jacobian and $\hat{\mathbf{d}}_k = \mathbf{d} - \mathbf{F}(\mathbf{m}_k) + \mathbf{J}_k (\mathbf{m}_k - \mathbf{m}_0)$. The Occam approach (Constable et al., 1987) is to differentiate Equation (3.44) w.r.t \mathbf{m} and then set to zero, then

$$\mathbf{m}_{k+1}(\lambda) = \left[\lambda \mathbf{C}_m^{-1} + \mathbf{\Gamma}_k^m \right]^{-1} \mathbf{J}_k^T \mathbf{C}_d^{-1} \hat{\mathbf{d}}_k + \mathbf{m}_0. \quad (3.45)$$

For each iteration, \mathbf{J}_k must be calculated, and a $M \times M$ system of equations, Equation (3.45) must be solved which is very time consuming.

Parker (1994) shows that the minimizer of (3.44) for iteration k can be expressed as a linear combination of rows of the smoothed sensitivity matrix $\mathbf{C}_m \mathbf{J}_k^T$:

$$\mathbf{m}_{k+1} - \mathbf{m}_0 = \mathbf{C}_m \mathbf{J}_k^T \beta_{k+1} = \sum_{j=1}^N \Upsilon_{kj} \beta_{k+1,j}. \quad (3.46)$$

Substituting Equation (3.46) into (3.44), one gets

$$\tilde{\mathbf{W}} = \beta_{k+1}^T \mathbf{\Gamma}_k^n \beta_{k+1} + \lambda^{-1} \left[(\hat{\mathbf{d}}_k - \mathbf{\Gamma}_k^n \beta_{k+1})^T \mathbf{C}_d^{-1} (\hat{\mathbf{d}}_k - \mathbf{\Gamma}_k^n \beta_{k+1}) \right]. \quad (3.47)$$

Differentiating Equation (3.47) w.r.t β and rearrange, one gets:

$$\beta_{k+1} = (\lambda \mathbf{C}_d + \mathbf{\Gamma}_k^n)^{-1} \tilde{\mathbf{d}}_k. \quad (3.48)$$

The inverse problem then becomes a search for the N real expansion coefficients instead of the M dimensional model. This is known as Data Space Occam inversion.

In `Rebocc` the subset of data with dimension L (out of $N, L < N$) are selected as representers which will be calculated at each iteration. For iteration $k + 1$, the solution is of the form:

$$\mathbf{m}_{k+1} = \mathbf{C}_m \mathbf{G}_k^T \alpha_{k+1} + \mathbf{m}_0, \quad (3.49)$$

where α_{k+1} is L -dimensional unknown coefficient vector for the reduced basis, and \mathbf{G}_k is the $L \times M$ subset sensitivity matrix.

The subset sensitivity is given by:

$$\mathbf{J}_k \approx \mathbf{B} \mathbf{G}_k, \quad (3.50)$$

where \mathbf{B} is an interpolation matrix of size $N \times L$. Substituting (3.49) and (3.50) into (3.44)

$$\tilde{\mathbf{W}} = \alpha_{k+1}^T \mathbf{\Gamma}_k^l \alpha_{k+1} + \lambda^{-1} \left[(\hat{\mathbf{d}}_k - \mathbf{B} \mathbf{\Gamma}_k^l \alpha_{k+1})^T \mathbf{C}_d^{-1} (\hat{\mathbf{d}}_k - \mathbf{B} \mathbf{\Gamma}_k^l \alpha_{k+1}) \right], \quad (3.51)$$

where $\mathbf{\Gamma}_k^l = \mathbf{G}_k \mathbf{C}_m \mathbf{G}_k^T$ is the data subspace cross-product matrix of dimension $L \times L$. By decomposing the term $\mathbf{C}_d^{-1} \mathbf{B}$ into $N \times N$ orthonormal matrix \mathbf{Q} and $N \times L$ matrix \mathbf{R}

$$\mathbf{C}_d^{-1} \mathbf{B} = \mathbf{Q} \mathbf{R},$$

then

$$\tilde{\mathbf{W}} = \tilde{\alpha}_{k+1}^T \tilde{\mathbf{\Gamma}}_k^l \tilde{\alpha}_{k+1} + \lambda^{-1} \left[\mathbf{C}_d^{-1/2} (\hat{\mathbf{d}}_k - \mathbf{Q} \mathbf{\Gamma}_k^l \alpha_{k+1})^T (\mathbf{C}_d^{-1/2} \hat{\mathbf{d}}_k - \mathbf{Q} \mathbf{\Gamma}_k^l \alpha_{k+1}) \right], \quad (3.52)$$

where

$$\tilde{\alpha}_{k+1} = (\hat{\mathbf{R}}^{-1})^T \alpha_{k+1}, \quad (3.53)$$

and

$$\tilde{\mathbf{\Gamma}}_k^l = \mathbf{R} \mathbf{\Gamma}_k^l \mathbf{R}^T.$$

Finally the last expressions can be written as:

$$\tilde{\mathbf{W}} = \tilde{\alpha}_{k+1}^T \tilde{\mathbf{\Gamma}}_k^l \tilde{\alpha}_{k+1} + \lambda^{-1} \left[\chi_{\min}^2 + (\bar{\mathbf{d}}_k - \bar{\mathbf{\Gamma}}_k^l \alpha_{k+1})^T (\bar{\mathbf{d}}_k - \bar{\mathbf{\Gamma}}_k^l \alpha_{k+1}) \right], \quad (3.54)$$

where $\mathbf{Q} \mathbf{Q}^T$ has been inserted on the right hand side of Equation (3.52) in between $\mathbf{\Gamma}_k^l$ and α_{k+1} . $\bar{\mathbf{d}}_k = \hat{\mathbf{Q}}^T \mathbf{C}_d^{-1/2} \hat{\mathbf{d}}_k$. The term $\chi_{\min}^2 = \|\mathbf{C}_d^{-1/2} \hat{\mathbf{d}}_k\|^2 - \|\hat{\mathbf{Q}}^T \mathbf{C}_d^{-1/2} \hat{\mathbf{d}}_k\|^2$ is the approximate minimum achievable total square misfit for the selected basis.

The unknown expansion can be derived by differentiating (3.54) with respect to α and

set to zero

$$\bar{\alpha}_{k+1} = (\lambda \mathbf{I} + \bar{\Gamma}_k^l)^{-1} \bar{d}_k. \quad (3.55)$$

After solving (3.55), the model is updated with (3.46) and (3.53), then calculate the forward problem to evaluate χ_{\min}^2 . This procedure is repeated to find best regularization parameter λ .

3.6.2 Representer

The unique features of the data subspace approach are the selection of the data points which determine the representer used in the model expansion. There are two classes of data subsets which worked well in `Rebbocc` namely p and $p - s$ checker. The example of two representer are shown in Figure 3.9 for $p = 6$ and $p = 4, s = 2$. Note that for `Rebbocc` the minimum $p = 2$, for $p = 1$ the problem is becoming standard Data Space Occam inversion. In this thesis $p = 2$ is selected. This is selected as the tipper data with good quality are quite limited.

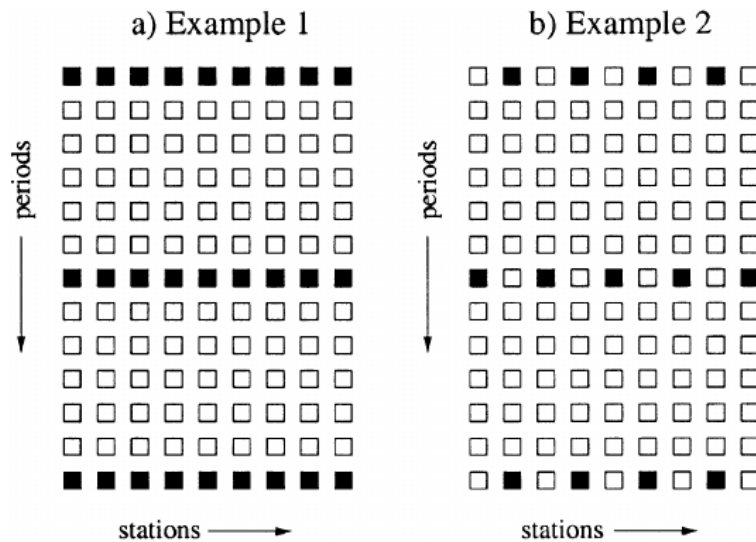


Figure 3.9: Examples of subsets of data used to calculate the representer. Representer are calculated for data corresponding to the filled squares; the open squares represent the remaining data. (a) First example: p^{th} -stripe pattern where every p^{th} period is selected for all sites (here $p = 6$). (b) Second example: $p^{\text{th}}, s^{\text{th}}$ -checker (with $p = 4$ and $s = 2$) pattern where the selected data form a checker pattern. Figure and text are from Siripunvaraporn and Egbert (2000).

The $p - s$ pattern is best used when the site spacing is small Siripunvaraporn and Egbert (2000), but I did not try this option. Of course this pattern would reduce storage and memory requirement which might be useful for a very large data set.

3.6.3 Calculation of λ

The feature of Occam algorithm is that the regularization parameter λ is selected in an automatic way. The method to select the λ is by taking the advantage of: (a) the misfit is a smooth function of λ , (b) the range of $\log_{10} \lambda$ is generally within the interval $[0,6]$ (for

default model variance $\eta^2(r) = 1$), and (c) the optimal choice of λ changes little between iterations (Siripunvaraporn and Egbert, 2000).

Both `Rebbocc` and `MARE2DEM` will start with the given λ that usually high 3 – 5 on a log10 scale. On the first iteration, three logarithmic spaced of λ in one decade are selected in `Rebbocc` (that is the given value ± 0.5), while in `MARE2DEM` it is more flexible (any positive number, on my experience, is the value between 0 – 20). Then the misfit would tell whether we go right, left or stop if the minimum is reached. When the minimum is reached, a parabolic interpolation is used on these three points to estimate the minimum misfit. These previous bracketing points then used for the next iteration and the process is repeated. Even though the optimal λ does not change that much between iterations to iterations, at least 3 λ values should be selected as trials.

Once a model having less than or equal the target misfit, the second phase begins. If two or more values of λ bracketing the minimum have the same (desired) misfit, the larger λ is chosen, which usually corresponds to a smaller model norm. This is accomplished by bracketing λ around the target misfit, and a parabolic interpolation is used to locate λ iteratively to find the largest value of λ at the target misfit.

3.7 Trial and Error

In order to maximize the full potential of CSRMT method, the data from near field and transition zones which are often removed from the interpretation should be taken into account. In these zones, the signal to noise ratio is much higher than in far-field zone. As mentioned before, there are some methods to interpret these data: (i) by taking directly the individual electromagnetic fields which require synchronization of the transmitter and receiver to process the data and also to take into account the displacement current on the forward modelling of the inversion code, (ii) by correcting the apparent resistivity to be far field zone which is difficult since the underlying earth structures are unknown and (iii) directly interpret the apparent resistivity and phase at every single station even some information might be lost on the conversion from the electromagnetic fields to the data. The third option also has an advantage due to a vivid boundary between the CSRMT field zones.

A trial and error procedure using `SLDMEM3f` which is also known as hedgehog inversion is one of the approaches to invert the near-field data. Unlike the `SLDMEM3t` which is now a routine in the IGM Cologne to interpret field data from time domain electromagnetic due to its efficiency, this is the first time `SLDMEM3f` applied to synthetic modelling (on Chapter 2) and real field data frequency domain electromagnetics. Note that the trial and error forward modelling is very time consuming and the results can be biased by the subjective choice of the parameter space. One approach is to use the inversion results from the RMT data as the starting model of the trial and error process. Therefore, I will limit my modelling on the field data to explain the physical phenomena as a starting point, and the final modelling is carried out with `MARE2DEM`.

3.8 MARE2DEM

The main intention of using MARE2DEM is to interpret the data including the near-field data in an automatic way. The trial and error forward modelling is a very time consuming process even though this process is advantageous when the situation is quite complicated as it is in Krauthausen. For a typical 2D problem, the modified MARE2DEM (Wang, 2017) can be applied to interpret the near-field CSRMT data (as well as the far field data) in the impedance format (Z_{xy}, Z_{yx}). The term “typical” here means that the receiver is located starting from 20 m in inline or broadside configuration. Wang (2017) modified MARE2DEM, which in original form for CSEM case only invert electric and magnetic fields, to handle the impedance data which are the format in our CSRMT and Enviro-MT data without any change to the inversion algorithm. However, the tipper data from the controlled source is still missing in this modification (the tipper inversion can only be carried out in the MT mode).

As stated before, MARE2DEM is a finite element code. MARE2DEM also applies an adaptive finite element scheme in the inversion. Thus, the user only needs to define the inverse parameter grid and the code would then automatically generate and refine the finite-element meshes during the inversion process (Key, 2016). Note that the grid design is also crucial to obtain reasonable results as in other codes. The minimum skin depth and Dirichlet boundary conditions should be taken into account. In the forward modelling codes (e.g. Key and Owall (2011) Li and Dai (2011)), the problem is solved on iteratively refined finite element meshes until the solution meets the desired tolerance. During the inversion process in MARE2DEM, the dual grid approach where the adaptively generated finite-element meshes conform to the parameter grid is applied. This adaptive refinement is performed at each iteration to ensure that the forward problem retains the accuracy while the model parameters change (Key, 2016).

3.8.1 Algorithm

MARE2DEM uses Occam approach is introduced in Equation (3.43) and (3.44). The method to find the optimal regularization parameter is exactly the same as in Section 3.6.3.

I will start with the sensitivity (first derivative) which describes the change of the fields with respect to the variation of the conductivity of the inverse parameter. Theoretically, this can be easily calculated by taking the partial derivatives of the objective function with respect to each parameter and then solving the finite element system. However, this direct approach is computationally expensive. Rather than calculating directly, the sensitivity in MARE2DEM is calculated with the adjoint reciprocity method introduced by McGillivray et al. (1994). Suppose we have p total measured electric and magnetic field components, the adjoint reciprocity formula requires only p additional solutions to the original finite element system. This would reduce a large computational effort compared to direct sensitivity solution when $n \gg p$, where n is the total number of model parameters.

The sensitivity for any EM fields F to the anisotropic conductivity σ_j is calculated

with the Fourier transform (Key, 2016):

$$\frac{\partial F}{\partial \sigma_j}(x, y, z) = \frac{1}{2\pi} \int_{-\infty}^{\infty} \hat{S}_j(k_x, y, z) e^{ik_x(x_r - x_s)} dk_x, \quad (3.56)$$

with $\hat{S}_j(k_x, y, z)$ is the Fourier kernel given by

$$\hat{S}_j(k_x, y, z) = \int_{A_j} \hat{\mathbf{E}}^a(-k_x, y, z) \cdot \left(\frac{\partial \bar{\sigma}}{\partial \sigma_j} \hat{\mathbf{E}}(k_x, y, z) \right) dA_j. \quad (3.57)$$

where $\hat{\mathbf{E}}^a$ is the adjoint electric field generated by turning the particular receiver component F into an adjoint source and $\hat{\mathbf{E}}$ is the wavenumber domain electric field generated by a source at the true source location. A_j is the cross-sectional area of the cell containing parameter σ_j and x_r and x_s are the along-strike positions of the receiver and true sources. The term $\frac{\partial \bar{\sigma}}{\partial \sigma_j} = 1$ for isotropic models considered in this thesis. The sensitivity of a given field component to all model parameters can be found with only a single additional finite-element solution for the adjoint field $\hat{\mathbf{E}}^a$. The output sensitivity is calculated from the sum of the Jacobian all the data normalized with the area of the triangle in the MAMBA2D.m (Key, 2016) since the area of element sizes vary:⁴

$$\text{sens}_j = \frac{1}{A_j} \sum_i |J_{ij}|. \quad (3.58)$$

In MARE2DEM a bound on the model parameter is also applied to prevent MARE2DEM produces unrealistic conductivity (either too high or too low) which are geologically unreasonable

$$l < m(x) < u, \quad (3.59)$$

where l and u are lower and upper bound respectively, however the transformed parameter x is unbounded

$$-\infty < x(m) < \infty. \quad (3.60)$$

There are two transformations applied in MARE2DEM namely the exponential transform and the bandpass transform. The exponential transform is given by:

$$m = \frac{ue^{\tilde{x}} + l}{e^{\tilde{x}} + 1} \quad \text{where} \quad \tilde{x} = x - (u + l)/2. \quad (3.61)$$

then the sensitivity is calculated as:

$$\frac{\partial m}{\partial x} = \frac{(u - l)e^{\tilde{x}}}{(1 + e^{\tilde{x}})^2}. \quad (3.62)$$

and the transformed variable:

$$x = \log(m - l) - \log(u - m) + (u + l)/2, \quad \text{where} \quad l < m < u. \quad (3.63)$$

⁴beta version, for plotting purposes only

The bandpass filter is started by considering the transform's of sensitivity scaling

$$\frac{\partial m}{\partial x} = \frac{1 - e^{c(l-u)}}{(1 + e^{-c(x-l)})(1 + e^{c(x-u)})}, \quad (3.64)$$

where c is constant that controls the decay of the scaling past the bounds. By taking $c = 15/(u - l)$ which works well in practice, then the bound model parameter is given by

$$m(x) = \frac{1}{c} \log \left(\frac{1 + e^{c(l-x)}}{1 + e^{c(u-x)}} \right) + u, \quad (3.65)$$

and the expression for x is given by:

$$x(m) = \frac{1}{c} \log \left(\frac{e^{c(m-l)} - 1}{1 - e^{c(m-u)}} \right) + l. \quad (3.66)$$

In most cases, the inversion will run without any bounds. However, it has been shown that the bounds are beneficial so that the extreme values are excluded from the inversion. Moreover, in my own experiences, the bound applied in the inversion also result in a lower RMS and a better model.

To stabilize the inversion, the model roughness \mathbf{R} is also introduced. It provides information for parts of the model which are poorly resolved by the data. It would also stabilize the inversion by providing a measure of the model variations. Therefore, the minimizations would like to drive the models from an unrealistic structure. The popular choice for L_2 norm is given by:

$$\|R(m)\|^2 = \int_{\Omega} \nabla m \cdot \nabla m \, d\Omega. \quad (3.67)$$

This term is to be added on the right hand side of the objective function of Equation (3.43). In MARE2DEM, the weighted sum is given by

$$\|\mathbf{Rm}\|^2 = \sum_{i=1}^m A_i \left[\sum_{j=1}^{N(i)} w_j \left(\frac{\Delta m_{ij}}{\Delta r_{ij}} \right)^2 \right], \quad (3.68)$$

where $\Delta m_{ij} = m_i - m_j$, $\Delta r_{ij} = \sqrt{(y_i - y_j)^2 + (z_i - z_j)^2}$, and $w_j = \frac{A_j}{\sum_{k=1}^{N(i)} A_k}$.

The model smoothness can be enhanced either to the horizontal or vertical direction by a slight modification on the distance measure

$$\Delta r_{ij} = \sqrt{\left(\frac{y_i - y_j}{w_{hv}} \right)^2 + (z_i - z_j)^2}. \quad (3.69)$$

When $w_{hv} > 1$, the vertical distance is expanded hence the horizontal smoothing is enhanced and vice versa when w_{hv} , the horizontal distance is expanded hence enhanced vertical smoothing. However, this roughness norm together with the vertical penalty weight (even $w_{hv} = 1$) might result in the wrong model when inverting the data with few large blocky parameters (Key, 2016). Thus the weight w_{hv} should be chosen correctly

on the inversion input for any given data. A trial and error approach to find the optimal weight is needed. As a result, the total time of the inversion with MARE2DEM would also be very time consuming⁵.

It is also possible to invert CSRMT-RMT data set jointly in MARE2DEM. The misfit functional χ^2 is:

$$\begin{aligned}\|\mathbf{W}(\mathbf{d} - \mathcal{F}(\mathbf{m}))\|^2 &= \|\mathbf{W}_1(\mathbf{d}_1 - \mathcal{F}_1(\mathbf{m}))\|^2 + \|\mathbf{W}_2(\mathbf{d}_2 - \mathcal{F}_2(\mathbf{m}))\|^2, \\ &= \chi_1^2 + \chi_2^2.\end{aligned}\quad (3.70)$$

where the data vector \mathbf{d} consist of MT (\mathbf{d}_1) and CSEM (\mathbf{d}_2) (which can be reversed) data with dimension of n_1 and n_2

$$\mathbf{d} = \begin{bmatrix} \mathbf{d}_1 \\ \mathbf{d}_2 \end{bmatrix}.\quad (3.71)$$

In the joint inversion case, sometimes one data set dominates another data set. Let n_1 and n_2 be the first and second data set respectively and consider when $n_1 \gg n_2$. In this case, the overall misfit will be dominated by n_1 . As a result, a joint inversion has no benefit over a single inversion of the data set. Let $p = n_1/n_2$ as the data density, where $p \gg 1$ and q is the misfit multiplier quantifies how much worse \mathbf{d}_2 is fit than its expected value of n_2 . Then the following relation holds:

$$\chi^2 = \chi_1^2 + \chi_2^2 = n_1 + qn_2 = pn_2 + qn_2.\quad (3.72)$$

The normalized joint misfit functional is proposed to overcome the above problem:

$$\|\alpha_1 \mathbf{W}_1(\mathbf{d}_1 - \mathcal{F}_1(\mathbf{m}))\|^2 + \|\alpha_2 \mathbf{W}_2(\mathbf{d}_2 - \mathcal{F}_2(\mathbf{m}))\|^2 = \frac{\chi_1^2}{n_1} + \frac{\chi_2^2}{n_2},\quad (3.73)$$

where

$$\alpha_i = \sqrt{1/n_i},$$

is the weight to balance the data which normalized each misfit functional. This weight is to ensure that both data sets have the same influence on the overall misfit. A model that fits both data sets will have

$$\frac{\chi_1^2}{n_1} + \frac{\chi_2^2}{n_2} \approx 1.\quad (3.74)$$

The RMS is given by

$$\text{RMS} = \sqrt{\frac{\chi^2}{n}} = \sqrt{\frac{1}{n} \sum_{i=1}^n \left[\frac{d_i - F_i(\mathbf{m})}{s_i} \right]^2},\quad (3.75)$$

where n is the number of data and s_i is the standard error of the i -th datum.

⁵The inversion of MARE2DEM is carried out in CHEOPS <https://rrzk.uni-koeln.de/cheops.html>

3.8.2 Point Dipole vs Finite Dipole

The very first issue to consider is the choice between a point dipole or a finite dipole length to be included on the inversion of the impedance data. MARE2DEM has the option to choose between a point dipole and a finite dipole length. Indeed, the calculation of a point source dipole would require fewer resources and computational time. Furthermore, the receivers close to the source in the finite dipole suffers from the finite dipole length effects. Consequently, the calculation of the electromagnetic fields would be inaccurate. The inaccurate region is shown as the red circle in Figure 3.10. Remember that the Figure 3.10 applies for low frequency CSEM method (< 10 Hz). For the CSRMT case, the red region where the solutions are inaccurate might be smaller in the high-frequency case.

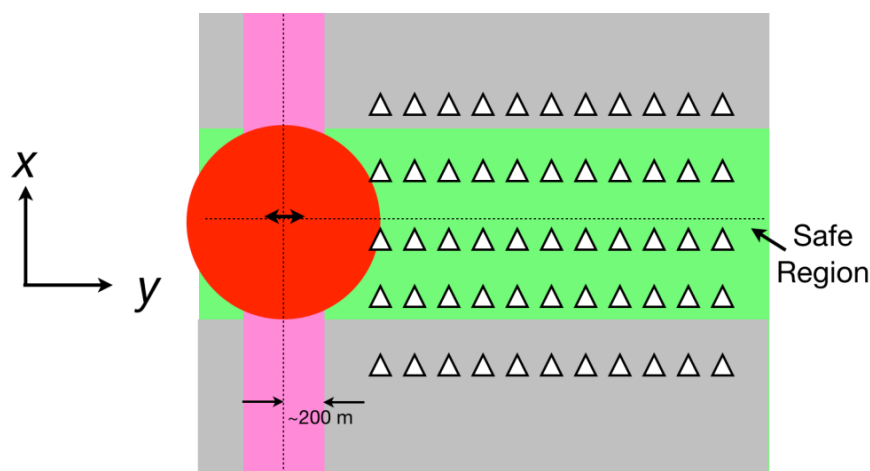


Figure 3.10: Geometry used in MARE2DEM, x is the strike direction. Only the green region is safe for the inversion of CSEM data in low frequency as marine settings. The red region is where the solutions have some singularities. Figure taken from http://mare2dem.ucsd.edu/?page_id=251

For this purpose, the considered model is $100 \Omega\text{m}$ halfspace with 100 stations and 20 m spacing. The far-field solutions are also used to check the validity of the designed grid. Note that the solutions are in terms of impedance (I will show in apparent resistivity and phase here) not in electric and magnetic field components as discussed in Streich and Becken (2010). The considered lengths are⁶ 0 (a point dipole), 100 and 1000 m.

Inline Configuration

Before making any analysis, one needs to check the designed grid. For this purpose, the last station (offset 2000 m) is used to ensure the far field condition is met. The solutions are then compared with the right solutions and given in Figure 3.11. It is quite clear from the figure that the designed grid performs well. Although, there is little bit error for low and high frequency and still less than 5% in apparent resistivity and 2° in phase.

The apparent resistivity and phase are plotted against the distance for the lowest frequency (1 kHz) shown in Figure 3.12. It is clear that the solutions differ significantly

⁶I also tested another dipole lengths of 50, 250, 500 and 750 m.

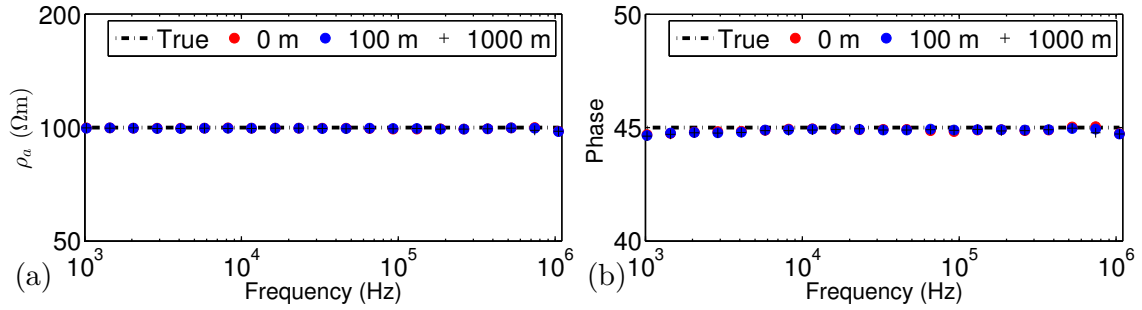


Figure 3.11: Grid check for MARE2DEM for inline configuration. The dashed black line is the true solution (100 Ωm of apparent resistivity and 45° of phase).

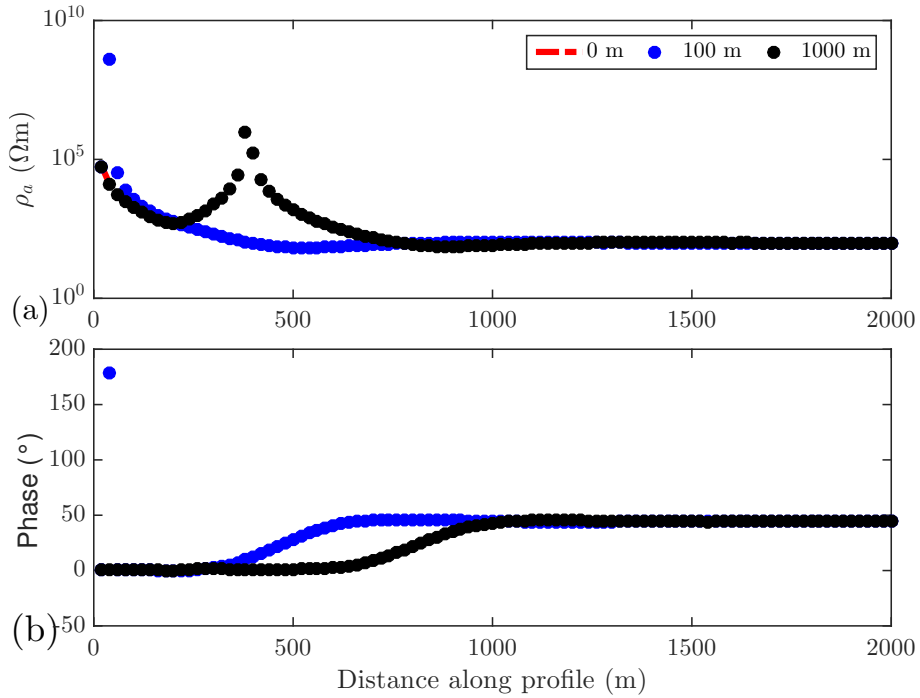


Figure 3.12: (a) Apparent resistivity and (b) phase plotted against the distance for frequency 1 kHz for inline configuration.

between 0 m, 100 m and 1000 m dipole. The differences depend on the frequency and distances. This numerical error might be caused by singularities discussed before.

To give a better idea, a relative and an absolute difference between a finite dipole and a point dipole is given in Figure 3.13 as contour plots. The relative difference between the finite dipole and the point dipole are much higher than the error floors used in the inversion (5 - 10 % in apparent resistivity and impedance, 2° in phase). There are also some regions with much higher values (not shown due to the limit on the colorbar used). Thus, a point dipole should be chosen for the inline configuration.

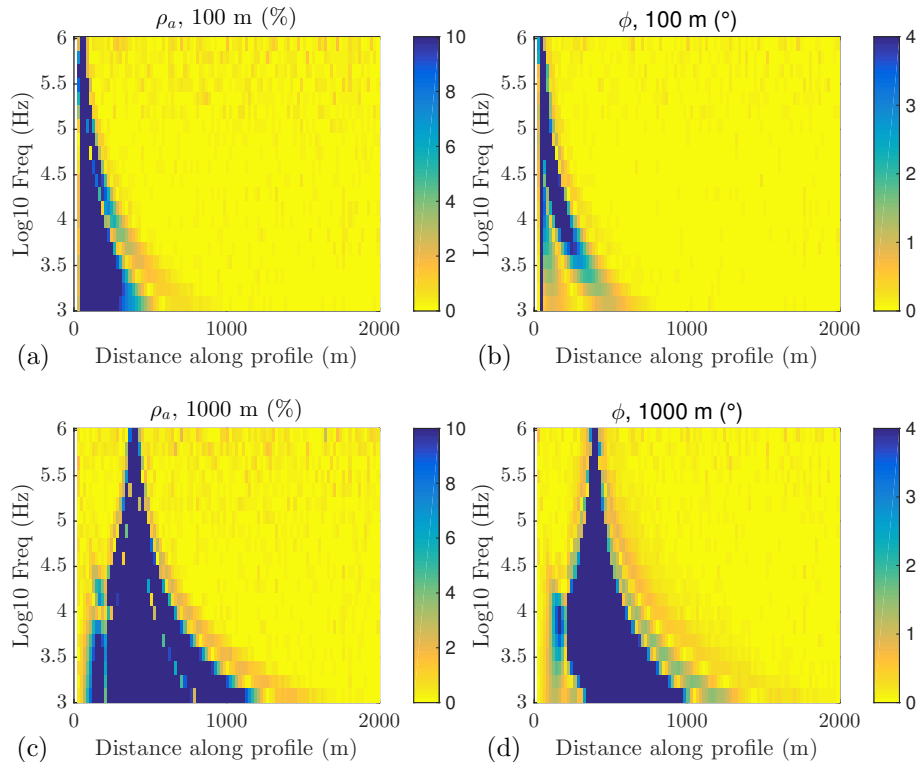


Figure 3.13: Relative and absolute difference between finite dipole and point dipole length for inline configuration. (a) Apparent resistivity of 100 m (b) phase of 100 m, (c) Apparent resistivity of 1000 m, and (d) phase of 1000 m. The relative difference for apparent resistivity is given in percent, while the absolute difference in phase is given in degree.

Broadside Configuration

For the broadside configuration, the procedure as before is repeated. First, the grid is checked for the last station (offset 2000 m) and the solutions for each dipoles compared with the true solution shown in Figure 3.14. As for the inline configuration, the designed grid also performs well for the broadside configuration. Although, there is little bit error in low and high frequencies but still less than 5% in apparent resistivity and 2° in phase.

The apparent resistivity and phase are plotted against the distance for the lowest frequency (1 kHz) shown in Figure 3.15. Unlike the inline configuration, the 100 m dipole differs more significantly compared with 1000 m dipole. But the differences are less than the inline configuration.

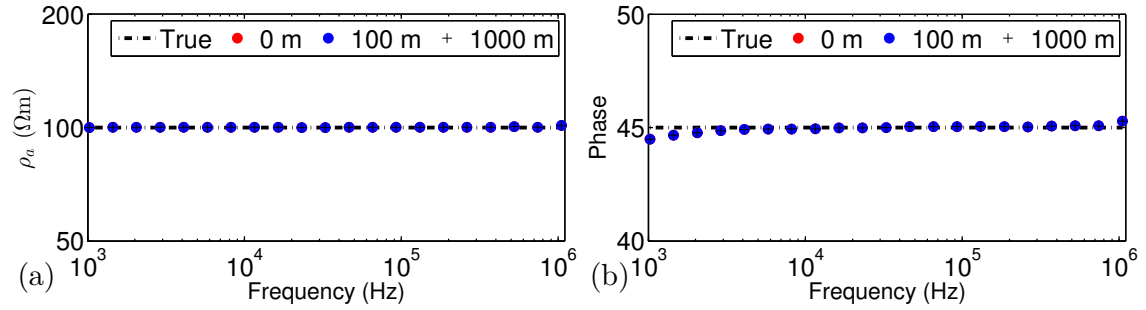


Figure 3.14: Grid check for MARE2DEM for broadside configuration. The dashed black line is the true solution ($100 \Omega\text{m}$ of apparent resistivity and 45° of phase).

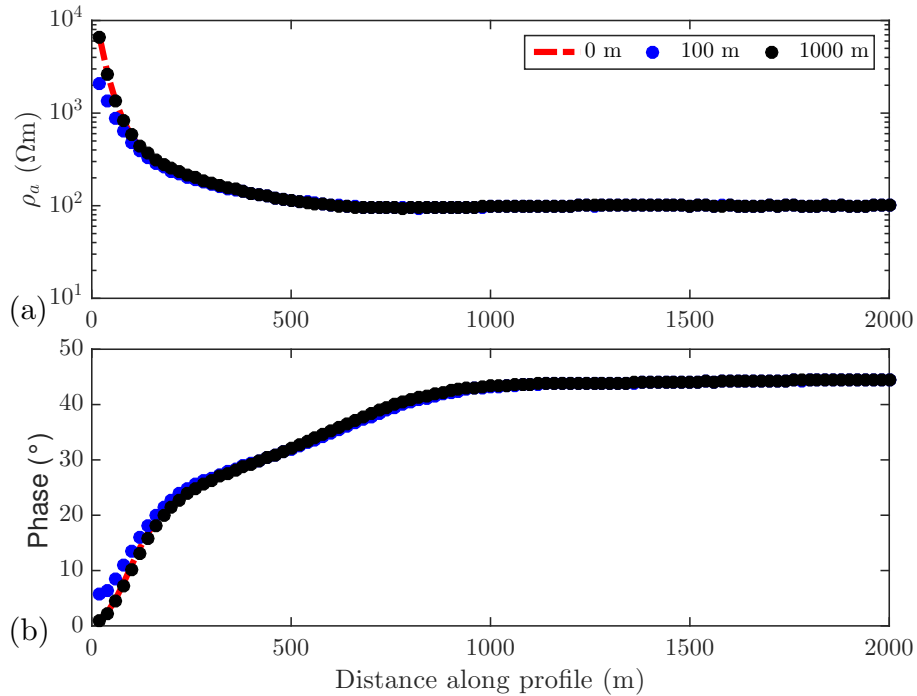


Figure 3.15: (a) Apparent resistivity and (b) phase plotted against the distance for frequency 1 kHz for broadside configuration.

The relative and absolute difference between a finite dipole and a point dipole are given in Figure 3.13. The relative difference between the finite dipole and the point dipole are higher than the error floors used for the inversion for 100 m dipole. But, for 1000 m dipole the error is less than the error floors used for the inversion. For broadside case, one should always check the solution between the finite dipole and point dipole in forward modelling and inversion with MARE2DEM.

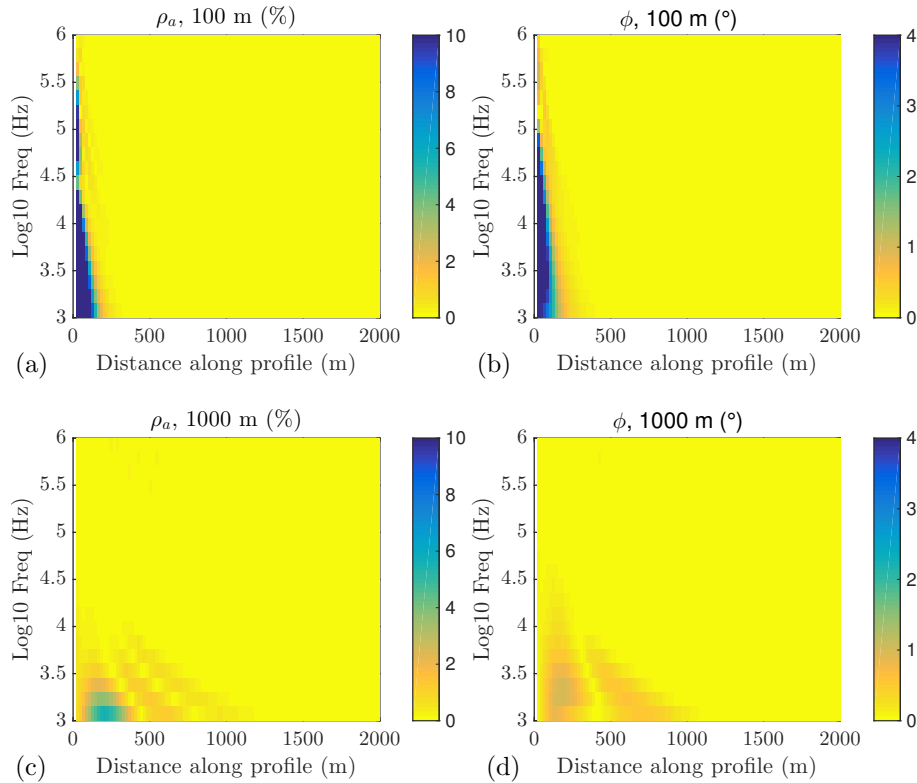


Figure 3.16: Relative and absolute difference between finite dipole and point dipole length for broadside configuration. (a) Apparent resistivity of 100 m (b) phase of 100 m, (c) Apparent resistivity of 1000 m, and (d) phase of 1000 m. The relative difference for apparent resistivity is given in percent, while the absolute difference in phase is given in degree.

3.9 MARE2DEM Synthetic Tests

Before applying the modified MARE2DEM code to invert real data synthetic tests should be carried out. Wang (2017) only applied MARE2DEM to the data with a maximum frequency of 12.5 kHz for magnetic dipole source. In our CSRMT system, not only a different source (transmitter geometry is horizontal electric dipole) is used but also the transmitter can inject the odd harmonics of the current up to the frequency of 1 MHz.

In modified MARE2DEM the type of the impedance data can be chosen as real and imaginary components ($\text{Re } Z$ and $\text{Im } Z$), amplitude of Z and its impedance phase as well as \log_{10} impedance. In this thesis, the data (impedance Z_{xy}, Z_{yx}) were converted to \log_{10} . It has been shown that this form to be more robust for inversion and lead to much faster convergence (Key, 2016; Wang, 2017).

In this synthetic study, both inline and broadside configurations are considered. More specifically the synthetic tests are based on the measured data from Vuoksa region, Russia for the inline configuration and Krauthasen, Germany (with some additional stations) for the broadside configuration. The synthetic data are calculated with MARE2DEM, having a point dipole located the origin for inline configuration (to the y direction) and both (point dipole and finite dipole length) for broadside configuration. During the experiment, the conventional RMT data were also measured, therefore the RMT data were also generated with MARE2DEM and then inverted separately as well as jointly.

There are three approaches to invert the CSRMT data including the near field zone data with MARE2DEM: (i) The near-field CSRMT impedance data + the far field RMT data known as the “classical” approach (by considering the field zones). (ii) By inverting all zones impedance data without worrying the vivid boundaries of the zones. (iii) Sequential and joint inversion with RMT the data. The sequential approach means that we first invert the RMT data and then use the result as the starting model of the controlled source data inversion. While a joint inversion means that the impedance data is inverted jointly with the RMT data. The second and third approach should be favoured for the CSRMT data inversion since the boundary between the field zones can be neglected.

3.9.1 Inline Configuration

The inline configuration was employed in the experiment in Vuoksa region, Russia to detect the buried fault in the far-field zone. Moreover, the profile was also extended to the near-field zone as close as 20 m offset from the source (one of the grounding electrodes), some of the receivers were located in the red zone of Figure 3.10. In the low-frequency CSEM method, this would result in an inaccurate model due to singularities: but how far should the receivers locate in the CSRMT case? The higher frequencies used in the CSRMT method, the receivers located near the transmitter might be still accurate. Furthermore, few blocky models might lead to wrong conductivity structures on the inversion result due to the roughness penalty (Key, 2016). Thus, a trial and error process is needed to find the optimal value of the penalty roughness w_{hv} .

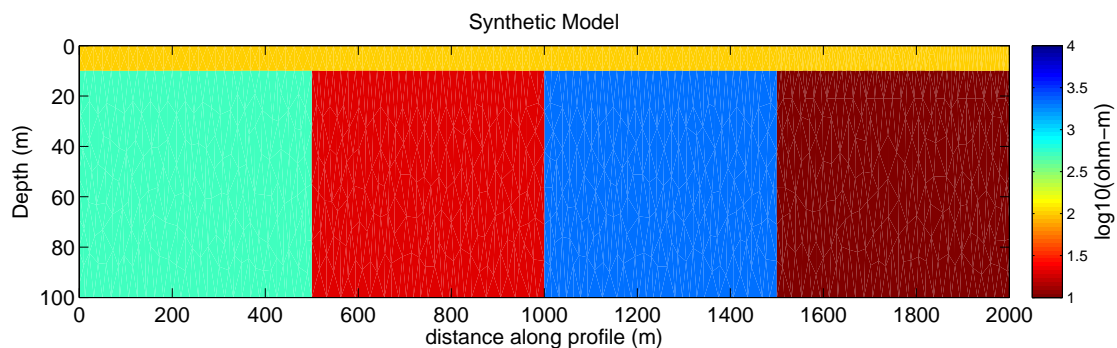


Figure 3.17: Synthetic model with few blocky vertical contacts. The source is located at 0,0 m.

The set up of the synthetic modelling is given in Figure 3.17. The first 10 m layer has a resistivity of 100 Ωm , and four different blocky vertical contacts of conductive and resistive bodies with 500, 20, 2000 and 10 Ωm , each block is 500 m wide. The starting

model for the inversion is set to be homogeneous halfspace of $100 \Omega\text{m}$, except for the sequential inversion where the result from the RMT data is used as the starting model of the inversion. There are 97 stations starting from 20 m were considered as in the field experiment with 20 m spacings. The field setup was using an inline dipole so that the data were in the TM mode. Only a point dipole is considered here. Moreover, Gaussian noise is added resulting 5% error in impedance and apparent resistivity and 2 degrees in impedance phase.

First, let's start with the RMT inversions of the TM mode with different roughness penalty w_{hv} and a starting model of $100 \Omega\text{m}$. The results of the RMT inversion of the TM mode are given in Figure 3.18. The boundaries between the vertical contacts are well mapped at 500, 1000, 1500 m in all the results. However, the additional parameter w_{hv} applied in MARE2DEM is a crucial one. Choosing a wrong w_{hv} might lead to a wrong inversion results. On this case, judging from the RMS only, the optimum w_{hv} in this particular case is either 0.5 or 1. It seems that putting more weight in horizontal direction $w_{hv} > 1$ is reducing the value of the resistive blocks. Yet, one might argue that RMT is generally poor to resolve more resistive structures.

Second, the result of the individual inversion of the impedance data from the inline point dipole is given in Figure 3.19(a) for individual and joint inversion of CSRMT impedance data with the RMT data (in Figure 3.19(b)). After testing different w_{hv} as in the RMT data, it was found that $w_{hv} = 0.5$ and $w_{hv} = 1$ are the optimum roughness penalty for the individual and the joint inversion respectively. In the individual inversion of the impedance data, there are some artefacts in the structure near the source. Furthermore, the first layer $100 \Omega\text{m}$ was not well reconstructed. However, the boundary (vertical contacts) between the conductivity structures were well mapped on the right locations. The result of the joint inversion of CSRMT and RMT data is closer to the true model than the result of single inversion of CSRMT data. In addition, two sequential inversions were also carried out by using the RMT inversion of Figure 3.18 (c) and (d). But in the sequential inversion, MARE2DEM stopped after one iteration since the starting model was near the true model which then gave the best result of all with the impedance. This also gives an idea that a good starting model would improve the inversion results.

From this simple synthetic data study at least we can conclude that the modification of MARE2DEM also works on HED source (our CSRMT system) with the impedance data in addition to the magnetic dipole source (Wang, 2017). When the RMT data are available, only with very little additional time on the field experiment, sequential and joint inversion of CSRMT-RMT data should be performed to improve the conductivity model compared to the individual inversion of the impedance from controlled source data. Moreover, the "optimum" penalty roughness should be sought by a trial and error process. Otherwise, the inversion might break down and produce a wrong conductivity model.

3.9.2 Broadside Configuration

During the experiment in Krauthausen, a "shifted" transmitter was observed. The theoretical far-field zone is shifted to the near-field zone due to current channelling. As a

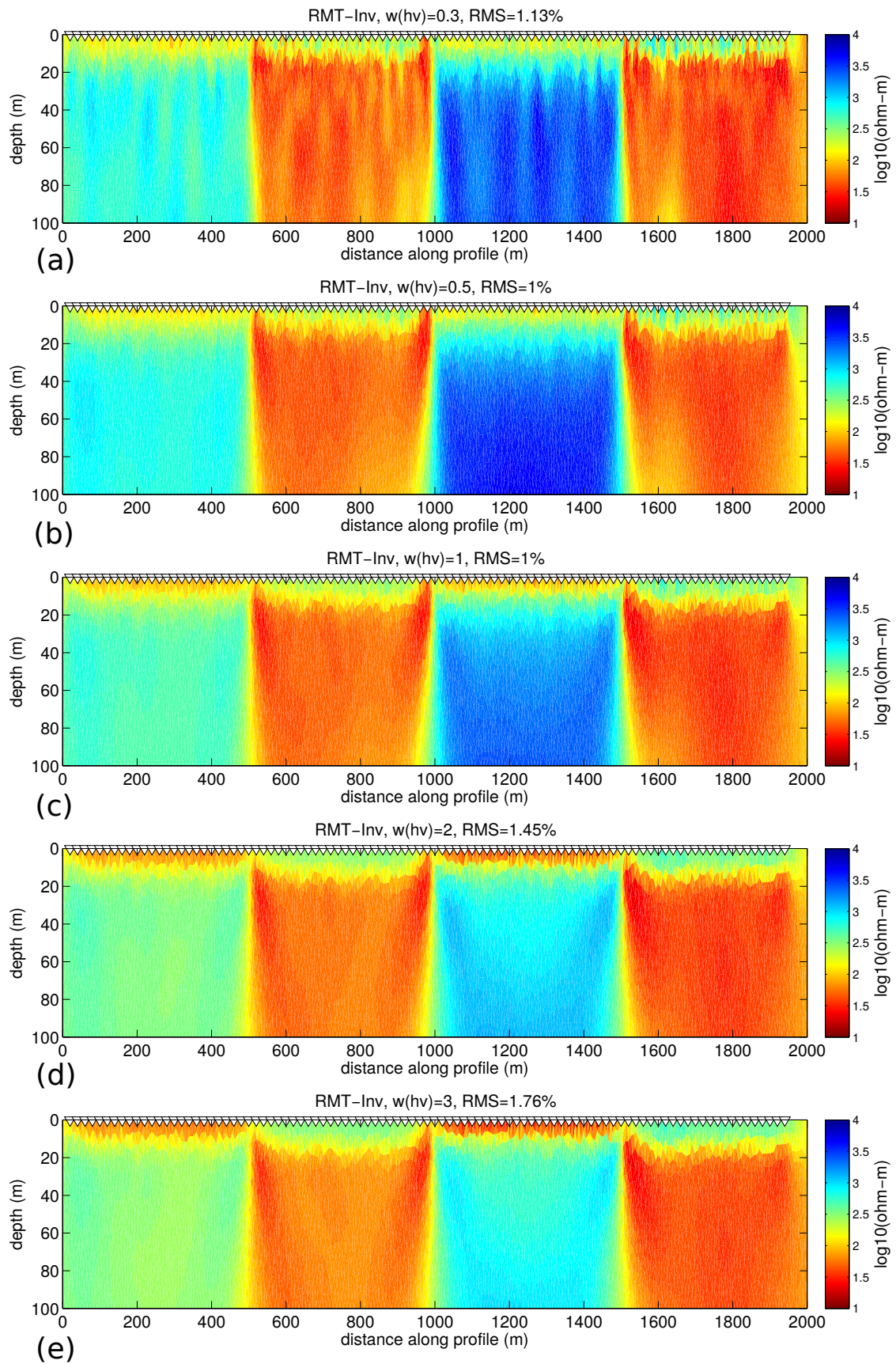


Figure 3.18: The model from the inversion results of synthetic RMT data with MARE2DEM with different w_{hv} (a) 0.3, (b) 0.5, (c) 1, (d) 2, (e) 3.

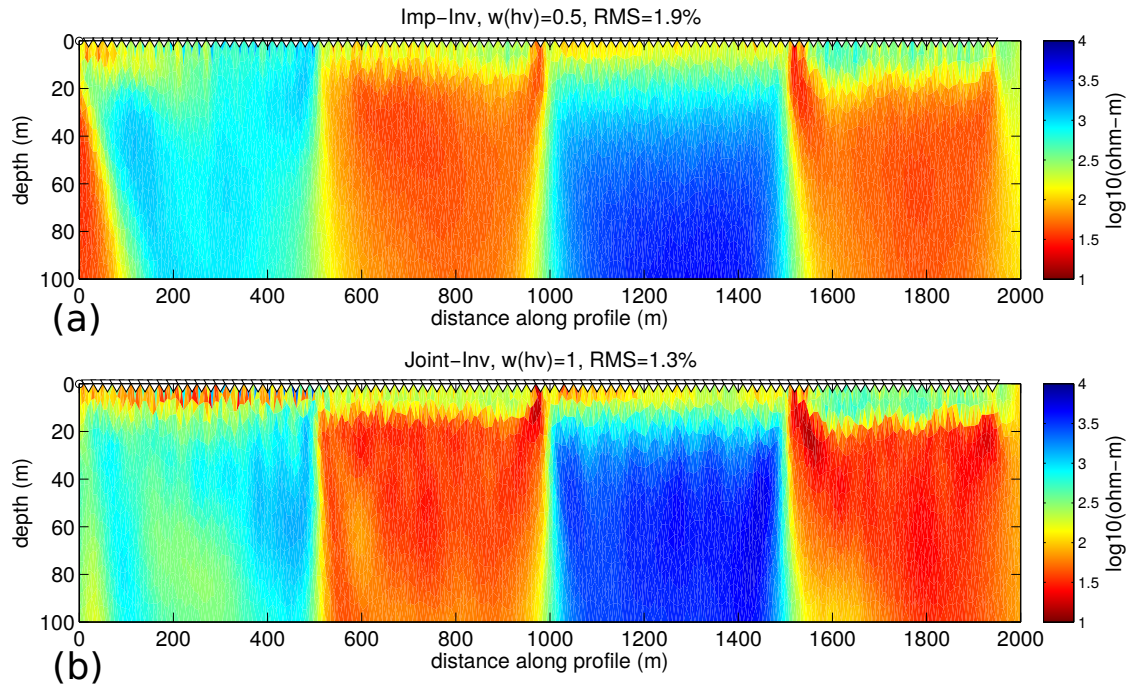


Figure 3.19: Inversion results of the synthetic impedance data considering the source with modification of MARE2DEM: (a) impedance data only. (b) joint inversion with the synthetic RMT data. The joint inversion result in (b) is better than the result of single inversion in (a).

result, the pipeline that channelled the injected current from the dipole acted as a broadside transmitter. In this synthetic study, the transmitter (pipeline) is approximated both by a point dipole and a finite source (1000 m). Note that the actual length of the pipeline is not known.

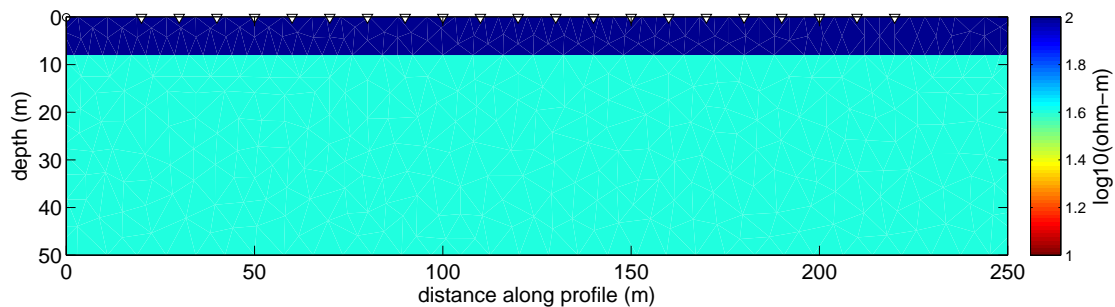


Figure 3.20: 1D synthetic model for broadside configuration, the source is located at 0,0 m. In the first option (Figure 3.21)(a), the receivers were located at $-100 - 100$ m with the source on y direction, while in the second option from $20 - 220$ m as in the figure (see also Figure 3.21(b)), with the source in x direction.

The general conductivity structure in Krauthausen is a one-dimensional two-layer case. The first layer (0 – 8 m) lies between 80 – 100 Ωm , while the second layer up to 20 m is 30 – 50 Ωm . For this synthetic study the model in Figure 3.20 with first layer of 100 Ωm up to 8 m and second layer of 50 Ωm is considered. Interpreting the CSRMT data with any MT inversion algorithm would lead to a wrong conductivity model. We have discussed in Chapter 2 in comparison to the far field solution, that for the near-field zone the apparent resistivity is higher while the impedance phase is lower. Therefore,

the model derived from the inversion with MT algorithm of the CSRMT data in the near field would result in very resistive structure even for a conductive layer.

The experiment in Krauthausen can be viewed in two ways as shown in Figure 3.21. The first scenario (Figure 3.21(a)), the transmitter is on the $-y$ direction, while the receivers located in $x = 30$ m and $-100 < y < 100$ m. The second scenario (Figure 3.21(b)), the transmitter is on the $-x$ direction, while the receivers located in $x = 0$ m and $20 < y < 220$ m.

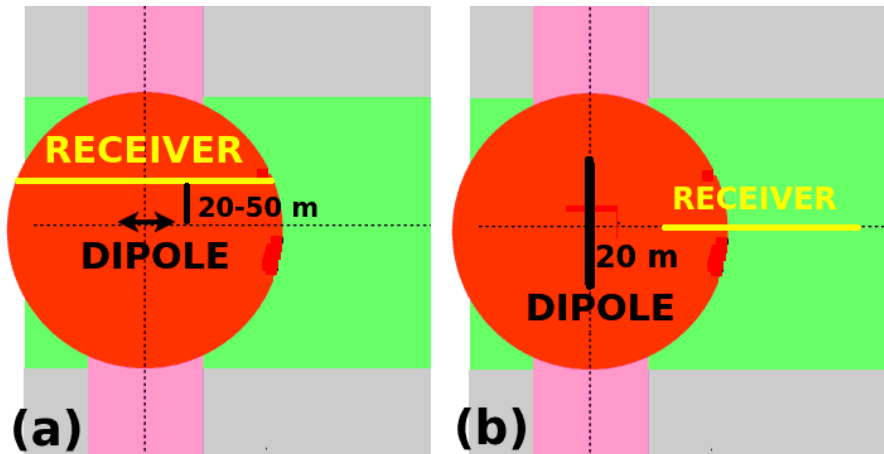


Figure 3.21: The modelling study of broadside configuration can be viewed in two ways (a). The transmitter is in y direction. (b) The transmitter is in x direction. This figure is modified version of Figure 3.10, the red region is where the solutions have many singularities.

For the inversion of broadside configuration, the synthetic data generated by a point dipole were inverted by a finite dipole and vice versa. Unfortunately, the inversion of the first scenario of Figure 3.21(a) did not work as expected (not shown), since all the stations were on the red region (many singularities of the solution). The first scenario should be performed when a 3D inversion code is available. For the second scenario, the inversion result of a point dipole is given in Figure 3.22(a) while the inversion result of 1000 m dipole is given in Figure 3.22(b). Both inversion results can produce the synthetic model quite well with low RMS, even without considering the RMT data. Thus, the second scenario should be chosen for the inversion of the CSRMT field data from Krauthausen in Chapter 6.

The broadside modelling study also shows a great promise to invert the Krauthausen data (on the first three stations). When the experiment configuration is broadside, it is advised to use real dipole length instead of a point dipole.

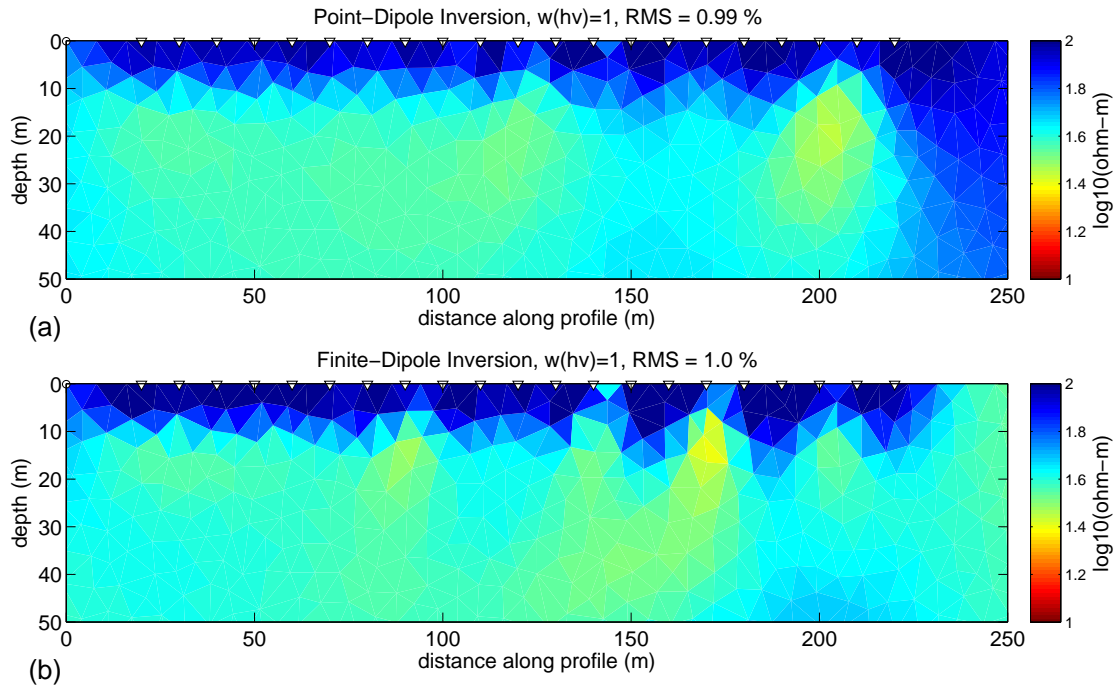


Figure 3.22: Inversion results for broadside configuration of the conductivity model in Figure 3.20 (a) point dipole source, (b) 1000 m finite dipole source. For both inversion, the starting model is homogeneous halfspace of $50 \Omega\text{m}$ with $w_{hv} = 1$.

3.9.3 Comments and Parameter Selection

The synthetic inversions examples on this chapter show a great promise that the modification MARE2DEM could be applied to real data in all zones from the experiment in Vuoksa region (Chapter 5) and the experiment in Krauthausen, Germany for current channelling phenomena (Chapter 6). Moreover by using this modification the boundaries between the zones that are somewhat vague than clear in the experiment can be ignored by just using the modified MARE2DEM and including the source in the inversion. The modified MARE2DEM also opens the opportunity just to carry out the experiment in the near field zone only where the signal to noise ratio is high and also reducing also the number of main frequencies. The difficulties in survey design might also be reduced and land permission for the transmitter would also be easier. Whenever the RMT data are available, it is much better to include the data on the inversion, by a sequential or a joint approach with the CSRMT data to improve the quality of the final model.

On MARE2DEM some parameters must be selected as the input for the inversion. (i) The dipole length, (ii) the roughness parameter, (iii) the starting regularization parameter, (iv) discretization with Mamba2D. ⁷Key (2016). The parameter I used as follows (this also applied to the real data): (i) A point dipole should be chosen for an inline configuration while a finite dipole length (as the field data) could be an option for a broadside configuration. (ii) The roughness parameter (w_{hv}) should be chosen in an optimal way depending on the situation. Otherwise, the result could be unrealistic. The values between 0.3 – 3 are reasonable as starting points. The starting regularization parameter should also be chosen correctly. Putting a high value may result in a very smooth model.

⁷It can be downloaded from the website along with the source code and plotting tools

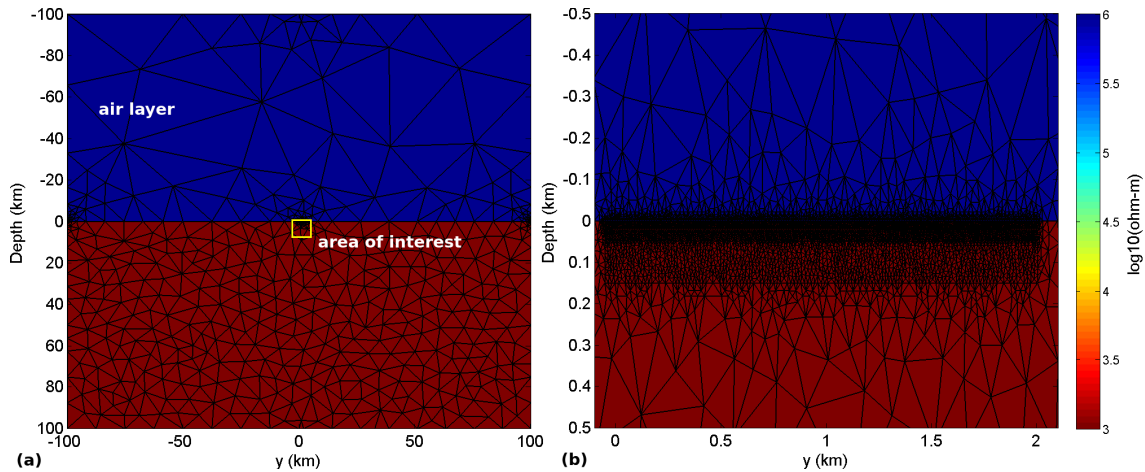


Figure 3.23: An example of grid design in MARE2DEM. (a) The whole grid, extended to 100 km to all directions in order to satisfy Dirichlet boundary condition, the area of interest where the receivers are located is marked with green rectangle. (b) Zoom in the area of interest of (a) on the yellow box including 500 m air layer. The air resistivity is $10^{13} \Omega\text{m}$.

In this case, the inversion process will stop even the RMS is still high but could not reduce any further. I suggest the value between 2 – 5 in \log_{10} as a starting value. (iv) The length of the triangle when designing the grid, in the region of interest (around receiver and transmitter plus 100 m to the right and left). Normally I chose between 4 – 10 m depending on the highest frequency of the data (thus the skin depth). A finer grid could also be chosen with the price of higher computational time. Moreover, to satisfy the Dirichlet boundary condition applied in MARE2DEM, on the region out of interest, I always use 10^5 m as the boundary on all directions with the length of the triangles at least 1 km as shown in Figure 3.23. Note that a good starting model would improve the solutions as stated before. It does not have to be homogeneous halfspace.

Chapter 4

Instrumentation and Data Processing

This chapter discusses the measuring device of the CSRMT method and also the field procedures. Afterwards, the available data processing and new processing algorithm are presented. It starts from the time series to the smooth impedance (apparent resistivity and phase) as well as the processing of the magnetic transfer function (tipper data) in a very practical way. The theoretical basis of the time series processing can be found for example in Chave (2017). The validation of the new processing algorithm, which is a very important step, is also given in this chapter. The tensor analysis of the transfer function (Zonge and Huges, 1991) is left out in the review since the data in this thesis are only in the scalar form.

4.1 CSRMT Instrument

The CSRMT instrument consists of transmitter and receiver. The transmitter includes a controlled source generator of rectangular signals operating in a frequency band of 1 - 150 kHz connected to a horizontal electric dipole grounded at both ends. The transmitter developed in the Russian Institute of power radio building (RIPR, St. Petersburg, Russia) has a small weight (about 7 kg) and a maximum output power 500 W using current 5 Ampere. A standard engine current generator can be used as a power supply for the transmitter. The new 5 channel receiver consists of 2 electric antennae, 3 magnetic coils and is connected to a GPS. The new receiver measures electromagnetic fields from 1 - 1000 kHz divided into 4 working bands. The 3 magnetic coils, 2 horizontal coils and a vertical coil, allow recording vertical magnetic fields. As a result, we now have a possibility to process the tipper data.

4.1.1 Transmitter

The transmitter produces a rectangular signal (half duty cycle) with main frequency that can be chosen by operator between 0.1 - 150 kHz (see Figure 4.1 (a)). To fulfill the whole CSRMT frequency range, 3 - 4 main frequencies (one or two main frequency in each band) with their odd harmonics are used in the field measurements. It is advised to inject 0.5, 5, 50 and 105 kHz during the measurements to cover the whole frequency range. In this

scenario at least 34 frequencies are transmitted to estimate the transfer functions. The maximum output voltage of the transmitter is 288 V and will generate current up to 5 A (Figure 4.1 (b)) depending on the grounding and main frequency transmitted, the higher frequency will generate lesser current. An example of autospectra and coherency from 0.5 kHz received at 900 m is given in Figure 4.1 (c)(d).

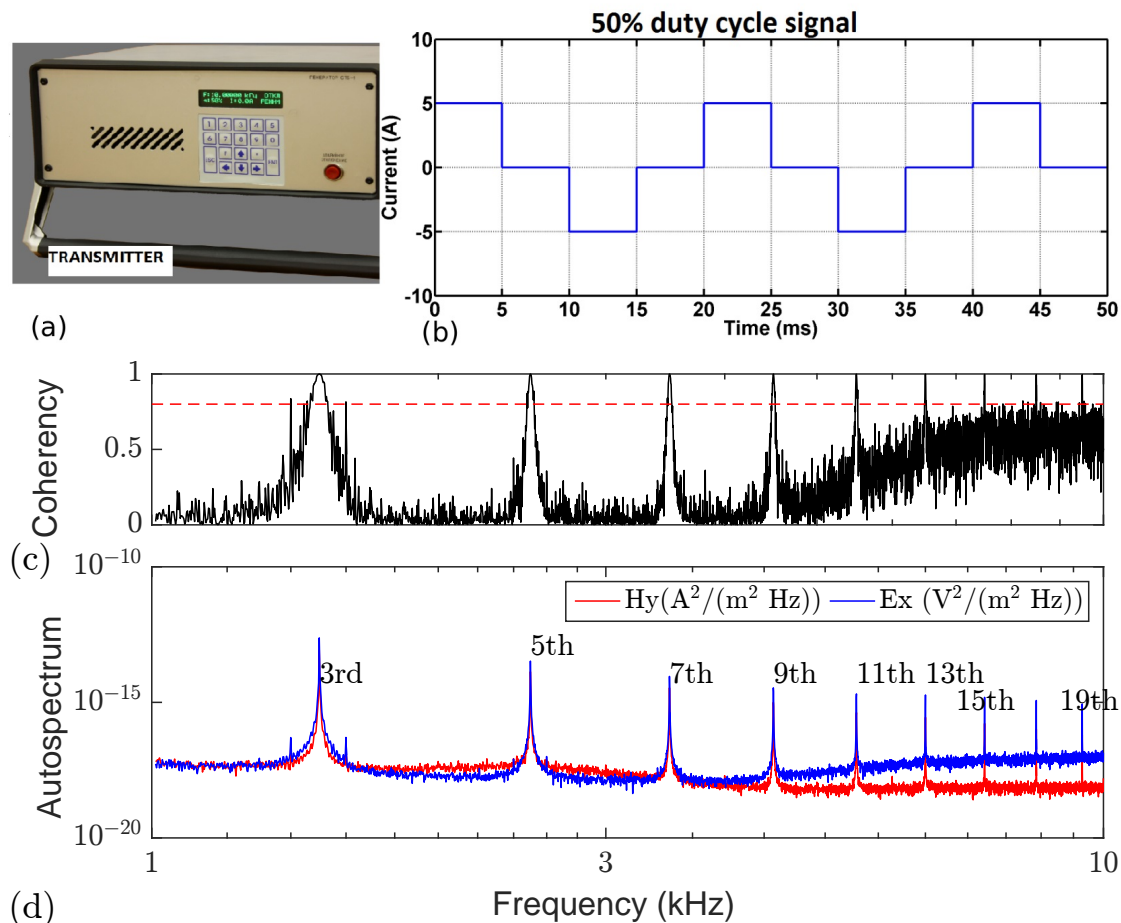


Figure 4.1: (a) Transmitter, (b) rectangular transmitted signal by the transmitter, note that the frequency is not used in the field. It is for simple illustration only, (c) coherency and (d) an autospectra of 0.5 kHz received on the receiver at 900 m distance from the experiment in Vuoksa, Region Russia in Chapter 5. It is clearly seen the harmonics of the transmitted signal up to 19th. Note that the main frequency is not shown here.

The dipole moment—that is the product due to the injected current and the dipole length (see Equation (2.31) - (2.35)) - is a very crucial issue of the transmitter. The higher of the injected currents and the longer of the dipole will be much better for the CSRMT experiment (the signal to noise ratio will be higher). Unfortunately, this might not be achievable in the field due to many difficulties, for examples: a very resistive area (could not inject high current), a road crossing, permission from the authorities/land owners etc (dipole length is limited).

The transmitter is connected to a HED, with length vary from 100 - 1000 m. At both ends, some electrodes (for our practical use only small electrodes 30 - 50 cm) are placed to inject the current to the ground as shown in Figure 4.2. To get a low contact resistance between the electrodes and the ground, sometimes salt (experiment in Vuoksa Region,



Figure 4.2: An example one of the dipole grounding. This picture is from the experiment in Rader-vormwald in Chapter 7.

Russia) or bentonite (experiment in Radevormwald, Germany) was also added (especially in a very resistive area). For a safety reason, one or more people should guard the electrodes on both ends. Depending on the situation to set up the transmitter a half day work is needed. Another half day work is also needed to collect the deployed transmitter.

4.1.2 Receiver

The new 5 channel receiver has 2 electric antennae (measuring the electric fields E_x and E_y) and 3 magnetic coils (measuring the magnetic fields H_x , H_y and H_z). This enables to process the measured data into full impedance tensor and also tipper data. The new receiver operates from 1 - 1000 kHz divided into 4 frequency bands given in Table 4.1. In our field measurements (CSRMT), usually, the D3 band is off since this band is overlapping with D4 band but with a lower high-end frequency (at 300 kHz only). The total memory of the receiver in the institute has 4 GB. By using the suggested sample length, each measurement point/sounding will take 23.9 MB memory for around 50 seconds (from the start pressing the button). In this case, 167 measurements/soundings are possible before the memory of the device is full. For the RMT measurement, the D1 band can also be switched off, since there is no radio transmitter operating in the frequency range between 1 - 10 kHz. For comparison, the old instrument on IGM Cologne has 2 bands only (D2 and D4), and the memory is limited around 100 MB (Tezkan, 2008). Furthermore, the receiver is also connected to the GPS to record the soundings' location.

Table 4.1: The frequency band of the new receiver and the suggested sample length of each band during the experiments.

Band	Freq Range (kHz)	Sampling Freq (kHz)	Sample Length (ms)
D1	1 - 10	39	8000
D2	10 - 100	312	2000
D3	100 - 300	832	off
D4	100 - 1000	2500	500

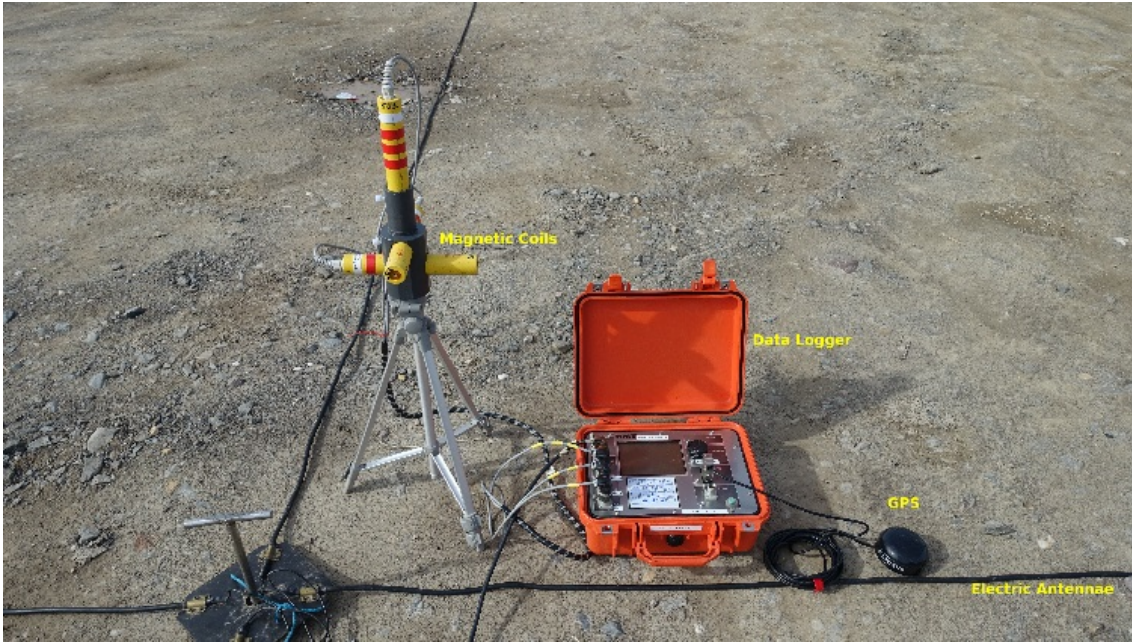


Figure 4.3: New data logger, electric antennae and magnetic coils

It is also important to select the correct gain during the measurement. The gain can be selected separately on different band. There are 3 options for the gain: 1, 4, 16. Unfortunately there is a bug on the H_z component on the D1 band which can only be set to 1. This can only be seen on the SM25M software.

The physical principles of the CSRMT measurements are as follows. In general, there exists a potential difference (or voltage) between any two points in an electric field. In the MT (and RMT), the electric field is determined by a measurement of the potential difference between those points. The electric field may be expressed in terms of the scalar (ϕ) and vector (\mathbf{A}) potentials as:

$$\mathbf{E} = -\nabla\phi - \partial_t\mathbf{A}, \quad (4.1)$$

where the magnetic fields can be expressed as

$$\mathbf{B} = \nabla \times \mathbf{A}. \quad (4.2)$$

The potential difference between two points depends on the path between the points, therefore, the electric field in Equation (4.1). This is the property of a non-conservative field. The potential difference $\phi_{12} = \phi(P_1) - \phi(P_2)$ is given by:

$$\phi_{12} = \int_{P_1}^{P_2} \mathbf{E} \cdot d\mathbf{s} \quad (4.3)$$

where s is a measurement path. For a straight-line path between the points defined by vector \mathbf{r} (extending from P_1 toward P_2) and a uniform electric field, the potential is given by

$$\phi_{12} = \mathbf{E} \cdot \mathbf{r}. \quad (4.4)$$

The electric field separated by distance l is given by

$$E = \frac{\phi}{l}. \quad (4.5)$$

In order to minimize the measurement error, it is necessary to have straight cable joining the electrodes (or points for capacitive electrodes) (Swift, 1967; Gomez-Trevino, 1987) and it is more crucial in higher frequencies. The non-straight wires might introduce some errors on the impedance data.

The non-grounded electric antennae which are normally used in the RMT method is more favourable since it makes the measurement much faster. This also has the advantage to use in wintertime and summertime also enable us to use on asphalt and concrete. Note that the grounded receiving lines are equivalent to double-length ungrounded lines (Saraev et al., 2017). The electric antennae then connected to the amplifiers. During the field measurements, one needs to make sure that the cables are connected properly.

The three magnetic coils are used to measure the magnetic induction \mathbf{B} in all three orthogonal directions. Their noise level is $25 \text{ fT}/\sqrt{\text{Hz}}$ with sensitivity of 20 mV/nT (Saraev et al., 2017). The principle of operation of induction coil magnetometers involves the induction of an electromotive force (EMF) in a coil by time variation of the component of the magnetic field parallel to the coil axis (Kaufman and Keller, 1981). In an idealized coil of negligible resistance, capacitance and inductance the EMF induced by a time-varying magnetic induction \mathbf{B} is given by:

$$\text{EMF} = nA\partial_t(\mathbf{a} \cdot \mathbf{B}), \quad (4.6)$$

where n is the number of turns of wire in the coil, A is the area of the coil, and \mathbf{a} is the unit vector parallel to its axis. The response depends on the direction of the magnetic field variations. Consequently, a vector measurement of the field requires three orthogonal sensors.

On the time series processing with bivariate analysis (the tensor estimation), one should assign errors either to one of the electric or magnetic fields. Of course, all of the time series contain some errors, but due to the limitation of the algorithm, only one should be assigned (Adcock, 1878; Chave, 2017). In our case (as in MT), the magnetic fields are set to be error free. As one can see from the instrument, the magnetic fields sensor is much more robust than the cable, at least from the field deployment (sometimes it is hard to get straight cable).

4.2 Time Series Processing

In practice, the estimation of the transfer functions from the measured time series can be summarized in the following steps:

1. Divide the recording segments into equal length.
2. Multiply each segment with a window function.

3. Fourier transform each segment with calibration.
4. Calculate the auto and cross spectra.
5. Estimation of the transfer functions and their errors.

Furthermore, to get better estimation more criteria can be applied such as coherency threshold between electric and magnetic fields and also the azimuth (deviation from the profile direction) distribution of the source.

First, the coherency of the electric and magnetic fields are given by:

$$\text{Coh} = \frac{\langle E^*B \rangle}{(\langle EE \rangle \langle BB \rangle)^{1/2}}. \quad (4.7)$$

The symbol * denotes the complex conjugation. Coherency is a linear correlation between electric and magnetic fields (in the frequency domain). The value lies between 0 to 1. In the ideal case, the coherence between the electric and magnetic fields ≈ 1 (electric fields perpendicular to the magnetic fields), since the ideal case is hard to find in field experiments, therefore the coherence is set to be at least 0.8. Almost all steps were done on SM25M, only the last step when estimating tensor and tipper differ between SM25M and SFA. More or less the processing steps from the time series to the transfer functions are similar with magnetotelluric data processing. However, the transmitters (either distant radio transmitters or horizontal electric dipole) are not distributed equally (only scalar source(s)). To accommodate this, another criterion can be added based on the azimuthal distribution of the transmitter; the azimuth is set to be smaller than 30° for the impedance data and 90° for the tipper data combined with rotation. The processing algorithm of RMT/CSRMT data with scalar estimation and azimuth can be found in the old RMT-SM25 manual (Mickrokor, 2005). Keep in mind that the azimuth definition is different between the SM25M and the SFA.

The final estimation of the impedance transfer functions are done in two ways, scalar (with SM25M or SM+ or SFA) and tensor (called as SFA). The differences between SM25M and SFA on the scalar estimation is on the way the azimuth distributions are calculated. One of the differences with the MT time series processing is the choice of centre frequency where the impedances are estimated. On MT time series processing, normally 6 - 10 log-spaced frequencies per decade are chosen as centre frequency (Simpson and Bahr, 2005). This can not be done in RMT-CSRMT case since the frequencies from distant radio transmitters which falls to azimuth criteria or the main frequency and its harmonics from the HED are not log-spaced. As a result, the impedances are evaluated on the known radio frequencies for RMT case or main frequency and its harmonics for CSRMT case. Finally, to get smooth sounding curves in which Weidelt's dispersion relation is fulfilled, MTS2DP1ot¹ based on Siegel's repeated median was used (Smirnov, 2003).

As mentioned before, the tipper data are estimated in separate ways. First, the azimuth is set to 90° to accommodate all the available radio transmitter since on the measurement days. Most of the times, the direction of the radio transmitters are not parallel or perpendicular to the profile. Afterwards, on one specific stable frequency, the tipper

¹an alpha version given directly by Prof. Smirnov.

data along the profile are rotated to a specific degree in order to minimize one of the tipper components.

It is worth mentioning that the output from the new processing software SFA is a universal MT format in the form of EDI file that can be easily exchanged with the MT community and can also be processed in industrial software such as WinGLink.

4.3 Fourier Transform on SM25M

As stated before, most of the processing steps are carried out in the SM25M software. The raw time series in the time domain are transformed to the spectra in the frequency domain.

The first step to process the data is to calculate the Fourier coefficients in order to perform the Fourier transform. The electromagnetic time series (E_x, E_y, H_x, H_y, H_z) recorded on the RMT five channel system are 16 byte with the sampling frequency (F_s) given in Table 4.1. The length of the recorded time series L_{seg} is 64 Ks (Kilosamples). During the measurements, the operator selects the number of segments. The total time of data acquisition T_{acq} is given by:

$$T_{acq} = \frac{N_{seg} L_{seg}}{F_s}. \quad (4.8)$$

Afterwards the complex Fourier coefficients on SM25M can be calculated according to complex Fourier transform formula:

$$C_m(f_k, r) = \sum_{j=1}^N \frac{(x_m(r, j) - x_{m,c}(r)) w_j}{W N \sqrt{\Delta f}} \exp \left[-\frac{i2\pi k(j-1)}{N} \right], \quad (4.9)$$

where $m = 1 \dots 5$ is the channel number, x_m is the recorded time series (either magnetic or electric) $N = L_{seg}$, $f_k = kF_s/N$ – frequency, $k = 1 \dots \frac{N}{2} - 1$, $\Delta f = F_s/N$, $r = 1 \dots N_{seg}$ and also

$$x_{m,c}(r) = \frac{1}{N} \sum_{i=1}^N x_m(r)_i,$$

while w_j on Equation (4.9) is the window factor which is either a rectangular or the Blackmann window selected by the user, and

$$W = \left(\sum_{j=1}^N w_j^2 \right)^{1/2}.$$

is the RMS of the window factor.

Finally, the spectrum (power spectrum density either measured electric or magnetic field in the frequency domain) are calculated according to:

$$S_{i,j}(f_k) = \frac{1}{N} \sum_{i=1}^N C'_i(f_k, r) C_j^{\dagger}(f_k, r), \quad (4.10)$$

with

$$C'_m(f_k, r) = \frac{C_m(f_k, r)}{K_m(f_k)},$$

where $K_m(f_k)$ are factors of respective analogous sections of the recorder. The $K_m(f_k)$ depend on a selected gain and are determined during the device calibration. The symbol \dagger is the Hermitian conjugation. These spectra are then further processed by scalar estimation and/or tensor estimation to get the sounding curves by SM25M and SFA.

Unfortunately, the calibration files coming along with the device may add some errors on the estimation of the transfer functions which may add errors of 1% for apparent resistivity and 1 degree for impedance phase (Mickrokor, 2005).

4.4 Impedance Data Processing

4.4.1 Scalar Estimation

The CSRMT receiver comes along with the SM25M software. This software is used to connect the receivers and computer/laptop to transfer the measured data. After transforming the spectra (including cross spectra and auto spectra), the scalar estimation of apparent resistivity and phase with the following calculations implemented on SM25M and SFA:

$$\rho_{xy} = \frac{1}{\mu_0\omega} \left(\frac{E_x E_x}{H_y H_y} \right) \quad \text{and} \quad \phi_{xy} = \tan^{-1} \left(\frac{\text{Im}[E_x H_y]}{\text{Re}[E_x H_y]} \right), \quad (4.11)$$

$$\rho_{yx} = \frac{1}{\mu_0\omega} \left(\frac{E_y E_y}{H_x H_x} \right) \quad \text{and} \quad \phi_{yx} = \tan^{-1} \left(\frac{\text{Im}[E_y H_x]}{\text{Re}[E_y H_x]} \right). \quad (4.12)$$

The distribution of the source (radio transmitter and horizontal electric dipole) on SM25M is estimated by:

$$A_z = \pm \tan^{-1} \sqrt{\left(\frac{E_y E_y}{H_x H_x} \right)}. \quad (4.13)$$

The azimuth is still calculated with electric and magnetic fields due to the historical development of the receiver of the (CS)RMT system. Mickrokor developed the RMT device back in early 2000 with two channels only (one electric antenna and one magnetic coil). To accommodate this, the estimation of the azimuth is realized with electric and magnetic field spectra. This scalar estimation (together with the old system) have been applied in IGM Cologne since 2005. Note that the azimuth on the SM25M is the deviation from the magnetic sensors. Hence the opening azimuth for the transmitter is double of the specified angle. In an ideal case, the azimuth is zero, however for the field measurement the azimuth can be set to 15° (which equals to 30° in the opening). The transmitters that are located outside the specified azimuth are rejected.

While on SFA the azimuth is calculated due to formula given by: Bastani (2001):

$$\Theta = \frac{\pi}{2} + 0.5 \tan^{-1} \frac{2\text{Re}[H_x H_y]}{H_x H_x - H_y H_y}. \quad (4.14)$$

With this formula, the azimuth is now calculated by the measured magnetic fields which are assumed to be error-free. The azimuth specified on SFA is the opening azimuth, which in my opinion is the correct one to process the (CS)RMT data.

The output of SM25M (apparent resistivity and phase estimation) can also be transformed to impedance file (*.imp) that can be further processed by MTS2DP1ot software to get better estimation with the following transformation:

$$\rho_{ij} = \sqrt{\frac{\text{Re}[Z_{ij}]^2 + \text{Im}[Z_{ij}]^2}{5}}, \quad (4.15)$$

$$\phi_{ij} = \tan^{-1} \left(\frac{\text{Im}[Z_{ij}]}{\text{Re}[Z_{ij}]} \right). \quad (4.16)$$

Note that the phase output from the SM25M is in degree, while in the imp file, the phase is in radian, after some algebra:

$$\text{Re}[Z_{ij}] = \sqrt{\frac{5\rho_{ij}}{1 + \tan^2 \phi_{ij}}}, \quad (4.17)$$

$$\text{Im}[Z_{ij}] = \text{Re}[Z_{ij}] \tan \phi_{ij}. \quad (4.18)$$

In SM25M (and SM+), the vertical component of the magnetic fields H_z are not processed any further (only transformed from the time series to the spectra). Because of that, there is no tipper information on these softwares.

4.4.2 Tensor Estimation

The tensor estimation in SFA applies the bivariate linear regression which first introduces by Vozoff (1972) for processing the MT time series. First, the impedances are estimated with a minimal error in E_x or E_y :

$$Z_{xy}^{E_x} = \frac{\langle E_x B_y^* \rangle \langle B_x B_x^* \rangle - \langle E_x B_x^* \rangle \langle B_x B_y^* \rangle}{\langle B_x B_x^* \rangle \langle B_y B_y^* \rangle - \langle B_x B_y^* \rangle \langle B_y B_x^* \rangle}, \quad (4.19)$$

$$Z_{yx}^{E_y} = \frac{\langle E_y B_x^* \rangle \langle B_y B_y^* \rangle - \langle E_y B_y^* \rangle \langle B_y B_x^* \rangle}{\langle B_x B_x^* \rangle \langle B_y B_y^* \rangle - \langle B_x B_y^* \rangle \langle B_y B_x^* \rangle}. \quad (4.20)$$

Here, the symbol $\langle \dots \rangle$ denotes the mean of spectra and * denotes complex conjugation. Afterwards the apparent resistivity and impedance phase can be calculated as:

$$\rho_{xy} = \frac{1}{\mu_0 \omega} (Z_{xy})^2 \quad \text{and} \quad \phi_{xy} = \tan^{-1} \left(\frac{\text{Im}[Z_{xy}]}{\text{Re}[Z_{xy}]} \right), \quad (4.21)$$

$$\rho_{yx} = \frac{1}{\mu_0 \omega} (Z_{yx})^2 \quad \text{and} \quad \phi_{yx} = \tan^{-1} \left(\frac{\text{Im}[Z_{yx}]}{\text{Re}[Z_{yx}]} \right). \quad (4.22)$$

The radio frequencies of the RMT method are not distributed equally (only scalar source), the tensor estimation applying bivariate linear regression will be worse than the scalar estimation. Only in ideal CSRMT tensor experiment the tensor estimation works

which unfortunately we could not do it do some reasons (current channelling, cultural noise and high contact resistance) during the PhD studies. For example, on one specific frequency, only one component can be observed. Then according to Equation (4.19) and (4.20) which require the other component of the spectra on the same frequency (for example the first term on numerator of Equation (4.19)) will be missing. The transfer function can also be computed by taking the mean (or square root) of two neighbouring frequencies, but this also introduces bias (Pedersen and Oskooi, 2004). Because of this reason, the transfer functions calculated by scalar estimation will be further processed.

My recommendation is to process different mode separately according to the observed frequencies. For TM mode to some specific frequencies and for TE mode to other specific frequencies.

4.4.3 Siegel's Repeated Median Estimator

The transfer function estimated both by the scalar and tensor calculation, most of the times, contain some outliers in which Weidelt's dispersion formula was not satisfied. Therefore, a smoothing algorithm is needed in this case. One of the established smoothing algorithms is Bootstrap M-estimator introduced by Smirnov (2003) implemented in `MTS2DPLOT`. The idea behind Bootstrap M-estimator is known as Siegel's repeated median estimator (Siegel, 1982). The transfer function estimated by this method is denoted as final and will be processed further for the inversion and modelling to get earth conductivity structure.

The Siegel's repeated median estimator algorithm can be described as follows. First, a linear regression can be written as

$$y_i = \mathbf{x}_i^T(\Theta) + e_i, \quad i = 1, \dots, \quad (4.23)$$

where y_i is the predicted value from the i th observation of a p dimensional vector x_i , e_i the i th prediction error, while Θ represents the p -dimensional vector of unknown regression parameters to be estimated. Siegel's repeated median estimator of a set of n observations $(\mathbf{x}_i, y_i), \dots, (\mathbf{x}_{in}, y_{in})$ is defined as follows. The j th component of Θ denoted as T^j is:

$$T_n^{(j)} = \text{med}_{i_1} \left\{ \dots \left\{ \text{med}_{i_{p-1}} \left\{ \text{med}_{i_p} \{ \Theta^{(j)}(i_1, \dots, i_p) \} \right\} \right\} \right\}, \quad (4.24)$$

where the median is taken over all indices $i_m = 1, \dots, n$.

In the bivariate linear regression model used to solve the impedance linear system:

$$y_1 = \Theta_1 x_{1i} + \Theta_2 x_{2i} + e_i, \quad (4.25)$$

the repeated median estimate is determined in this way. If the unknown parameter is a complex vector, then the equation is split into two independent equations for real and imaginary parts that are solved separately. In the `MTS2DPLOT` software there are two choices: apparent resistivity-phase space and real-imaginary impedance space. The com-

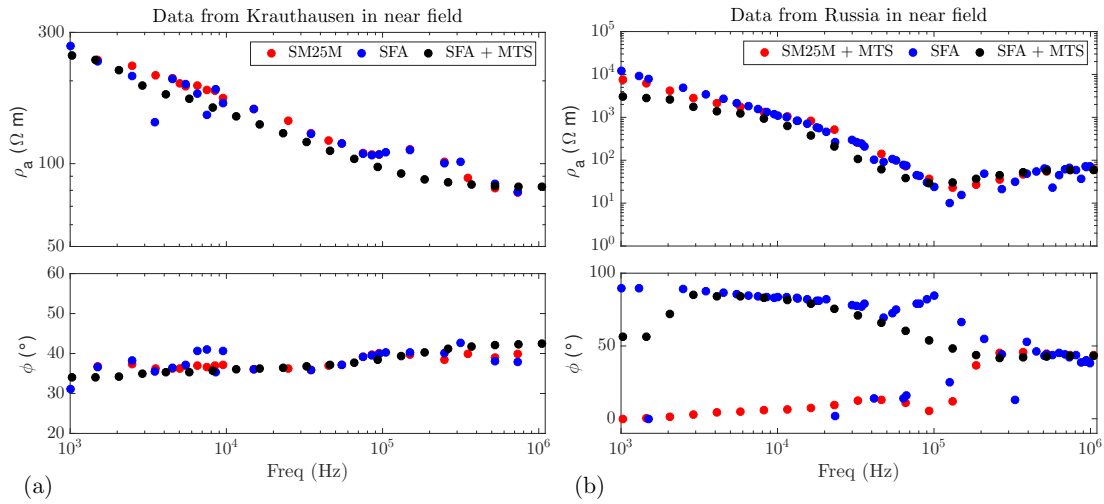


Figure 4.4: Comparison of data processed with SM25M and SFA. The data observed from Krauthausen test site on profile 2.

ponents of the vector parameter Θ are estimated separately, for instance, for Θ_1^* we have:

$$\Theta_1^* = \text{med}_i \text{med}_{j \neq i} \frac{y_j x_{2j} - y_j x_{2i}}{x_{1i} x_{2j} - x_{1j} x_{2i}}. \quad (4.26)$$

It means that for each i th observation first the median of combinations with all j observations is calculated and then finally the median of those $n - 1$ medians form the final estimation.

On the `MTS2DP1ot` software, there are options for the number of centre logarithmic frequencies per decade to estimate the transfer functions: 2, 4, 7 and 14. On this thesis, all data are estimated with 7 frequencies per decade from at least 9 data points (from the observed harmonics on CSRMT data) with smoothing factor 1.5 – 2. Simpson and Bahr (2005) suggested that the evaluation frequencies per decade (log-spaced) are between 6 – 10. Thus 7 frequencies per decade is an ideal number. However, sometimes there are only 4 – 5 frequencies per decade after smoothing especially in the RMT method.

4.4.4 Comparison of Processing Algorithm

To illustrate and validate the newly developed processing algorithm, an example of the data from the survey in Krauthausen, Germany is given in Figure 4.4(a) and the data from Vuoksa region in the near field is given in Figure 4.4(b).

In the Krauthausen data, all the processing algorithm gave an identical result for apparent resistivity and impedance phase of the CSRMT data. The data from other surveys also give similar behaviour for both RMT and CSRMT data. This was also observed in the Vuoksa far field data. However, in the near-field data from Vuoksa region, the phase impedance from SFA estimation is worse than the SM25M estimation. Since the phase impedance estimation from the SFA is different from SM25M and the theory in Chapter 2. The impedance phase was high (nearly 90°) with very high apparent resistivity. This is because of the average calculation applied on the SFA, and there is no noise subtraction in the processing algorithm. For example, on the centre frequency the impedance phase

is zero, but on the neighbouring frequencies (maybe from the noise) are around 90° . Thus the resulting average of the impedance phase is around 90° . For this reason, on the near-field data from Vuoksa region on Chapter 5, the transfer functions were calculated with the `SM25M` software, and the final estimation is given after `MTS2DP1ot`.

4.5 Tipper Data Processing

The new 5 channel receiver developed by Mickrokor gives the possibility to record the vertical magnetic field therefore to process the tipper data. In the framework of this project, the tipper data will be processed and tested (as well as validated). Unfortunately, Mickrokor has not yet processed the tipper data which make the comparison of developed processing algorithm difficult. The tipper data are estimated in the `SFA` also in two ways: scalar and tensor. Before starting on the tipper processing, I will write again the relation between the vertical and horizontal magnetic fields which are related through complex valued vertical magnetic transfer function known as the tipper vector:

$$\begin{bmatrix} H_z \end{bmatrix} = \begin{bmatrix} A_x & B_y \end{bmatrix} \begin{bmatrix} H_x \\ H_y \end{bmatrix}, \quad (4.27)$$

where A_x and B_y are the components of the tipper vector.

First the tipper vector components in scalar estimation given by:

$$\text{Re}[A_x] = \frac{\sqrt{H_z H_z}}{\sqrt{H_x H_x}} \cos \left(\tan^{-1} \left(\frac{\text{Im}[H_z H_x]}{\text{Re}[H_z H_x]} \right) \right), \quad (4.28)$$

$$\text{Im}[A_x] = \frac{\sqrt{H_z H_z}}{\sqrt{H_x H_x}} \sin \left(\tan^{-1} \left(\frac{\text{Im}[H_z H_x]}{\text{Re}[H_z H_x]} \right) \right), \quad (4.29)$$

$$\text{Re}[B_y] = \frac{\sqrt{H_z H_z}}{\sqrt{H_y H_y}} \cos \left(\tan^{-1} \left(\frac{\text{Im}[H_z H_y]}{\text{Re}[H_z H_y]} \right) \right), \quad (4.30)$$

$$\text{Im}[B_y] = \frac{\sqrt{H_z H_z}}{\sqrt{H_y H_y}} \sin \left(\tan^{-1} \left(\frac{\text{Im}[H_z H_y]}{\text{Re}[H_z H_y]} \right) \right), \quad (4.31)$$

where Re and Im are the real and imaginary part of the tipper vector components respectively. The estimation is directly separating between the real part and imaginary part of the tipper vector. In the tensor estimation, the tipper vector components are calculated by the following formula:

$$A_x = \frac{\langle H_z H_x^* \rangle \langle H_y H_y^* \rangle - \langle H_z H_y^* \rangle \langle H_x H_x^* \rangle}{\langle H_x H_x^* \rangle \langle H_y H_y^* \rangle - \langle H_x H_y^* \rangle \langle H_y H_x^* \rangle}, \quad (4.32)$$

$$B_y = \frac{\langle H_z H_y^* \rangle \langle H_x H_x^* \rangle - \langle H_z H_x^* \rangle \langle H_x H_y^* \rangle}{\langle H_y H_y^* \rangle \langle H_x H_x^* \rangle - \langle H_y H_x^* \rangle \langle H_x H_y^* \rangle}. \quad (4.33)$$

In the tensor estimation, the real and imaginary parts are separated after the calculation.

Theoretically, the best results of processing tipper data are obtained by using two transmitters whose frequencies are close and whose azimuth differ by 90° . In Europe and North America, it is usually possible to find two transmitters with a small frequency

separation and optimal azimuths (Pedersen and Oskooi, 2004). The scalar estimation with azimuth 90° should be chosen for further processing and modelling. The azimuth is chosen to take into account all the available radio transmitters on the TE mode and also a non-perfect field set up between the strike direction and profile direction (it is hard to deploy perfect 90° between profile and strike direction, and the transmitter are on the profile direction). To make a point, a comparison between the scalar and tipper with 30° and 90° is given in Figure 4.5. The azimuth was first increased from 30° to 90° and compare all the magnitude at all the stations and frequencies. Only at scalar 90° the magnitude < 1 is achieved which is most of the tipper processing unless in the near-field zone.

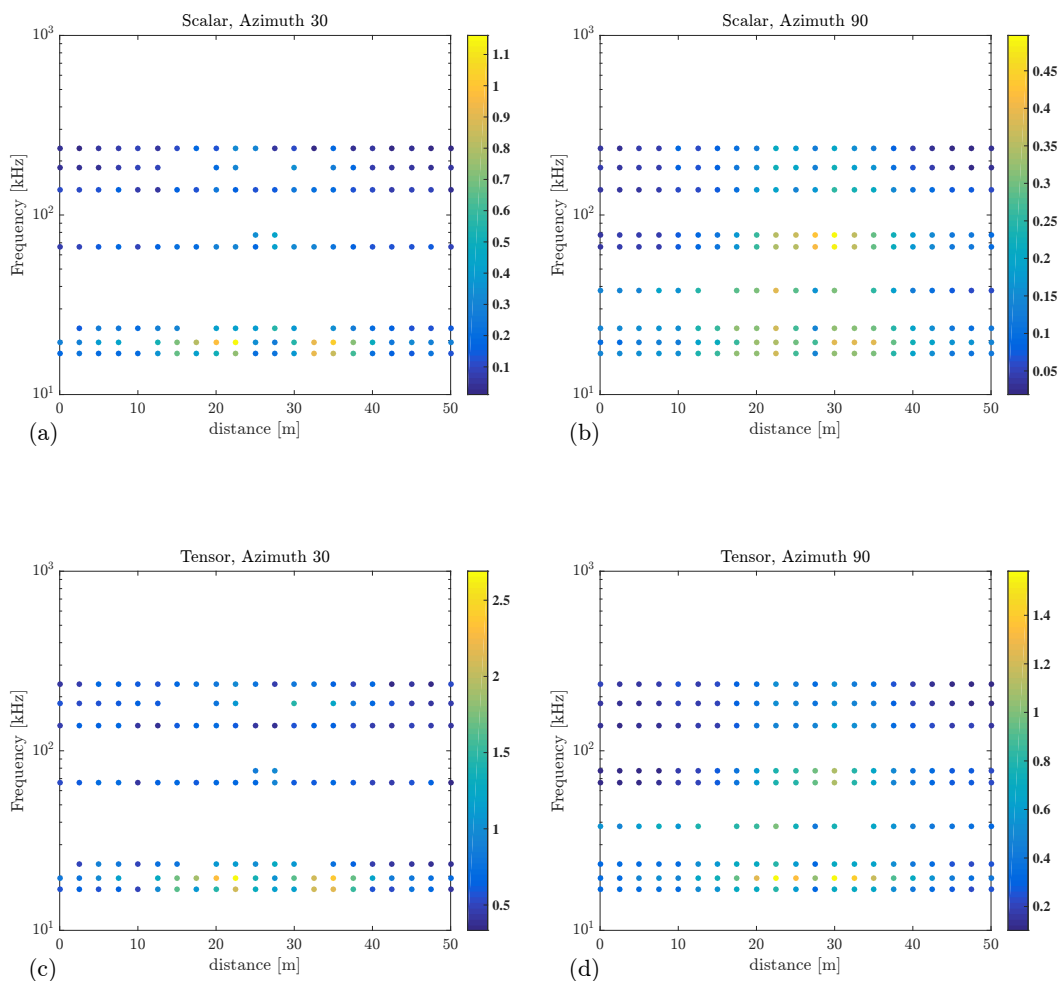


Figure 4.5: Tipper magnitude on Aachener Weiher Köln along the profile for all frequencies, (a) scalar, azimuth 30° (b) scalar, azimuth 90° (c) tensor, azimuth 30° , (d) tensor, azimuth 90° . Note on different colour scale.

An example of how different azimuth affects the tipper estimation is given in Figure 4.5. The data are from Aachener Weiher Köln one of a test area for our Institute (normally for teaching purposes for bachelor student). It is known that there is a buried pipeline that is a very good test area to test the tipper processing of the new device. In Figure 4.5 (a) is the scalar tipper with azimuth 30° , in Figure 4.5(b) is

the scalar tipper with azimuth 90° , in Figure 4.5(c) is the tensor estimation with azimuth 30° and in Figure 4.5(d) is the tensor estimation with azimuth 90° . Note that the colour scale is different for all figures to show the maximum tipper magnitude for all possibilities. It can be clearly seen from the Figure 4.5(b) that scalar estimation with azimuth 90° give the best estimate, not only the magnitude is reasonable, but more frequencies are also visible.

4.5.1 Rotation of tipper data

In an ideal 2D situations, the data can be separated into TE and TM modes. In this case, all tipper information are in TE mode, while in TM mode the tipper is zero (Section 2.2.2). However, the situation in the field such as radio transmitter(s) azimuth, strike direction, profile direction and error on the receivers will mix the modes (mixing mode situation). The tipper must be rotated to some angles to get one of the components to zero if possible or at least to minimize it. In order to take into account the profile direction which might be not straight and radio transmitters distribution, every point should be rotated to different rotation angles. But this method is very cumbersome. Accordingly, one rotation angle is enough for one frequency in the whole profile. The rotated transfer functions are given by equation:

$$\begin{pmatrix} A \\ B \end{pmatrix} = \begin{pmatrix} \cos \phi & \sin \phi \\ -\sin \phi & \cos \phi \end{pmatrix} \begin{pmatrix} A' \\ B' \end{pmatrix}, \quad (4.34)$$

subject to the conditions

$$B_{\min} = (-A' \sin \phi + B' \sin \phi), \quad \phi = -45, \dots, 45. \quad (4.35)$$

The rotation angle is only defined for maximum or a total 90° since $> 45^\circ$ rotation angle would change the TE mode to the TM mode.

An example of the tipper rotation is given in Figure 4.6. On the unrotated tipper data $B \neq 0$. On the left are all components of tipper from 23.4 kHz while on the right are all components from 183 kHz. The original (non-rotated) tipper data are given on the blue dot. It is clearly seen that the B components are not zero, in this case, they should be rotated and minimized. It was found that 30° and 40° are the best rotation angles for 23.4 kHz and 183 kHz respectively.

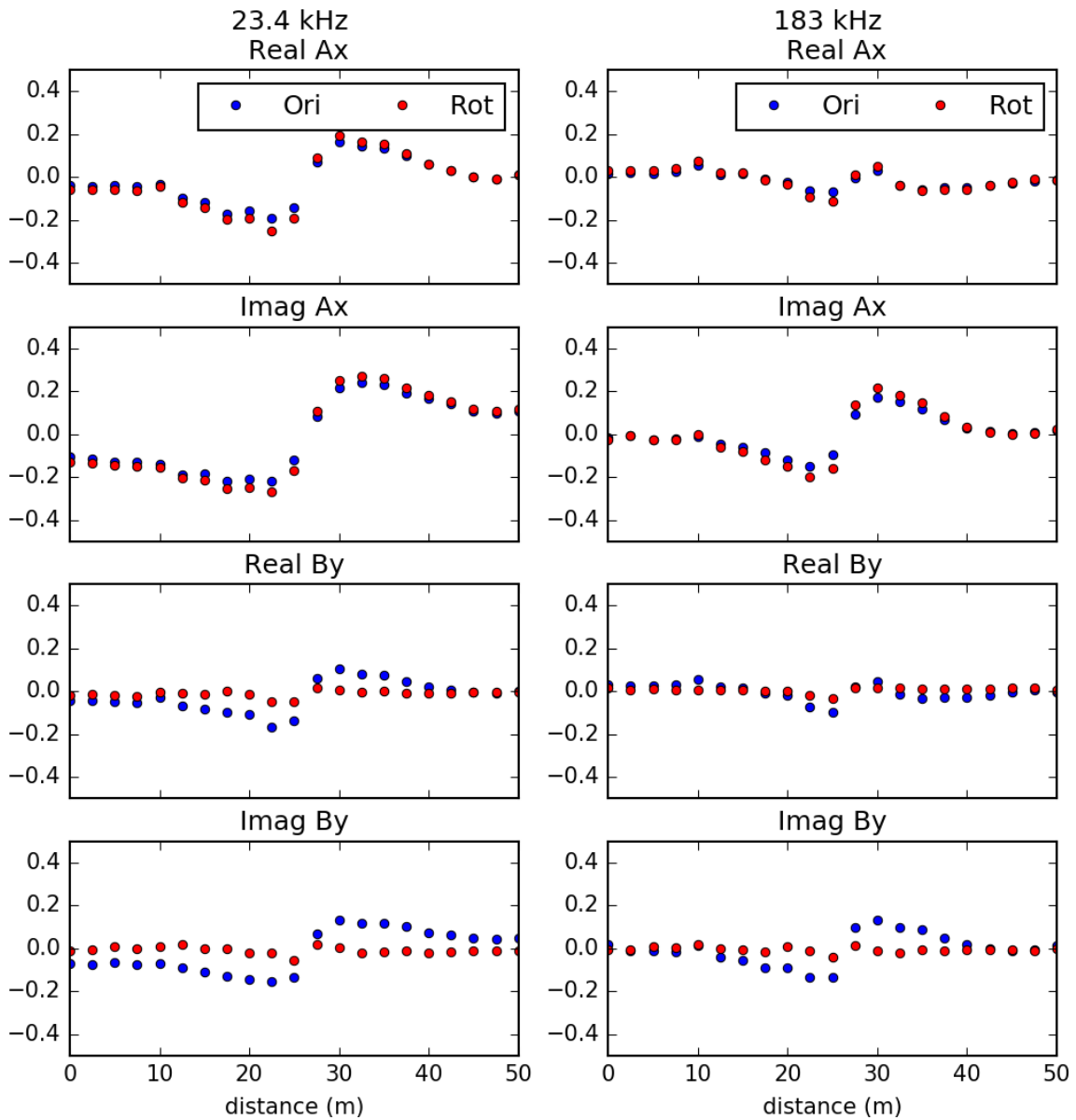


Figure 4.6: Tipper test on Aachener Weiher Koeln 23.4 kHz (left), 183 kHz right. The blue dots represent non rotated tipper, the red dot represents the rotated tipper. The rotation angles for 23.4 kHz is 30° while for 183 kHz is 40° .

4.5.2 Validation of tipper processing

The tipper estimation from *SFA* is compared with the tipper data from RMT-CHYN on the same profile on Aachener Weiher Köln to validate the tipper data processing of *SFA*. The results are given in Figure 4.7 for frequency 23.4 and 183 kHz. On the left are the real part of A_x and on the right are the imaginary part of A_x . On the top are 183 kHz not flipped (Figure 4.7(a),(b)), on the middle are 183 kHz flipped (Figure 4.7(c),(d)) and on the bottom are 23.4 kHz (Figure 4.7(e),(f)). It is clearly seen that for 183 kHz, only one agrees with the CHYN (flipped or not flipped). The real part of 23.4 kHz agrees well with the CHYN results but not so much on the imaginary part. One needs to note that the

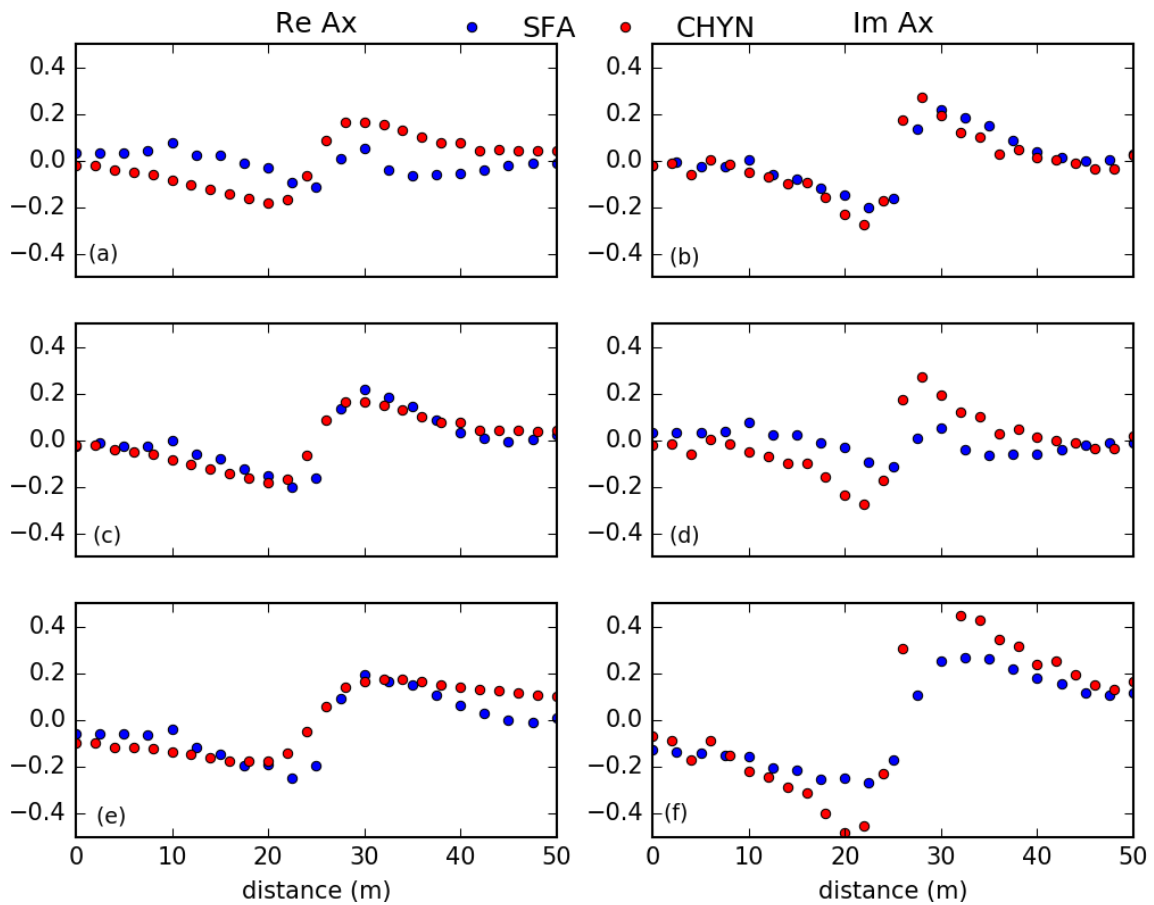


Figure 4.7: Comparison of tipper from new 5 channel receiver derived from *SFA* with CHYN on Aachener Weiher Köln.

CHYN data were from 2012 while the *SFA* data were from the end of 2015. Furthermore, *SFA* has 21 stations while CHYN has 26 stations on the 50 m profile. Generally speaking, the processed tipper data seems promising and can be applied to others field data.

Chapter 5

Field Measurements: Vuoksa Region, St Petersburg, Russia

5.1 Introduction

The first CSRMT measurements in the framework of the PhD thesis was carried out in Vuoksa Region around 100 km north of St. Petersburg, Russia in an area near the Finland border¹. The main aim of the survey was the detection of buried faults with the CSRMT method in the far-field zone of the test area. The survey area mainly consists of crystalline bedrock covered by thin sediments (5 - 10 m). The 2D conductivity structures on the far-field zone of the survey area are known from 3 previous RMT surveys (Simakov, 2015). The geological map was derived by the Institute of Earth Sciences of the St. Petersburg University during a geological excursion to the survey area. There exists a lot of faults striking mainly in NW-SE directions, but there are also mapped faults striking in different directions. Based on the simplified geological map, we chose our CSRMT/RMT test profile relatively perpendicular to the known strike direction of the local faults (see Figure 5.1). The 2D conductivity structure also enables us to process the tipper data in the TE mode of RMT data if there exists a strong and stable signal from the distant radio transmitter. Furthermore, in order to maximize the potential of the CSRMT method, the profile was also extended towards the transmitter's location to acquire near-field zones data where the signal to noise ratio is much higher than the far-field zone.

The CSAMT method with the horizontal electric dipole is an effective method for defining an outline of geological structures around a fault up to several hundred meters deep and also to define a resistivity boundary between different kinds of bedrock with a fault contact (Suzuki et al., 2000). The CSRMT method from Uppsala University (using a magnetic dipole source) has been successfully applied to map a normal fault in the Volvi basin (Bastani et al., 2011) and also for geotechnical purposes in Sweden (Wang, 2017). There have been many publications of the correlation between conductivity structure (more specifically conductivity contrasts) and earthquakes, i.e. Wannamaker et al. (2004); Nurhasan et al. (2006); Bastani et al. (2011); Widodo et al. (2016). Recently the

¹Part of this chapter is submitted to Pure and Applied Geophysics with a title Mapping of buried faults using the 2D modelling of far-field controlled source radiomagnetotelluric data.

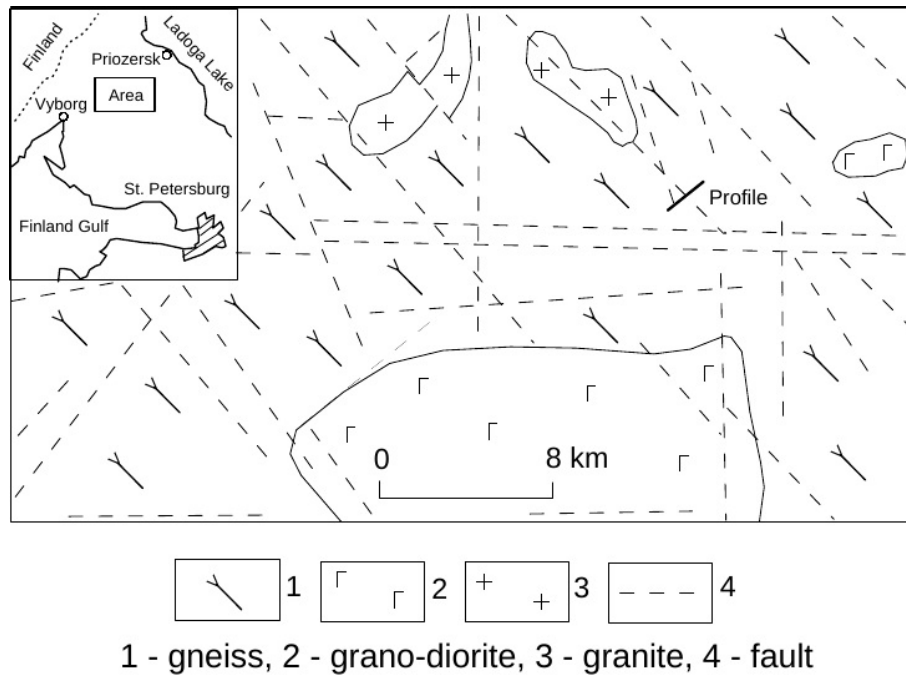


Figure 5.1: The location of the survey area north of St. Petersburg and the simplified unpublished local geological map of the survey area by the Institute of Earth Sciences of the St. Petersburg University. The CSRMT profile crossing two faults is also indicated.

new developed CSRMT method -which is also used in this thesis- has been applied as geophysical support of an onshore gas pipeline construction and survey at a site of the ore-dressing factory construction (Saraev et al., 2017).

This chapter is organized as follows. First, the survey design is introduced, then the raw data and processing are described. Afterwards, the modelling of the field data. Starting from the classical one in the far-field zone and then expanded to the near-field zones data. Finally, I will give the conclusion of the survey.

5.2 Survey Design and Geology of Test Site

The geology situation of the test site is mainly dominated by the bedrocks covered by a thin sediment cover (Figure 5.1). The thin sediments consist of a mixture of different types of glacial rocks, loams, sands and also clays, while the bedrocks consist of different gneiss and granites. Based on the simplified geological map, we have chosen our CSRMT/RMT test profile relatively perpendicular to the known strike direction of the local faults.

The CSRMT measurements in Vuoksa Region were carried out in May 2015. A dipole with 700 m length was deployed as a source only in inline configuration due to difficulty regarding the accessibility of the survey area (Figure 5.2). The injected currents and 4 main frequencies during the survey were given in Table 5.1. By using these main frequencies and their odd harmonics, the whole CSRMT frequencies range from 1 - 1000 kHz can be fulfilled. The profile was located along the road as shown in Figure 5.3 (b) around 2 km long. In order to decrease the high contact resistance which was 400 Ω , some

salt was added on the electrodes, and the contact resistance could be decreased to around 100Ω .



Figure 5.2: Locations of the 700 m long transmitter dipole and the CSRMT profile crossing two fault structures. Near-field - transition and far-field zones are marked. TM-mode CSRMT transfer functions in the far-field zone are interpreted by a 2D conductivity model.

Table 5.1: Current injected during CSRMT measurements in Vuoksa region, Russia

Main freq (kHz)	Current (A)	Band
0.5	3	D1-D2
11.3	1.8	D2
30	1.8	D2-D4
105	0.7	D4

During the CSRMT measurements, the conventional RMT method was additionally measured when the transmitter was shut down. The available signal from distant radio transmitters were: 16, 19.6, 20.2, 20.9, 22.1 23.4, 44.2, 66.6, 77.5, and 138 kHz. The RMT data from the distant radio transmitters have valuable information that is useful for the interpretation of the CSRMT data.

In the far field zone, these measured RMT data enable us to compare both methods (RMT and CSRMT) and also to test the validity of MT approximation on the far-field zone of the CSRMT data which might be still effected by the horizontal electric dipole (Zonge and Huges, 1991). While in the near field zone, the data from conventional RMT can be used jointly to invert the CSRMT near-field zones data with the MARE2DEM as shown in the synthetic example in Chapter 3. The inverted model is improved by jointly inverting the CSRMT and RMT data. As stated before, the survey design was using an inline transmitter only. Therefore only the TM mode of the CSRMT data was available. This survey design is more favourable to detect lateral conductivity changes in the measured impedance data. On the other hand, the tipper data would be not observed from the dipole source, but they should be available in the TE mode of the RMT data.



Figure 5.3: Photos from survey (a) the transmitter was located on the car, (b) the profile is located on the road

5.3 Raw Data and Processing

The measured CSRMT and RMT time series data were processed with the algorithm described in Chapter 4. First, the spectra were calculated in *SM25M* software. An example of autospectra and its coherency is given in Figure 5.4 for D2 band. The main frequency of 11.3 kHz and its harmonics were seen in the receiver. Moreover, another sharp spectra of frequency 19.6, 23.4, 44.1, 66.6 and 77.5 kHz were also received from the distant radio transmitters. Afterwards, the impedances were calculated in *SFA* in scalar estimation on the main frequencies and their odd harmonics for CSRMT data and on the known radio frequencies for RMT data in the far-field zone. In addition, *SM25M* was also used to estimate the impedance of the near field zone CSRMT data due to an inconsistency of phase estimation on *SFA*. The sectoral azimuth was 30° on *SFA* which equals to 15° in the *SM25M*. The minimum coherency was set to be 0.8. Finally, the Siegel's repeated median estimation Siegel (1982); Smirnov (2003) was applied to get smooth curves of apparent resistivity and phase. Moreover, the tipper data were also estimated with *SFA* on the existing radio frequency. Since the test area is far from the urbanization, the cultural noise is very minimal.

It is always a tricky task to categorize in which zone the observed data belong when the true resistivity between transmitter and receivers is not known, and the geology is not homogeneous halfspace and has a more resistive basement. The method that the far field zone starts at the offset $> 5\delta$ (Zonge and Huges, 1991) is difficult to apply on this situation. On a continuous profile starting right near the transmitter, it would be very helpful to plot the apparent resistivity and impedance phase as a function of distance for the lowest frequency. Normally, the transition between near field and far field would be not as clear as shown in Figure 5.5 for the impedance phase. It would be a smooth transition between near field to far field data. However, in this particular case, due to the underlying geology (vertical contact between a resistive structure and a conductive structure), there is a jump on the impedance phase. Remember that in the impedance phase in the near field zone are low, while the apparent resistivity when plotted as a function of distance would not bring much information of the near field zone behaviour.

The observed CSRMT data were categorized into the far field zone when the data contain no single influence of the near field zone effect on the whole CSRMT frequency

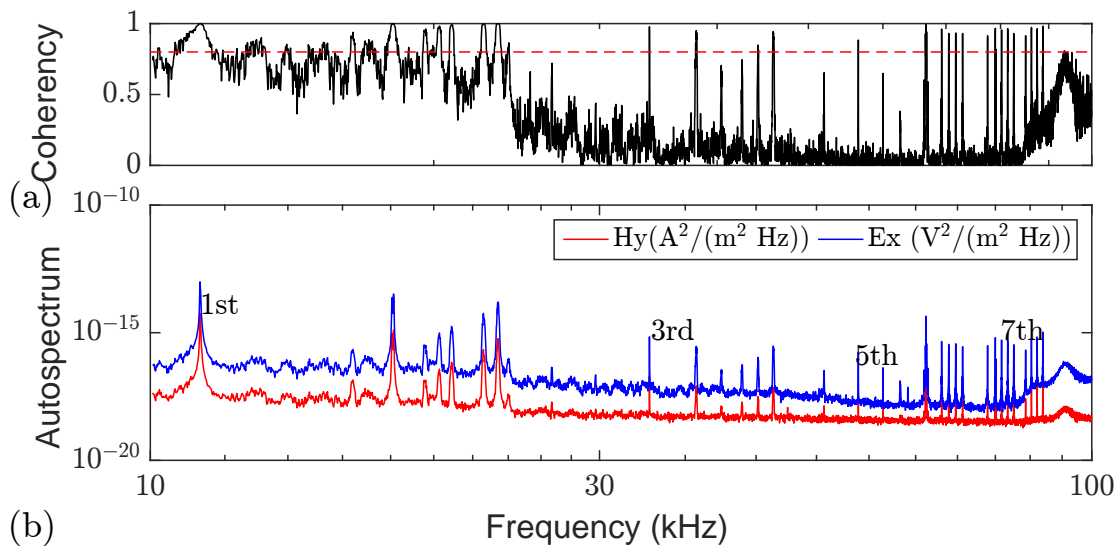


Figure 5.4: The coherency (a) and the autospectra (b) of 11.3 kHz received at 900 m distance in the Vuoksa experiment. It is clearly seen the harmonics of the transmitted signal up to 7th which is the last harmonics on the D2 band (10 – 100 kHz). The sharp lines beside the main frequencies and its harmonics were coming from distant radio transmitters.

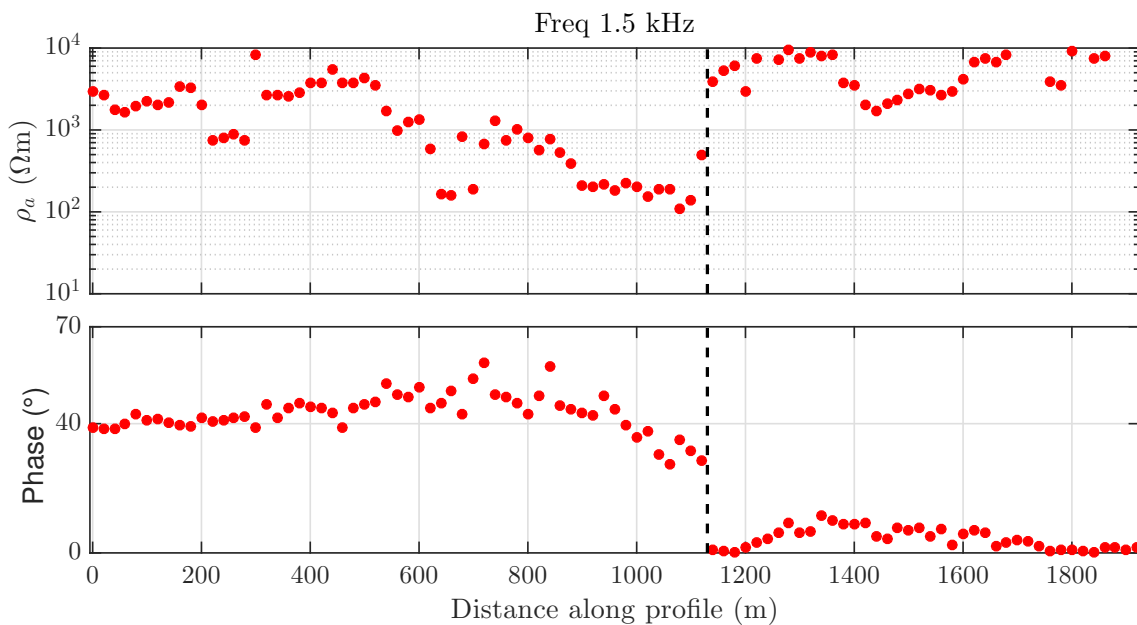


Figure 5.5: Apparent resistivity and phase for frequency 1.5 kHz plotted as a function of distance, the transmitter is located at the right side at 1950 m (not shown). There is a jump on the phase at around 1130 m marked by black dashed line which is considered as the boundary between near-field zone and far field zones.

range from 1 - 1000 kHz. When there is at least one data point (especially on the lowest frequency) influenced by the near-field zone effect (low phase - high apparent resistivity), the data were categorized as the near field zone data. By this criterion, the first 40 stations (offset up to 800 m) were categorized as near-field zone data, and the remaining 57 stations were far field data. In the Figure 5.5, the zones boundary is located at 1130 m. To validate this, the CSRMT data were also plotted together with the RMT data at every station as a joint sounding curve. For the interpretation, the far field CSRMT data then were inverted with `Rund2Inv` while the near field zone CSRMT data were interpreted with `MARE2DEM`. The observed RMT data were inverted with `Rund2Inv` and tipper data were interpreted using `Rebbocc`.

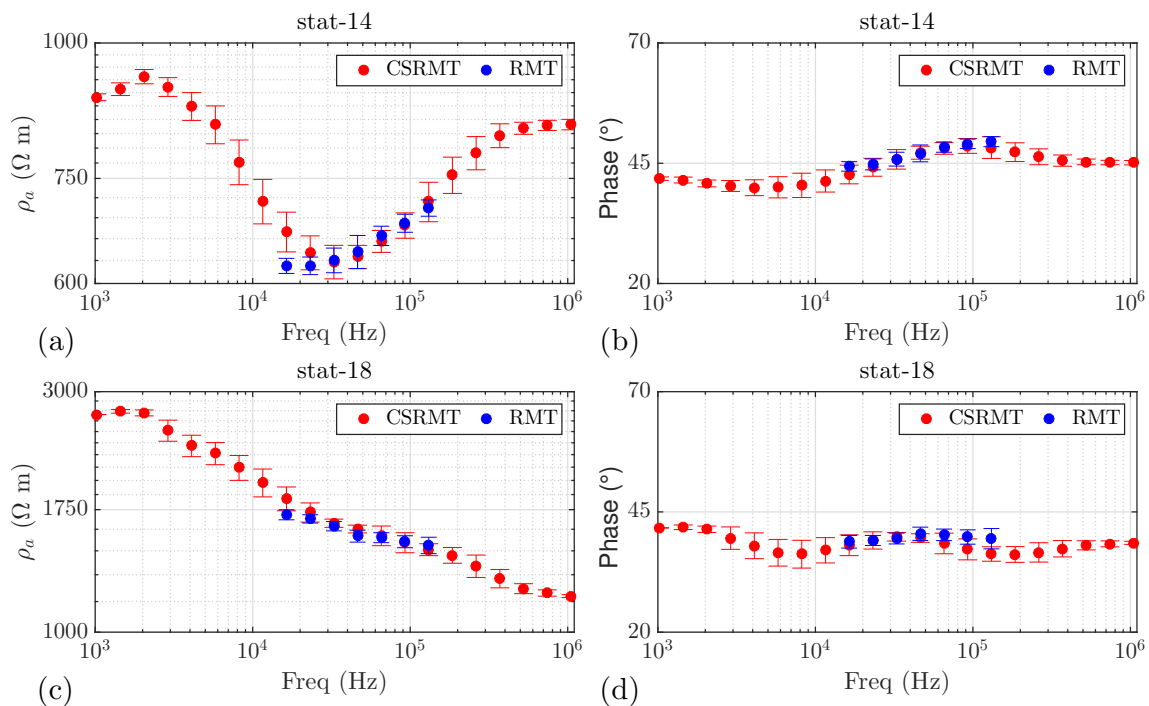


Figure 5.6: Data examples from the far field zone: (a) Apparent resistivity, (b) impedance phase from CSRMT and RMT data from station 14. (c) Apparent resistivity, (d) impedance phase from CSRMT and RMT data from station 18.

Figure 5.6 shows an example of apparent resistivity and phase from two stations located in the far-field zone near the expected fault for CSRMT and RMT data. Figure 5.6(a)(b) is from station 14 (280 m) and Figure 5.6 (c)(d) is from station 18 (300 m) for apparent resistivity and phase. The curves show a smooth dependence of frequency indicating the reliability of the CSRMT method. It is clear from both sounding curves that there is a jump in the resistivity values before and after the fault. On station 14 the apparent resistivity is less than 1000 Ωm , while on station 18 the apparent resistivity is bigger than 1000 Ωm . It is also clear that in the far-field zone, the CSRMT and RMT data are consistent to each other on the TM mode. Consequently, both data can be joined to one sounding curves and also compared the inversion results from both methods. Two examples of near-field zone transfer functions are given in Figure 5.7, for station 93 (1840 m, offset 100 m, Figure 5.7(a)(b)) and station 63 (1240m, offset 700 m, Figure 5.7(c)(d)). It is also clear from Figure 5.7(c)(d) that the CSRMT near-field data are not consistent with the RMT data. Note that, for the inversion with `MARE2DEM` including the source, the data

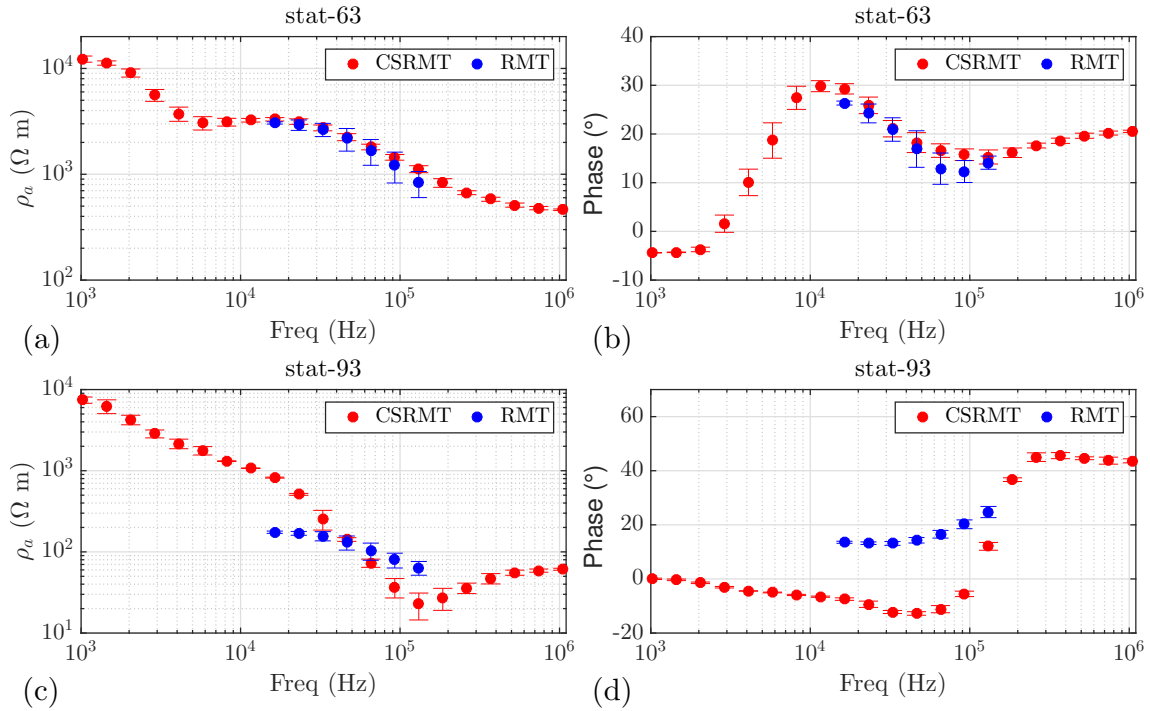


Figure 5.7: Data examples from the near field zone: (a) Apparent resistivity, (b) impedance phase from CSRMT and RMT data from station 63. (c) Apparent resistivity, (d) impedance phase from CSRMT and RMT data from station 93.

were transformed to the impedance Z_{yx} for the TM mode as the survey design.

The 2D conductivity structure in the far-field zone enables us to process the tipper data from the distant radio transmitters. However since our direction of the measurement was along the non-straight road on the profile, the 2D assumption is not fulfilled. In this case, the best that one can do is to minimize one of the observed tipper component (close to zero). On the observed data, either A or B components have to be minimized. An example of tipper data for frequency 66.6 kHz is given in Figure 5.8 and minimized B components by rotating to -30° . While in the near-field zone, the rotation is -35° for the same frequency as shown in Figure 5.9.

It is not always possible to set one of the components to zero as shown in Figure 5.8 for example real B component around 1000 m. The cause might be due to 3D effects, a non-straight profile, transmitter (source) direction, transmitter overprint on magnetic fields (far field assumption was not fulfilled) and bias in processing. The tipper data from the dipole source are not processed yet since MARE2DEM up to now still does not invert the tipper. Note that on the near-field zone, the tipper data are not zero even for a homogeneous halfspace solution.

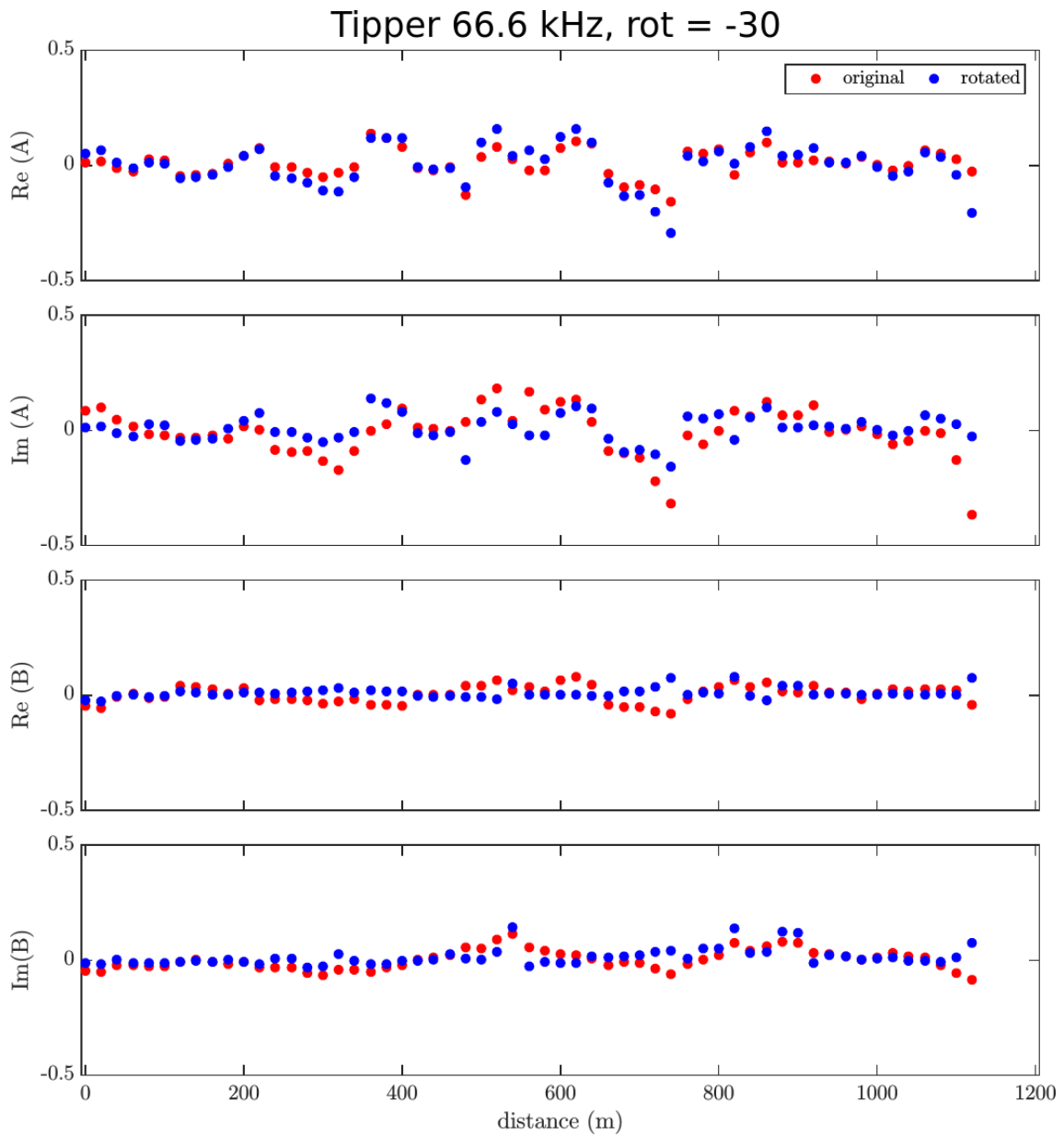


Figure 5.8: Tipper data along the profile in the far field zone for frequency 66.6 kHz, rotation -30° .

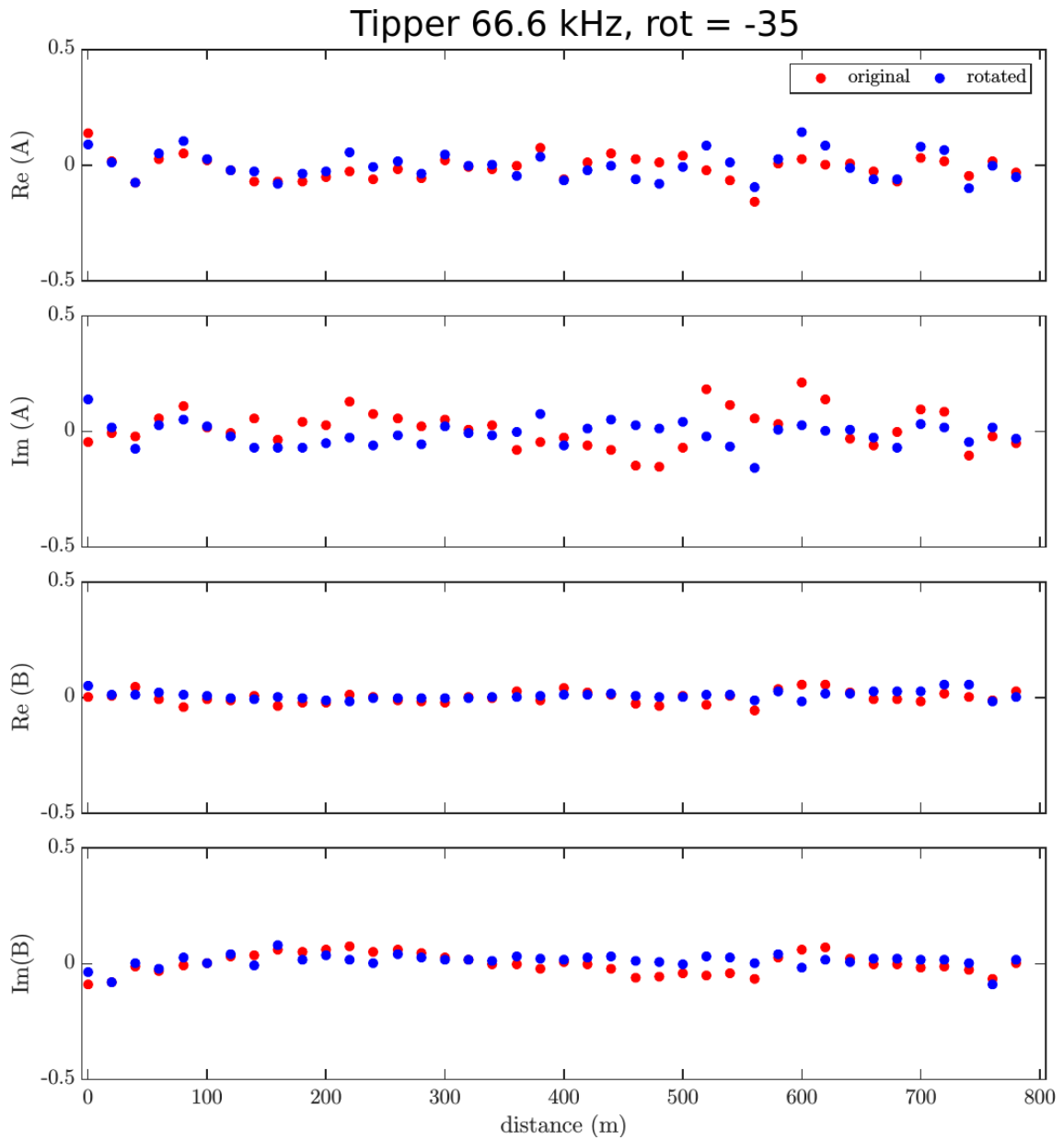


Figure 5.9: Tipper data along the profile in the near field zone for frequency 66.6 kHz from RMT data, rotation -35° .

5.4 Modelling

The survey design was inline configuration only thus the data were only in the scalar form of the TM mode. In this case, the dimensional analysis could not be performed. I will start the modelling with the classical approach, that is defining the boundary of the field zones. In the far field zone, the CSRMT and RMT data are inverted with `Rund2Inv`. Both results are then compared in order to see the similarities or differences between both models. Sometimes on the far field zone CSRMT data, the source effect might still be present (Zonge and Huges, 1991). In the near-field zone, I will invert the CSRMT data with `MARE2DEM` including the source and compare it with the result from RMT data inverted with `Rund2Inv`. Lastly, the tipper data from the RMT measurement are inverted with `Rebbocc`.

5.4.1 The Far Field Zone

The far-field zones have been studied previously as a test site for RMT measurements for the University of St. Petersburg. There are at least two apparent faults showing conductivity contrasts. For the inversion of the data, different starting homogeneous halfspace models were tested: 50, 100, 250 and 1000 Ωm . Other than to see the influence of the starting model on the inversion results, the different starting models are also needed to determine the DOI_s according to Seher and Tezkan (2007). The error floors used for the inversion with `Rund2Inv` were 5% in the apparent resistivity and 2.5% in the phase.

The first step is to determine the “corner” of the L-curve. The L-curve for each starting model are given in Figure 5.10 for the CSRMT data and in Figure 5.11 for the RMT data. As previously discussed in Chapter 3, the “corner” is hard to find and depends on the scale we use to display the data. On all the inversions with different starting models, the values between 5 – 50 for the trade-off parameter λ seem to be the corner.

After determining the maximum curvature of the L-curve, the conductivity model is derived. By using the model with different starting model, the DOI_s is determined then plotted along with the sensitivity and also $2z^*$. However, the DOI_s , $2z^*$ are on very low sensitivity reaching more than 800 m for the CSRMT data and more than 300 m for the RMT data, while the 10^{-3} sensitivity lies between 50 – 100 m only for the CSRMT data and 30 – 50 for the RMT data. For this reason, the inversion models are only plotted up to 100 m. The details are given in Appendix B. After analyzing the inversion results with different starting models, a homogeneous halfspace of 50 Ωm gave best results for both CSRMT and RMT data in the far-field zone in terms of RMS. The other results look similar with a higher RMS (not shown). The inversion results of the CSRMT data with a starting model of 100 Ωm with $\lambda = 20$ is given in Figure 5.12(a), the overall RMS value is 1.99%. The result of the inversion of the RMT data is taken at $\rho_0 = 100$, $\lambda = 20$ with RMS value of 1.5% is given in Figure 5.12(b). Both conductivity models agree quite well. Thus, the method to approximate the far field zone works. However, the RMS of the CSRMT data was a little bit worse than the RMT data. One of the reason is, the number of CSRMT data were much larger than the number of RMT data. The data fit for selected stations against the frequency (as Figure 5.6) are given in Figure 5.13 and for selected frequency of 1.5 kHz are given in Figure 5.14. In general, the data were fitted well.

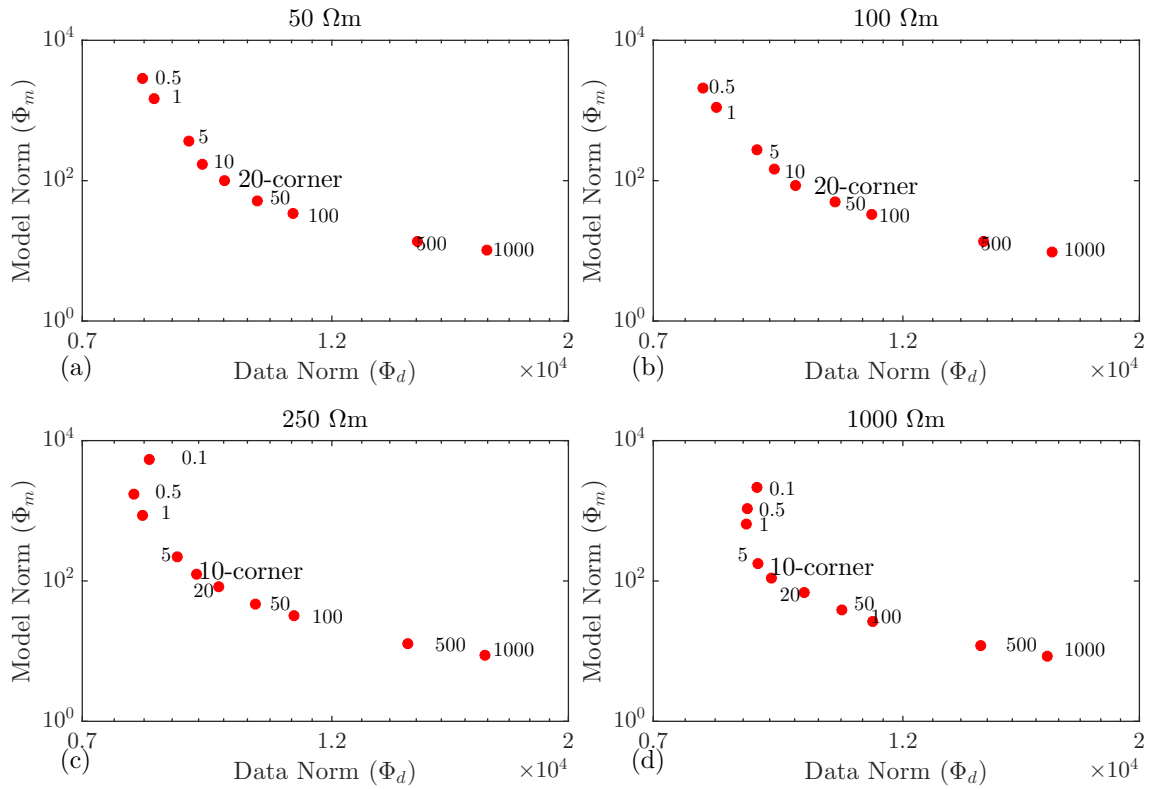


Figure 5.10: L curve of the inversion of CSRMT far field data for different starting models (a) $\rho_0 = 50 \Omega\text{m}$, (b) $\rho_0 = 100 \Omega\text{m}$, (c) $\rho_0 = 250 \Omega\text{m}$, and (d) $\rho_0 = 1000 \Omega\text{m}$. The optimal regularization parameter λ is marked for each curve.

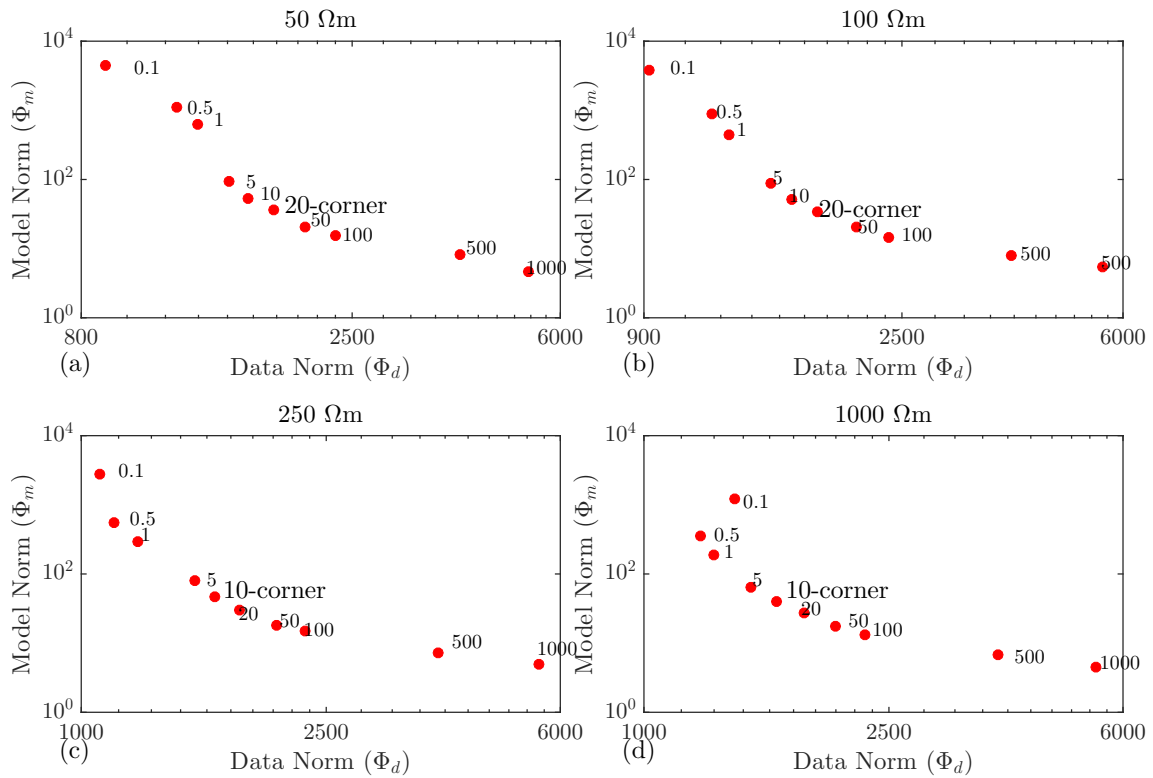


Figure 5.11: L curve of the inversion of RMT far field data for different starting models (a) $\rho_0 = 50 \Omega\text{m}$, (b) $\rho_0 = 100 \Omega\text{m}$, (c) $\rho_0 = 250 \Omega\text{m}$, and (d) $\rho_0 = 1000 \Omega\text{m}$. The optimal regularization parameter λ is marked for each curve.

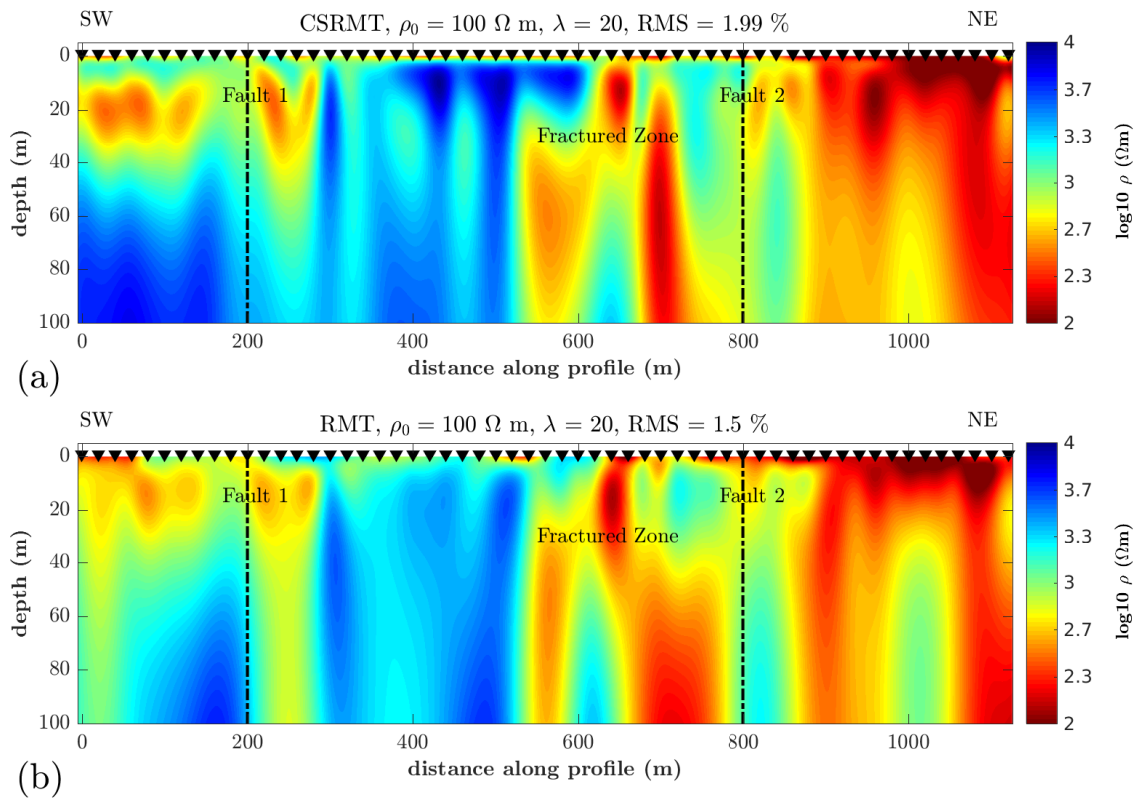


Figure 5.12: (a) Conductivity model from the CSRMT data, $\rho_0 = 100 \Omega \text{ m}$, $\lambda = 20$ RMS=1.99%. (b) Conductivity model from the RMT data, $\rho_0 = 100 \Omega \text{ m}$, $\lambda = 20$ RMS=1.5%.

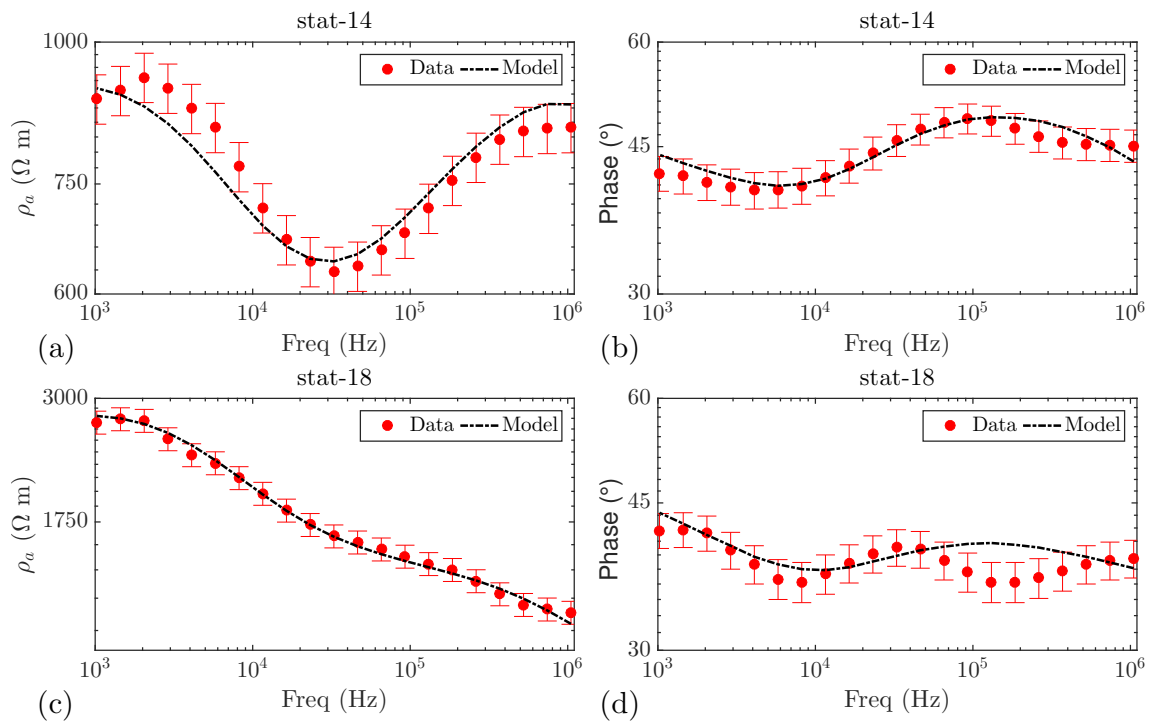


Figure 5.13: Data fit for two stations of the CSRMT data in Figure 5.6. The error bar in the figures are the error floor used in the inversion.

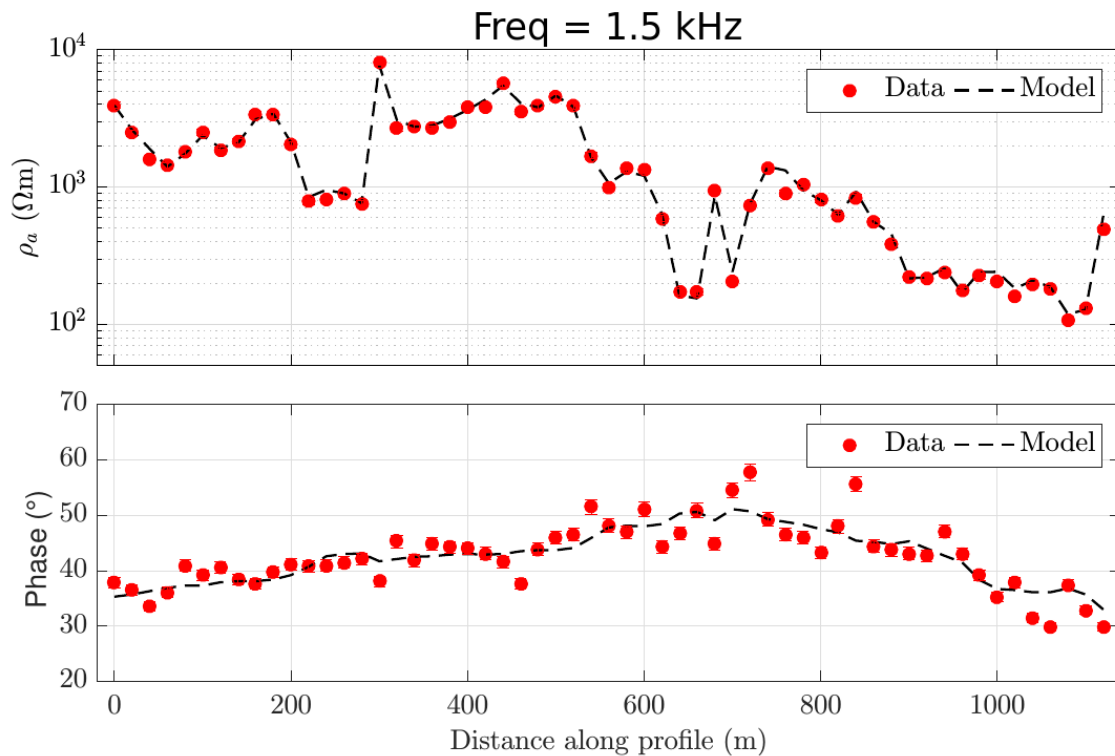


Figure 5.14: Data fit for frequency 1.5 kHz against the distance. The error bar in the figures are the error floor used in the inversion.

I carried out inversions with the `Rebbocc` to interpret the tipper data. The starting model is 100 Ωm halfspace with starting regularization parameter of $\log_{10} \lambda = 3$. The error floors used for the inversion were 5% of apparent resistivity, 2° of phase and 0.025 of tipper data. In order to have a balance of the data on the model fit, the numbers of the data on one input (TM, TE and tipper) are kept the same, since `Rebbocc` does not apply a “dynamic” weighting scheme as `MARE2DEM`.

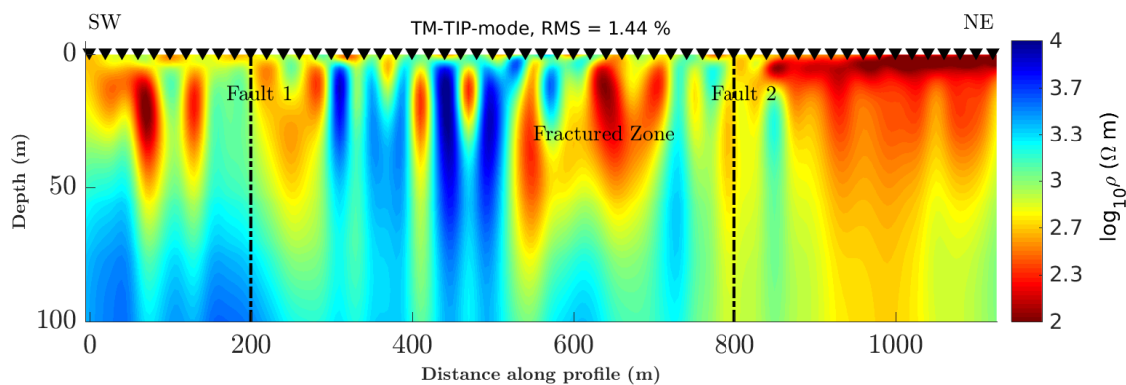


Figure 5.15: Inversion results of RMT data with `Rebbocc` including tipper data in the far field zone profile.

The result of the tipper inversion is given in Figure 5.15. I did not include the TE mode data since the TE mode data quality, however, is not as good as the TM mode data quality. The result of the tipper inversion is in agreement with the results of `Rund2Inv` as in Figure 5.12. The fit of the tipper data of real and imaginary parts in the far-field zone

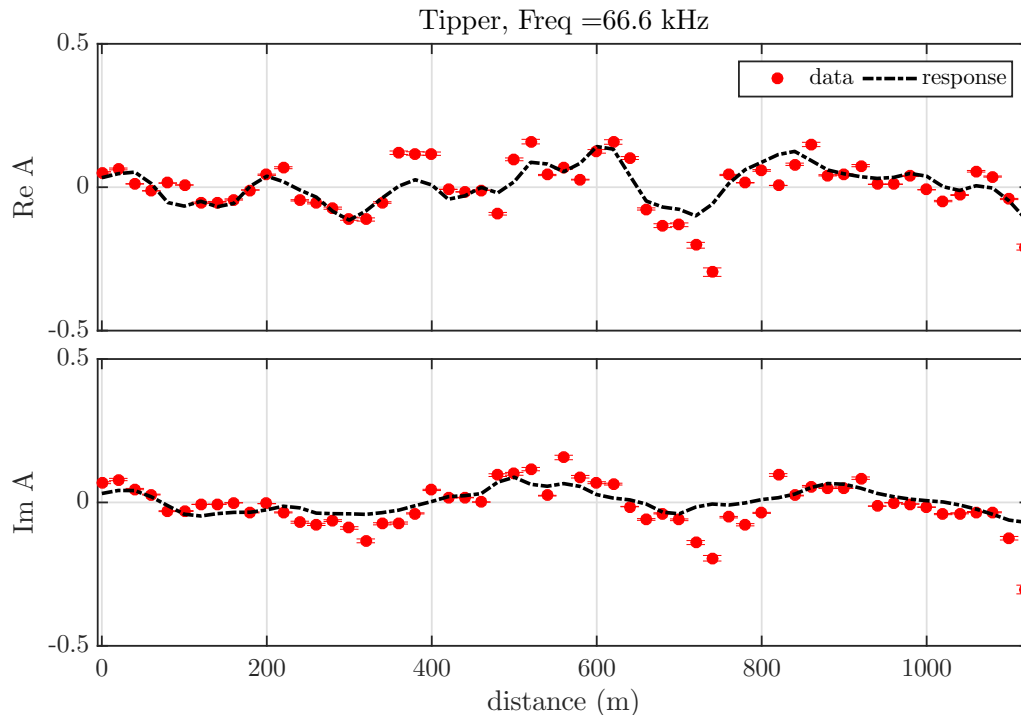


Figure 5.16: Data fit for tipper for selected frequency 66.6 kHz in the far field zone of the RMT data.

profile is given in Figure 5.16. The tipper data are well fitted, it means that the processing scheme (tipper estimation with the rotation) applied is working well on the “real” field data.

To complete the modelling, the inversion result of impedance data by taking into account the source (as well as the near field data) is given in Figure 5.17. The near field data are necessary to carry out this inversion, otherwise the result of the inversion will be wrong. However, the second fault from this inversion is not as pronounced as far field modelling with MT algorithm before.

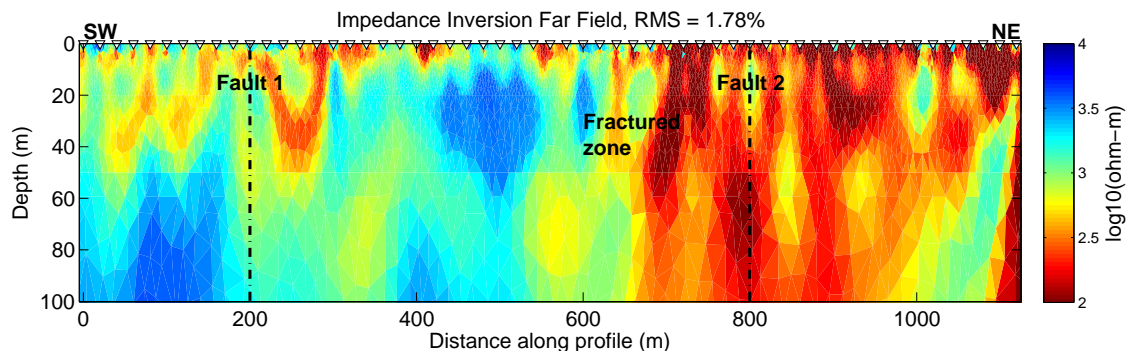


Figure 5.17: Inversion results of impedance CSRMT data with MARE2DEM including source in the far field zone profile.

As expected from the geological mapping of the faults, the 2D inversion shows lateral inhomogeneities in the resistivity at profile meters 200 and 800 m. However, the 2D inversion result also indicates a very clear high conductive fractured structure between profile

meter 500 and 700 m which were also visible on the transfer function. This buried structure was not known by the geologists and could not be mapped geologically. Moreover, the conductive structure after 800 m up to the end of far field profile also explains the jump on the observed impedance phase data. The data fit in Figure 5.13, Figure 5.14 and Figure 5.16 is also an indication that the observed CSRMT and RMT data were reliable and could be interpreted by means of 2D conductivity model.

5.4.2 The Near Field Zone

In the near-field zone, the data were treated separately, the RMT data were inverted with `Rund2Inv`, while the CSRMT data (impedance) were inverted with `MARE2DEM` and the tipper data were inverted with `Rebbocc`. The error floors used in the near field zone were the same as in the far field zone for the inversion with `Rund2Inv` and `Rebbocc`. In addition, the error floor of impedance is 10% of $\log_{10} Z_{yx}$.

First, the RMT data were inverted with different starting models and different regularization parameters with `Rund2Inv`. The L-curve for the inversions with different starting models is given in Figure 5.18.

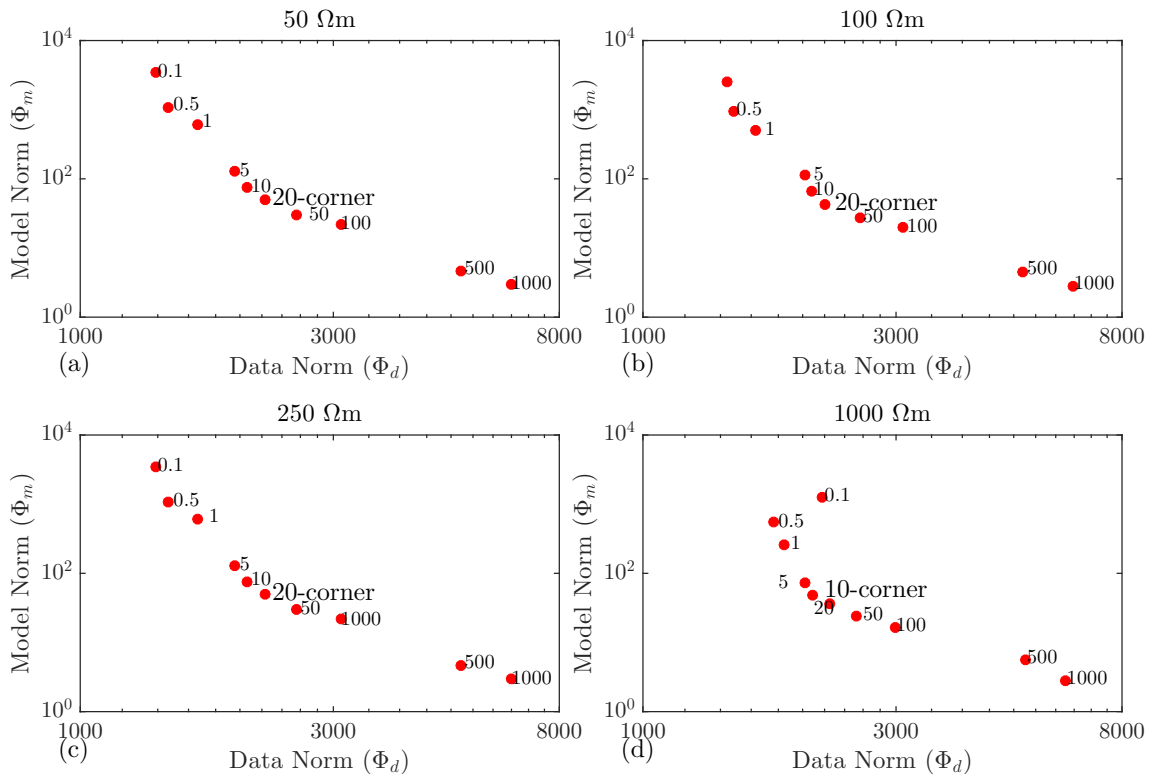


Figure 5.18: L curve of the inversion of RMT near field data for different starting models (a) $\rho_0 = 50 \Omega\text{m}$, (b) $\rho_0 = 100 \Omega\text{m}$, (c) $\rho_0 = 250 \Omega\text{m}$, and (d) $\rho_0 = 1000 \Omega\text{m}$. The optimal regularization parameter λ is marked for each curve.

As in the far field data case, the sensitivity and $2z^*$ were located in low sensitivity region. The inversion result of the RMT data with starting model of $100 \Omega\text{m}$ halfspace and $\lambda = 20$ is given by Figure 5.19.

There are 3 strategies to invert the impedance data in general: (i) a single inversion of the impedance data, (ii) a sequential inversion of the impedance data by taking the RMT

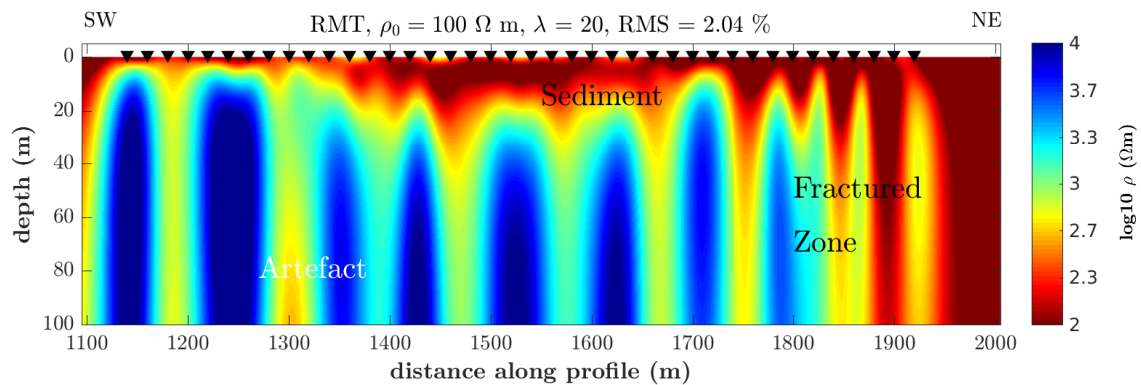


Figure 5.19: Inversion of the RMT data in the near field zone with the starting model of $\rho_0 = 100 \Omega \text{m}$ $\lambda = 20$.

model from the inversion result as the starting model and (iii) a joint inversion with the RMT data. The inversion result is given in Figure 5.20 for impedance CSRMT data only (by also taking into account the far field data which will be discussed later). The inversion result of near-field CSRMT data shows a quite good agreement with single inversion of RMT data with `Rund2Inv`.

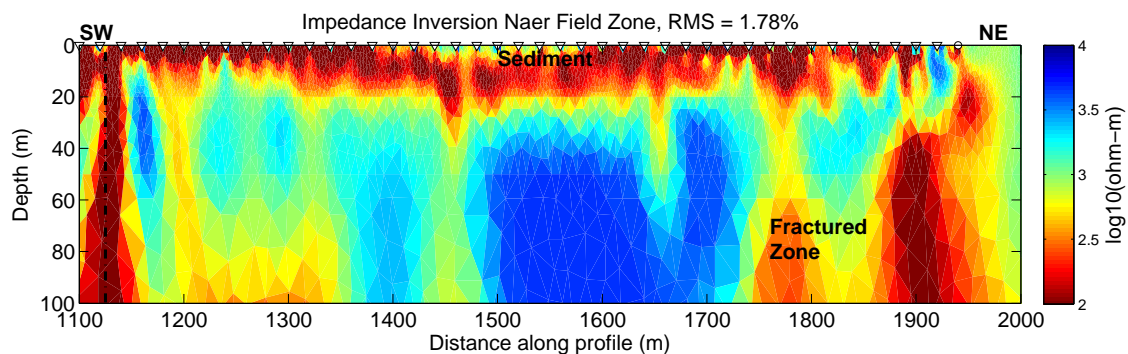


Figure 5.20: Inversion of CSRMT data in the near field zone with `MARE2DEM` the starting model $100 \Omega \text{m}$ halfspace with $w_{hv} = 1$.

The data fit for station 63 and 93 plotted against the frequency are given in Figure 5.21. The data fit of the selected frequency of 1.5 kHz are given in Figure 5.22. Note, the inversion with `MARE2DEM` including the source is using \log_{10} impedance, then the data fit is also shown in \log_{10} impedance.

We see in the inversion results of RMT and CSRMT data in the near field zone that a 2D structure is also expected. As on the far field zone for the tipper data, inversions with the `Rebbocc` were carried out. The starting model is $100 \Omega \text{m}$ halfspace with starting regularization parameter $\log_{10} \lambda = 3$. The result of TM and tipper data inversion is given in Figure 5.23.

The data fit for the model of TM mode, and tipper data was 1.79%. However, since the TE mode data quality is not as good as the TM mode data quality, therefore the TE mode data was discarded. The result is an agreement with the results of `Rund2Inv` and `MARE2DEM`. The fit of the tipper data of real and imaginary part are given in Figure 5.24.

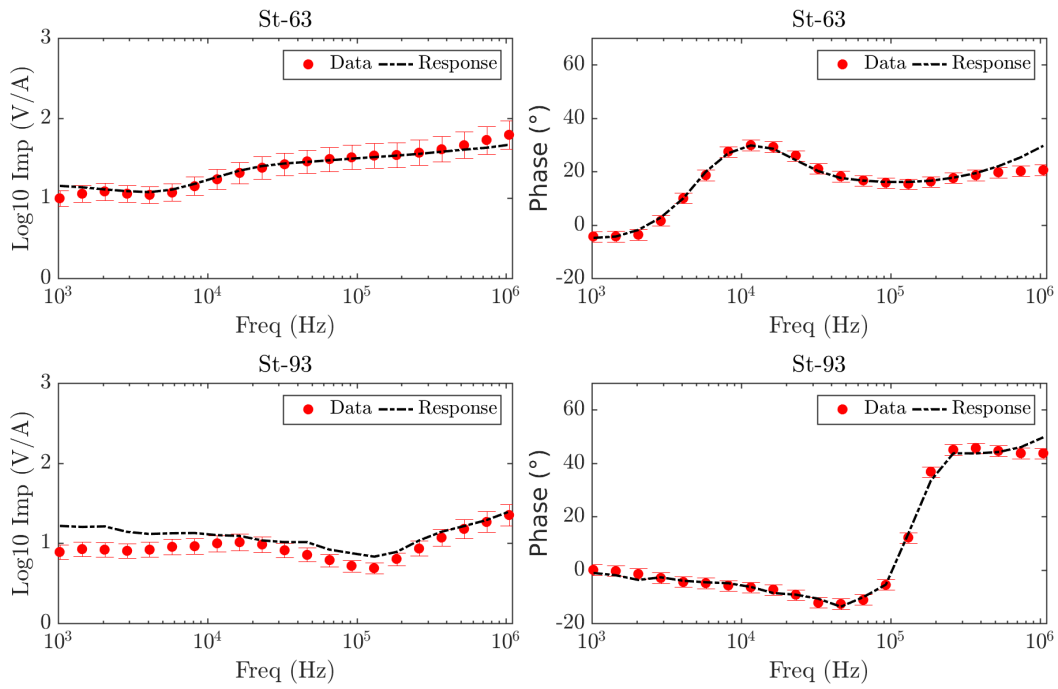


Figure 5.21: Data fitting for station 63 (offset 700 m) and 93 (offset 100 m) plotted against frequency.

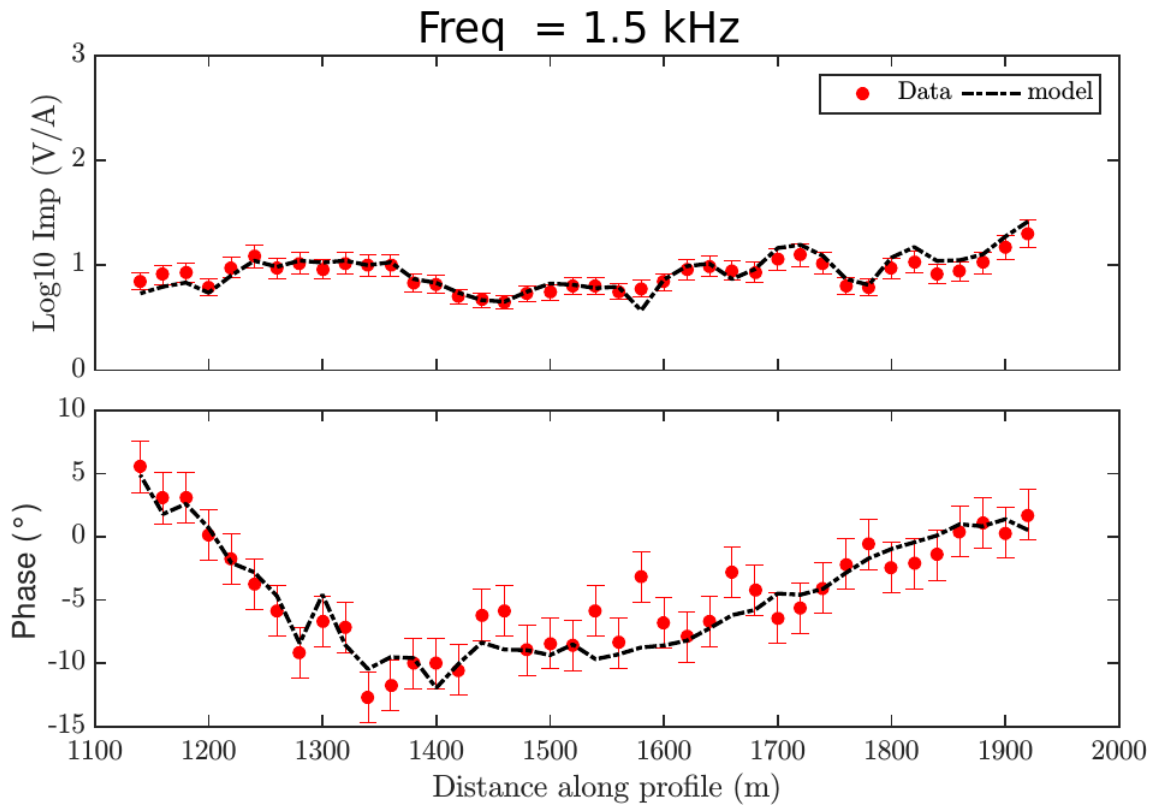


Figure 5.22: Data fit for frequency 1.5 kHz plotted against the distance.

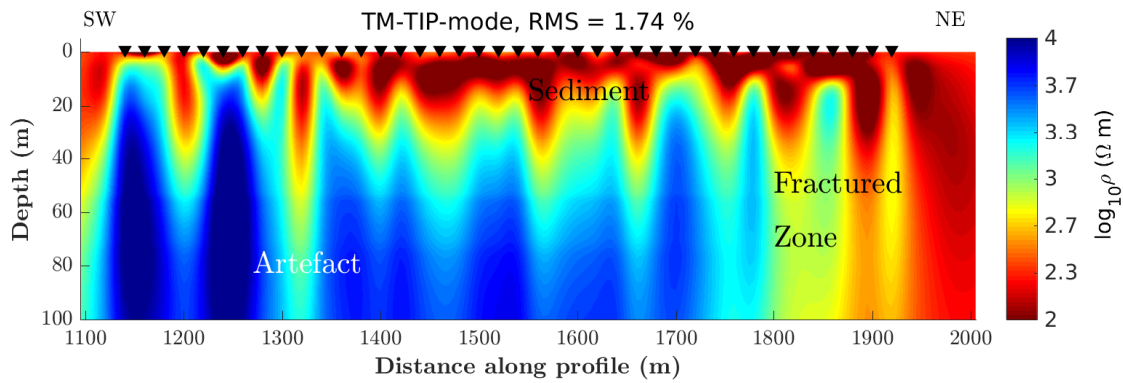


Figure 5.23: Inversion results of RMT data with `Rebbocc` including tipper data on the near field zone.

The tipper data are well fitted as one can see in Figure 5.24, it means that the processing scheme (tipper estimation with the rotation) applied is also working well in the near-field zone profile.

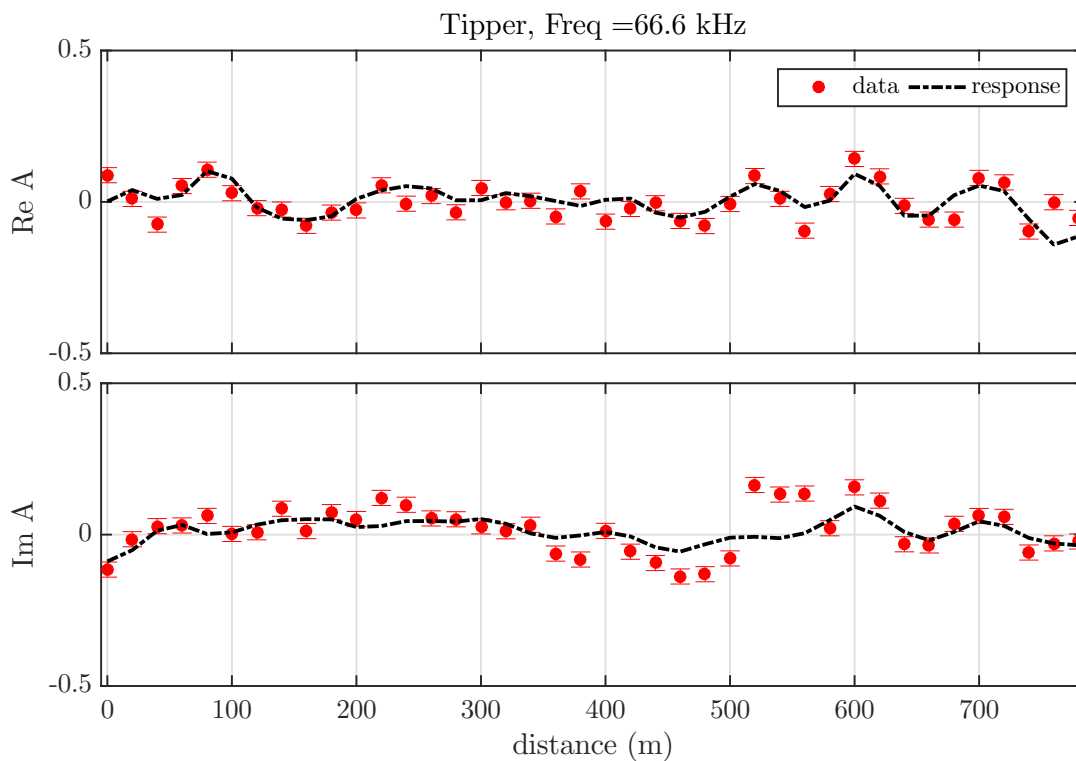


Figure 5.24: Data fit of tipper, frequency 66.6 kHz in the near field zone.

From the inversion results, the near-field zones are dominated by thin sediment with low resistivity of $40 - 100 \Omega\text{m}$. This, combined with low resistivity on the beginning of far field profile, might also be the reason why the far field zone begins quite early. It seems that the conductivity of the first layer has a dominant influence on the electromagnetic fields from the grounded electric dipole. From the inversion results, there are many resistive structures with a low sensitivity which might be just inversion artefact.

5.4.3 All zones impedance

The exact boundaries between the zones are vague than clear. It is hard to really determine the exact boundary between these field zones as shown in the processing of the field data in this chapter. The average resistivity is 800Ω , then by the condition that the far field zone starts at offset 5δ . In this case, all the stations should be affected by the near-field zone effect. However, the modified MARE2DEM opens an opportunity to neglect these zones by inverting the impedance data only by including the source as it has been shown for the synthetic data in Chapter 3.

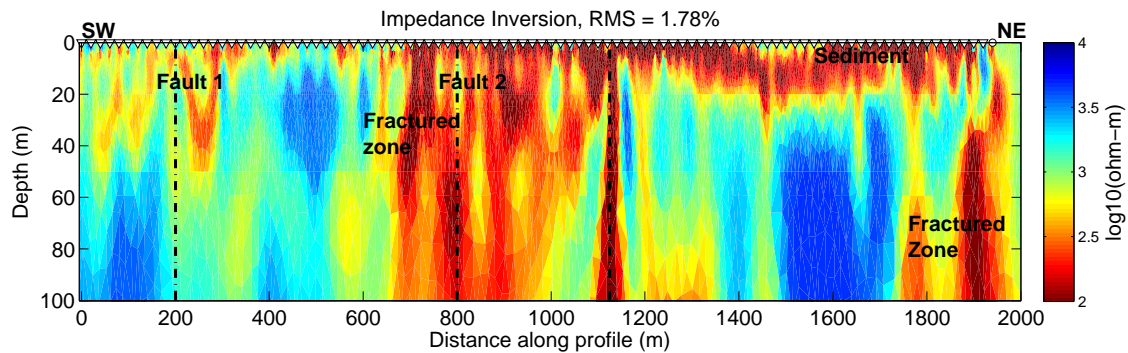


Figure 5.25: Impedance inversion of CSRMT data in the all field zone with MARE2DEM with starting model $1000 \Omega\text{m}$ halfspace $w_{hv} = 0.8$.

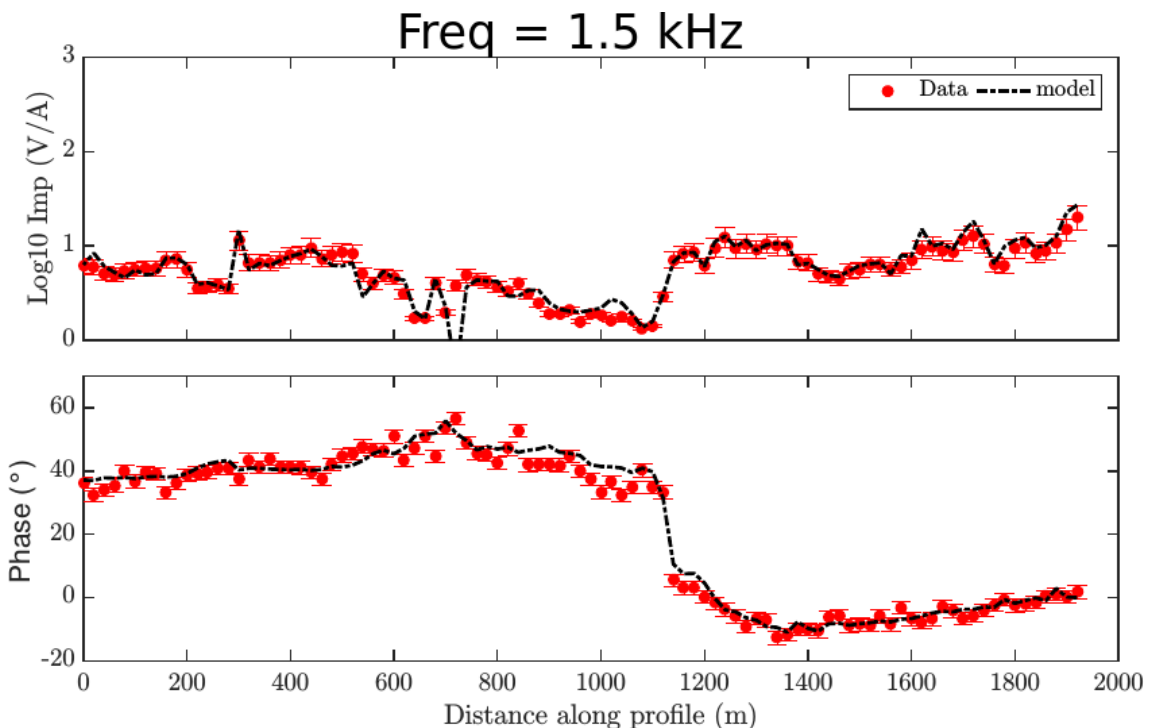


Figure 5.26: Data fit for frequency 1.5 kHz plotted against the distance in all zones considering the source.

The inversion is now extended from the near-field zone to the far field zone (97 stations). The setup is similar to the near-field zone inversion. The starting model is $1000 \Omega\text{m}$ and the optimal $w_{hv} = 0.8$. The results are given in Figure 5.25. It can be clearly

seen that the inversion result agree well with the near field and far field results before. The data fit for frequency 1.5 kHz along the profile is given in Figure 5.26. Note that to include the source on the far field data, a good background between transmitter and receiver should be correct, otherwise the results would be unreasonable (not shown). For this reason, the far field zone data (by assuming that the zones' boundary is known) should be interpreted with MT algorithm.

5.5 Discussion

We have a successful CSRMT measurement in Vuoksa region Russia. The data observed from 1 - 1000 kHz were smooth along the profile in all zones that indicate the reliability of the CSRMT method. The 2D modelling of the CSRMT data in the far-field zone show the location of the buried faults as expected and show a good agreement with the conventional RMT data. Furthermore, another fault in the far-field zone was also detected which cannot be mapped geologically. The data measured in the near-field zone were also successfully modelled and interpreted with 2D conductivity structure. The 2D structures on the survey area also allow us to process the tipper data from the RMT method. The tipper data were also successfully interpreted by means of 2D conductivity model. In general, the 2D conductivity model derived from all zones can explain the near-field data, far field data and tipper data.

The exact boundary locations of the field zones are somehow hard to find with the conventional method. The simplest method is to plot the lowest frequency along the profile and to compare every CSRMT sounding to the RMT sounding when the RMT data are available.

The study showed that the CSRMT technique, which uses an electric dipole as a transmitter and only injects 4 base frequencies, is a powerful near-surface geophysics method. The extended frequency range to lower frequencies enables a larger penetration depth than the conventional RMT method. The CSRMT method does not depend on the direction of the transmitter, a big advantage in comparison to the RMT method. The profile direction can be chosen according to the geological strike direction. The method can also be used in remote areas where no or fewer transmitters are available.

Chapter 6

Field Measurements: Krauthausen Area, Germany

6.1 Introduction

The second field measurement of CSRMT was carried out in Krauthausen test area (located around 10 km northwest of the city of Düren), Germany. The objective of the experiment is to study the conductivity distribution in a hydrogeological test area with the CSRMT method. The survey area (the location of the receivers) has been studied intensively by many geophysical methods, for example velocity of groundwater measurement (Englert, 2003), direct current (Gössling, 2004), radiomagnetotelluric (Nix, 2005), aquifer hydraulic conductivity estimation from surface geoelectrical measurements (Niwas et al., 2011) and hydraulic conductivity from spectral IP measurement (Hördt et al., 2007) as well as time domain IP (Langenbach, 2017). The results from the previous DC and RMT measurements, the survey area has a more conductive layer (from 6 up to 20 m) than the upper layer (below 6 m), see Table 6.1 for details. The geology of the test area shows a roughly one-dimensional conductivity structure.

Table 6.1: Compilation of the average resistivity from previous DC and EM measurements. The $\bar{\rho}$ is calculated after Spies (1989), with the maximum depth of penetration derived from various method is assumed 20 m, after Langenbach (2017).

	d_1	ρ_1	d_2	ρ_2	d_3	ρ_3	d_4	ρ_4	$\bar{\rho}$
Gössling (2004)	0	60	1	400	3	60			60
Nix (2005)	0	40	2	> 120	6	25			30
Blaschek (2006)	0	60	1	500	5	80			90
Hördt et al. (2007)	0	100	1.5	560	3	140	10	70	90
Langenbach (2017)	0	60-100	1.25	350-500	4	150	10.6	40	70

Unfortunately, there are many nearby cultural noise sources around the test area which is a typical situation in Germany. On the west side, there are railways and powerlines, while on the south side there is a power plant, and some pipelines are also located on the east side. The buried pipeline, which connected the transmitter to the receivers, was known after analyzing the measured data. There was no sign and information the

presence of the buried pipeline near the receiver site to the transmitter site. The time series on the test area is not affected by the pipeline since there is no strange behaviour on the time series as shown by Escalas et al. (2013). But the effect of this buried pipeline on the CSRMT experiment was current channelling, where the current density flows in the pipeline direction and making the pipeline as the “extended” source. In this case, the theoretical far-field zone was shifted to the near-field zone. As a result, the CSRMT data were not suitable for inversion with MT algorithm, but the data should be inverted with MARE2DEM.

This chapter is organized as follows. First, the survey design is introduced, then the raw data and processing are given. Afterwards, the modelling of the classical MT algorithm is presented. Since the classical approach fails to explain the CSRMT data, a qualitative modelling study is needed by taking the pipeline as the transmitter that shifts the field zones. Afterwards, the quantitative modelling with MARE2DEM is discussed. Finally, I will give the conclusion of the survey.

6.2 Survey Design and Geological Setting



Figure 6.1: Krauthausen location and field setup. The perpendicular dipole is located at around 1.5 km from the test site (yellow box). (Google, 2018)

The Krauthausen test site is located in the southern part of the Lower Rhine Embayment, Germany and operated by the Agrosphere, ICG-IV, Forschungszentrum Jülich (FJZ), Germany (Figure 6.1). It is located approximately 10 km northwest of the city of

Düren, 7 km southeast from the FZJ and has a dimension of 200×70 m. The topography of the area is flat as shown in Figure 6.2.



Figure 6.2: The Krauthausen test site area during the survey. Photos by Imamal Muttaqien.

The CSRMT measurements in Krauthausen area were carried out at the beginning of June 2016. Two perpendicular dipoles which share a common centre point were placed around 1.5 km from the test site as shown in Figure 6.1. The average resistivity of the survey area is $90 \Omega\text{m}$. When considering such a case, the far-field zone should begin at around 800 m from the source according to Zonge and Huges (1991). Both of the dipoles were not symmetric. The inline dipole (NW - SE) was 125 m (NW arm) and 250 m (SE arm), while the broadside dipole (SW-NE) was 250 m (SW arm), and 125 m (NE arm). By having two perpendicular dipoles, tensor CSRMT measurements can be realized. The inline dipole, with NW-SE as our x direction, would give xy polarizations, while the broadside dipole would give yx polarizations. The grounding for both dipoles were around 50Ω . As a result, high currents could be injected and are given in Table 6.2.

Table 6.2: Current injected during CSRMT measurements in Krauthausen, Germany

Main freq (kHz)	Inline (A)	Broadside (A)	Band
0.5	4.5	4.2	D1
5	4	3.9	D2
50	2	2	D4
105	0.9	0.8	D4

Since the dipoles share a common middle point, the inline dipole was first used, and after all the stations were measured, the inline dipole was disassembled. Afterwards, the broadside dipole was built, switched on and then disassembled. This procedure is to make sure that we did not mess up with the connections of the transmitter. In the receivers' site, three profiles were measured as shown Figure 6.3. Due to bad weather during the measurements, profile 1 has only 11 stations while profile 2 and 3 have 21 stations. The pipeline (blue line) was found after analyzing the CSRMT data.

The geology of the surface area is shown in Figure 6.4. The rough structure consists of an approximately 9 m thick aquifer, with the base starting from approximately 11 m,

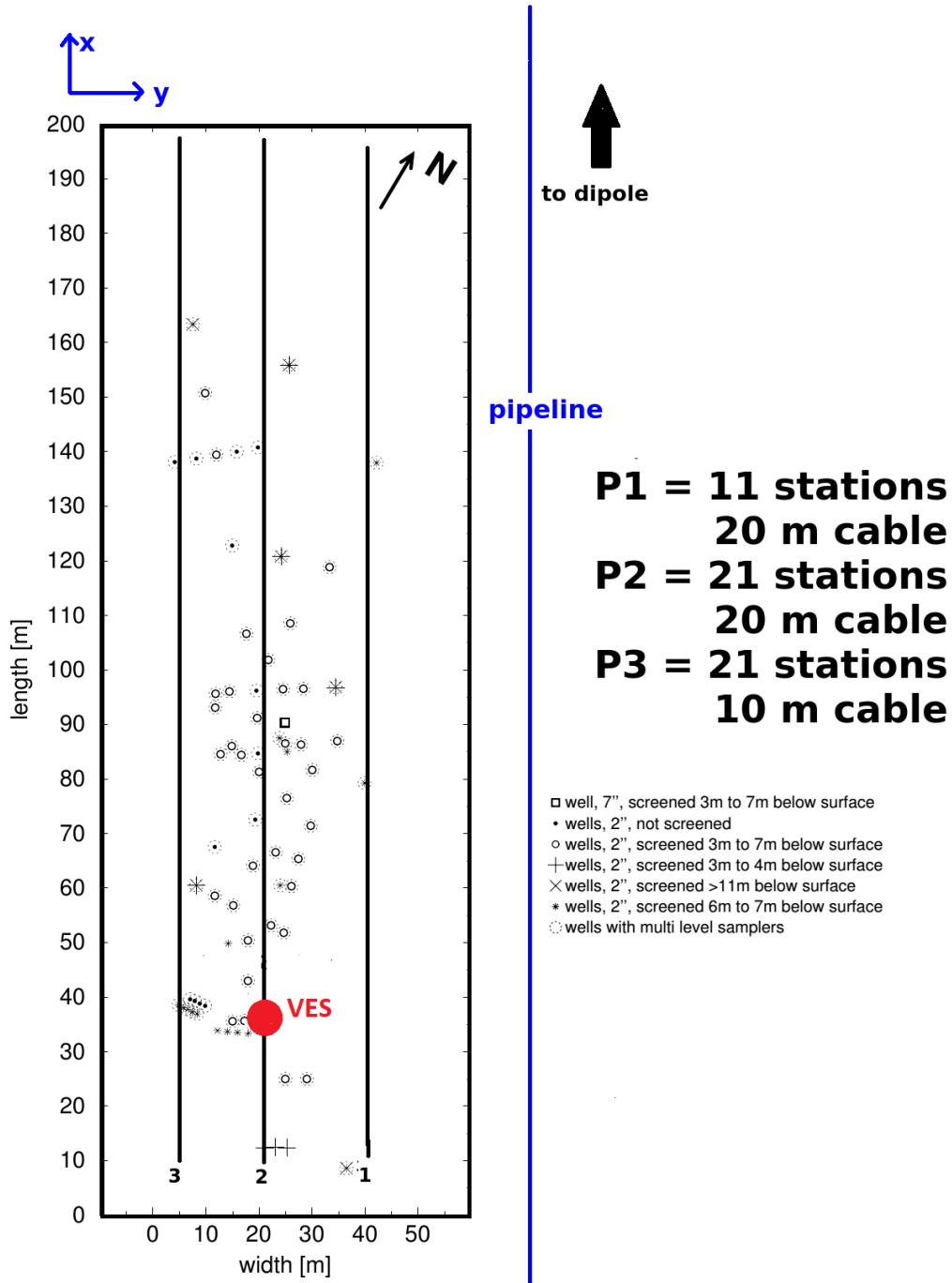


Figure 6.3: Simplified sketch of the receiver site, modified from Englert (2003). Note that the pipeline was found after analyzing the data. The distance between the profiles to the pipeline are 15, 25 and 35 m. The location of VES sounding is on the profile 2 at 40 m.

and a surface soil layer above. The aquifer is characterized by different layers of sand and gravel corresponding to Rur sediments, partly exhibiting a non-uniform grain size distribution. A clay layer at approximately 11 m depth forms the base of the aquifer, followed by fine sands corresponding to Upper Rhine sediments.

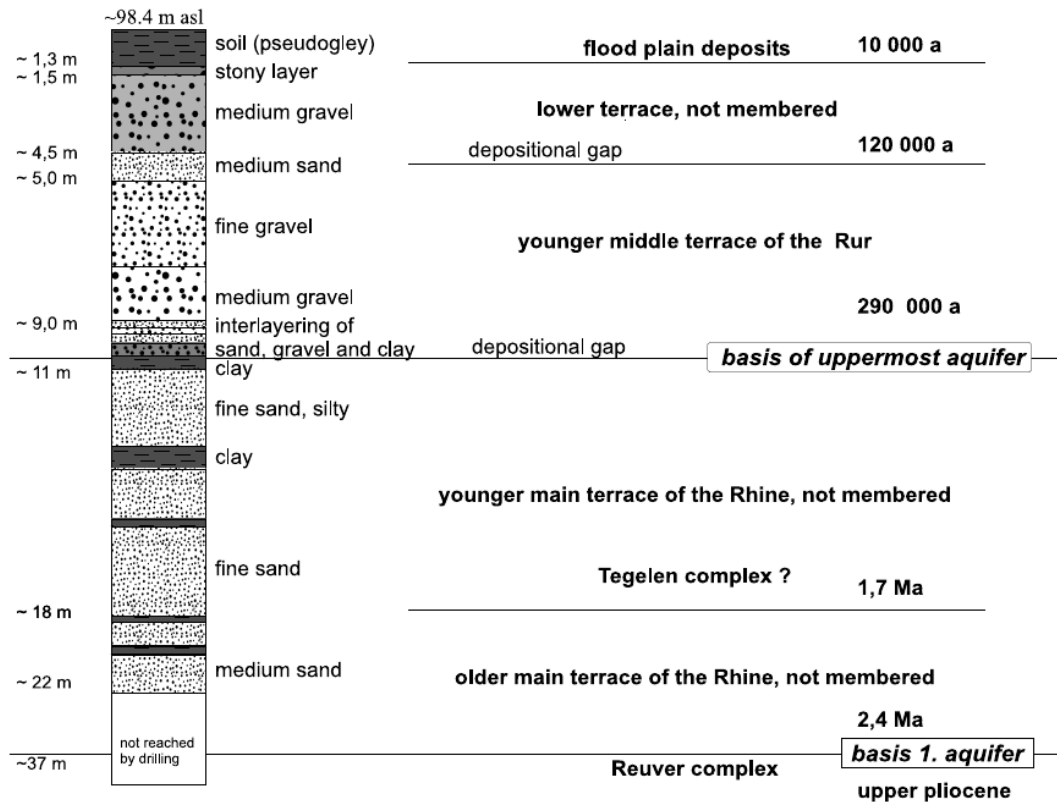


Figure 6.4: Lithology of Krauthausen test site, taken from Englert (2003)

6.3 Raw Data and Processing

The measured CSRMT and RMT time series data were processed with the algorithm described in Chapter 4. First, the spectra were calculated in SM25M software. Afterwards the impedance was estimated in SFA with scalar calculation, and finally, the Siegel's repeated median estimation was applied to get smooth curves of apparent resistivity and phase. The calculated spectra and derived impedances are discussed in the following paragraphs. In the processing I only estimate the data with SFA, the estimations are comparable with the SM25M.

As stated before, the far field zone should start at a distance of 800 m from the transmitter. The distance between the common point of our deployed perpendicular transmitter to the receiver test site is around 1.5 km. In this survey design, our CSRMT receivers were located in the far field zones. Thus the sounding curves of CSRMT data and RMT data have to be similar in magnitude in their corresponding polarizations (the TM and TE modes). The perpendicular dipole would give two different polarizations. However, the measured CSRMT data do not show the expected behaviour.

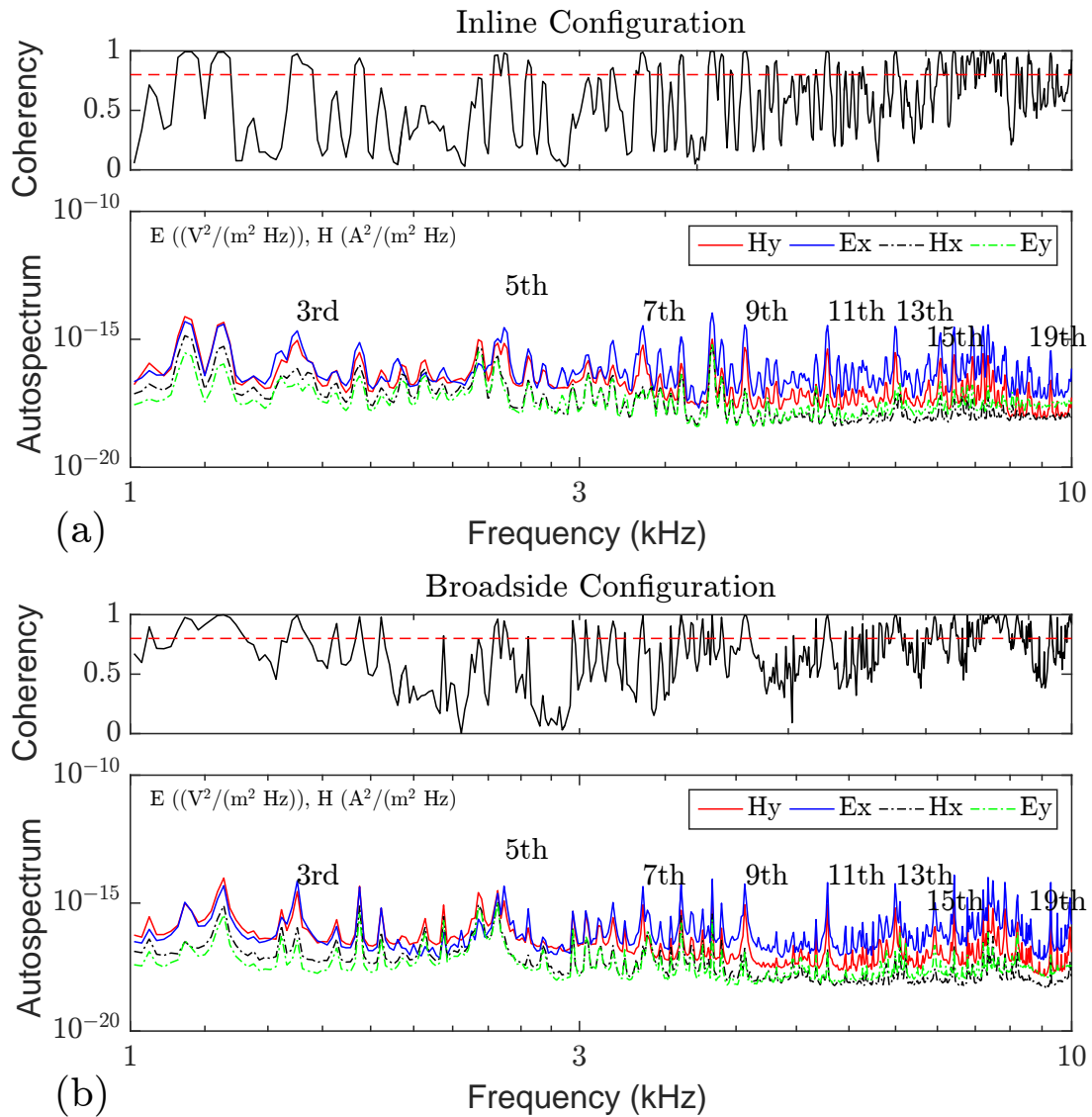


Figure 6.5: Autospectra for (a) inline and (b) broadside configuration for station 1 in the second profile.

First, only one polarization is observed in the spectra (Figure 6.5). As a result, the apparent resistivity and impedance phase from the CSRMT transmitter derived from the observed spectra were in one polarization only. Figure 6.6(a)(b) show the distribution of CSRMT frequencies observed in all stations of profile 2 (this situation is also on profile 1 and 3) for inline configuration (Figure 6.6(a)) and broadside configuration (Figure 6.6(b)). These distributions were calculated from the spectra of Figure 6.5. The observed electromagnetic fields from the inline and broadside configurations were on the same polarization (xy) which is different from the theory and the survey design. The inline configuration should be observed in polarization 1 (xy), and the broadside configuration should be observed in polarization 2 (yx). The apparent resistivity and phase derived from the spectra of Figure 6.5 were given in Figure 6.6(c)(d).

Second, since theoretically the receiver side is located in the far field zone. The CSRMT data should be comparable both in magnitude and trend with the RMT data as our experience in Russia (Chapter 5) and also shown by Saraev et al. (2017). Unfortu-

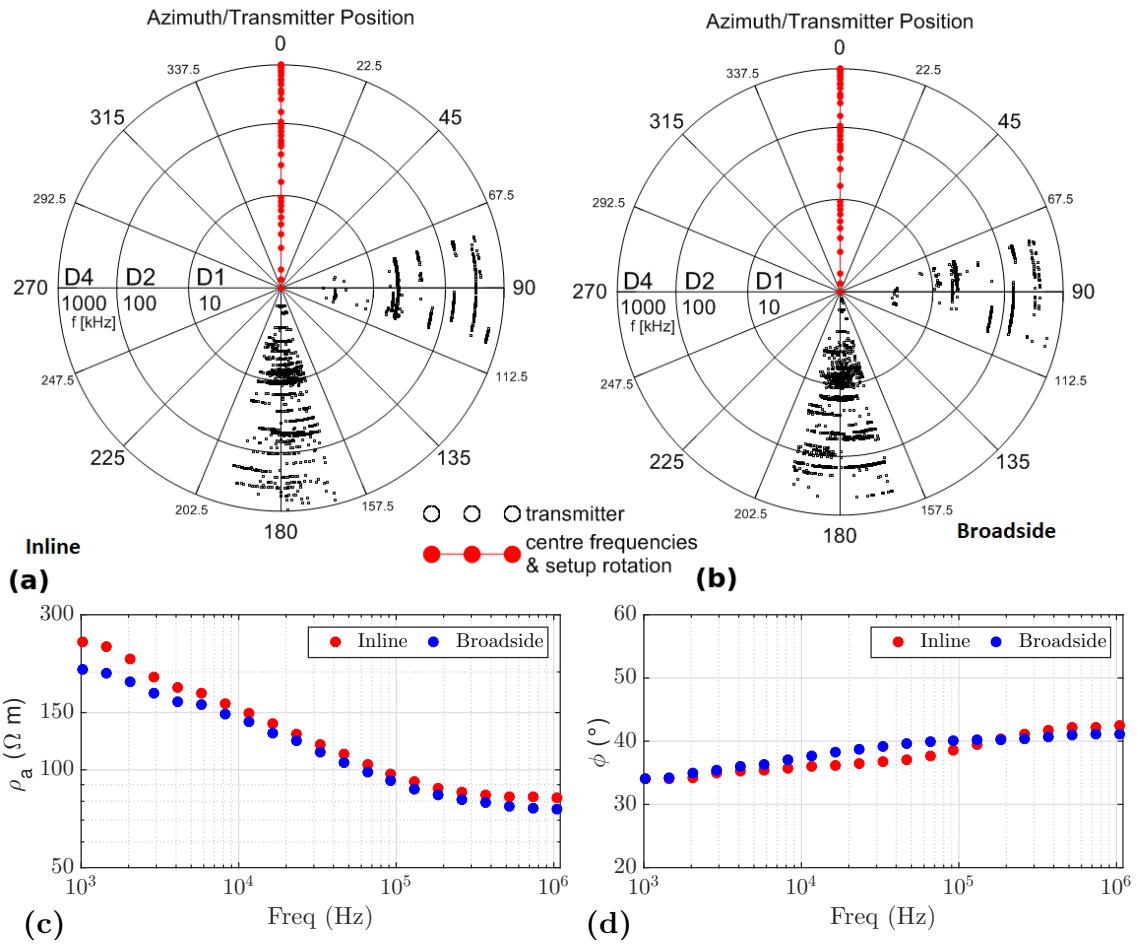


Figure 6.6: (a) Azimuth distribution of data from inline transmitter, (b) azimuth distribution of data from broadside transmitter. Most of the data from both transmitter were observed from 157.5 – 202.5° which is defined for polarization 1. (c) Apparent resistivity, (d) impedance phase of CSRMT data from inline and broadside transmitter derived from the spectra in Figure 6.5.

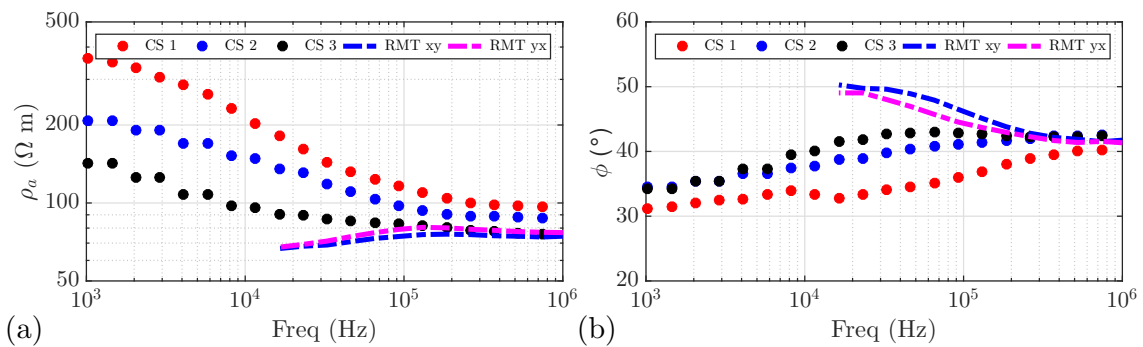


Figure 6.7: (a) Apparent resistivity, (b) impedance phase for CSRMT data from all profiles plotted with RMT data.

nately, this situation is not the case and is getting much worse since the behaviour also varies on the different parallel profile as shown in Figure 6.7. The CSRMT data show a typical near-field transition zone data behaviour of a broadside configuration. The observed RMT data on both polarization are in agreement with the RMT survey of Nix (2005), and other previous geophysical EM methods are given in Table 6.1. Inverting both CSRMT and RMT data sets with the MT algorithms (for example `Rund2Inv` or `Rebbocc`) would result in different conductivity models (especially for the depth > 6 m). Note that for the CSRMT method, since the inline and broadside data were observed on the same polarization, the final transfer functions are the average of the two.

6.4 Additional Measurement

After analyzing the data, two additional experiments were carried out in order to fully understand the phenomenon of the measured CSRMT data. First measurements were conducted by using cable locator to locate the conductive structure. The second measurement was VES sounding at one point to see the general conductivity distribution in the survey area.

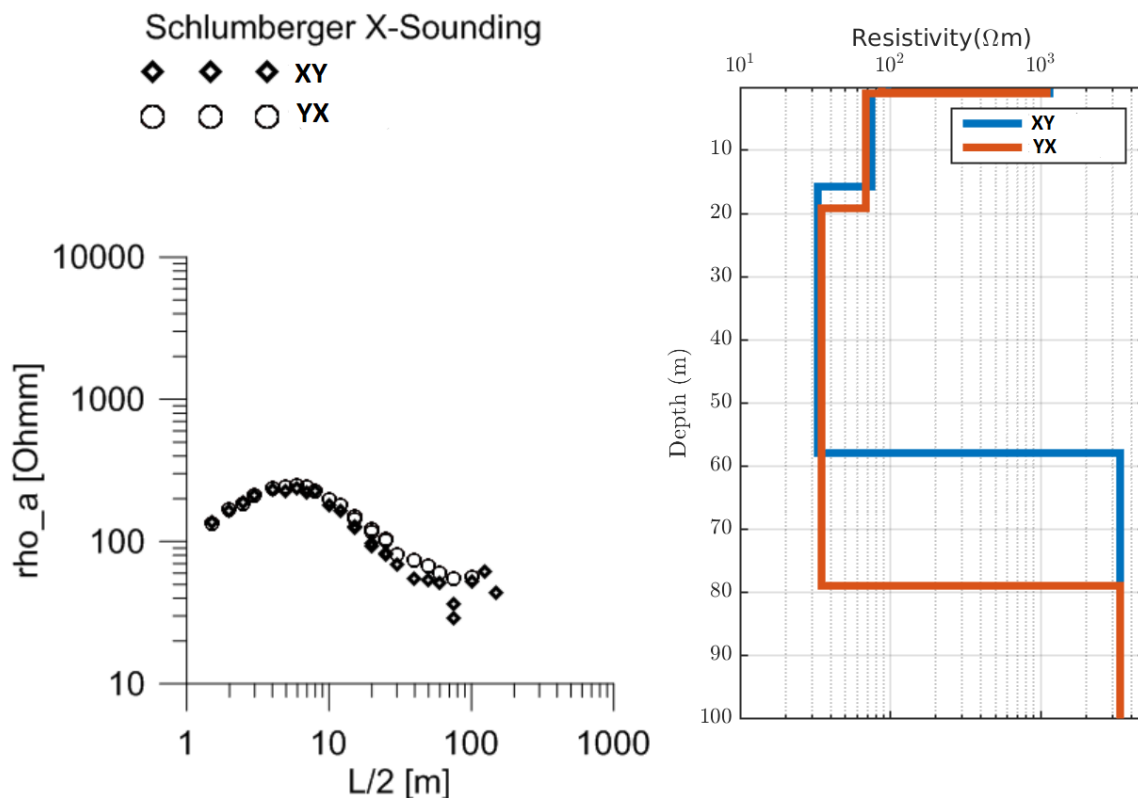


Figure 6.8: The measured VES data (left) and 1D inversion of the data (right)

The cable locator measurement was conducted from the receiver site to the transmitter site. It was found that there is continued positive anomaly from the transmitter to the receiver (or vice versa). The VES measurement (Figure 6.8) at one point on the second profile confirmed that the lower layer (> 6 m) is more conductive than the upper layer (0–6 m) and is also in agreement with the RMT measurement.

6.5 Modelling

6.5.1 Inversion of Both Data Sets

To start with modelling, first, the observed CSRMT and RMT data are inverted with Rund2Inv. For comparison, both data set were inverted in the TM mode. The optimal regularization parameter was sought by the L-curve criterion given in Figure 6.9 for the CSRMT data and in Figure 6.10 for the RMT data. The starting models for both data set are 10, 20, 50 and 100 Ωm .

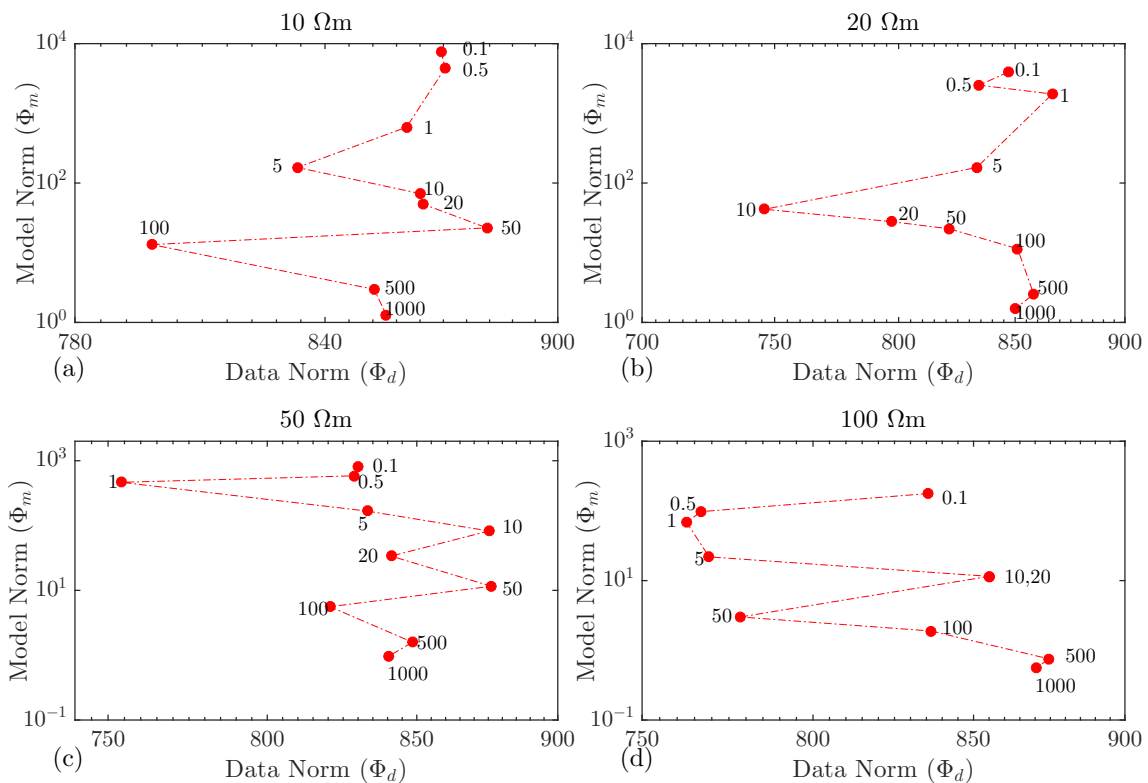


Figure 6.9: L curve for CSRMT data with different starting model (a) 10 Ωm , (b) 20 Ωm , (c) 50 Ωm , (d) 100 Ωm . The optimal regularization parameter for each starting model is hard to find due to a high oscillation.

The L-curves in the CSRMT data shows oscillatory behaviour as discussed in Chapter 3. Choosing “corner” for optimal regularization parameter becomes more difficult. For the RMT data, the corners can be better distinguished than the CSRMT data. For interpretation, the starting model of 50 Ωm and $\lambda = 20$ is chosen for both CSRMT and RMT data. The RMS for CSRMT data is 1.02 % and for RMT data is 0.97 %. In this case, both data sets are well fitted.

However, the results of the inversions from CSRMT and RMT data in profile 2 shown in Figure 6.11 are totally opposite in the lower layer (> 8 m) as already indicated in the measured data. This profile is chosen since the setup was maximum in terms of electric antennae length and stations spacing and also the VES sounding was carried out in this profile. The most prominent difference between the models was observed in profile 1, and the smallest was in profile 3 like already seen in the measured data. The RMT models were consistent with the previous geophysical electromagnetic surveys in the test site

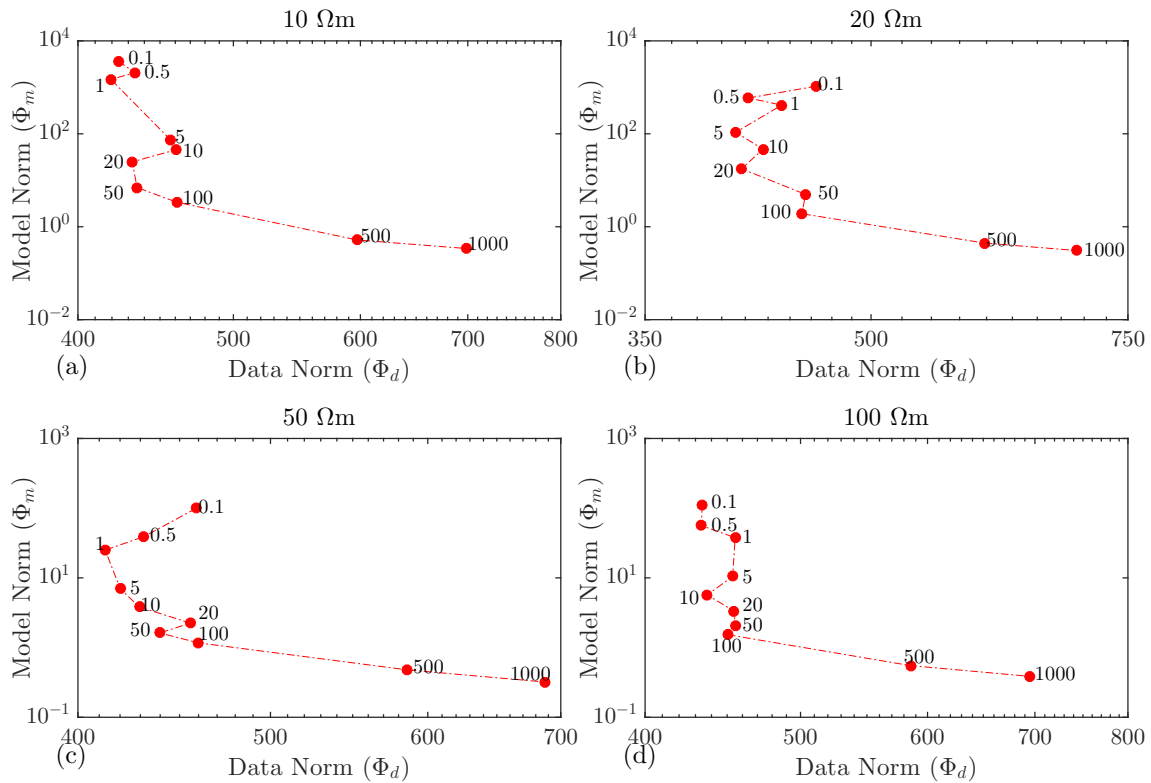


Figure 6.10: L curve for RMT data with different starting model (a) 10 Ωm , (b) 20 Ωm , (c) 50 Ωm , (d) 100 Ωm . The optimal regularization parameter for each starting model is quite hard to find due to a small oscillation.

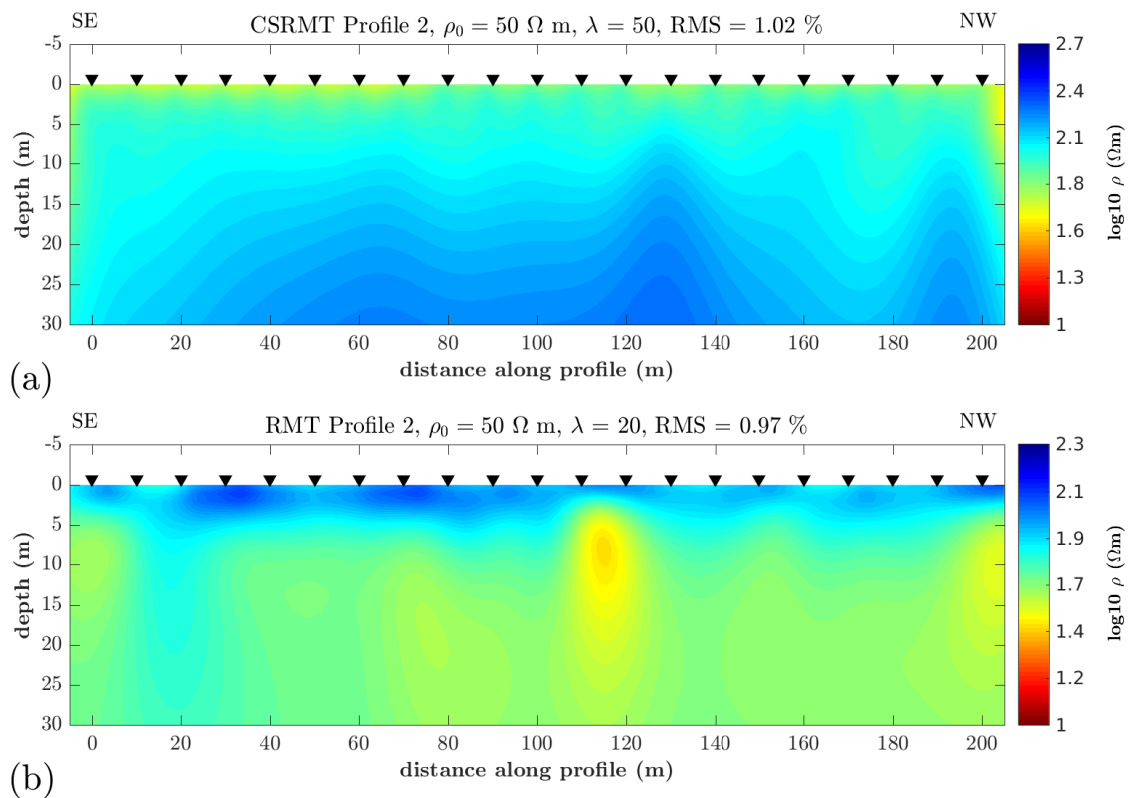


Figure 6.11: Inversion result of (a) CSRMT and (b) RMT data for profile 2. Note on different color scale used in both models. The inversion from the CSRMT data show a more resistive structure while the inversion from the RMT data show a more conductive structure.

with some variations in the upper layer as tabulated in Table 6.1. The results from the RMT data show a conductive structure in the lower layer (8 – 20 m), while the CSRMT models have a more resistive lower layer (from 8 – 20 m) with different resistivity values depending on the profile.

The 2D inversion of RMT data is a plausible result, but the 2D inversion of the CSRMT data with `Rund2Inv` (or other MT algorithm) is unlikely true since the latter results contradict the geological structure and all previous geophysical surveys. To summarize of the inversion with `Rund2Inv`, the results of the inversion of both data sets are given in the Table 6.3.

Table 6.3: Compilation of the average resistivity from the inversion of RMT data and CSRMT data inverted with MT algorithm. The CSRMT models are not consistent with previous studies and geology.

	d_1	ρ_1	d_2	ρ_2	d_3	ρ_3	d_4	ρ_4	d_5	ρ_5
RMT 1	0	60	6	80	10	40				
RMT 2	0	70	4	80	10	50				
RMT 3	0	70-80	4	85	10	50				
CSRMT 1	0	60-80	4	90-120	12	200-400	32	300-400	80	> 500
CSRMT 2	0	87-97	6	100-115	10	120-190	30	200	40	> 300
CSRMT 3	0	70-80	4	90-110	8	90	11.2	120	36	> 200

6.5.2 3D Forward Modelling Study

The aim of the 3D modelling is to show qualitatively (due to unknown conductivity of the pipeline, its depth and size) that RMT data are not (or just very little) affected by the presence of the pipeline and to show how the pipeline affected the CSRMT data and to explain the phenomena observed in the CSRMT data. This 3D forward modelling study is carried out with `SLDME3f` for both RMT and CSRMT data. The first attempt is to include the pipeline in the forward modelling of the measured RMT and CSRMT data given by Figure 6.12. The conductivity of the pipeline is taken to be 10000 S/m^1 , has a dimension $1 \times 1 \text{ m}$, 4 km long and located on $z = 1 \text{ m}$ depth. The conductivity structure is taken from the VES (Figure 6.8) and the RMT data in Table 6.3.

The results of the RMT modelling by taking into account the pipeline is shown in Figure 6.13. From the modelling study, the presence of the pipeline does not have any effect on the RMT data on both polarizations. Thus the RMT data can be directly interpreted with `Rund2Inv` (or any MT inversion software). The electromagnetic fields generated by distant radio transmitters are not channelled through the pipeline.

The results of the CSRMT data modelling including the pipeline is shown in Figure 6.14. It is clear that the CSRMT data were affected by the pipeline since the pipeline is connecting the transmitter to the receiver site. However, the inclusion of the pipeline in the modelling could not explain the polarization problem and also could not fit the measured data. Remember that the measured data on broadside configuration was not observed on yx polarization.

¹This value is only an approximation with a higher value, and the true value is unknown.

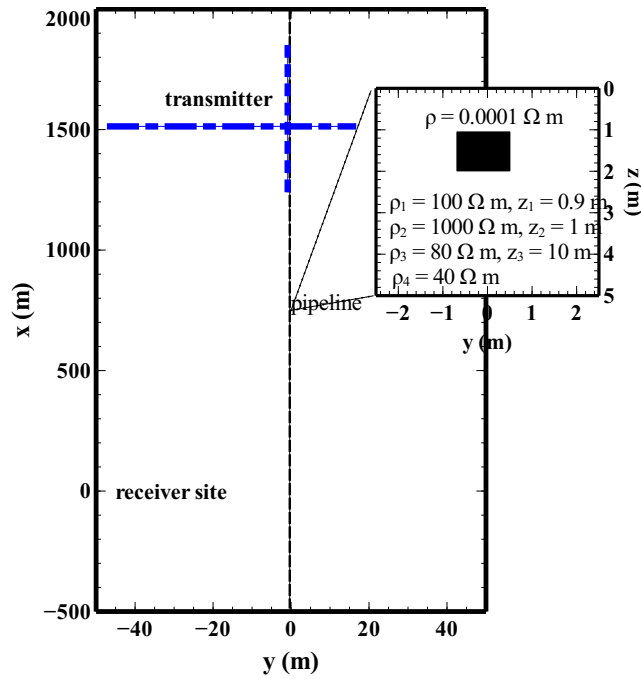


Figure 6.12: Simplified pipeline modelling of the observed data. Note that for extended dipole, the pipeline acts as transmitter

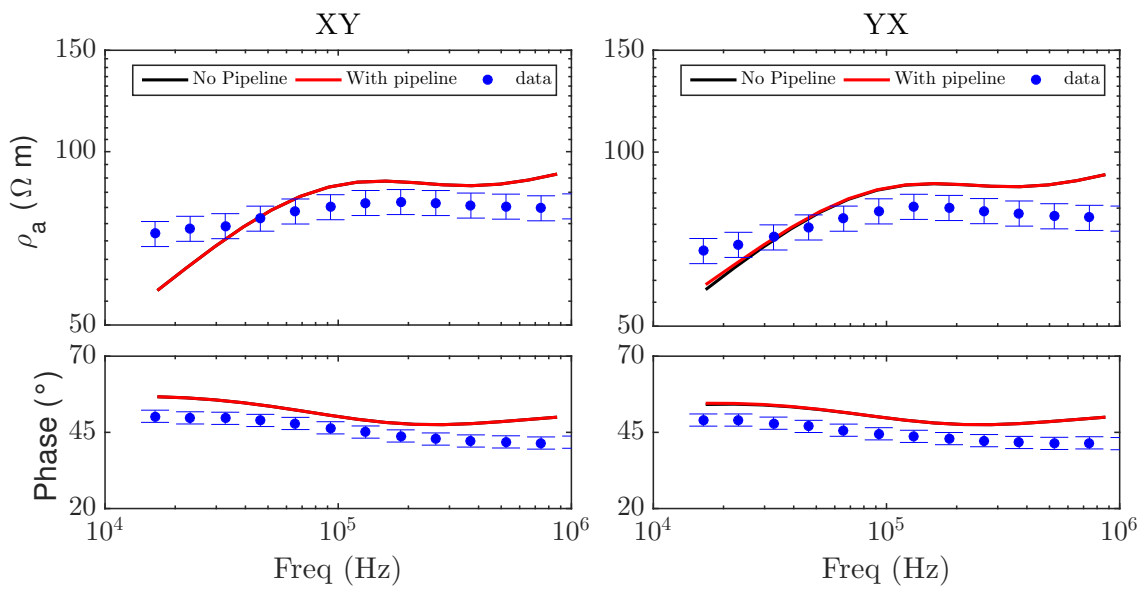


Figure 6.13: RMT data fit by considering the presence of the pipeline. Note that the data are almost not affected on both polarizations.

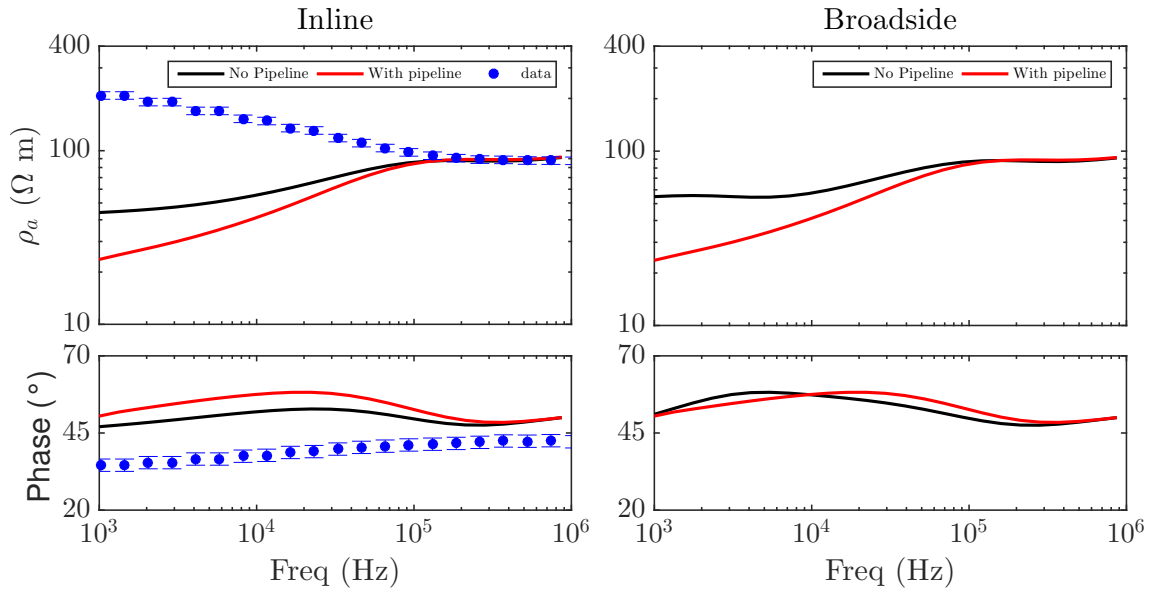


Figure 6.14: CSRMT data modelling by considering the presence of the pipeline. The data can not be fitted and the problem of mixing polarizations can not be explained.

After analyzing carefully the measured data and the fact that there exists long active pipeline which turns out to channel the injected current from both perpendicular transmitters. The pipeline should be treated as our “shifted” transmitter. By considering the pipeline as our transmitter in $-x$ direction (towards the north-west) only explains why only one polarization observed from two perpendicular transmitters. In this “shifted” transmitter phenomenon, a standard CSEM processing would fail. One could not normalize the measured electric field to the dipole moment of the transmitter since now the exact transmitter length is unknown. Then the modelling of the data would also lead to a wrong conductivity model. The distance between the pipeline and the profiles are 15, 25 and 35 m for profile 1, 2, and 3 respectively. It means that our receivers were located in the near-field zone. As a result, the measured CSRMT data were not suitable to be interpreted with the MT inversion algorithm as shown before in Figure 6.11 but they must be inverted with MARE2DEM.

Once considering the pipeline as extended dipole and taking the 1D conductivity model from RMT data, the CSRMT data are also well fitted as shown in Figure 6.15 for profile 1 (top), for profile 2 (middle) and profile 3 (bottom). Qualitatively, the measured data could be well explained by the current channelling phenomenon. The quantitative modelling is discussed in the next section.

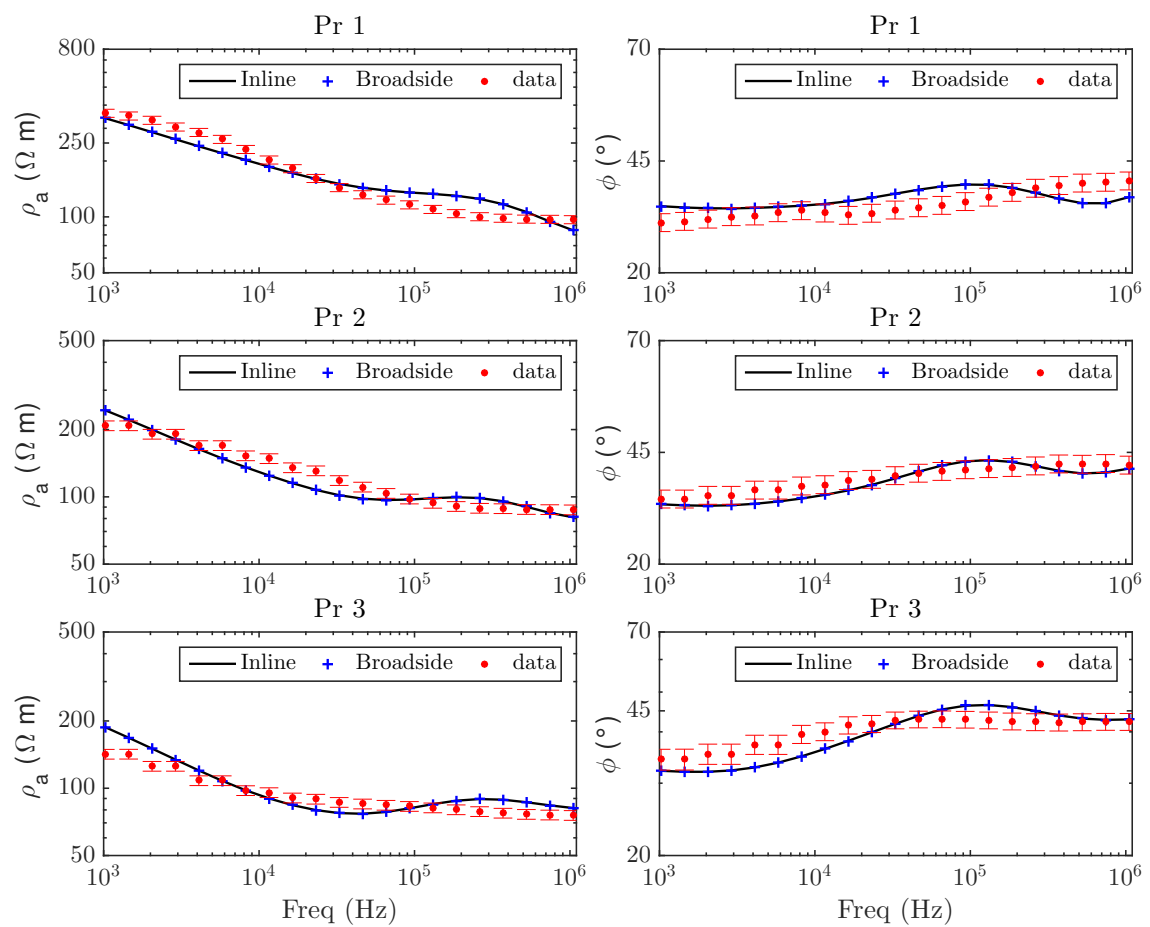


Figure 6.15: Data fitting by considering the pipeline as the shifted/extended dipole for first profile (top), second profile (middle), and third profile (bottom). The error bar on the data is the standard error bar used in the inversion, 5% in the apparent resistivity and 2° in the phase. The solutions for the inline and broadside configuration in this case coincide.

6.5.3 Inversion with MARE2DEM

The inversion with MARE2DEM is carried out in broadside configuration by taking the NW-SE as the x direction in MARE2DEM as the survey design. It has been discussed in Chapter 3 that to invert the data in the NW-SE configuration (the profiles described before) requires a 3D code. In the 2D case, the profile should be viewed in SW-NE direction. As a result, there are 21 profiles in total, 11 profiles have 3 stations, and 10 profiles have 2 stations. Clearly, putting 21 stations in the x direction with the same y coordinate would not make any sense since the strike direction in the code is to the x direction. For the inversion, the long pipeline is approximated as 1000 m dipole located in 0,0 m. The inversion results of a point dipole in this particular case is similar to the 1000 m dipole both in terms of model and RMS. The distances between stations are 15, 25 and 35 m from the dipole respectively for the profile with 3 stations. For the profile with 2 stations, the distances are 25 and 35 m from the dipole. The starting model is 50 Ωm halfspace with $w_{hv} = 1$. The error floor for impedance is 10% and for the phase is 2°.

As an example of the inversion results, the results of the profile with 3 stations is given in Figure 6.16(a) and the results with 2 stations is given in Figure 6.16(b). The data fit for the inversion with MARE2DEM is given in Figure 6.17.

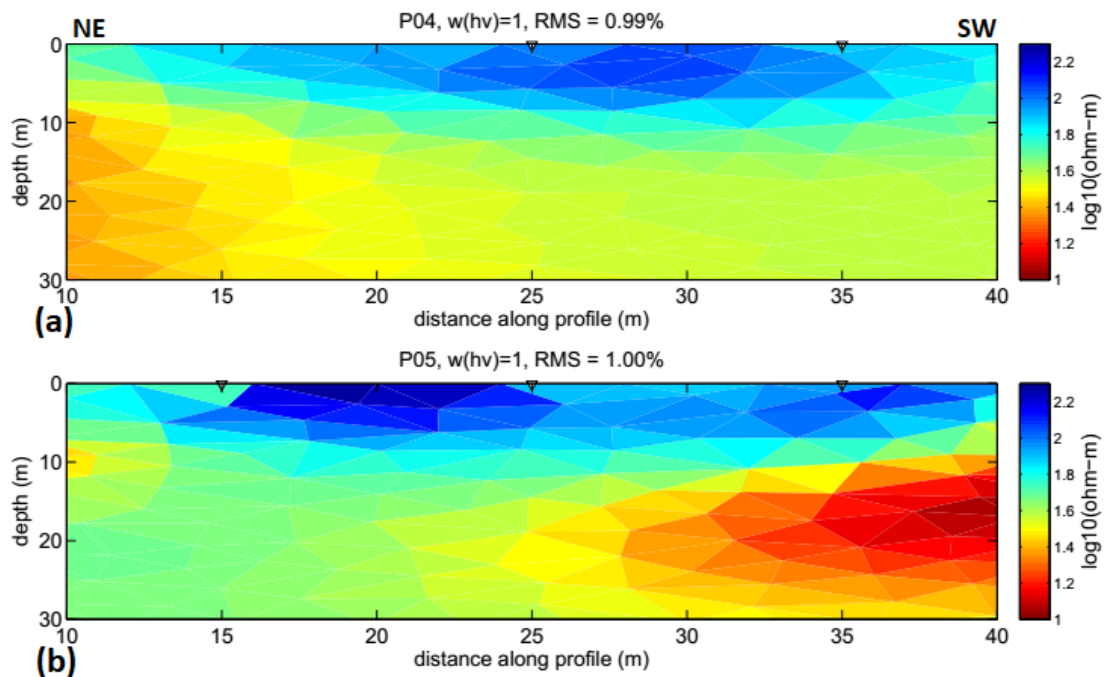


Figure 6.16: Inversion results of MARE2DEM. The pipeline is approximated as a finite dipole length (1000 m) in broadside configuration. There are in total 21 pairs consist of 2 (a) and 3 stations (b).

The result of the profile 2 in Figure 6.11 with MARE2DEM inversion results. The results from MARE2DEM are extracted from every station as 1D conductivity model. Then these 1D conductivity models were stitched to form a “quasi” 2D conductivity models. An example from profile 2 (distance 25 m from the pipeline) is given in Figure 6.18. The result is in agreement with the data derived from the RMT model in Figure 6.11(b).

To summarize, the average conductivity structure in Krauthausen test area from the

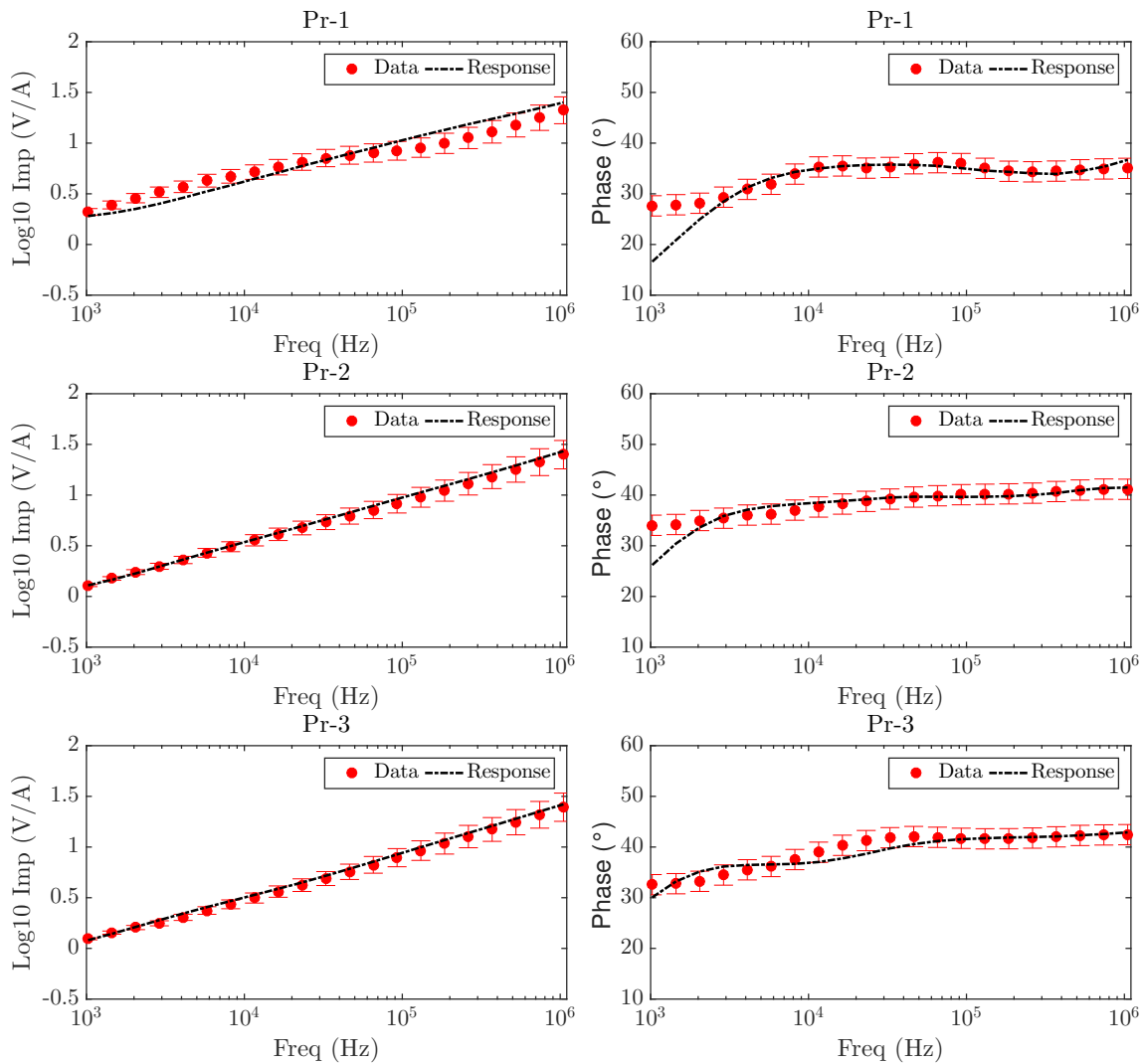


Figure 6.17: Data fit as Figure 6.15 after the inversion with MARE2DEM by considering the pipeline as the transmitter. Instead of apparent resistivity, the data were transformed into \log_{10} impedance.

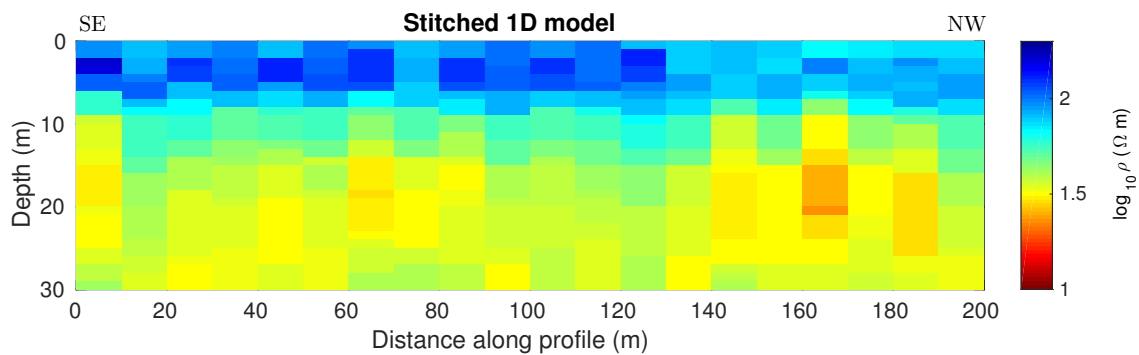


Figure 6.18: A quasi 2D conductivity model of profile 2. The 1D conductivity models were extracted from Figure 6.16.

CSRMT survey is comparable from the previous geophysical EM measurements. The results are tabulated in Table 6.4.

Table 6.4: A revisited compilation of the average resistivity of Table 6.3 from the inversion of RMT data inverted with MT algorithm and CSRMT data inverted with `MARE2DEM`. The CSRMT models are now consistent with previous studies and geology.

	d_1	ρ_1	d_2	ρ_2	d_3	ρ_3
RMT 1	0	60	6	80	10	40
RMT 2	0	70	4	80	10	50
RMT 3	0	70-80	4	85	10	50
CSRMT 1	0	60	6	80	10	40
CSRMT 2	0	70	4	80	10	50
CSRMT 3	0	70-80	4	85	10	50

6.6 Discussion

We successfully carried out the CSRMT measurements in Krauthausen test area to study the conductivity of the hydrogeology test area. We had good groundings in inline and broadside configuration thus the injected currents were almost maximum for all main frequencies. However, the spectra were only observed in one polarization.

The data from the survey posed a really great challenge for the interpretation. That is even the survey design is in the far field zone area; the CSRMT data differ with the RMT data. For this reason, we also carried out a VES experiment at one point and then compared to the CSRMT and RMT data. Finally, it was found out that there was a long pipeline that acted as a transmitter which channelled our injected current from the transmitter to the receiver. As a result, the CSRMT data were shifted from the far field zone to the near field zone. A traditional modelling with any MT algorithm would fail to produce a model which fit the geology. Even in the furthest profile from the pipeline (profile 3), the structure of the lower layer would still be more resistive compared to the first layer, which is the opposite of the true conductive structure. This shows that the interpretation including transition zone data which are not easily removed in CSAMT (Zonge and Huges, 1991) would result in a wrong conductivity structure.

Only after considering the pipeline as the source after the current channelling effect (I call it “shifted” transmitter), the two challenges could be solved, and the conductivity model is reasonable in comparison with previous surveys and the RMT data. There was not so much variation of the conductivity structure compared with the previous surveys of Nix (2005), Hördt et al. (2007) Langenbach (2017); therefore the interpretations of data were also successful.

As stated before, the place we chose to build the transmitter was the only option we had. It looked “clean” from the cultural noise. When designing the experiment, one must also find the distribution of the cables and pipelines which sometimes are hard to find even from the authorities and sometimes there is no sign of them. However `MARE2DEM` opens an opportunity to apply the CSRMT near field zone experiment. Consequently, in the future, the field experiments would be more flexible both in the experiment design (the cultural noise can be minimized) and also data interpretation.

Chapter 7

Field Measurements: Radevormwald Airport, Germany

7.1 Introduction

It is now quite common to find a hydrocarbon contaminated area which requires quick remediation due to the threat they pose to our everyday lives. Boreholes would be the best method to study the hydrocarbon contaminated areas, but this method is expensive. Some geophysical electromagnetic methods such DC (i.e. Vanhala (1997); Sauck et al. (1998)) and RMT (Tezkan, 2008) could be the alternatives and have been applied to make the assessments of the hydrocarbon contaminated areas. Indeed, the advantage of the EM geophysical methods is much less expensive compared to the boreholes. However, the drawback is that the RMT method is useful in detecting a conductive target and less effective for a resistive target such as the case for most hydrocarbon contamination in soil. Even though surface geophysical methods are useful for large scale identification structures of the contaminated sites, a finer resolution is also needed to find the correlation between the contamination and geophysical signals which can be achieved with cross-hole measurement (Cassiani et al., 2014). An example of a successful application of the RMT method to study known hydrocarbon contaminated area (around 30 years when the study was conducted) can be found on Tezkan et al. (2005).

A controlled source radiomagnetotelluric measurement was carried out in May 2017 to investigate a probable¹ hydrocarbon contamination in Luftsportverein (LSV) Radevormwald Germany as my third experiment in my PhD studies. Up to now, there is no complain from the people live nearby about any contamination, unlike the study reported by Tezkan et al. (2005). The study area was around a filling station on the airport since it was the only option to perform a sounding and to make a profile (many buildings nearby). The system of the filling station in the LSV Radevormwald is a very simple one. The fuel dispensers are placed above the ground. In the past, there was no concrete on the top of the filling stations covering the soil from a possible spill when the plane was refuelled. The aim of the survey is to investigate such a possibility of the oil spill with the CSRMT method.

¹There might or might not be any hydrocarbon contamination.

Unfortunately, there exists dominant active cultural noise (either a cable or a pipeline carrying current) at the receiver site (quite urbanized area) which complicate the interpretation of the data. Moreover, it was difficult for us to get high dipole moment in the NS direction due to high contact resistance and also limited land permission from the owner. We also had a problem with the connection of the electric antennae to the amplifier which is connected to the receiver on one polarization.

This chapter is organized as follows. First, the hydrocarbon contamination in soil is reviewed. Since I have a loose connection of the electric antennae, I will also discuss this problem in order to understand the measured data. Afterwards, the survey design is introduced, then the raw data and processing are given, and the modelling of the classical MT algorithm is presented. Finally, I will give the conclusion of the survey.

7.2 Hydrocarbon Contamination in Soil

The signature of hydrocarbon contamination in soil in terms of electrical conductivity is very complicated. The electrical conductivity of the contaminated site may decrease, increase or does not change at all depend on many factors such as the age of the spills, a biodegradation process, and also the amount of the spills itself. Let's only consider when the amount of the spills is enough to make a change in the conductivity distribution. Otherwise, there would be no change of the conductivity that can be detected by geophysical methods.

The decrease of electrical conductivity of soils due to the hydrocarbon contamination can be explained by Archie's law:

$$\sigma = a\sigma_W S_W^n \phi^m, \quad (7.1)$$

where σ is the bulk conductivity of the porous medium, σ_W is the electrical conductivity of the fluid, ϕ is porosity, m is the cementation factor, a is a constant, S_W is water saturation, and n is the empirical factor. Hydrocarbon is a typical Light Non-Aqueous Phase Liquid (LNAPL) which is a groundwater contaminant that is not soluble in the water. It has a lower density than the water, so the hydrocarbon will float at the top of the water. When the contamination occurs, there is a partial replacement of pore waters with the low conductivity (σ_W) LNAPL. It will result in lower bulk conductivity σ since there is a linear relationship between the Equation (7.1). This model is true for a "fresh" or "short-term" spills. The short-term means a time frame weeks to several years when the change on chemical and biological of LNAPL on the contaminated zones can be neglected, and only the physical separation of the LNAPL into the different phases has occurred. This short-term may be up to 30 years as shown by Tezkan et al. (2005), where they conducted RMT surveys on the 30 years oil contaminated sites and also observed a low conductive anomaly.

The contaminated sites might also show higher conductivity caused by biodegradation process. This might be the case on a long-term LNAPL contaminated sites investigation. Geoelectrical investigations in aged (i.e., altered) hydrocarbon spill sites have documented higher bulk conductivities coincident with the zones of hydrocarbon impact (Sauck et al., 1998; Werkema et al., 2003). Further, other studies have documented

attenuated GPR reflections, most likely from increased bulk conductivity in regions with subsurface hydrocarbon contamination (Sauck et al., 1998). Another possibility of the increase of conductivity is caused by the increase of total dissolved solids within pore fluid of rocks. This phenomenon occurs because oil can detach ions from the particle surfaces to the electrolyte (Vanhala, 1997).

Due to the complex signatures of the hydrocarbon contamination in the soils (both spatial and temporal variations). Even though the anomaly is detected, it is difficult to draw any conclusions from a single geophysical EM survey on it without any other microbial and geochemical information conducted on LNAPL contaminated sites (Atekwana and Atekwana, 2010; Cassiani et al., 2014). Furthermore, the geophysical response of hydrocarbon contaminated areas is highly site-dependent (the type of hydrocarbon and release history) (Cassiani et al., 2014).

7.3 Problem with the Connection

As stated at the beginning of this chapter, during the measurements, sometimes a problem with the connection of the amplifier to the electric antennae on the orange wagon occurred. The response of the time series and derived impedance are similar to the results of Escalas et al. (2013) described in Section 2.6. As a result, it is actually difficult to decide whether the strange behaviour on the time series is caused by a loose connection or cultural noise or both. We carried out a RMT experiment crossing the active pipeline and time series also show the behaviour. The time series looks like a loose connection (even the autospectra), but the derived transfer functions show normal behaviour. With the knowledge of tipper magnitude, one can decide to include or exclude the resulting impedance to the inversion and modelling.

We did a test in Vorgerbirgspark, Köln to demonstrate this situation (see Figure 7.1). On the same point, we measure the RMT signals with and without the wagon 5 times each and then rotate the polarization by 90° . The problem of the time series of the wagon is consistent. For instance, the first problem is on the N-S direction (polarization 1), then when we rotate 90° thus the polarization 1 now is to the E-W direction, the problem also rotates to this direction (E-W direction). Without the wagon, all the time series show no problem (Figure 7.1 (b)). The spectra from “bad” and “good” time series are given in Figure 7.2. It is clearly seen that the problematic time series result in problematic spectra. On the estimation of transfer functions, the noise would affect the apparent resistivity and phase impedance, although nothing can be said about the tipper from this time series.

The tipper magnitude derived from the time series in Figure 7.1 is given in Figure 7.3. The tipper magnitudes, both from the problematic time series and normal time series do not exceed 1. We can safely say that the problematic time series on the electric fields have no impact on the tipper data and there is no cultural noise nearby affected the magnetic fields. The impedance (apparent resistivity and phase) are given in Figure 7.4. It can be clearly seen that one of the problematic time series results in problematic impedance estimation. On this case, the data should be discarded from further modelling and inversion since they will lead to a wrong conductivity model. Furthermore, since the tipper data are not affected by the “problematic” time series, this tipper data can also be included in the inversion.

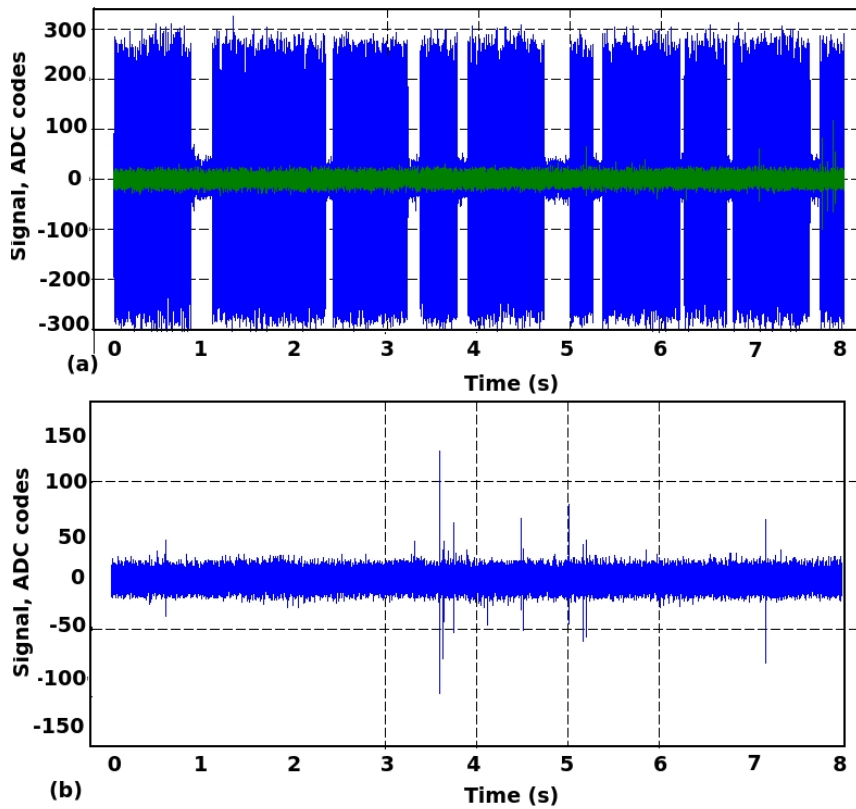


Figure 7.1: (a) Problematic time series from a loose connection on the electric field antennae, (b) Good (normal) time series.

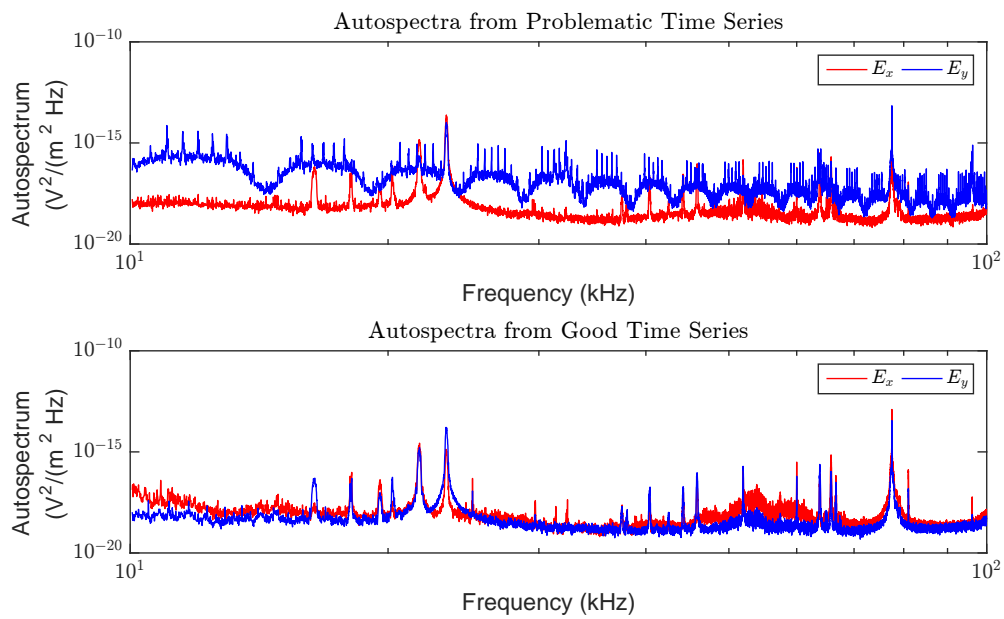


Figure 7.2: Autospetra from the problematic (Figure 7.1(a)) and good (Figure 7.1(b)) times series of the electric fields.

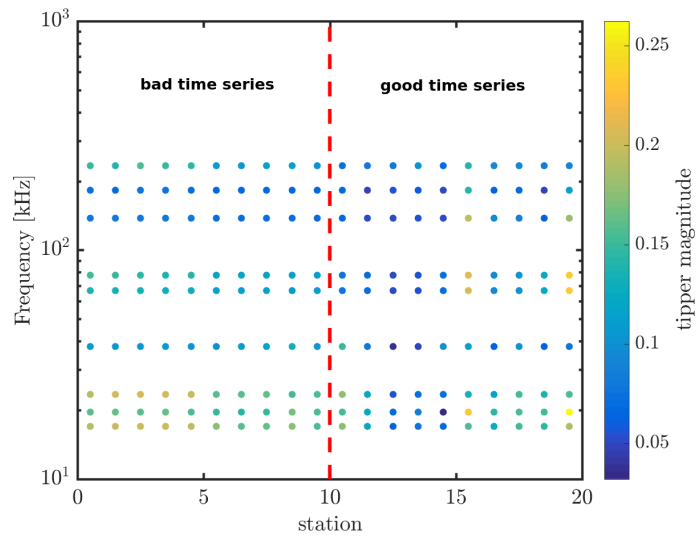


Figure 7.3: The calculated tipper magnitude from the problematic and good time series. When there is no nearby sources of the electromagnetic fields, only the impedance are affected by the problematic while the tipper data are not affected.

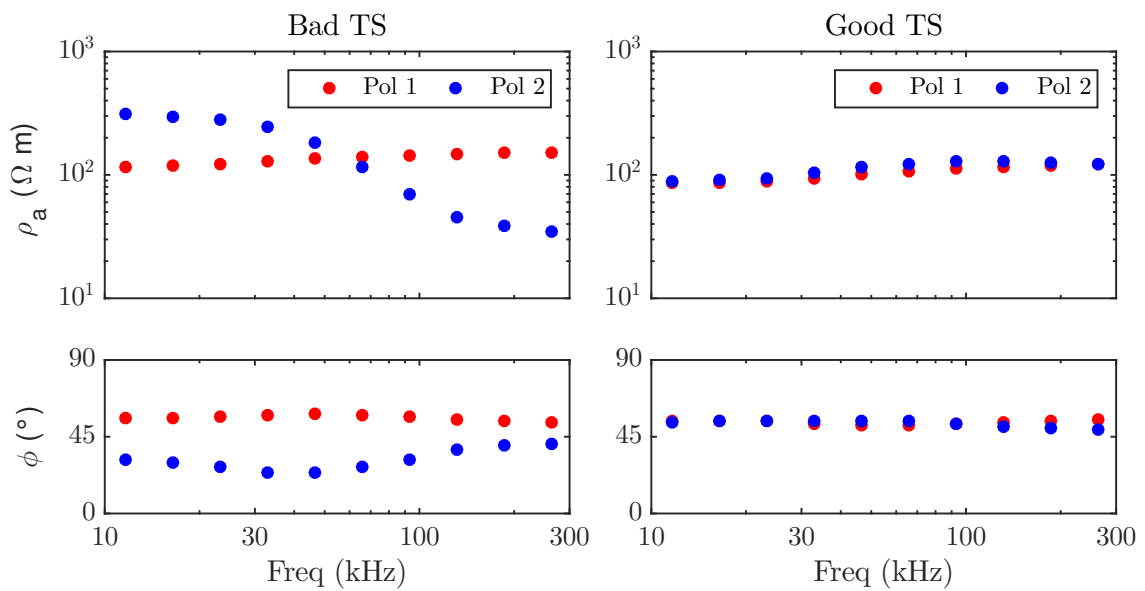


Figure 7.4: Apparent resistivity and phase derived from problematic time series (left) and normal time series (right)

7.4 Survey Design

A controlled source radiomagnetotelluric measurement was carried out in May 2017 to investigate probable hydrocarbon contamination in Luftsportverein (LSV), a small airport, Radevormwald Germany (see Figure 7.5(a)). The geology of the survey area is dominated by clay, siltstone and subordinate sandstone.

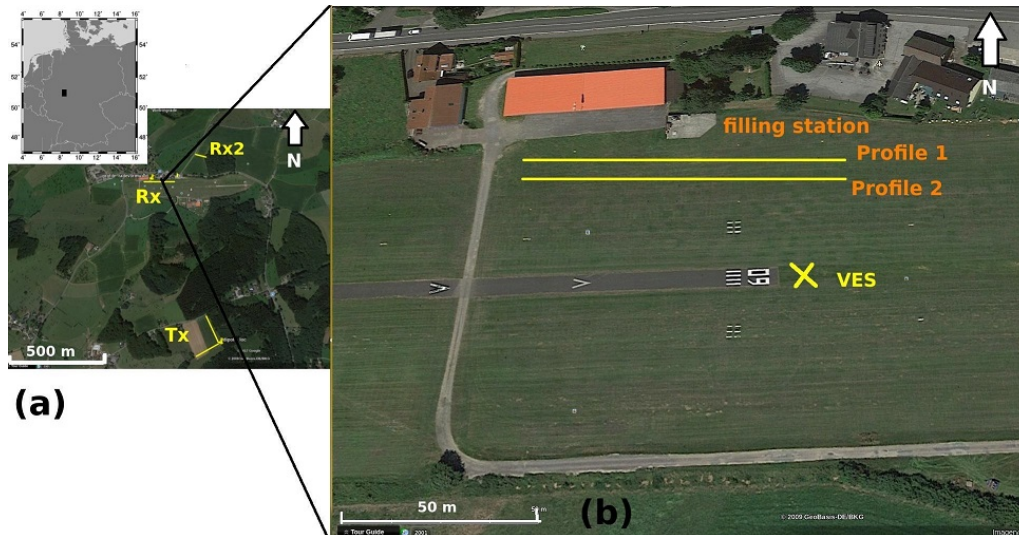


Figure 7.5: Survey design of CSRMT experiment in Radevormwald airport. Tx is the transmitter location, Rx is the receiver location on the airport, Rx2 is the reference profile.

As stated before, the system of the filling station in the LSV Radevormwald is a simple one. The fuel dispensers are placed above the ground (see Figure 7.7). In the past, there was no concrete on the top of the filling stations to cover from possible spill to the ground when the plane was refuelled. Furthermore, the airport has been changed (levelled) around the filling station (target area) for the runway which changed the geology. 7.5(a).

The transmitter site is located around 1.5 km from the LSV Radevormwald. It was the only place where we got the permission from the farmers. The set up was an L

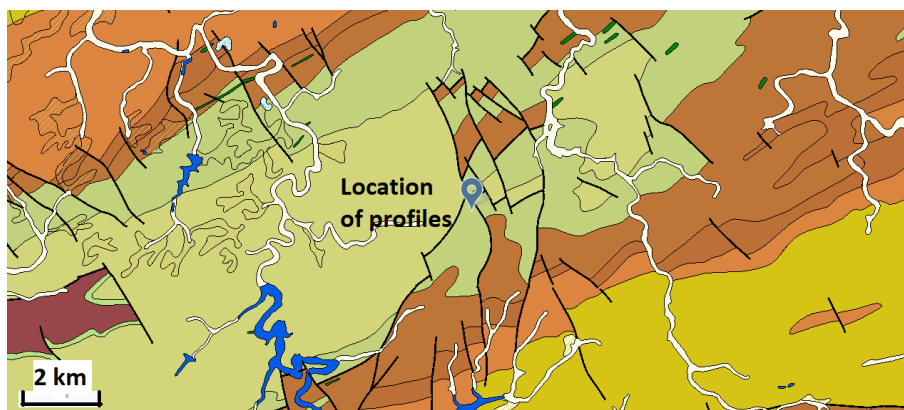


Figure 7.6: Geology situation in Radevormwald. The location of the main profile is dominated by clay, siltstone and subordinate sandstone. Figure from <https://www.geoportal.nrw/themenkarten>.



Figure 7.7: The simple filling station on Radervormwald airport. There was no concrete in the past covering the ground. There might be some hydrocarbon spills into the soil.

configuration approximately NW-SE and NE-SW, each arm was approximately 200 m long (see Figure 7.5 (a)). The contact resistance during the survey was around 200Ω which was quite high even though salt and bentonite were added to get it lower. The rocks were just some centimetres below the soils in the survey area. The injected currents during the survey are given in Table 7.1. Due to this very low injected current, therefore a low dipole moment -on the NS configuration-, the odd harmonics can only be seen on D4 band. This is even worse with the broken electric antennae and also cultural noises around the area in NS direction. We also tried to find other locations for the transmitter, but we could not get any permissions from the farmers.

Table 7.1: Current injected during CSRMT measurements in Radevormerwald, Germany

Main freq (kHz)	N-S (A)	E-W (A)	Band
0.5	1.3	1.5	D1
5	1.1	1.2	D2
50	1	1	D4
105	0.9	0.8	D4

In the airport area near the filling stations, we set up two parallel 100 m profiles (see Figure 7.5(b)). On the profile 1 there were 17 stations with 5 m distance in the middle part (from 20 to 80 m) and 10 m in the outer part. While on profile 2 there were 11 stations each with 10 m spacing. The reference profile was 60 m long with 10 m spacing with NS transmitter only (around 300 m from the filling stations). Additionally, conventional RMT data were also measured along both profiles (there were 17 stations at each profile). Furthermore, a VES sounding was also carried out near the runaway in NS and EW direction to see general conductivity distribution.

On the reference profile, only the data from RMT were available. We used the N-S dipole combined with a loose connection to the electric field which makes the CSRMT data unusable. There are 6 stations in the reference profile.

7.5 Raw Data and Processing

The recorded time series show strange behaviour on the N-S direction as shown in Figure 7.8. It was found after the survey that the electric antennae on the wagon were broken

(see Section 7.3). It has also been discussed in Escalas et al. (2013) that a typical on-off (not stable) time series were observed when a cultural noise was present or due to the loose connection of the electric field. For this reason, the N-S time series are discarded on further data processing and modelling.

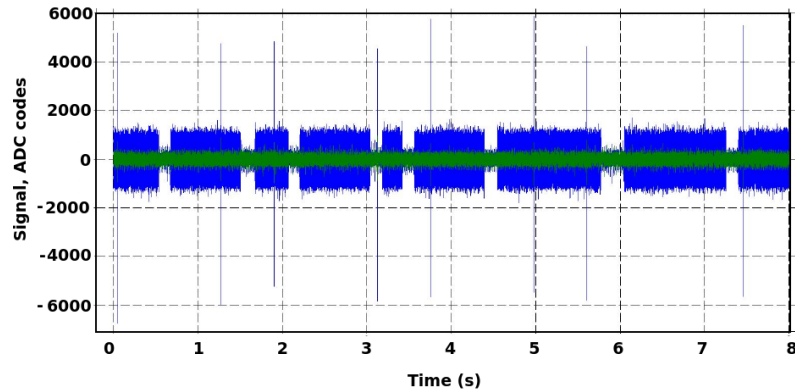


Figure 7.8: A typical electric field time series, blue is N-S, green E-W.

The time series were processed in standard ways as discussed in Chapter 4. First, the spectra were calculated with *SM25M* then the apparent resistivity and phase impedance were estimated with *SFA*. As usual, the additional criteria of the maximum azimuth and minimum coherence were 30° and 0.8 respectively. Finally, the Siegel's repeated median was applied to get a smooth sounding curve of apparent resistivity and impedance phase. An example of typical data is shown in Figure 7.9.

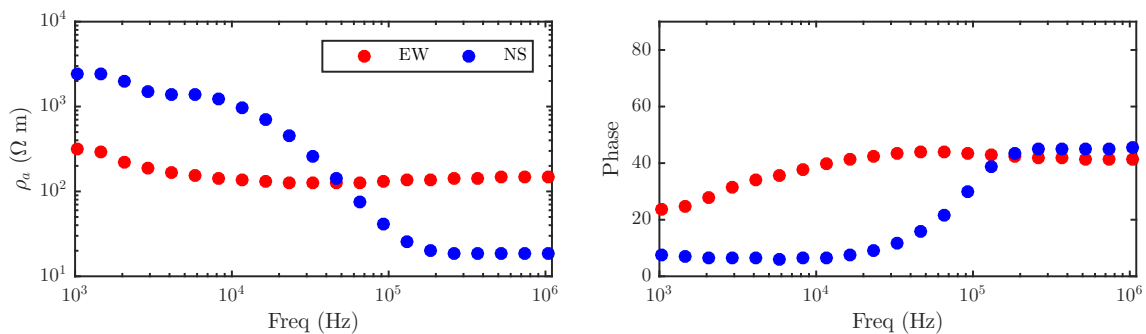


Figure 7.9: A typical transfer functions from CSRMT measurements on the Radevormwald airport.

As stated before, consequently to this behaviour of the measured data, the N-S data were excluded from the inversion with *Rund2Inv*. Notice that the transfer functions are derived by averaging the spectra of the harmonics and some neighbouring noise (broken time series). In this case, the noise is much more dominant in the NS direction since the spectra were not observed. Furthermore, on the D2 band, the distance radio transmitter should be seen. However, the transfer functions were also not suitable for further processing and modelling. Thus even though the electric field were not broken, there would be no CSRMT data on D1 and D2 band since we had difficulties to get a high dipole moment (the area was too resistive, and the land use was also limited).

The tipper data were estimated with the azimuth of 90° . The tipper magnitude observed on 2 profiles are more than 1 (Figure 7.10). This might also suggest a signature

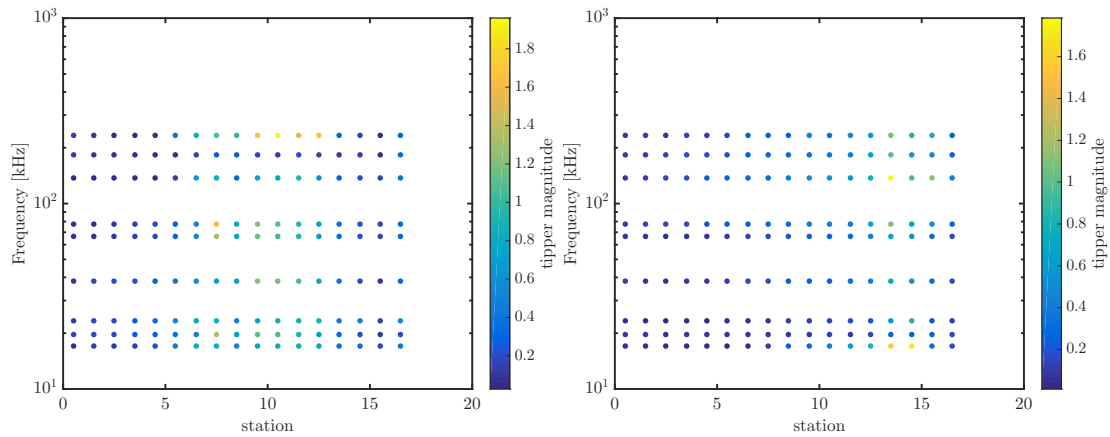


Figure 7.10: Tipper magnitude derived from RMT data on profile 1 and profile 2. Notice on different colour scale. Both maximum magnitude were > 1 .

of near field structure affected the magnetic fields. Unfortunately, we could not find the most dominant cultural noise affecting the data. If there were no near field structure affected the data, the magnitude of the tipper should be < 1 even if the electric antennae were broken as shown in Section 7.3. Since the tipper data are > 1 in magnitude, the data were not further processed to get conductivity model.

7.6 Modelling

The apparent resistivity and impedance phase for all the stations (main profile and reference profile) coincide with the CSRMT and RMT data. It has been shown in Chapter 5, in the far-field zone, the model derived from both data sets are comparable. Thus, it is better to carry out inversion with both data set. Note that the data only available on the E-W direction, therefore only in the TM mode. It would not also make any sense to invert the data with MARE2DEM considering the source, since only two stations can be inverted (the profile direction would be NS; as a result there would be 17 pairs) as the case for Krauthausen data in Chapter 6 which are more suitable with a 3D CSEM inversion code. Furthermore, the conductivity structures between the transmitter and receivers are not exactly known.

Let's start with the main profiles in the airport area near the filling stations. Since I combined the CSRMT and RMT data, both profiles now have 17 stations. The L-curve for both inversions are given in Figure 7.11 for the profile 1 and Figure 7.12 for the profile 2 for different starting models of 10, 20, 50 and 100 Ωm .

From both L-curve figures, the "corner", -the optimal regularization parameter-, could not easily be seen. The best way to evaluate is to see directly the inversion results on both profiles. I found that the best value of λ is 70 for profile 1 and 50 for profile 2 with starting model of 100 Ωm . The inversion results for both profiles are given in Figure 7.13. The measured data were well fitted by both models as indicated in the low RMS which are 0.98% and 1.02% for profile 1 and profile 2 respectively. The data fit for station 10 on profile 1 is given in Figure 7.14 and for frequency 65 kHz is given in Figure 7.15.

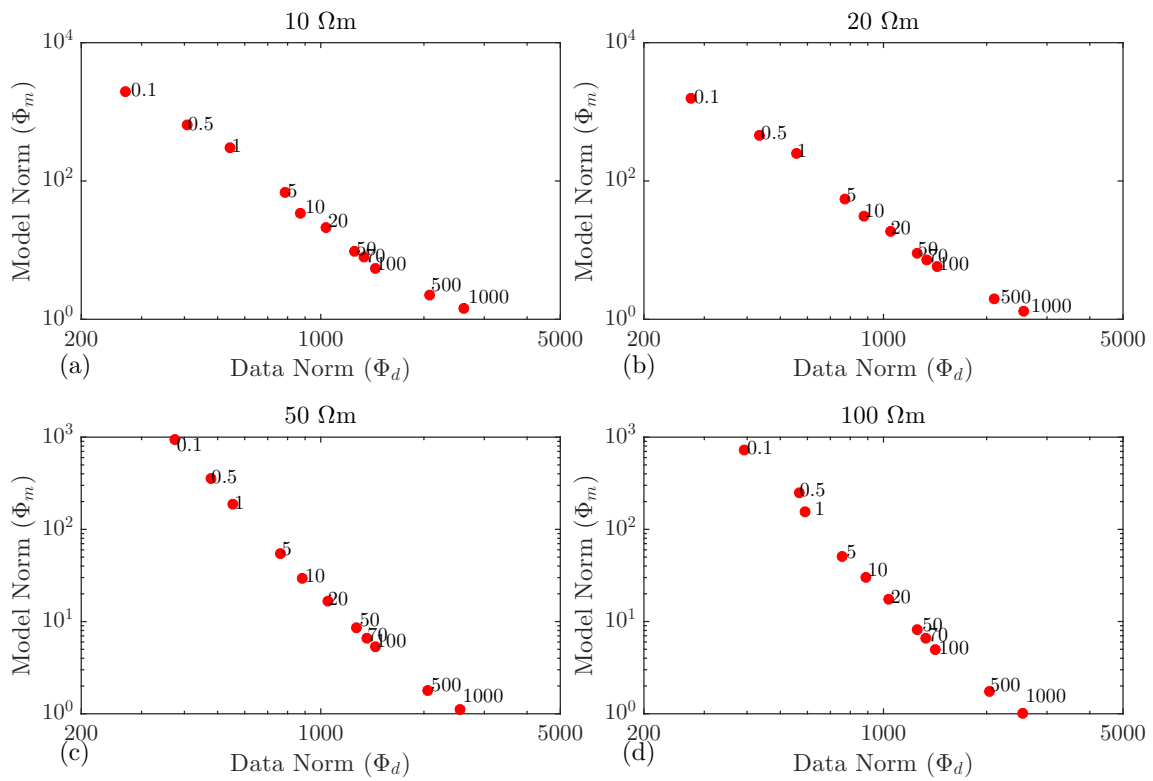


Figure 7.11: L curve for different starting model in profile 1.

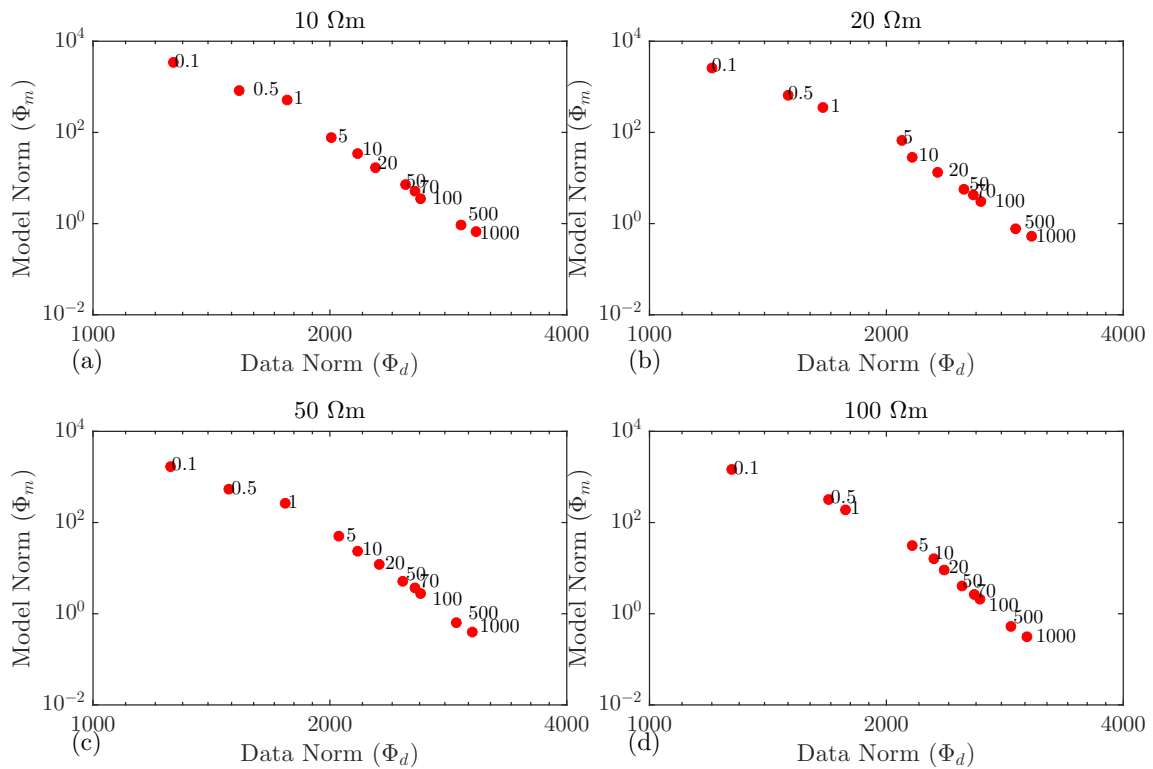


Figure 7.12: L curve for different starting model in profile 2.

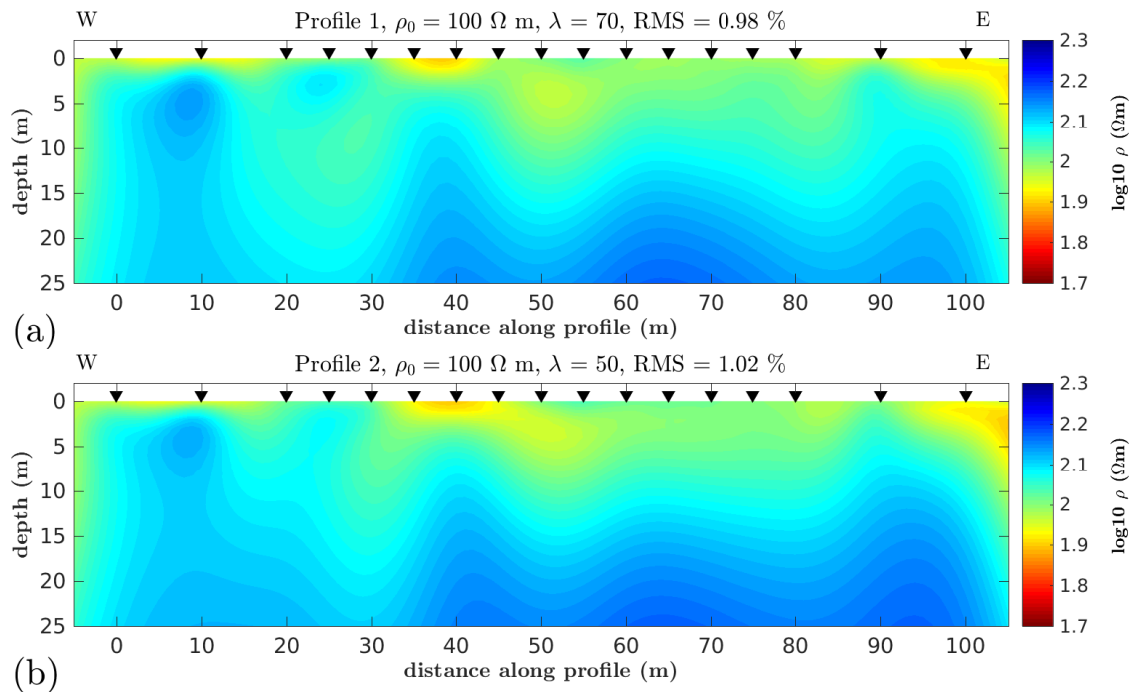


Figure 7.13: Conductivity models from profile 1 and profile 2. There is only a small variation from the model

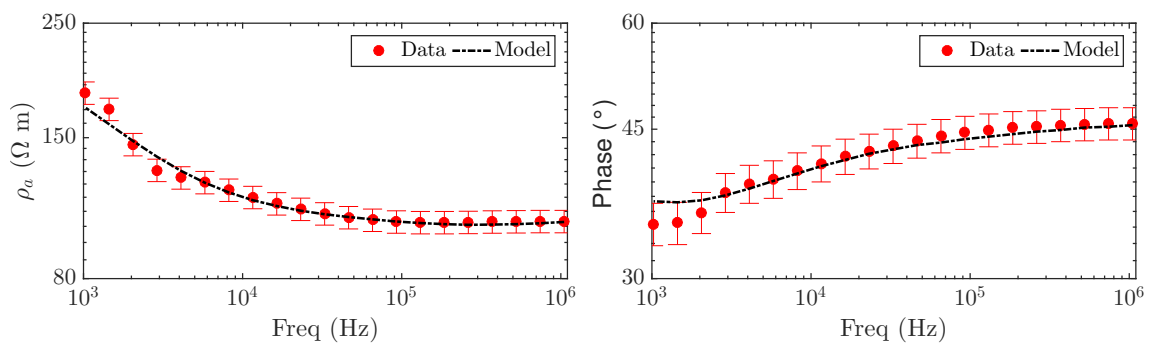


Figure 7.14: An example of data fitting of apparent resistivity and phase against the frequency in station 10 of profile 1.

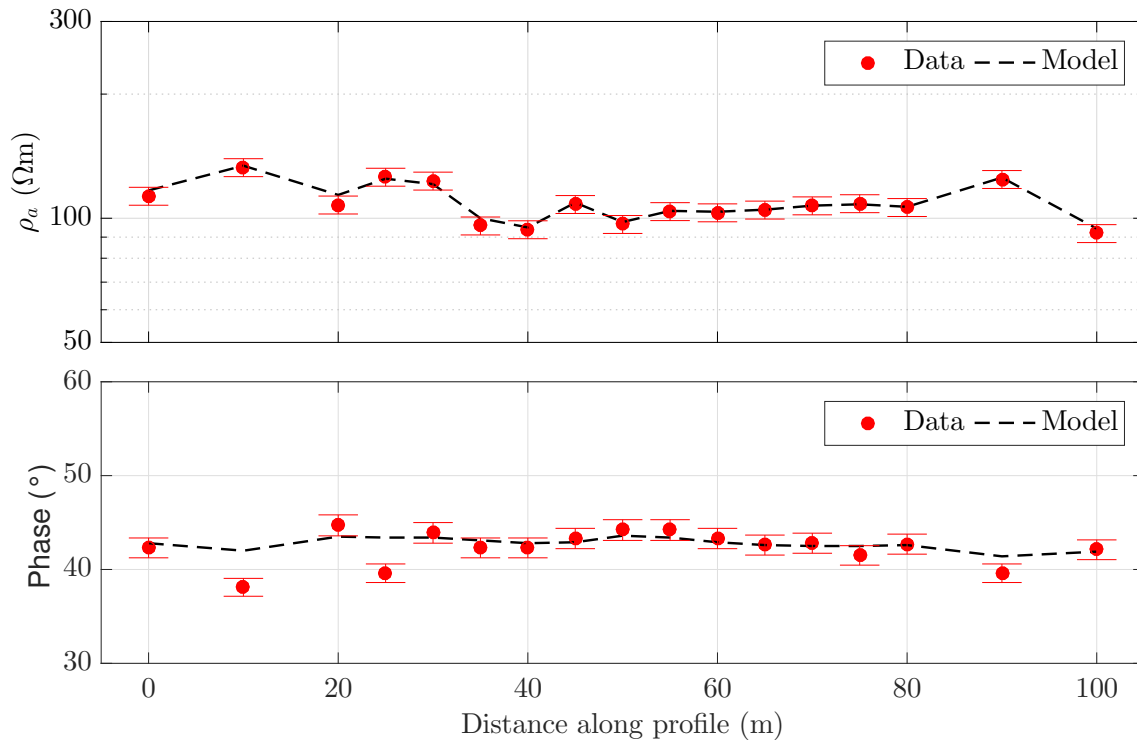


Figure 7.15: An example of data fitting of frequency 65.5 kHz against the distance of profile 1.

Comparing the inversion results with the geological information. The first 10 m probably dominated by a mixture of rocks and clay. After 15 m depth, it is dominated with rocks. There is no anomaly associated with hydrocarbon contamination between 40–60 m along the profile direction on both profiles. At least this is in agreement with no complaint from the people live nearby the airport. Even if there were an anomaly, it would not be straightforward to associate with a hydrocarbon contamination (Atekwana and Atekwana, 2010; Cassiani et al., 2014).

The reference profile was around 300 m from the main profile (and the filling stations), the inversion result from this profile is given in Figure 7.16. The data were also well fitted by the model with RMS 0.97%. The reference profile, after 10 m, is more resistive

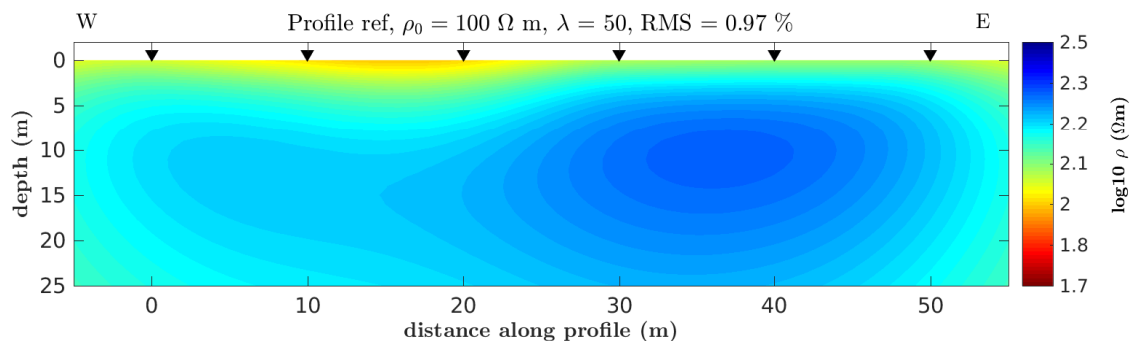


Figure 7.16: Conductivity model of the reference profile. The second layer in the reference profile is more resistive than the second layer from the main profiles

compared to the main profile. This might be an indication that there is no hydrocarbon contamination in the survey area.

The VES sounding was carried out near the runway on the N-S and W-E direction. Although, it was quite limited on the NS direction (only up to 60 m). The data and the inversion result is given in Figure 7.17. From the VES survey, the structure might be 2D with only a little variation.

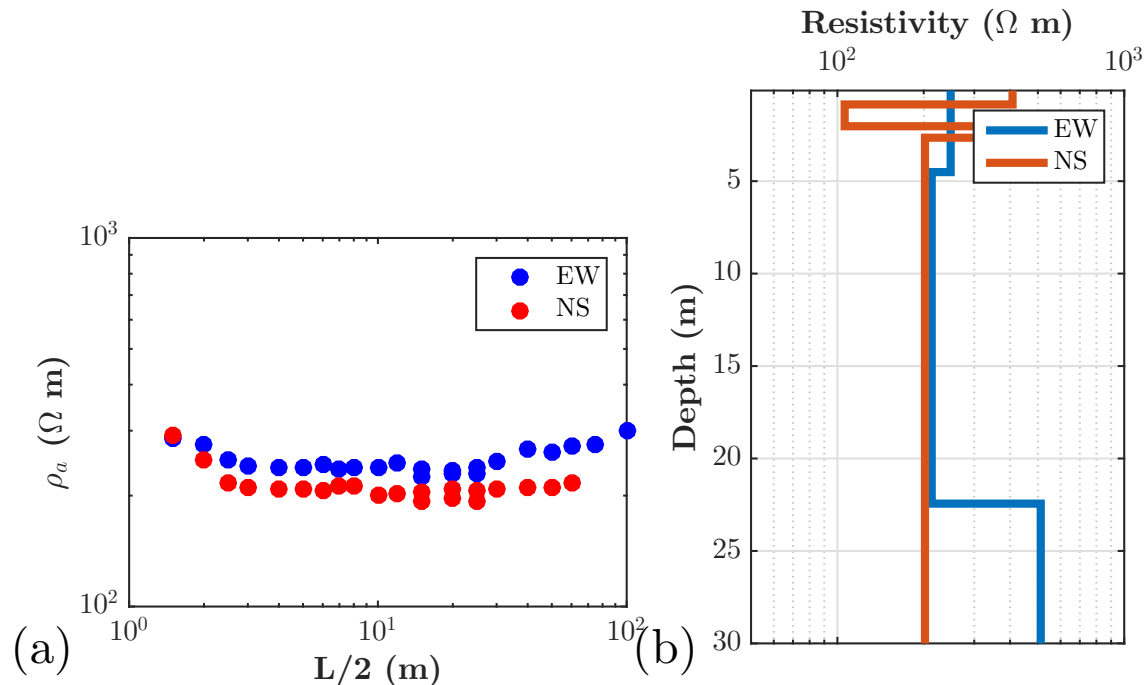


Figure 7.17: (a) VES data and (b) the resistivity model from the VES data.

I also compare 1D inversion results of the 1 sounding curves from the first profile (station 10), VES data on E-W direction and the reference profile (station 2) in Figure 7.18. The station in the main profile has smallest resistivity structure (it is true in the whole profile) compared to the reference profile. Although the value is between 100–300 Ω m.

From the data and inversion results above, I conclude that there is no hydrocarbon contamination in the survey area caused by the filling stations.

7.7 Discussion

The CSRMT experiments in Radervormwald posed some challenges. It was not easy to get a low grounding in N-S direction, as a consequence, the injected currents were also low. Combining this and the fact that the electric antennae connection was loose (in the N-S direction too) resulted only in a scalar CSRMT measurement as in Vuoksa and Krauthausen.

Detecting the hydrocarbon contamination in soil with one single geophysical EM method only is already difficult. In most of the cases, even the contamination level is high; the signal is weak for geophysical methods (Cassiani et al., 2014). The weak signal from the anomaly and in fact any other microbial and geochemical information are needed to analyze the data from experiments conducted on LNAPL contaminated sites

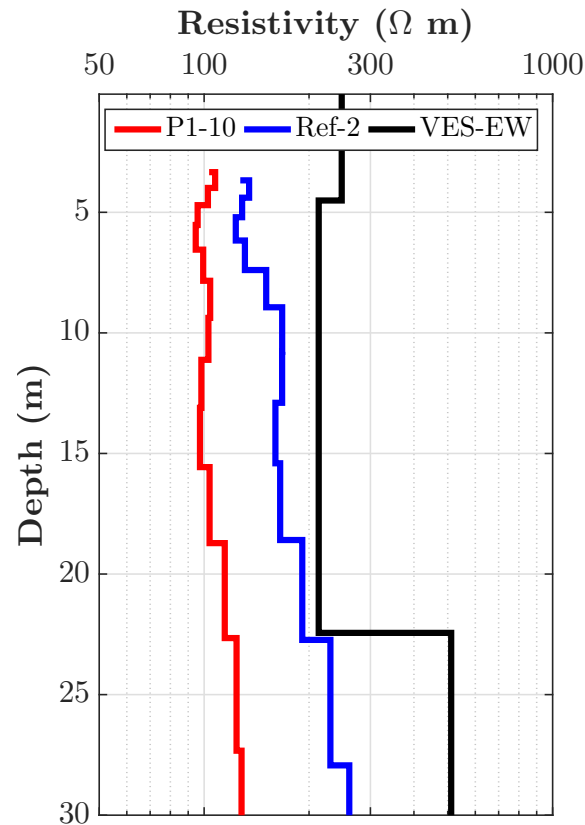


Figure 7.18: 1D inversion results of station 10 of profile 1 (near to the filling station), station 2 of reference profile and VES sounding on E-W direction.

(Atekwana and Atekwana, 2010; Cassiani et al., 2014). Fortunately, we did not see any anomaly to be associated with hydrocarbon contamination around the filling stations. Furthermore, the tipper data is more than 1 which indicates nearby cultural noise which we could not find. Up to now, the grass is still green, and there is no single complaint reported by the people live nearby. To this point, the simple filling stations in LSV Radevormwald is safe for the environment.

In the future, as stated before, a near field experiment might also be conducted. The MARE2DEM now could handle the near-field data as shown in previous chapters (the modified code was only available after all the experiments). Thus the difficulties with the transmitter (permissions, grounding, etc.) could be minimized. In order to really test the applicability of the CSRMT method on a hydrocarbon contamination area, it would be great to find the known location as shown in Tezkan et al. (2005).

Chapter 8

Summary & Conclusion

This thesis focuses mainly on the interpretation of the CSRMT field data. The CSRMT method is the modified version of the RMT method. The discussion starts from the RMT perspective rather than from the CSEM perspective. The differences between the CSRMT method and the RMT method lies on the field zones. In the conventional RMT, it is assumed that the radio transmitters are located very far away. Thus the soundings are only performed in the far field zone. However, in the CSRMT method, the near-field zone data are also measured, and even the far field zone data sometimes are affected by the near-field zone effect depending on the conductivity structure of the survey area. The electromagnetic fields behave differently depending on the distance between the source and observation point controlled by the induction numbers. In this case, before the measurement, an experimental setup is necessary at least to define the theoretical field zones. This can be realized with `SLDMEM3F`, which has never been applied to any CSEM frequency domain method before.

The modelling and inversion of the CSRMT data depend on the field zones. Only in the far-field zone, the classical MT algorithms could be applied to interpret the data. Whereas in the near field-transition zones data, the MT algorithms fail and would result in wrong conductivity model. In this thesis, a new modification `MARE2DEM` was validated with synthetic data up to 1 MHz in all zones. Furthermore, `MARE2DEM` was also applied to invert the field data. The modification of `MARE2DEM` also opens an opportunity to neglect the boundary of the zones as shown in the synthetic examples and field data experiments.

The discussion of displacement current cannot be avoided in the CSRMT frequency range. This frequency range is a “transition” between the known MT-AMT method (neglecting displacement current) to the GPR method (taking into account the displacement current). For the CSRMT method, the displacement current should be taken into account on the electric and magnetic fields generated by HED as well as the tipper data. However, the displacement current can be neglected when the data are in impedance (as well as apparent resistivity) and impedance phase. As a result, the data in this thesis were interpreted without taking into account the displacement current. Indeed, it would be beneficial to develop 2D/3D CSEM algorithm (forward and inversion) which take into account the displacement current to interpret the field data.

The new 5 channel receiver allows us to measure the vertical magnetic fields. During this PhD study, a new processing scheme was also developed by Dr M. Gurk to estimate the transfer functions (impedance and tipper) in the scalar and tensor scheme. Later it was found that for scalar sources, the scalar estimation of impedance is better than the tensor estimation. In this thesis, the new processing algorithm was validated and applied to the measured data from the RMT-CSRMT experiments, both for the impedance and the tipper data. The new processing algorithm combined with smoothing algorithm from Smirnov (2003) result in smooth sounding curves of apparent resistivity and impedance phase. However, the tipper data could also be improved by applying dispersion relation proposed by Marcuello et al. (2005). Unfortunately, due to experimental design and problem during the experiment, the real tensor measurement was not achieved. Therefore, the more advanced processing such as strike analysis, and dimensionality analysis could not be realized.

The first measurement was carried out in Vuoksa Region, north of St. Petersburg Russia, near the Finland border. The aim of the survey was to detect the fault (conductivity contrast as a vertical contact) in the far field zone. Furthermore, the profile was also extended to the near field and transition zones. The data from all zones were successfully interpreted. In the far field zone, the apparent resistivity and impedance phase were interpreted with `Rund2Inv`. While the tipper data were interpreted with `Rebbocc`. The expected fault could be mapped successfully. The modified `MARE2DEM` was applied to interpret the near field zone data, and the results are in agreement with the inversion of RMT data with `Rund2Inv` and `Rebbocc` (including tipper data). The inversion with `MARE2DEM` was also extended to include the far field zone data. By this method, the boundary of the field zones could be neglected.

The experiment in Krauthausen, Germany tells different story due to cultural noises around the test area. The aim of the survey was to study the conductivity distribution of the test area. The survey design was in the far-field zone using a tensor setup of perpendicular sources. However, the measured CSRMT data were not as expected in the theoretical survey design. The RMT data and the derived models are in agreement with the previous studies and lithology. However in the CSRMT data, we observed a phenomenon called current channelling by long pipeline connecting the transmitter to the receiver site. As a result, the theoretical far-field zone was shifted to the near-field zones. Moreover, only one polarization was observed from two perpendicular dipole which reduces our tensor setup. To interpret the data, we should treat the pipeline as the "shifted" sources in one polarization only. Afterwards, the measured CSRMT data were successfully interpreted by a trial and error forward modelling with the `SLDMEM3f` and an inversion with modified `MARE2DEM`.

A different challenging task was to conduct and to interpret the data from the experiment in Radervomwald, Germany. First, it was hard to inject enough current to the very resistive ground. Second, one of the electric antennae was broken and third, it was cultural noise seen in the tipper data (the magnitude > 1). Even without those challenges, interpreting the data in an oil-contaminated area is already a difficult task for a single geophysical EM measurement. Our results from the experiment do not show any anomaly associated with any hydrocarbon contamination. At this point, the method of filling the aeroplane in the LSV Radrvormwald is safe for the environment (does not

harm the environment).

The experiments carried out in this thesis show the strengths and limitations of the new developed CSRMT method. In the future, for any near surface task, probably it is better to work in the near field zone where the signal to noise ratio is high in combination with the RMT method. A high signal to noise ratio would probably reduce the requirement of “good” grounding, yet a high current is better. The difficulties setting up the transmitter might be reduced (i.e. finding a suitable place and permission). The measured near-field data can easily be inverted with `MARE2DEM` even with anisotropy, which can be measured with a tensor experiment. Furthermore, adding the information from the near-field zone tipper data would complete the multidimensional interpretation of the data.

Bibliography

- Adcock, R., 1878, A problem in least squares: The Analyst.
- Adrian, J., 2017, Interpretation of DC and IP Time-Domain Data Observed on a Copper Deposit in Turkey Using a Newly Developed 2D Finite Element Inversion With Unstructured Meshes: PhD thesis, Universität zu Köln.
- Archie, G. E., 1942, The Electrical Resistivity Log as an Aid in Determining Some Reservoir Characteristics: Petroleum Transactions of AIME.
- Atekwana, E. A., and E. A. Atekwana, 2010, Geophysical Signatures of Microbial Activity at Hydrocarbon Contaminated Sites: A Review: Surveys in Geophysics, **31**, 247–283.
- Babaour, K., and J. Mosnier, 1980, Direct determination of the characteristics of the currents responsible for the geomagnetic anomaly of the Rhinegraben: Geophys. J. R. astr. Soc, **6**, 327–331.
- Bastani, M., 2001, EnviroMT - a new controlled source radio magnetotelluric system: PhD thesis, Uppsala University.
- Bastani, M., A. Savvaidis, L. Pedersen, and T. Kalscheuer, 2011, CSRMT measurements in the frequency range of 1250 kHz to map a normal fault in the Volvi basin, Greece: Journal of Applied Geophysics, **75**, 180 – 195.
- Berdichevsky, M., V. Dmitriev, and E. Pozdnjakova, 1998, On two-dimensional interpretation of magnetotelluric soundings: Geophysical Journal International, **133**, 585.
- Berdichevsky, M. N., I. A. Bezruk, and O. M. Chinavera, 1973, Magnetotelluric sounding with the use of mathematical filters: Izv. Akad. Nauk. SSSR Fiz. Zeml, **3**, 72–92.
- Beylich, A. A., E. Kolstrup, T. Thyrssted, N. Linde, L. B. Pedersen, and L. Dynesius, 2004, Chemical denudation in arctic-alpine Latnjavagge (Swedish Lapland) in relation to regolith as assessed by radio magnetotelluric-geophysical profiles: Geomorphology, **57**, 303 – 319.
- Blaschek, R., 2006, Aspekte der Inversion von Daten der Spektralen Induzierten Polarisation: PhD thesis, Universität zu Bonn.
- Bostick, F. X., 1977, A Simple Almost Exact Method of MT Analysis: Workshop on Electrical Methods in Geothermal Exploration, **359**, 174–183.
- Cagniard, L., 1953, Basic theory of the magnetotelluric method of geophysical properties: Geophysics, **18**, 605 – 635.
- Cassiani, G., A. Binley, A. Kemna, M. Wehrer, A. F. Orozco, R. Deiana, J. Boaga, M. Rossi, P. Dietrich, U. Werban, L. Zschornack, A. Godio, A. JafarGandomi, and G. P. Deidda, 2014, Noninvasive characterization of the trecate (italy) crude-oil contaminated site: links between contamination and geophysical signals: Environmental Science and Pollution Research, **21**, 8914–8931.
- Chave, A. D., 2017, Estimation of the magnetotelluric response function: The path from

- robust estimation to a stable-maximum likelihood estimator: *Surveys in Geophysics*, **38**, 837–867.
- Constable, S., A. Orange, and K. Key, 2015, And the geophysicist replied: “which model do you want?”: *Geophysics*, **80**, E197–E212. (n/a).
- Constable, S. C., R. L. Parker, and C. G. Constable, 1987, Occams inversion: A practical algorithm for generating smooth models from electromagnetic sounding data: *Geophysics*, **52**, 289–300.
- Druskin, V., and L. Knizhnerman, 1994, Spectral approach to solving three-dimensional Maxwell’s diffusion equations in the time and frequency domains: *Radio Science*, **29**, 937–953.
- Englert, A., 2003, Measurement, Estimation and Modelling of Groundwater Flow Velocity at Krauthausen Test Site: PhD thesis, RWTH Aachen.
- Escalas, M., P. Queralt, J. Ledo, and A. Marcuello, 2013, Polarisation analysis of magnetotelluric time series using a wavelet-based scheme: A method for detection and characterisation of cultural noise sources: *Physics of the Earth and Planetary Interiors*, **218**, 31 – 50.
- Evans, R. L., 2012, Earth’s electromagnetic environment, 3A. Conductivity of Earth Materials, *in* *The Magnetotelluric Method: Theory and Practice*: Cambridge University Press, 50 – 95.
- Goldstein, M. A., and D. W. Strangway, 1975, AudioFrequency Magnetotellurics with a Grounded Electric Dipole Source: *Geophysics*, **40**, 669–683.
- Gomez-Trevino, E., 1987, Should The Electric Line be Straight in Magnetotelluric Surveys?: *Geophysical Prospecting*, **35**, 920–923.
- Gössling, K., 2004, Geoelektrische Tomographie zur Überwachung eines Tracherverschus auf dem Testfeld Krauthausen: Diploma thesis, Universität zu Köln.
- Grant, F., and G. West, 1965, Interpretation theory in applied geophysics: McGraw-Hill Book Company. International Series in the Earth Sciences.
- Grayver, A., 2013, Three-dimensional controlled-source electromagnetic inversion using modern computational concepts: PhD thesis, Freie Universität Berlin.
- Groom, R. W., and K. Bahr, 1992, Corrections for near surface effects: Decomposition of the magnetotelluric impedance tensor and scaling corrections for regional resistivities: A tutorial: *Surveys in Geophysics*, **13**, 341–379.
- Hadamard, J., 1902, Sur les problèmes aux drivées partielles et leur signification physique: *Princeton University Bulletin*, 49–52.
- Hansen, P. C., and D. P. OLeary, 1993, The Use of the L-Curve in the Regularization of Discrete Ill-Posed Problems: *SIAM Journal on Scientific Computing*, **14**, 1487–1503.
- Haroon, A., 2016, Development of Novel Time-Domain Electromagnetic Methods for Off-shore Groundwater Studies: A Data Application from Bat Yam, Israel: PhD thesis, Universität zu Köln.
- Hördt, A., R. Blaschek, A. Kemna, and N. Zisser, 2007, Hydraulic conductivity estimation from induced polarisation data at the field scale - the Krauthausen case history : *Journal of Applied Geophysics*, **62**, 33 – 46.
- Ismail, N., G. Schwarz, and L. B. Pedersen, 2011, Investigation of groundwater resources using controlled-source radio magnetotellurics (CSRMT) in glacial deposits in Heby, Sweden: *Journal of Applied Geophysics*, **73**, 74 – 83.
- Jiracek, G. R., 1990, Near-surface and topographic distortions in electromagnetic induc-

- tion: *Surveys in Geophysics*, **11**, 163–203.
- Jones, A., 1983, The problem of current channelling: A critical review: *Surveys of Geophysics*, **6**, 79–122.
- Jones, A. G., 2012, Distortion of magnetotelluric data: its identification and removal: *The Magnetotelluric Method: Theory and Practice*, 219.
- Jonscher, A. K., 1977, The “universal” dielectric response: *Nature*, **267**, 673–679.
- Junge, A., 1996, Characterization of and correction for cultural noise: *Surveys in Geophysics*, **17**, 361–391.
- Kalscheuer, T., L. B. Pedersen, and W. Siripunvaraporn, 2008, Radiomagnetotelluric two-dimensional forward and inverse modelling accounting for displacement currents: *Geophysical Journal International*, **175**, 486–514.
- Kaufman, A. A., and G. V. Keller, 1981, *The magnetotelluric sounding method*: Elsevier. *Methods in Geophysics and Geochemistry*.
- Key, K., 2016, Mare2dem: a 2-d inversion code for controlled-source electromagnetic and magnetotelluric data: *Geophysical Journal International*, **207**, 571–588.
- Key, K., and J. Owall, 2011, A parallel goal-oriented adaptive finite element method for 2.5-d electromagnetic modelling: *Geophysical Journal International*, **186**, 137–154.
- Langenbach, H., 2017, Anwendung des neu entwickelten 3D Zeitbereichs-Inversionsalgorithmus IP3DInv für die Induzierte Polarisation auf Messdaten aus Krauthausen, Deutschland: PhD thesis, Universität zu Köln.
- Ledo, J., 2005, 2-D Versus 3-D Magnetotelluric Data Interpretation: *Surveys in Geophysics*, **26**, 511–543.
- Levenberg, K., 1944, A Method for The Solution of Certain Non-Linear Problems in Least Squares: *Quarterly of Applied Mathematics*, **2**, 164–168.
- Lezaeta, P., and V. Haak, 2003, Beyond magnetotelluric decomposition: Induction, current channeling, and magnetotelluric phases over 90: *Journal of Geophysical Research: Solid Earth*, **108**. (2305).
- Li, Y., and S. Dai, 2011, Finite element modelling of marine controlled-source electromagnetic responses in two-dimensional dipping anisotropic conductivity structures: *Geophysical Journal International*, **185**, 622–636.
- Lu, X., M. Unsworth, and J. Booker, 1999, Rapid relaxation inversion of CSAMT data: *Geophysical Journal International*, **138**, 381.
- Mackie, R. L., B. R. Bennett, and T. R. Madden, 1988, Long-Period Magnetotelluric Measurements Near the Central California Coast: A Land-Locked View of the Conductivity Structure Under the Pacific Ocean: *Geophysical Journal*, **95**, 181–194.
- Madden, T. M., and R. L. Mackie, 1989, Three-dimensional magnetotelluric modelling and inversion: *Proceedings of the IEEE*, **77**, 318–333.
- Marcuello, A., P. Queralt, and J. Ledo, 2005, Applications of dispersion relations to the geomagnetic transfer function: *Physics of the Earth and Planetary Interiors*, **150**, 85 – 91. (Electromagnetic Induction in the Earth).
- Martin, R., 2009, Development and application of 2D and 3D transient electromagnetic inverse solutions based on adjoint Green functions: A feasibility study for the spatial reconstruction of conductivity distributions by means of sensitivities: PhD thesis, Universität zu Köln.
- McGillivray, P. R., D. W. Oldenburg, R. G. Ellis, and T. M. Habashy, 1994, Calculation of sensitivities for the frequency-domain electromagnetic problem: *Geophysical Journal*

- International, **116**, 1–4.
- Mickrokor, 2005, RMT-F1 and SM25 user manual: St. Petersburg University.
- , 2015, RMT-F1 and SM25M user manual: St. Petersburg University.
- Miensopust, M., 2010, Multidimensional magnetotellurics: A 2d case study and a 3d approach to simultaneously invert for resistivity structure and distortion parameters: PhD thesis, DIAS.
- Newman, G. A., S. Recher, B. Tezkan, and F. M. Neubauer, 2003, 3D inversion of a scalar radio magnetotelluric field data set: *Geophysics*, **68**, 791–802.
- Niblett, E. R., and C. Sayn-Wittgenstein, 1960, Variation of electrical conductivity with depth by the magnetotelluric method: *Geophysics*, **25**, 998–1008.
- Niwas, S., B. Tezkan, and M. Israil, 2011, Aquifer hydraulic conductivity estimation from surface geoelectrical measurements for Krauthausen test site, Germany: *Hydrogeology Journal*, **19**, 307–315.
- Nix, B., 2005, Radiomagnetotellurik-Messungen zur räumlichen und zeitlichen Ausbreitung eines Grundwasser-Tracers: Diploma thesis, Universität zu Köln.
- Nurhasan, Y. Ogawa, N. Ujihara, S. B. Tank, Y. Honkura, S. Onizawa, T. Mori, and M. Makino, 2006, Two electrical conductors beneath Kusatsu-Shirane volcano, Japan, imaged by audiomagnetotellurics, and their implications for the hydrothermal system: *Earth Planet Spaces*, **58**, 1053 – 1059.
- Oldenburg, D. W., and Y. Li, 1999, Estimating depth of investigation in dc resistivity and ip surveys: *GEOPHYSICS*, **64**, 403–416.
- Palacky, G. J., 1988, Resistivity characteristics of geologic targets, *in* *Electromagnetic Methods in Applied Geophysics: Soc. Expl. Geophys.*, **1**, 531–29.
- Parker, R., 1994, *Geophysical inverse theory*: Princeton University Press. Princeton series in geophysics.
- Parker, R. L., 2010, Can a 2-D MT frequency response always be interpreted as a 1-D response?: *Geophysical Journal International*, **181**, 269.
- Parkinson, W., 1959, Directions of rapid geomagnetic variations: *Geophys J R Astr Soc*, **2**, 1 – 14.
- Pedersen, L. B., M. Bastani, and L. Dinesius, 2005, Groundwater exploration using combined controlled-source and radiomagnetotelluric techniques: *Geophysics*, **70**, G8–G15.
- , 2006, Some characteristics of the electromagnetic field from radio transmitters in Europe: *Geophysics*, **71**, G279–G284.
- Pedersen, L. B., and B. Oskooi, 2004, Airborne VLF Measurements and Variations of Ground Conductivity: A Tutorial: *Surveys in Geophysics*, **25**, 151–181.
- Persson, L., and L. B. Pedersen, 2002, The importance of displacement currents in RMT measurements in high resistivity environments: *Journal of Applied Geophysics*, **51**, 11 – 20.
- Polak, E., 1971, *Computational method in optimization: A unified approach*: Academic Press.
- Qian, W., and L. B. Pedersen, 1991, Industrial interference magnetotellurics: An example from the Tangshan area, China: *Geophysics*, **56**, 265–273.
- Recher, S., 2002, Dreidimensionale Erkundung von Altlasten mit Radio-Magnetotellurik - Vergleiche mit geophysikalischen, geochemischen und geologischen Analysen an Bodenproben aus Rammkernsondierungen: PhD thesis, Universität zu Köln.

- Rikitake, T., 1951, Changes in earth current and their relation to the electrical state of the earth's crust: *Bull. earthq. Res. Inst. Univ. Tokyo*, **29**, 271 – 276.
- Rodi, W., and R. L. Mackie, 2001, Nonlinear conjugate gradients algorithm for 2-D magnetotelluric inversion: *Geophysics*, **66**, 174–187.
- Rodi, W. L., and R. L. Mackie, 2012, *The Inverse Problem, in The Magnetotelluric Method: Theory and Practice*: Cambridge University Press, 347 – 414.
- Saraev, A., A. Simakov, A. Shlykov, and B. Tezkan, 2017, Controlled source radiomagnetotellurics: A tool for near surface investigations in remote regions: *Journal of Applied Geophysics*, **146**, 228 – 237.
- Sasaki, Y., M.-J. Yi, J. Choi, and J.-S. Son, 2015, Frequency and time domain three-dimensional inversion of electromagnetic data for a grounded-wire source: *Journal of Applied Geophysics*, **112**, 106 – 114.
- Sauck, W., E. Atekwana, and M. Nash, 1998, High conductivities associated with an Inapl plume imaged by integrated geophysical techniques: *Journal of Environmental and Engineering Geophysics*, **2**, 203–212.
- Schmucker, U., 1970, Anomalies of Geomagnetic Variations in The Southwestern United States : *Bulletin Scripps The Institute of Oceanography*.
- Schwalenberg, K., V. Rath, and V. Haak, 2002, Sensitivity studies applied to a two-dimensional resistivity model from the Central Andes: *Geophysical Journal International*, **150**, 673.
- Seher, T., and B. Tezkan, 2007, Radiomagnetotelluric and Direct Current Resistivity measurements for the characterization of conducting soils: *Journal of Applied Geophysics*, **63**, 35 – 45.
- Shlykov, A., and A. Saraev, 2015, Estimating the Macroanisotropy of a Horizontally Layered Section from Controlled-Source Radiomagnetotelluric Soundings: *Izvestiya, Physics of the Solid Earth*, **51**, 583–601.
- Siegel, A., 1982, Robust regression using repeated medians: *Biometrika*, **69**, 242–244.
- Simakov, A., 2015: Personal Communication.
- , 2016: Personal Communication.
- Simpson, F., and K. Bahr, 2005, *Practical magnetotellurics*: Cambridge University Press.
- Siripunvaraporn, W., and G. Egbert, 2000, An efficient datasubspace inversion method for 2-d magnetotelluric data: *GEOPHYSICS*, **65**, 791–803.
- Smirnov, M. Y., 2003, Magnetotelluric data processing with a robust statistical procedure having a high breakdown point: *Geophysical Journal International*, **152**, 1.
- Spies, B. R., 1989, Depth of investigation in electromagnetic sounding methods: *GEOPHYSICS*, **54**, 872–888.
- Streich, R., 2016, Controlled-source electromagnetic approaches for hydrocarbon exploration and monitoring on land: *Surveys in Geophysics*, **37**, 47–80.
- Streich, R., and M. Becken, 2010, Electromagnetic fields generated by finitelength wire sources: comparison with point dipole solutions: *Geophysical Prospecting*, **59**, 361–374.
- Streich, R., M. Becken, U. Matzander, and O. Ritter, 2011, Strategies for land-based controlled-source electromagnetic surveying in high-noise regions: *The Leading Edge*, **30**, 1174–1181.
- Suzuki, K., S. Toda, K. Kusunoki, Y. Fujimitsu, T. Mogi, and A. Jomori, 2000, Case studies of electrical and electromagnetic methods applied to mapping active faults beneath the

- thick quaternary: *Engineering Geology*, **56**, 29 – 45.
- Swift, C. M., 1967, A Magnetotelluric Investigation of an Electrical Conductivity Anomaly in the Southwestern United States: PhD thesis, MIT.
- Szarka, L., 1988, Geophysical aspects of man-made electromagnetic noise in the earth—A review: *Surveys in Geophysics*, **9**, 287–318.
- Tang, K. T., 2007, *Mathematical methods for engineers and scientists 2*: Springer Berlin Heidelberg.
- Telford, W. M., L. P. Geldart, and R. E. Sheriff, 1990, *Applied geophysics*: Cambridge University Press.
- Tezkan, B., 2008, Radiomagnetotellurics, *in* *Groundwater geophysics - a tool for hydrogeology*: Springer-Verlag Berlin-Heidelberg, 295 – 317.
- Tezkan, B., P. Georgescu, and U. Fauzi, 2005, A radiomagnetotelluric survey on an oil-contaminated area near the Brazi Refinery, Romania: *Geophysical Prospecting*, **53**, 311–323.
- Tezkan, B., M. Goldman, S. Greinwald, A. Hördt, I. Müller, F. Neubauer, and G. Zacher, 1996, A joint application of radiomagnetotellurics and transient electromagnetics to the investigation of a waste deposit in cologne (germany): *Journal of Applied Geophysics*, **34**, 199 – 212.
- Tikhonov, A. N., 1950, On determination of electric characteristics of deep layers of the earth's crust: *Dokl. Acad. Nauk SSSR*, **151**, 295 – 297.
- Turberg, P., I. Müller, and F. Flury, 1994, Hydrogeological investigation of porous environments by radio magnetotelluric-resistivity (RMT-R 12240 kHz): *Journal of Applied Geophysics*, **31**, 133 – 143.
- Vanhala, H., 1997, Mapping oil-contaminated sand and till with the spectral induced polarization (sip) method: *Geophysical Prospecting*, **45**, 303–326.
- Vozoff, K., 1972, The magnetotelluric method in the exploration of sedimentary basins: *Geophysics*, **37**, 98–141.
- Wait, J. R., 1954, On The Relation Between Telluric Currents and The Earth's Magnetic Field: *GEOPHYSICS*, **19**, 281–289.
- Wang, S., 2017, Joint inversion and integration of multiple geophysical data for improved models of near-surface structures: PhD thesis, Uppsala University, Geophysics.
- Wannamaker, P. E., T. G. Caldwell, W. M. Doerner, and G. R. Jiracek, 2004, Fault zone and seismicity in compressional and extensional environments inferred from electrical conductivity: the New Zealand Southern Alps and U.S. Great Basin: *Earth Planet Spaces*, **56**, 1171 – 1176.
- Ward, S. H., and G. W. Hohmann, 1988, Electromagnetic Theory for Geophysical Applications, *in* *Electromagnetic Methods in Applied Geophysics*: Tulsa: SEG, **1**, 131 – 311.
- Weidelt, P., 1972, The inverse problem of geomagnetic induction: *Z: Geophysics*, **38**, 257–289.
- , 2000, Numerical modelling of transient-electromagnetic fields in three-dimensional conductors: A comparative study , *in* *Elektromagnetische Tiefenforschung*, 18. Kolloquium: Dt. Geophys. Gesellschaft, 216–231.
- Weidelt, P., and P. Kaikkonen, 1994, Local 1-D interpretation of magnetotelluric B-polarization impedances: *Geophysical Journal International*, **117**, 733.
- Werkema, D. D., E. A. Atekwana, A. L. Endres, W. A. Sauck, and D. P. Cassidy, 2003, Investigating the geoelectrical response of hydrocarbon contamination undergoing

- biodegradation: *Geophysical Research Letters*, **30**, n/a–n/a. (1647).
- Widodo, M. Gurk, and B. Tezkan, 2016, Multi-dimensional Interpretation of Radiomagnetotelluric and Transient Electromagnetic Data to Study Active Faults in the Mygdonian Basin, Northern Greece: *Journal of Environmental and Engineering Geophysics*, **21**, 121–133.
- Wiese, H., 1962, Geomagnetische Tiefentellurik Teil II: Die Streichrichtung der untergrundstrukturen des elektrischen Widerstandes, erschlossen aus geomagnetischen Variationen: *Geofisica Pura e Applicata*, **52**, 83103.
- Yee, K., 1966, Numerical solution of initial boundary value problems involving Maxwell's equations in isotropic media: *IEEE Transactions on Antennas and Propagation*, **14**, 302–307.
- Yogeshwar, P., 2014, A resistivity-depth model of the central Azraq basin area, Jordan: 2D forward and inverse modeling of time domain electromagnetic data: PhD thesis, Universität zu Köln.
- Yogeshwar, P., B. Tezkan, M. Israil, and M. Candansayar, 2012, Groundwater contamination in the Roorkee area, India: 2D joint inversion of radiomagnetotelluric and direct current resistivity data : *Journal of Applied Geophysics*, **76**, 127 – 135.
- Zonge, K. L., and L. J. Huges, 1991, Controlled source audio-frequency magnetotellurics, *in* *Electromagnetic Methods in Applied Geophysics*: Tulsa: SEG, **2**, 713 – 809.

Appendix A

Example of SLDMEM3f Grid

In this Appendix, an example for the grid design for SLDMEM3f and the output are given. Before I start, I will give the description of the required inputs for the SLDMEM3f, the implementation can be found on the example. Hopefully, it would be self-explaining.

Name	description
ms	number of steps
eps	threshold, 10E-10
is1	subspace step, 100
is2	subspace step, 100
istr	subspace step, 100
lotem	not defined in frequency domain, put 0
npc	number of receiver(s) $npc = nxye + nxym$
nxye	number of electric receiver(s)
nxym	number of magnetic receiver(s)
nt	number of angular frequency
tm	angular frequency list ($2\pi f$)
nx	number of grid discretization on x direction
rx	grid point on x direction
ny	number of grid discretization on y direction
ry	grid point on y direction
nz	number of grid discretization on z direction
rz	grid point on z direction
np x	location of receivers in $-x$ direction, electric field receivers are in first
np y	location of receivers in $-y$ direction, electric field receivers are in first
np z	location of receivers in $-z$ direction, electric field receivers are in first, put 0.1 m for this
np l	direction of receivers, 1 is x , 2 is y , 3 is z
nie	number of electric sources on the grid
nim	location of magnetic sources on the grid
nix	location of electric sources on the grid for x direction

Continued on next page

Table A.1 – continued from previous page

Name	description
niy	location of magnetic sources on the grid y direction
niz	location of magnetic sources on the grid z direction
nil	direction of sources,
ti	source amplitude
teta	only defined for natural source (MT), all the source parameter could be set to zero and teta should be 0.1
nbl	number of conductivity block
fon	background conductivity
shx	shift conductivity on x direction
shy	shift conductivity on y direction
xl	left boundary of conductivity block(s) in x direction
xp	right boundary of conductivity block(s) in x direction
yl	left boundary of conductivity block(s) in y direction
yp	right boundary of conductivity block(s) in y direction
zl	top boundary of conductivity block(s) in z direction
zp	bottom boundary of conductivity block(s) in z direction
sg	conductivity of block(s)

A.1 Grid Example

& START

ms= 10000 ,eps= 9.99999975E-06 ,

is1= 100 ,is2= 100 ,istr= 100 ,

lotem= 0 ,

npc= 4 ,nxye= 2 ,nxym= 2,

nt = 10,

tm =

6.283185e+03, 7.234431e+03, 8.329690e+03, 9.590767e+03, 1.104276e+04,

1.271459e+04, 1.463952e+04, 1.685587e+04, 1.940778e+04, 2.234602e+04,

nx= 63,

rx=

-2.0000 , -1.9000, -1.8000, -1.7000, -1.6000, -1.5000, -1.4000, -1.3000, -1.2000,

-1.1000, -1.0000, -0.9000, -0.8000, -0.7000, -0.6000, -0.5000, -0.4000, -0.3500,

-0.2000, -0.1000, 0.1000, 0.2000, 0.3500, 0.3510, 0.3520, 0.3530, 0.3570, 0.3630,

0.3700, 0.3900, 0.4100, 0.4300, 0.4500, 0.4700, 0.4900, 0.5100, 0.5300, 0.5500,

0.5700, 0.5900, 0.6100, 0.6300, 0.6500, 0.6700, 0.6900, 0.7100, 0.7300, 0.7500,

0.7700, 0.7900, 0.8100, 0.9000, 1.0000, 1.1000, 1.2000, 1.3000, 1.4000, 1.5000,

1.6000, 1.7000, 1.8000, 1.9000, 2.0000,

ny= 41 ,

ry=

-2.0000, -1.9000, -1.8000, -1.7000, -1.6000, -1.5000, -1.4000, -1.3000, -1.2000,

-1.1000, -1.0000, -0.9000, -0.8000, -0.7000, -0.6000, -0.5000, -0.4000, -0.3000, -

0.2000, -0.1000, 0, 0.1000, 0.2000, 0.3000, 0.4000, 0.5000, 0.6000, 0.7000, 0.8000,

```
0.9000, 1.0000, 1.1000, 1.2000, 1.3000, 1.4000, 1.5000, 1.6000, 1.7000, 1.8000,
1.9000, 2.0000,
nz= 65 ,
rz=
0.000 , 0.7284E-03, 0.1558E-02, 0.2401E-02, 0.3261E-02, 0.4139E-02,
0.5037E-02, 0.5959E-02, 0.6908E-02, 0.7888E-02, 0.8903E-02, 0.9957E-02,
0.1106E-01, 0.1221E-01, 0.1342E-01, 0.1469E-01, 0.1605E-01, 0.1749E-01,
0.1903E-01, 0.2068E-01, 0.2245E-01, 0.2438E-01, 0.2647E-01, 0.2875E-01,
0.3125E-01, 0.3399E-01, 0.3701E-01, 0.4035E-01, 0.4405E-01, 0.4816E-01,
0.5275E-01, 0.5786E-01, 0.6359E-01, 0.7002E-01, 0.7723E-01, 0.8535E-01,
0.9449E-01, 0.1048 , 0.1164 , 0.1296 , 0.1445 , 0.1613 ,
0.1804 , 0.2020 , 0.2266 , 0.2544 , 0.2860 , 0.3219 ,
0.3627 , 0.4090 , 0.4617 , 0.5216 , 0.5897 , 0.6671 ,
0.7552 , 0.8555 , 0.9695 , 1.099 , 1.247 , 1.415 ,
1.607 , 1.824 , 2.072 , 2.355 , 2.676 ,
npx=
30, 31,
30, 31,
npy=
21, 21,
21, 21,
npz=
1, 1,
1, 1,
npl=
1, 1,
2, 2,
nie= 6 ,nim=0,
nix=
18, 19, 20, 21, 22, 23,
niy=
21, 21, 21, 21, 21, 21,
niz=
1, 1, 1, 1, 1, 1,
nil=
1, 1, 1, 1, 1, 1,
ti=
1.000 , 1.000 , 1.000 , 1.000 , 1.000 , 1.000 ,
& END
& MODEL
nbl= 1 ,fon= 0.002 ,
shx= 0.00000000 , shy= 0.00000000 ,
xl=-50,
xp=50,
yl=-50,
yp=50,
```

```

zl=0.04,
zp=0.05,
sg=0.0002,
& END

```

A.2 Output

The output of the program (electromagnetic fields) is given on the `sldmem.logfile`. The first column is the angular frequency. The electromagnetic fields are given in Real and Imaginary part. For example if we only specify one receiver either electric or magnetic fields in any direction, column 2 is the real part and column 3 is the imaginary part. When the electric E and magnetic B fields are calculated, the electric fields are first printed out. If the lengths are in km, the output are in mV/km and mV/km² for electric and magnetic fields respectively. An example of `sldmem.logfile` without any header. The maximum number of column is 500 in one line.

angular frequency	E (real)	E (imag)	B (real)	B (imag)
1	1	1	1	1
⋮	⋮	⋮	⋮	⋮
end	end	end	end	end

Appendix B

Vuoksa Experiment Extended

In this appendix, I will show the sensitivity, DOI according to Seher and Tezkan (2007) and $2z^*$ mapping for the experiment in Vuoksa region, Russia in Chapter 5. In addition, data fits for selected frequency and stations are also given.

B.1 The far field zone

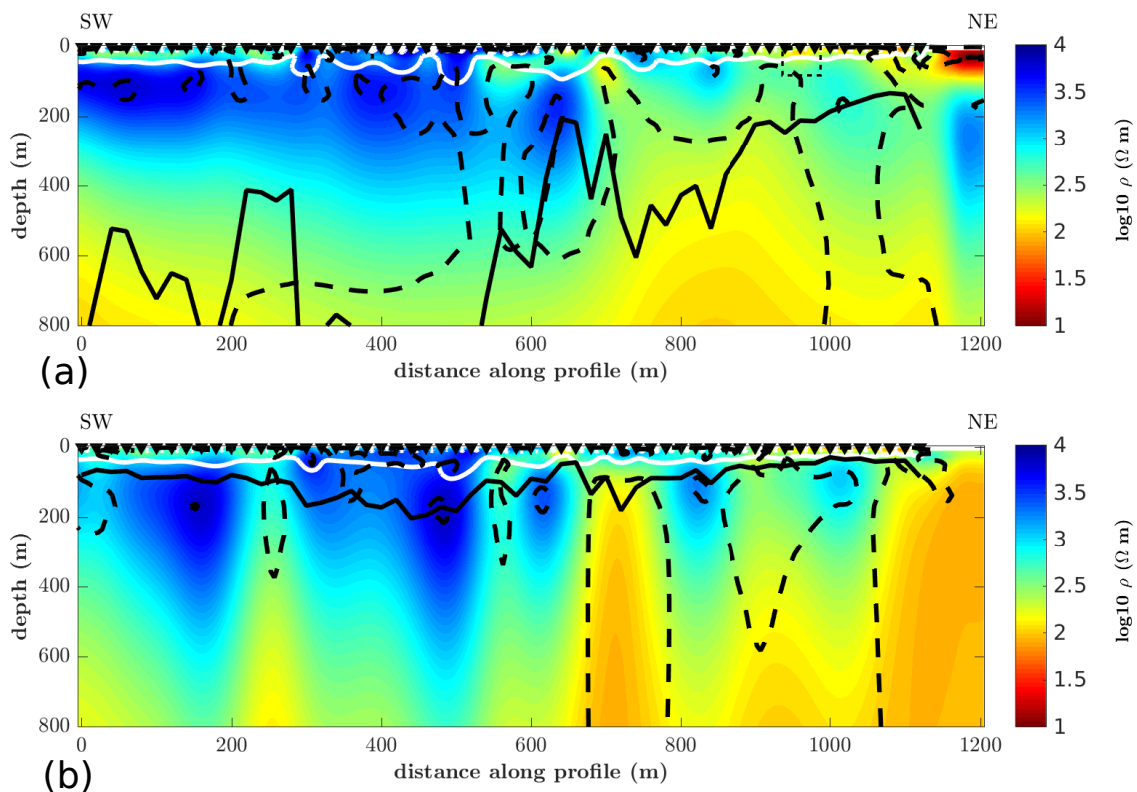


Figure B.1: Sensitivity of 10^{-3} in white solid line, DOI according to Seher and Tezkan (2007) in dashed back line and $2z^*$ in solid black line of (a) CSRMT data and (b) RMT data in the far field zone profile of Vuoksa experiment in Chapter 5. With this reason, the models are plotted up to 100 m.

B.2 The near field zone

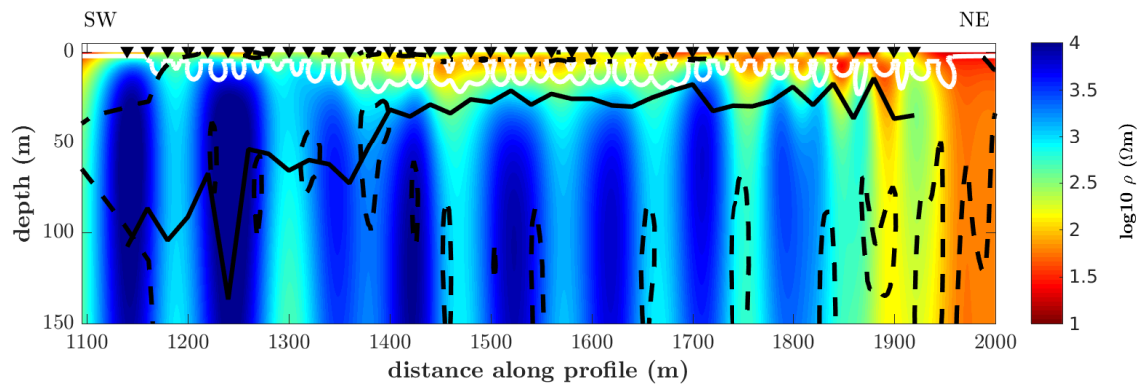


Figure B.2: Sensitivity of 10^{-3} in white solid line, DOI according to Seher and Tezkan (2007) in dashed back line and $2z^*$ in solid black line of CSRMT data (up) and RMT data (down) in the near field zone profile of Vuoksa experiment in Chapter 5. With this reason, the models are plotted up to 100 m.

Appendix C

Krauthausen Experiment Extended

In this appendix, I will show the sensitivity, DOI according to Seher and Tezkan (2007) and $2z^*$ mapping for the experiment in Krauthausen test area, Germany in Chapter 6.

C.1 DOI

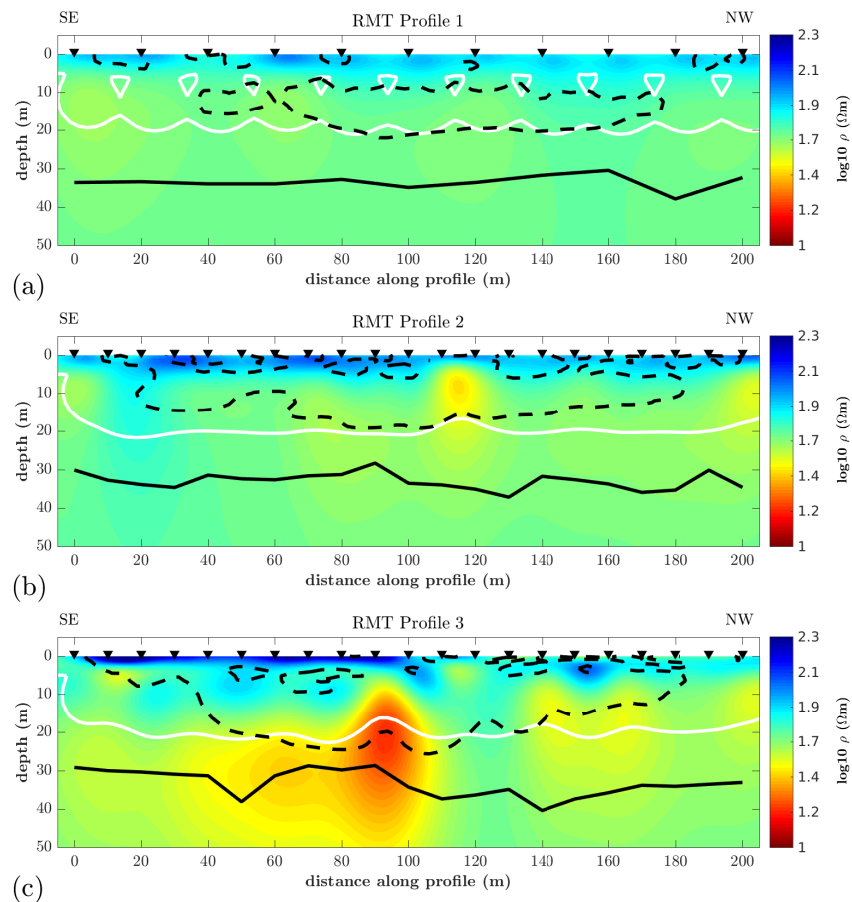


Figure C.1: Sensitivity of 10^{-3} in white solid line, DOI according to Seher and Tezkan (2007) in dashed back line and $2z^*$ in solid black line of (a) Profile 1 and (b) Profile 2 (c) Profile 3 for the RMT data measured in Krauthausen test area discussed in Chapter 6. With this reason, the models are plotted up to 30 m.

Appendix D

Radervormwald Experiment Extended

In this appendix, I will show the sensitivity, DOI according to Seher and Tezkan (2007) and $2z^*$ mapping for the experiment in LSV Radervormwald, Germany in Chapter 7. Furthermore, data fit of selected stations are also displayed.

D.1 DOI

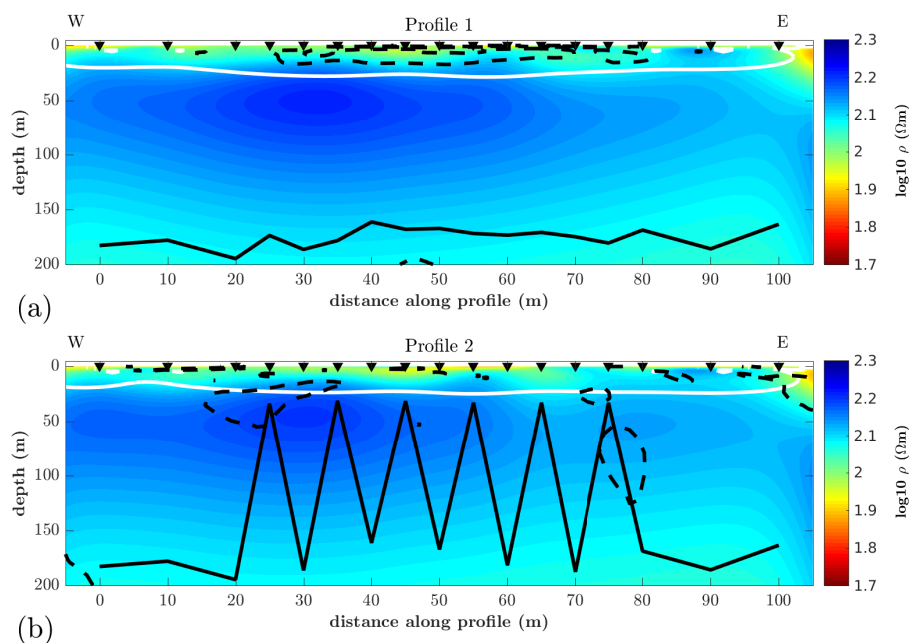


Figure D.1: Sensitivity of 10^{-3} in white solid line, DOI according to Seher and Tezkan (2007) in dashed back line and $2z^*$ in solid black line of (a) Profile 1 and (b) Profile 2 for the measured data discussed in Chapter 7. Note that for the Profile 2, the CSRMT and RMT data were inverted together, thus the $2z^*$ shows an oscillation due to different lowest frequency in both methods. With this reason, the models are plotted up to 30 m.

D.2 Additional Data Fit

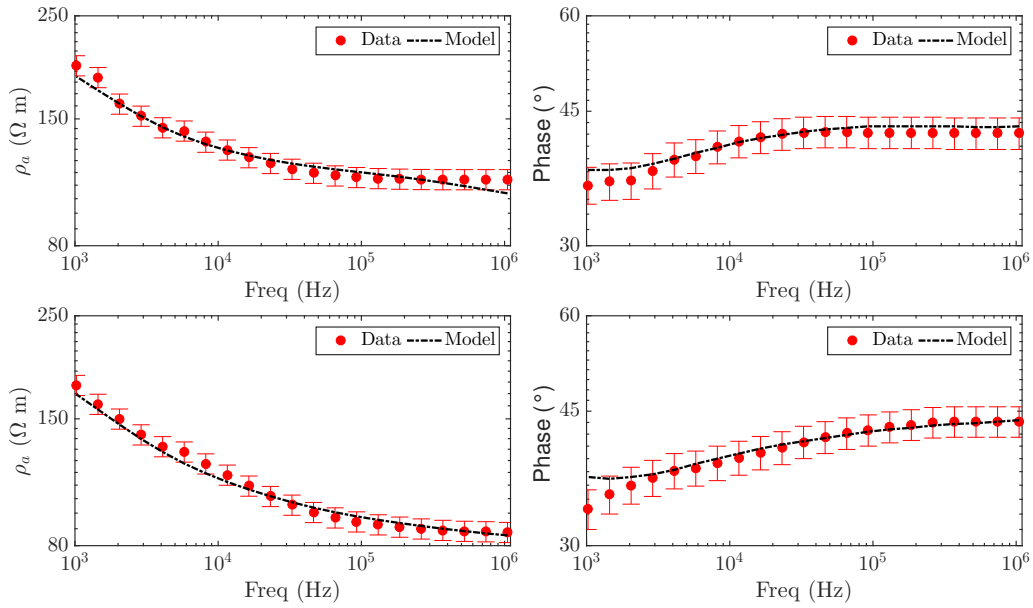


Figure D.2: Data fit for station 1 (up) and 17 (down) of Profile 1

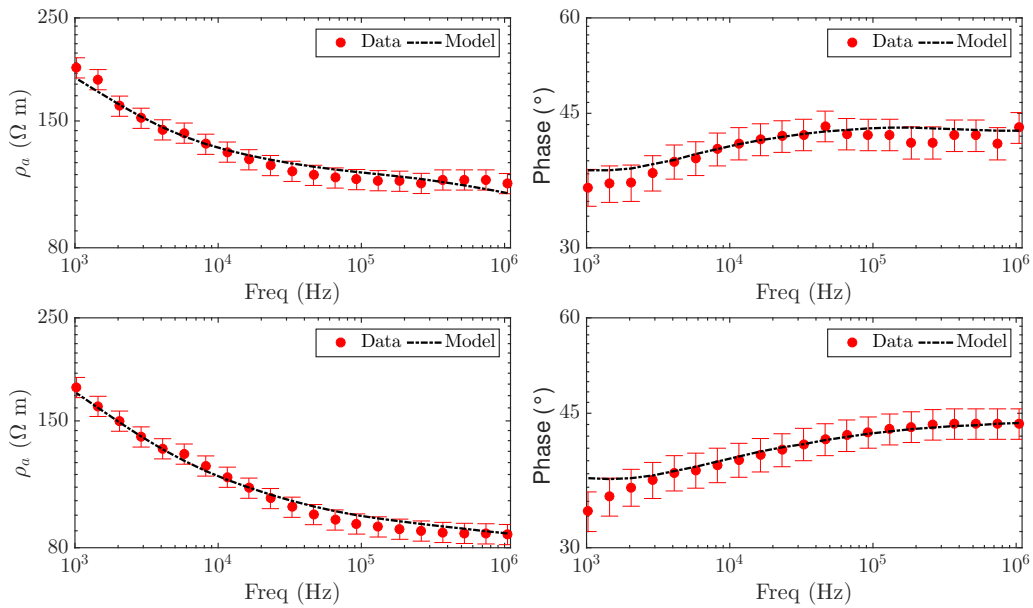


Figure D.3: Data fit for station 1 (up) and 17 (down) of Profile 2.

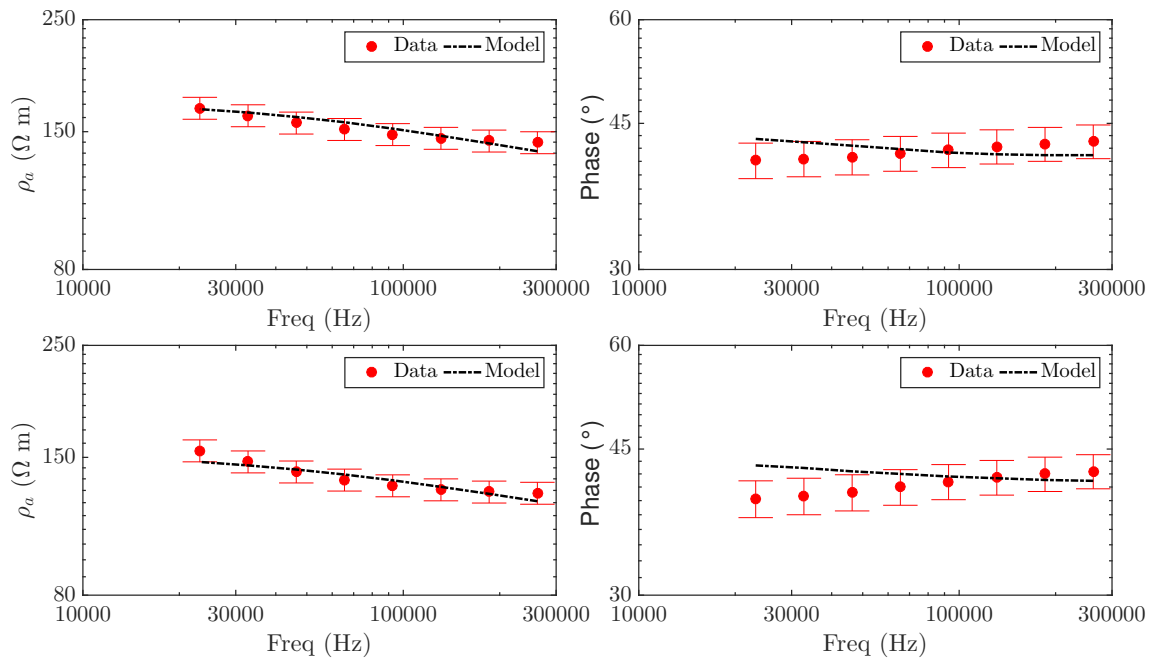


Figure D.4: Data fit for station 1 (up), 10 (middle) and 17 (down) for the reference profile.

Acknowledgment

I would like to thank:

- Prof. Dr. Bülent Tezkan who gave me the opportunity to join the group and teaches me electromagnetic geophysics.
- Prof. Dr. Andreas Junge for appraising this thesis.
- Dr. Marcus Gurk who shared many things in the office in the last 2 years, his experiences in geophysics helped me a lot.
- Dr. Pritam Yogeshwar who helped me when I first came to the Institute with his experiences in the RMT method.
- Dr. Jan Wittke, Wiebke Mörbe, and Dr. Ismael Ibraheem who peer reviewed my thesis and gave many corrections and suggestions.
- People who helped me in during field works. Vuoksa: Dr. Alexander Saraev and his students, Alex Simakov. Krauthausen: Janine Böckamnn, Mira Küpper, Amir Haroon, David Ossen, Sascha Janser, Ismail Ibraheem. Radervormawald experiment: Ismail Ibraheem, Amir Haroon, Janine Böckamnn, Nadine Pützer, Paula Ruff (GFZ), Diego, Cai Ji and Wiebke Mörbe.
- All members of Geophysics group.
- Dr. A. Shlykov for his CS1D code and Dr. Shunguo Wang for modified MARE2DEM.
- MORA Scholarship from Indonesian Government and GSGS Funding for the travel grant to Thailand and the financial support (GSGS Fellowship Grant No. GSGS-2018A-F03).
- Prof. Dr. Umar Fauzi and Dr. Widodo gave me some advice to successfully study in Köln.
- My family.
- My wife, Icha, who has been very supportive since the beginning of my PhD.

Erklärung

Ich versichere, dass ich die von mir vorgelegte Dissertation selbständig angefertigt, die benutzten Quellen und Hilfsmittel vollständig angegeben und die Stellen der Arbeit - einschließlich Tabellen, Karten und Abbildungen-, die anderen Werken im Wortlaut oder dem Sinn nach entnommen sind, in jedem Einzelfall als Entlehnung kenntlich gemacht habe; dass diese Dissertation noch keiner anderen Fakultät oder Universität zur Prüfung vorgelegen hat; dass sie -abgesehen von unten angegebenen Teilpublikationen- noch nicht veröffentlicht worden ist sowie, dass ich eine solche Veröffentlichung vor Abschluss des Promotionsverfahrens nicht vornehmen werde. Die Bestimmungen dieser Promotionsordnung sind mir bekannt. Die von mir vorgelegte Dissertation ist von Prof. Dr. Bülent Tezkan betreut worden.

Köln, 23.07.2018

Imamal Muttaqien

Teilpublikationen

B. Tezkan, I. Muttaqien, and A. Saraev, *Mapping of buried faults using the 2D modelling of far-field controlled source radiomagnetotelluric data*, under review from Pure and Applied Geophysics.